Cargèse Summer School

Background Information

accompagning the lecture

Anisotropic Interactions

Beat H. Meier, Physical Chemistry, ETH Zurich, beme@ethz.ch

NOTE that this is NOT the a copy of the lecture slides but a scriptum containing the background information.

1 NMR Hamiltonians, a recapitulation

1.1 Interaction With an External Field B_0

The interaction of a spin with the external magnetic field, that is always described classically, is called the *Zeeman interaction* and is of the form:

$$\hat{\mathcal{H}}_z = -\sum_i \gamma_i \hat{\vec{I}}_i \cdot \vec{B_0} \qquad [1.1]$$

or, assuming $\vec{B_0} = (0, 0, B_0)$

$$\hat{\mathcal{H}}_z = \sum_i \omega_{0i} \hat{I}_{iz} \ . \qquad [1.2]$$

Equation [1.1] can easily be derived from the classical energy of a magnetic dipole $\vec{\mu}$ in a magnetic field ($E_{pot} = -\vec{\mu} \cdot \vec{B}$,) and the gyromagnetic equation ($\vec{\mu} = \gamma \vec{L}$) using the principle of correspondence.

Note that only the externally applied field $\vec{B_0}$ is considered here. There is a usually small difference between $\hat{\mathcal{H}}_{BI}$ (Chapter 4.12) and $\hat{\mathcal{H}}_z$. $\hat{\mathcal{H}}_z$ is the interaction with the applied external field B_0 only. The magnetic field at the site of the nuclei k, $\vec{B_k}$ is modified through the electronic environment. This effect, the chemical shift, is excluded from the Zeeman Hamiltonian.

1.2 Interaction With an Rf-Field B_1

The interaction with either a *linearly polarized* rf field:

$$\vec{B_1} = B_1(t)(\cos[\omega_{rf}t + \varphi(t)], 0, 0) \qquad [1.3]$$

or a *circularly polarized* rf field:

$$\vec{B_1} = B_1(t)(\cos[\omega_{rf}t + \varphi(t)], \sin[\omega_{rf}t + \varphi(t)], 0) \qquad [1.4]$$

is described, in complete analogy to the Zeeman Hamiltonian (Eq. [1.1]), as

$$\hat{\mathcal{H}}_{rf}(t) = -\sum_i \gamma_i \vec{\hat{I}}_i \cdot \vec{B_1}(t) \qquad [1.5]$$

In multiple-resonance experiments, $\vec{B_1}$ consists of a sum of individual fields.

1.3 Interaction Frame Representation

An interaction-frame representation is a concept that generalizes the rotating-frame representation that we have discussed earlier. We describe the spin system in an interaction frame with respect to the interaction $\hat{\mathcal{H}}_0 = \sum_i \omega_{rf,i} \hat{I}_{iz}$. Here, $\omega_{rf,i}$ will be chosen close to $\omega_{0,i}$ and $\hat{\mathcal{H}}_0 \approx \hat{\mathcal{H}}_z$. An operator $\hat{A}'$ in the interaction frame of reference is related to the original operator $\hat{A}$ by:

$$\hat{A}' = \hat{R}(t)\hat{A}\hat{R}^{-1}(t) \ . \qquad [1.6]$$

We choose the rotation matrix as

$$\hat{R}(t) = e^{i\hat{\mathcal{H}}_0 t} \qquad [1.7]$$

For the case where only one type of nuclei is considered, we have

$$\hat{\mathcal{H}}_0 = \sum_l \omega_{rf,l} \hat{I}_{lz} = \omega_{rf} \hat{F}_z \qquad [1.8]$$

with the *total spin operator* $\hat{F}_z = \sum_l \hat{I}_{lz}$.

To evaluate the time dependence of the density operator in the rotating frame $\hat{\sigma}'$, we need to know the equivalent of the Liouville-von Neumann equation in the interaction frame. The procedure followed is reminiscent of the transformation to the rotating frame in the classical description. The relationship between $\hat{\sigma}$ and $\hat{\sigma}'$ is given by Eq. [1.6]:

$$\begin{aligned} \hat{\sigma}' &= \hat{R}(t)\hat{\sigma}\hat{R}^{-1}(t) \\ \hat{\sigma} &= \hat{R}^{-1}(t)\hat{\sigma}'\hat{R}(t) \end{aligned} \qquad [1.9]$$

$$
\begin{aligned}
&\frac{d}{dt}(\hat{R}^{-1}\hat{\sigma}'\hat{R}) = -i[\hat{\mathcal{H}}\hat{R}^{-1}\hat{\sigma}'\hat{R} - \hat{R}^{-1}\hat{\sigma}'\hat{R}\hat{\mathcal{H}}] \\
&-i\omega_{rf}\hat{F}_z\hat{R}^{-1}\hat{\sigma}'\hat{R} + \hat{R}^{-1}\frac{d}{dt}\hat{\sigma}'\hat{R} + \hat{R}^{-1}\hat{\sigma}'i\omega_{rf}\hat{F}_z\hat{R} = -i[\hat{\mathcal{H}}\hat{R}^{-1}\hat{\sigma}'\hat{R} - \hat{R}^{-1}\hat{\sigma}'\hat{R}\hat{\mathcal{H}}] \\
&\hat{R}^{-1}\frac{d}{dt}\hat{\sigma}'\hat{R} = -i[\hat{\mathcal{H}}\hat{R}^{-1}\hat{\sigma}'\hat{R} - \hat{R}^{-1}\hat{\sigma}'\hat{R}\hat{\mathcal{H}} - \omega_{rf}(\hat{F}_z\hat{R}^{-1}\hat{\sigma}'\hat{R} - \hat{R}^{-1}\hat{\sigma}'\hat{F}_z\hat{R})] \\
&\frac{d}{dt}\hat{\sigma}' = -i[\hat{R}\hat{\mathcal{H}}\hat{R}^{-1}\hat{\sigma}' - (\hat{\sigma}'\hat{R}\hat{\mathcal{H}}\hat{R}^{-1} - \omega_{rf}(\hat{F}_z\hat{\sigma}' - \hat{\sigma}'\hat{F}_z))] \\
&\frac{d}{dt}\hat{\sigma}' = -i[\hat{\mathcal{H}}' - \omega_{rf}\hat{F}_z, \hat{\sigma}']
\end{aligned}
\qquad [1.10]
$$

Here $\hat{\mathcal{H}}' = \hat{R}\hat{\mathcal{H}}\hat{R}^{-1}$ is the transformed Hamiltonian. In going from line 3 to line 4, we have multiplied, from the left with $\hat{R}$ and from the right with $\hat{R}^{-1}$. We have used that $\hat{F}_z$ commutes with $\hat{R}$ (because of [1.8]). Note that the last line in Eq. [1.10] is **not** just equal to the Liouville-van Neumann equation for the dashed operators but that:

$$\frac{d}{dt}\hat{\sigma}' = -i[\hat{\mathcal{H}}' - \hat{\mathcal{H}}_0, \hat{\sigma}'] \qquad [1.11]$$

A new term $-\hat{\mathcal{H}}_0$ appears which represents the fact that the new coordinate system is accelerated with respect to the original coordinate system. Eq. [1.11] is valid irrespective of the choice of $\hat{\mathcal{H}}_0$. Often, the identification $\hat{\mathcal{H}}'' = \hat{\mathcal{H}}' - \hat{\mathcal{H}}_0$ is made and $\hat{\mathcal{H}}''$ is then called the interaction-frame Hamiltonian. Then, we recover the standard Liouville-van Neumann equation:

$$\frac{d}{dt}\hat{\sigma}' = [\hat{\mathcal{H}}'', \hat{\sigma}'] \qquad [1.12]$$

Care has to be exercised not to mix up $\hat{\mathcal{H}}'$ and $\hat{\mathcal{H}}''$. By going into the interaction frame, we have not only changed the active Hamiltonian $\hat{\mathcal{H}}''$ but we have also manipulated the time dependence of the Hamiltonian.

For the operators $\hat{I}_x$, $\hat{I}_y$ and $\hat{I}_z$, we find:

$$
\begin{aligned}
&\hat{I}'_x \to \hat{I}_x\cos(\omega_{rf}t) + \hat{I}_y\sin(\omega_{rf}t) \\
&\hat{I}'_y \to \hat{I}_y\cos(\omega_{rf}t) - \hat{I}_x\sin(\omega_{rf}t) \\
&\hat{I}'_z \to \hat{I}_z
\end{aligned}
\qquad [1.13]
$$

If we compare Eq. [1.13] with the expression for the transformation of a classical vector to the rotating frame (Eq. [2.2]) we find that they are fully equivalent.

The rf-Hamiltonian in the interaction frame is given by (for simplicity, we set $\varphi(t) = 0$):

$$\hat{\mathcal{H}}'_{rf} = -\sum_i \gamma_i B_1 \hat{I}'_{ix} \qquad [1.14]$$

For arbitrary values of $\varphi(t)$, we have:

$$\begin{aligned}\hat{\mathcal{H}}'_{rf} &= -\sum_i \gamma_i B_1 (\hat{I}'_x \cos\varphi(t) + \hat{I}'_y \sin\varphi(t)) \\ &= \sum_i \omega_{1i} (\hat{I}'_x \cos\varphi(t) + \hat{I}'_y \sin\varphi(t))\end{aligned} \qquad [1.15]$$

Often, the dash in, e.g., $\hat{I}'_x$ is left away. The interaction-frame Hamiltonian $\hat{\mathcal{H}}''$ for a spin system with a lab-frame Hamiltonian of $\hat{\mathcal{H}} = \hat{\mathcal{H}}_z + \hat{\mathcal{H}}_{rf}$ is given by:

$$\hat{\mathcal{H}}'' = \hat{\mathcal{H}}'_{rf} + \Omega \hat{F}_z \qquad [1.16]$$

where $\Omega = \omega_0 - \omega_{rf}$ and for $\Omega = 0$ by

$$\hat{\mathcal{H}}'' = \hat{\mathcal{H}}'_{rf}. \qquad [1.17]$$

Box I: Rotating Frame

By transforming into the rotating frame, we have:

- Changed the Hamiltonian, i.e., for $\omega_{rf} = \omega_0$, we have removed the Zeeman term.
- Removed the time-dependence from the rf Hamiltonian.
- Usually, the remaining time-dependent terms are neglected. This approximation is called the secular approximation and must be justified on a case-by-case basis.

1.4 The Chemical-Shift or Chemical Shielding Hamiltonian

The magnetic field at the site of different nuclei k, $\vec{B}_k$ differs from the applied magnetic field, due to the interaction with the surrounding electrons. It is *shielded* by the electrons and leads to a *shift* of the resonance line in the NMR spectrum. We express the field at the position of the nucleus as

$$\vec{B}_k = \vec{B}_0 + \vec{B}_S \qquad [1.18]$$

The correction field $\vec{B}_S$ is proportional to the static field $\vec{B}_0$ and we can write:

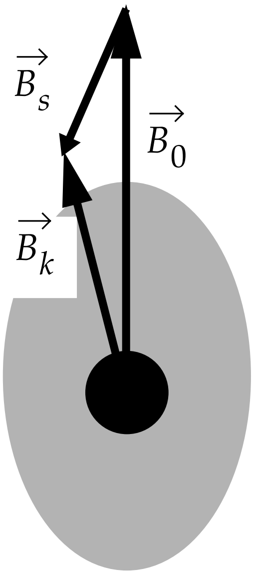

Figure 1.1: Local B Field

$$\begin{bmatrix} B_{S,x} \\ B_{S,y} \\ B_{S,z} \end{bmatrix} = -\begin{bmatrix} \sigma_{xx}^{(k)} & \sigma_{xy}^{(k)} & \sigma_{xz}^{(k)} \\ \sigma_{yx}^{(k)} & \sigma_{yy}^{(k)} & \sigma_{yz}^{(k)} \\ \sigma_{zx}^{(k)} & \sigma_{zy}^{(k)} & \sigma_{zz}^{(k)} \end{bmatrix} \begin{bmatrix} 0 \\ 0 \\ B_0 \end{bmatrix} \qquad [1.19]$$

The Hamiltonian that describes the interaction with the correction field is, therefore, given by

$$\hat{\mathcal{H}}_S = \sum_k \gamma_k (\hat{I}_{kx}, \hat{I}_{ky}, \hat{I}_{kz}) \begin{bmatrix} \sigma_{xx}^{(k)} & \sigma_{xy}^{(k)} & \sigma_{xz}^{(k)} \\ \sigma_{yx}^{(k)} & \sigma_{yy}^{(k)} & \sigma_{yz}^{(k)} \\ \sigma_{zx}^{(k)} & \sigma_{zy}^{(k)} & \sigma_{zz}^{(k)} \end{bmatrix} \begin{bmatrix} 0 \\ 0 \\ B_0 \end{bmatrix} \qquad [1.20]$$

or, in compact form:

$$\hat{\mathcal{H}}_S = \sum_k \gamma_k \vec{\hat{I}}_k \cdot \underline{\sigma}^{(k)} \cdot \vec{B}_0 \qquad [1.21]$$

The resulting Hamiltonian is a scalar operator. The quantity $\underline{\sigma}$ is the anisotropic chemical-shielding tensor (CSA).

In the interaction frame (high-field approximation), the transverse terms $\hat{I}'_x$ and $\hat{I}'_y$ are time-dependent with the Larmor frequency with an average value of zero. They can, therefore, be neglected as "non-secular" terms in a good approximation. In the interaction frame, the chemical-shielding Hamiltonian simplifies to:

$$\hat{\mathcal{H}}'_S = \sum_k \gamma_k \sigma_{zz}^{(k)} B_0 \hat{I}_{kz} \qquad [1.22]$$

The transition frequency in the Hamiltonian is given by $\omega_{12} = -\sigma_{zz}^{(k)}\omega_0$ and the spectrum consists of a single line at position ω_{12} (if given in angular frequencies) or at $-\sigma_{zz}^{(k)}$ if given in ppm. If the three principal values of $\underline{\sigma}^{(k)}$ are identical, we can replace them by a scalar quantity, the so-called isotropic chemical shift, σ_{iso}, times a unity matrix.

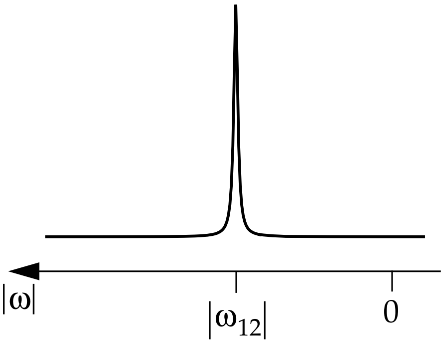

Figure 1.2: Chemical Shift

The isotropic chemical shift is given by:

$$\sigma_{iso} = \frac{1}{3}(\sigma_{xx} + \sigma_{yy} + \sigma_{zz}) \qquad [1.23]$$

Such an isotropic interaction is also obtained in liquid phase where the tumbling of the molecules leads to an averaged chemical shift. Here, σ_{iso} takes then the role of $\sigma_{zz}^{(k)}$ in Eq. [1.22].

The isotropic chemical shift is zero for a bare nucleus. Nuclei in molecules are almost always more shielded than the bare nucleus. They have positive values of the chemical shielding and, therefore, lower resonance frequencies (because $\omega_0 = -\gamma B_0$). Often *chemical shifts* denoted by δ are used instead of the *chemical shielding* σ:

$$\delta = \frac{\sigma_{reference} - \sigma}{1 - \sigma_{reference}} \approx \sigma_{reference} - \sigma \qquad [1.24]$$

The second relationship is usually a very good approximation because shieldings are in the order of some parts per million (ppm). For proton and carbon spectroscopy TMS (tetramethylsilan) is often taken as the reference compound. Protons as well as carbons are well shielded in this compound and the chemical shifts of most compounds on this scale is positive. It should be noted that NMR spectra of nuclei with a positive γ are conventionally drawn with the frequency axis going from right to left (see Box II). This is quite natural because the frequencies are negative. Often the sign of the frequency is, however, dropped and then it looks like the frequency axis would increase from right to left. Typical values for ^{13}C are given in Box III.

Box II: : Conventions for the Representation of an NMR Spectrum

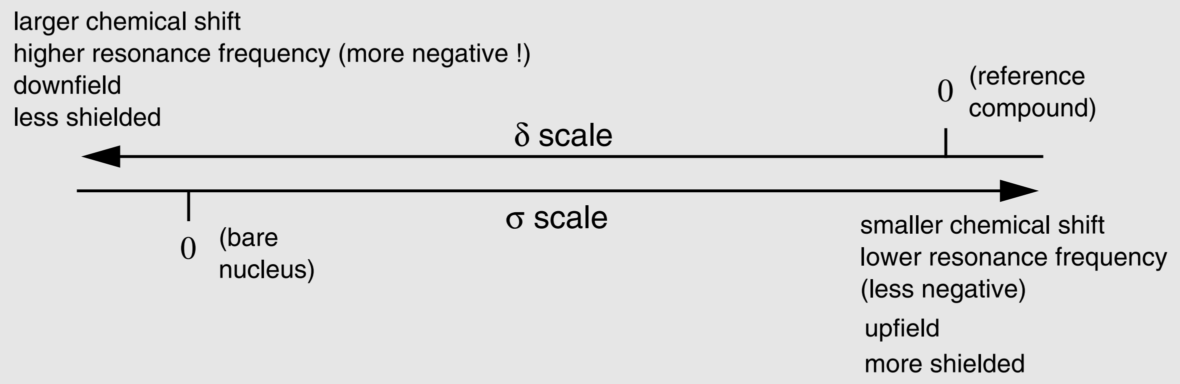

Box III: : Typical Chemical-Shift Values For Carbons (Isotropic Values)

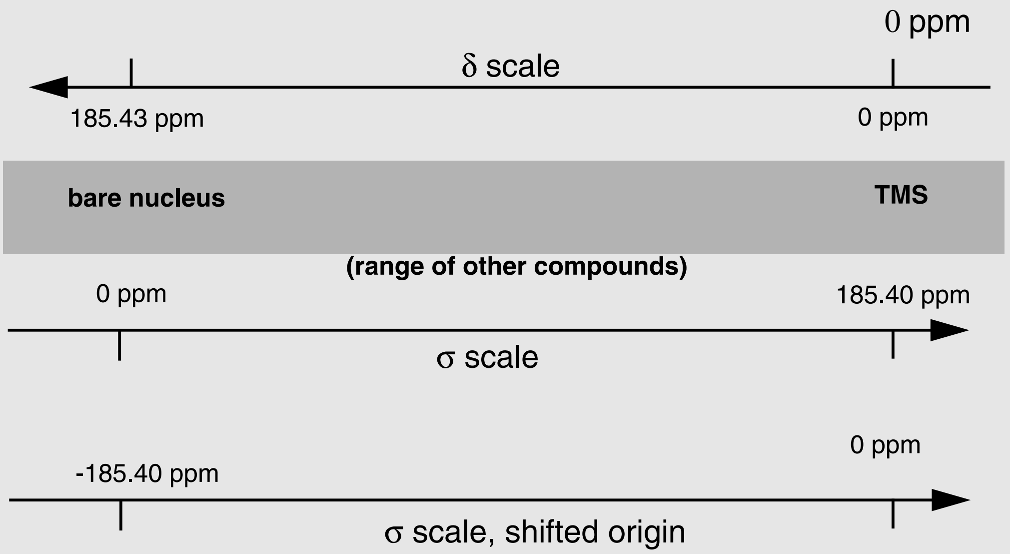

1.4.1 Origin of the Chemical Shielding

The numerical values for the tensor elements of $\underline{\sigma}$ can be calculated by quantum-chemical methods for isolated molecules which are not too large (density-functional methods). We can distinguish four important effects that contribute to the chemical shielding. There are diamagnetic and paramagnetic effects.

1.4.1.1 Diamagnetic Effect

In a magnetic field $\vec{B}_0$ the electron cloud precesses and generates a reaction field $\vec{B}_d$ that counteracts $\vec{B}_0$. This effect is called the *Lamb-Shift*.

An elementary calculation using the Biot-Savart law leads to:

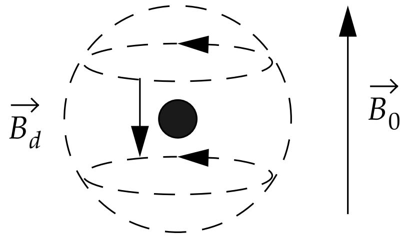

Figure 1.3: Lamb Shift

$$\sigma_{iso} = \frac{\mu_0 e^2}{3m_e} \int_0^{\infty} r\rho(\vec{r})dr \qquad [1.25]$$

Note the increasing weight of the electron density $\rho(\vec{r})$ at larger distances r. Differences in the diamagnetic Lamb shift are the dominant effect for observed proton shifts but are less important for the heavier nuclei.

1.4.1.2 Paramagnetic Effect

The paramagnetic effect is caused by a (partial) excitation of the *electrons* (by the magnetic field) into a paramagnetic state. This leads to a amplification of the applied field. Low-lying electronic states

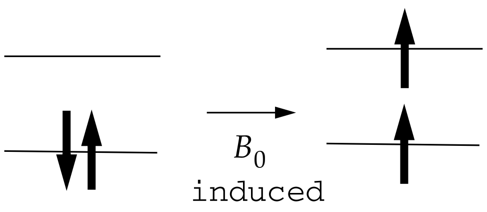

Figure 1.4: Paramagnetic Shift

cause a stronger paramagnetic effect. For the understanding of the isotropic carbon shifts the paramagnetic shift is an important contribution.

	excited states	paramagn. ^{13}C shift	^{13}C shift (TMS)
alkanes	high lying	small	10-50 ppm
alkenes	medium	medium	110-150 ppm
aromatics	medium	medium	110-140 ppm
ketones	low	high	170-230 ppm

1.4.1.3 Ring-Current Effects

A magnetic field can induce a ring-current within a π system. The effect is similar to the Lamb shift except that the current flows through several bonds. The current produces a field of the form shown in the figure. Inside the ring, a diamagnetic effect is observed, outside the ring a paramagnetic effect. The effect is anisotropic and depends on the direction of the field $\vec{B}_0$ with respect to the ring plane.

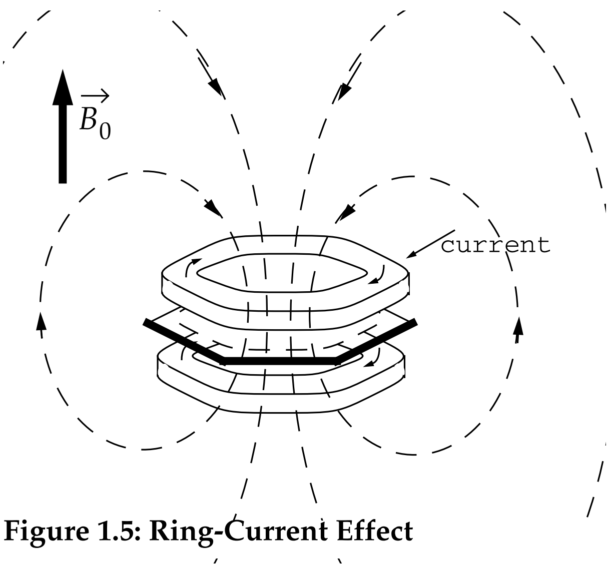

Figure 1.5: Ring-Current Effect

Figure 1.6a shows an example for strong ring-current effects in 15,16-Dihydro,15,16-dimethylpyren on the isotropic chemical shifts. The chemical shifts of protons of the CH_3 groups on top of the rings are shifted upfield to -4.23 ppm while the protons outside the ring are shifted downfield to +8.6 ppm. The proton chemical-shift effects close to a benzene ring as a function of the position are graphically shown in Fig. 1.6b.

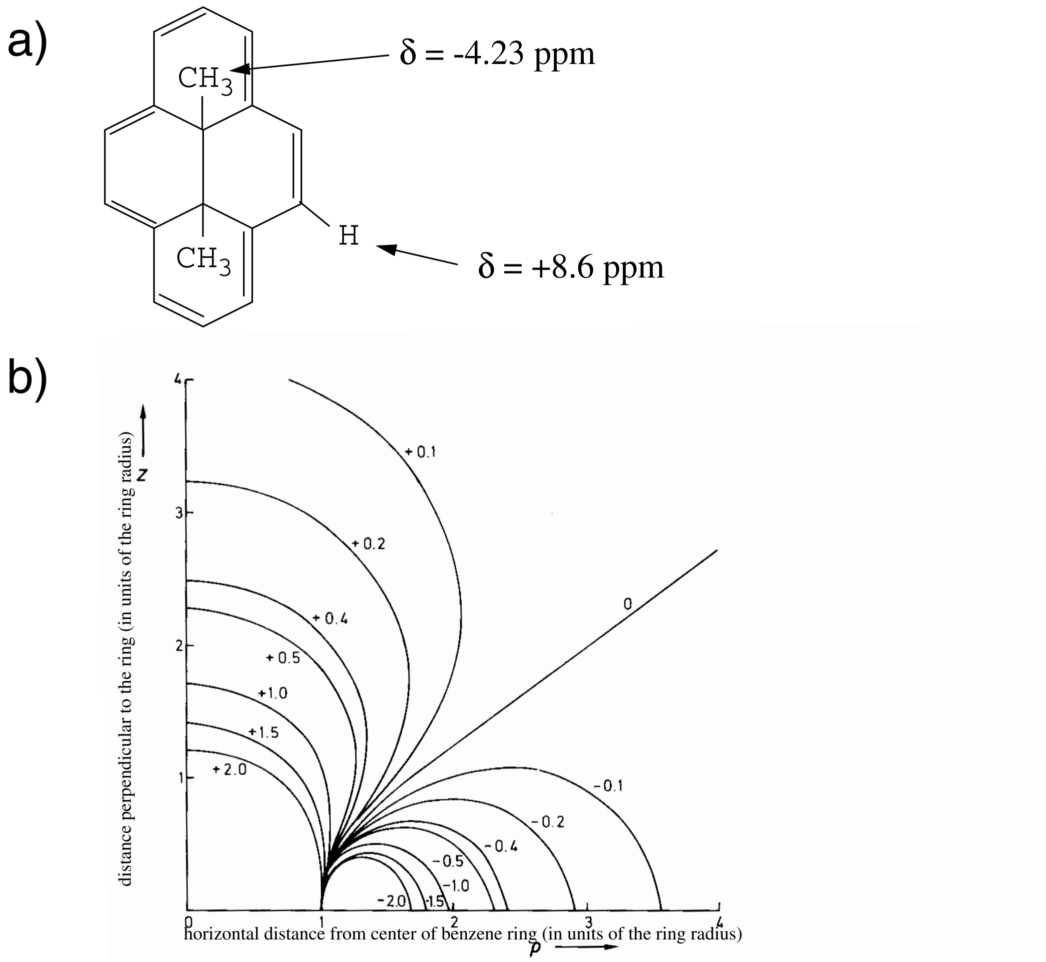

Graphic representation of the influence of the magnetic anisotropy of the benzene ring on proton resonance frequencies (after Ref. 1)

From: H. Günter: "NMR Spectroscopy", Wiley.

Figure 1.6: Ring-Current Effects

1.4.1.4 Anisotropic Neighbor Effect

The electron density centered at a neighboring nucleus polarizes the electron density and leads to an induced dipolar moment $\vec{\mu}_{ind}$. The field of this induced moment at the position of spin S leads to an additional field. If the induced moment has a magnitude which is independent of the direction of $\vec{B}_0$, the effect vanishes in the isotropic average and is only observed in oriented phases, if $|\vec{\mu}_{ind}|$ depends on the direction of the external field, an isotropic contribution arises.

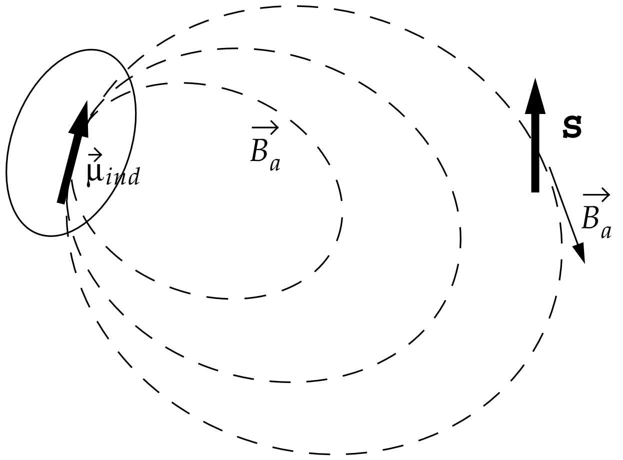

Figure 1.7: Anisotropic Neighbor Effects

Figure 1.8 shows as an example the molecule acetylene. If the axis of the molecule is parallel to the field, a large $\vec{\mu}_{ind}$ is induced leading to a diamagnetic shielding, if the axis is perpendicular, a weak paramagnetic shielding is obtained.

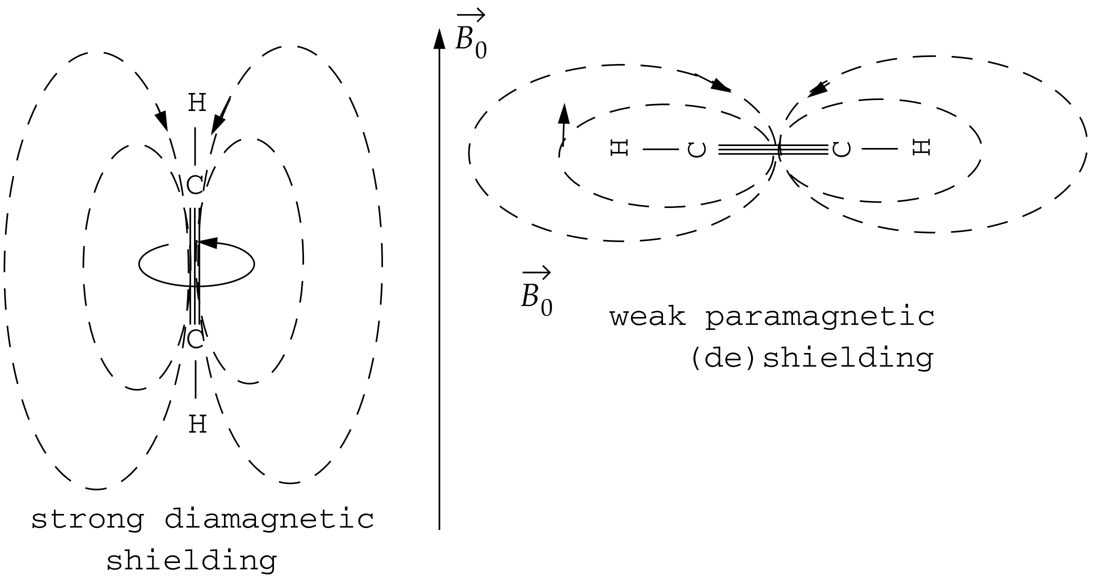

Figure 1.8: Anisotropic Neighbor Effects

1.4.2 Some Examples For Isotropic Chemical-Shift Values

The typical proton chemical-shift range lies between 0 and 11 ppm. For carbons, a range between 0 and 180 ppm is most commonly found. Figure 1.9 shows the typical chemical-shift ranges for protons and carbons found for characteristic groups in organic molecules.

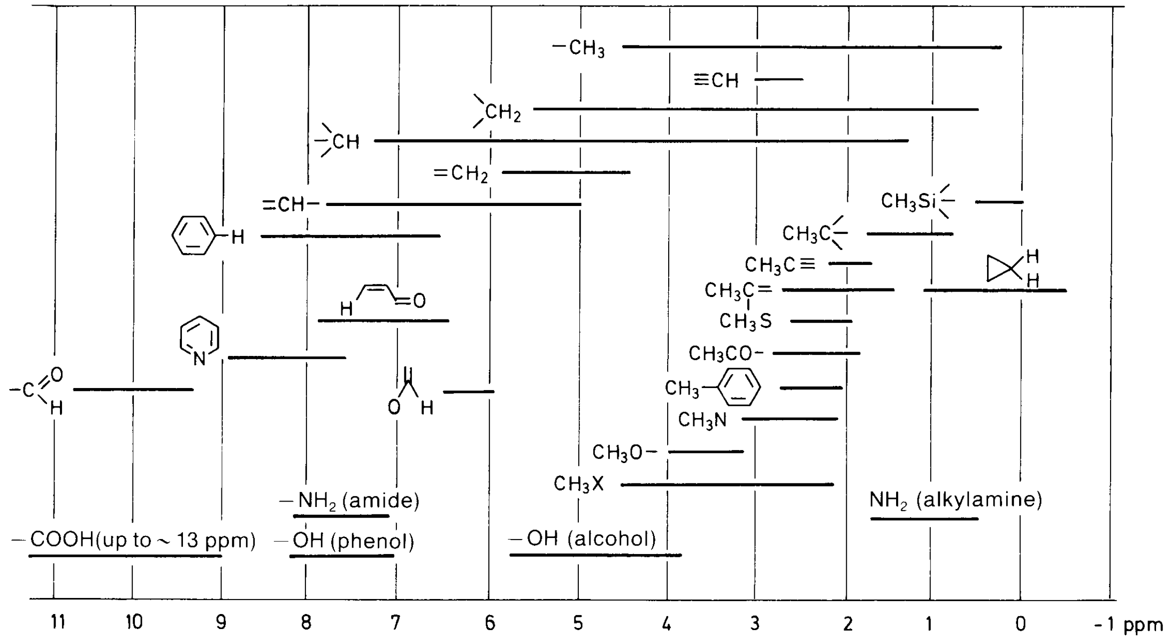

Figure 2.6 δ-Scale of chemical shifts of proton resonances in organic compounds

From: H. Günter: "NMR Spectroscopy", Wiley.

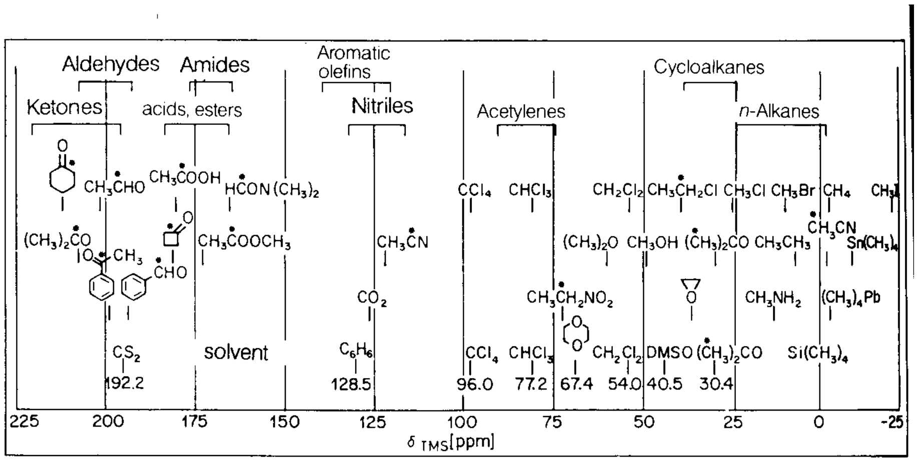

Figure 12.3 ^{13}C chemical shift diagram (Ref. 40)

From: H. Günter: "NMR Spectroscopy", Wiley.

Figure 1.9: Typical Chemical Shifts for protons and Carbons

1.4.3 Single-Crystal Spectra

The resonance frequency is proportional to the zz-element of the shielding tensor in the laboratory frame. Because the chemical shielding tensor is defined with respect to a molecule-fixed coordinate system we must first transform it into the laboratory frame to obtain the resonance frequency by:

$$\underline{\sigma}^{(k)} = R\underline{\sigma}^{(k)}_{MF}R^{-1} \tag{1.26}$$

A particular molecular fixed coordinate system is the principal axis system (*PAS*), where $\underline{\sigma}$ is diagonal:

$$\underline{\sigma} = \begin{bmatrix} \sigma^{(k)}_{11} & 0 & 0 \\ 0 & \sigma^{(k)}_{22} & 0 \\ 0 & 0 & \sigma^{(k)}_{33} \end{bmatrix} \tag{1.27}$$

The diagonal values of this matrix are called the *principal values* of the chemical-shielding tensor, the direction of the axis system, *the principal directions*. The ordering of the principal values is chosen such that:

- $\sigma^{(k)}_{11}$ is the least shielded component (see Box II),
- $\sigma^{(k)}_{33}$ is the most shielded component,
- $\sigma^{(k)}_{22}$ lies in between.

The rotation matrices R that transform from one coordinate system to the other are usually expressed in term of the three Euler angles α, β, γ. The rotation matrix $R(\alpha, \beta, \gamma)$ is constructed from three successive rotations:

$$R(\alpha, \beta, \gamma) = R_{z''}(\gamma) \cdot R_{y'}(\beta) \cdot R_{z}(\alpha) \tag{1.28}$$

This convention implies three rotations of the coordinate system:

- first by α around the original z-axis
- second by β around the new y′-axis
- last by γ around the new z″-axis

The original axes (x,y,z) are rotated to the new axis (x″,y″,z″)

The inverse rotation $R(\alpha, \beta, \gamma)^{-1}$ is given by:

$$(R(\alpha,\beta,\gamma))^{-1} = R(-\gamma,-\beta,-\alpha) = R_{z''}(-\alpha)\cdot R_{y'}(-\beta)\cdot R_z(-\gamma) \qquad [1.29]$$

If we transform from the PAS (original) to the Lab (final) system (Fig. 1.11), we call the Euler angles (α, β, γ), if we transform from the Lab (original) to the PAS (final), we call them (φ, θ, χ). They fulfill the relationship:

$$\alpha = -\chi \qquad \beta = -\theta \qquad \gamma = -\varphi \qquad [1.30]$$

$$R(\alpha,\beta,\gamma) = (R(\varphi,\theta,\chi))^{-1}: \qquad [1.31]$$

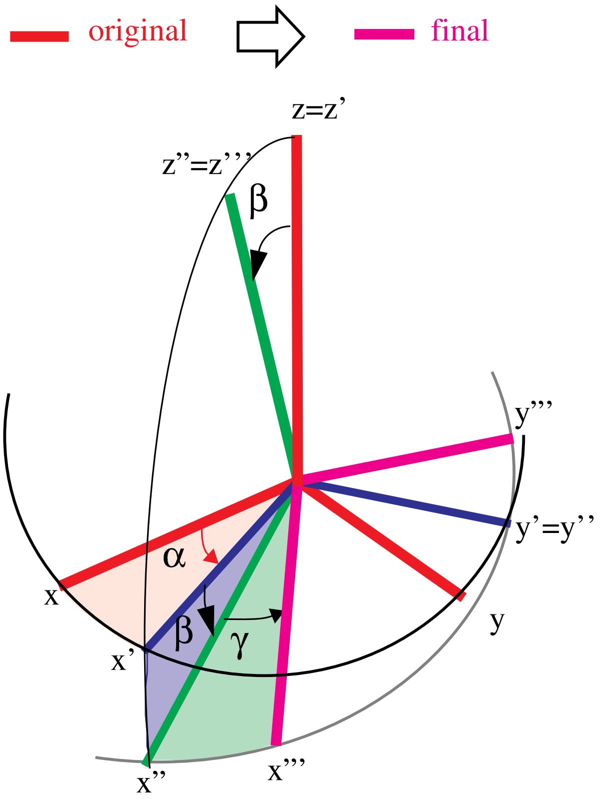

Figure 1.10: Euler Angle Rotation
The Euler-angle rotations use three successive rotations to describe the coordinate transformation. First we have a rotation about the z-axis by an angle α, then a rotation about the y' axis by an angle β, and last a rotation about the z''-axis by an angle γ.

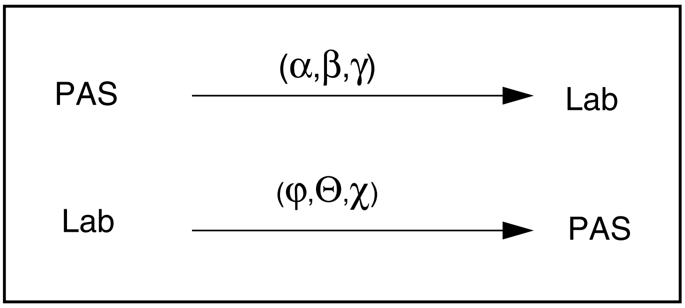

Figure 1.11: Coordinate Transformations

Since the definition of the Euler angles allows only for rotations about the y and z axis, rotations around other axis have to be constructed from these using the sequence:

- Rotation by θ around z-axis: $R(0, 0, \theta)$
- Rotation by θ around y-axis: $R(0, \theta, 0)$
- Rotation by θ around x-axis: $R(-\pi/2, \theta, \pi/2)$

The cartesian matrix representation of R is, for the rotation around the z axis:

$$R_z = \begin{bmatrix} \cos\psi & \sin\psi & 0 \\ -\sin\psi & \cos\psi & 0 \\ 0 & 0 & 1 \end{bmatrix} \tag{1.32}$$

and around the y-axis:

$$R_y = \begin{bmatrix} \cos\psi & 0 & -\sin\psi \\ 0 & 1 & 0 \\ \sin\psi & 0 & \cos\psi \end{bmatrix} \tag{1.33}$$

and, therefore, for the combination of the three Euler rotations:

$$R(\alpha, \beta, \gamma) = \begin{bmatrix} \cos\alpha\cos\beta\cos\gamma - \sin\alpha\sin\gamma & \sin\alpha\cos\beta\cos\gamma + \cos\alpha\sin\gamma & -\sin\beta\cos\gamma \\ -\sin\alpha\cos\gamma - \cos\alpha\cos\beta\sin\gamma & -\sin\alpha\cos\beta\sin\gamma + \cos\alpha\cos\gamma & \sin\beta\sin\gamma \\ \cos\alpha\sin\beta & \sin\alpha\sin\beta & \cos\beta \end{bmatrix} \tag{1.34}$$

1.4.4 Determination of Principal Axes and Principal Values in a Single Crystal

In a single crystal the principal value and the principal directions of the CSA tensor with respect to a crystal-fixed coordinate system can be determined by measuring at least six different, non-degenerate orientations (α, β, γ) of the single crystal with respect to the external field.

In practice, the orientation dependence is measured by rotating the single crystal around an axis perpendicular to the magnetic field and measuring the spectrum as a function of the rotation angle (e.g. β). An example for such a rotation pattern is given in Fig. 1.12. Usually, 3 rotations around orthogonal axes are performed, in principle, two around non-orthogonal axes are sufficient. The diagram of the resonance frequency as a function of each of the rotation angles is called the *rotation plot* and from these data, the six parameters ($\alpha,\beta,\gamma,\sigma_{11},\sigma_{22},\sigma_{33}$) that define the chemical-shielding tensor can be determined.

If the orientation of the molecule with respect to the crystal axis system is known, i.e., if the X-ray or neutron structure is known, the orientation of the CSA in

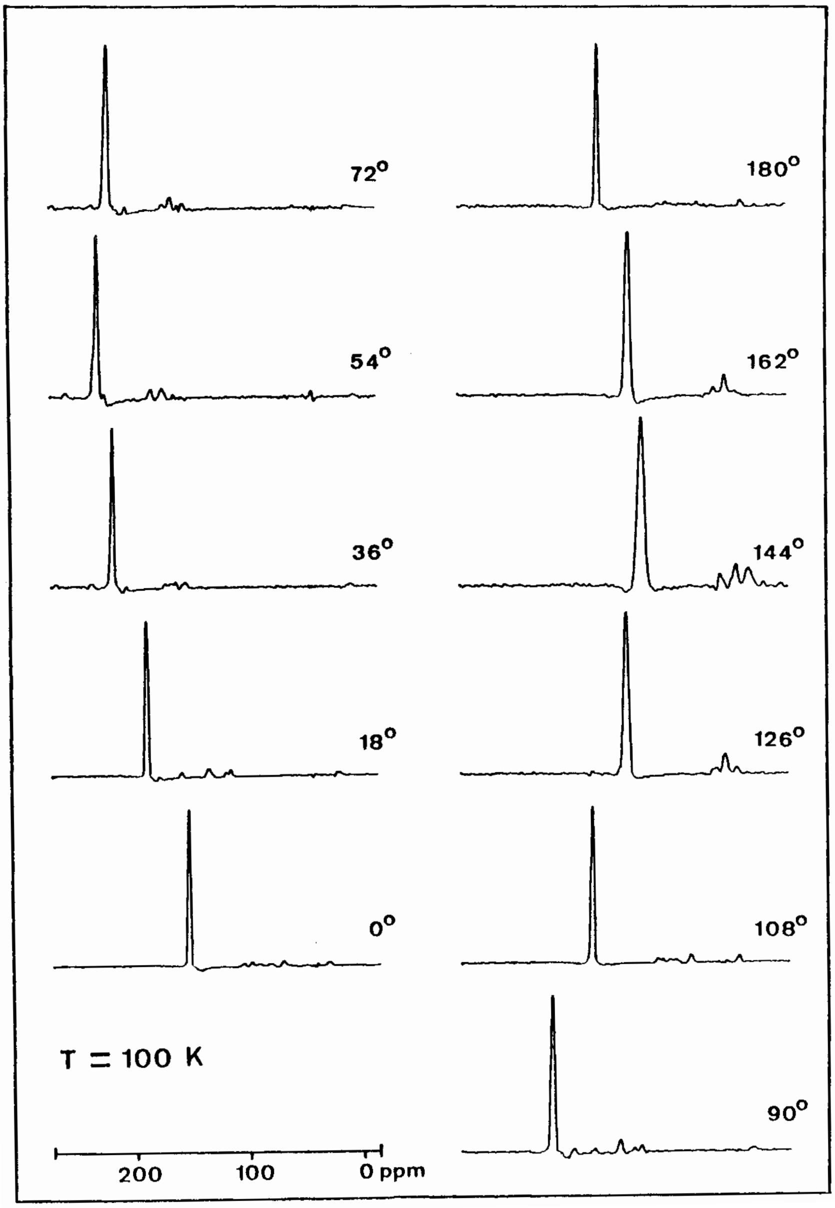

Figure 1.12: ^{13}C spectrum of a benzoic acid single crystal
^{13}C enriched at the carboxylic position, as a function of the rotation angle.

the molecular coordinate system can be calculated. If the orientation of the CSA with respect to the molecular axes is known (see below), the orientation of the molecule in the crystal axes system can be determined.

1.4.5 The Spectrum of a Powder Sample

For a powder sample, the FID (and the spectrum) is the weighted superposition of the possible crystallite orientations:

$$s(t) = \frac{1}{8\pi^2}\int_0^{2\pi}\int_0^{\pi}\int_0^{2\pi} s(\alpha, \beta, \gamma, t)\delta\alpha \sin\beta\delta\beta\delta\gamma \qquad [1.35]$$

Because of the axial symmetry around the direction of the applied field, the last rotation γ which is around the direction of $\overrightarrow{B_0}$ does not influence the NMR signal and can be evaluated immediately in the above integral, leading to:

$$s(t) = \frac{1}{4\pi}\int_0^{2\pi}\int_0^{\pi} s(\alpha, \beta, \gamma, t)\delta\alpha \sin\beta\delta\beta\,. \qquad [1.36]$$

The spectrum of a powdered sample (Fourier transform of Eq. [1.36]) is shown in Fig. 1.13.

From the edges of the powder pattern, the principal values of the CSA tensor can immediately be determined. If two of the principal values are identical, the tensor is called *axially symmetric*.

Instead of $\sigma_{11}, \sigma_{22}, \sigma_{33}$ one sometimes uses the isotropic value σ_{iso}, the anisotropy δ and the asymmetry η to characterize a tensor:

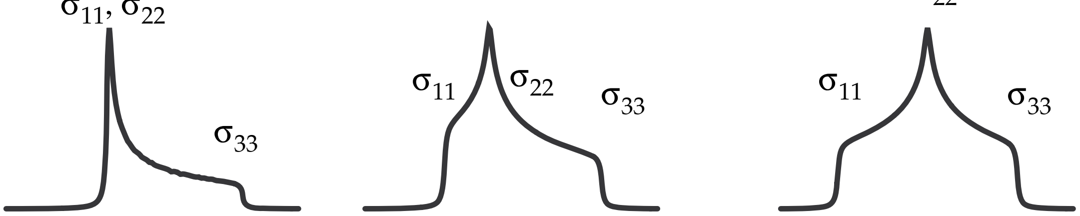

Figure 1.13: Powder patterns observed in solid phase.

$$\sigma_{iso} = \frac{1}{3}tr\{\underset{\sim}{\sigma}\} = \frac{1}{3}(\sigma_{xx} + \sigma_{yy} + \sigma_{zz}) \qquad \delta = \sigma_{zz} - \sigma_{iso} \qquad \eta = \frac{\sigma_{yy} - \sigma_{xx}}{\delta} \qquad [1.37]$$

$\sigma_{xx}, \sigma_{yy}, \sigma_{xx}$ are the same as the $\sigma_{11}, \sigma_{22}, \sigma_{33}$ except of the ordering which is done using the convention:

$$|\sigma_{zz} - \sigma_{iso}| \geq |\sigma_{xx} - \sigma_{iso}| \geq |\sigma_{yy} - \sigma_{iso}| \qquad [1.38]$$

Here, $\eta = 0$ denotes an axially symmetric tensor and η varies between 0 and 1. The shape of the tensor is only determined by η while δ gives the width of the pattern and a negative δ leads to the mirror image of the tensor.

The orientation of the principal axes of the CSA tensor with respect to a molecular frame of reference, however, cannot be determined from powder spectra. It is sometimes fixed by symmetry constraints but in general it must either be calculated or estimated using the empirical rules given in Box IV. The width of the tensors is often in the same order of magnitude as the entire isotropic chemical shift range (examples for ^{13}C see Fig. 1.14)

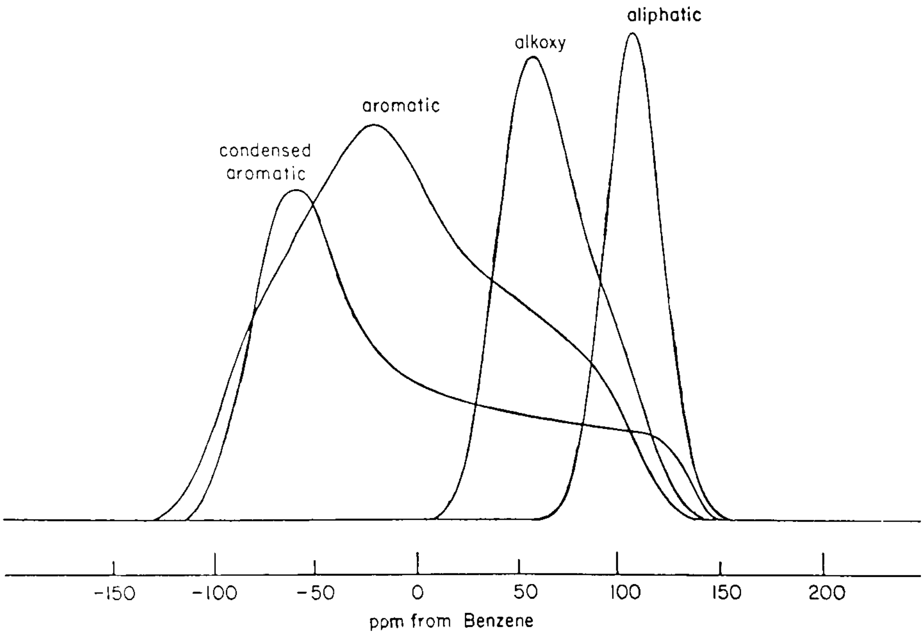

Figure 1.14: Typical ^{13}C Chemical-Shift Tensors

Box IV: Empirical rules for the orientation of the ^{13}C tensor principal axis with respect to a molecular coordinate system:

1) Methyl carbons have almost axially symmetric tensor with the unique axis along the local threefold symmetry axis.

The tensor is averaged due to classical or tunnelling motion around the C_3 axis.

2) Ring carbons possess three distinct tensor elements with

- the most shielded axis perpendicular to the plane and
- the least shielded axis bisecting the C-C-C angle of the ring carbons

3) The most shielded direction is

- perpendicular to the ring in aromatic carbons,
- along the C_3 axis for methyl carbons, and
- perpendicular to the sp^2 plane for carbonyl and carboxylic carbons

4) The least shielded direction is

- in the ring plane for carbon rings, bisecting the C-C-C angle,
- perpendicular to the C_3 axis for methyl carbons and perpendicular to a plane of symmetry in which the methyl group is connected
- in the sp^2 plane for carbonyl and carboxyl carbons

5) The intermediately shielded direction is

- tangential to the ring for aromatic carbons,
- for non-averaged methyl groups perpendicular to the C_3 axis in the plane of symmetry,
- in the sp^2 plane and perpendicular to the C-C bond for carboxyl carbons

A partially ordered sample will lead to a different pattern as illustrated in Fig. 1.15.

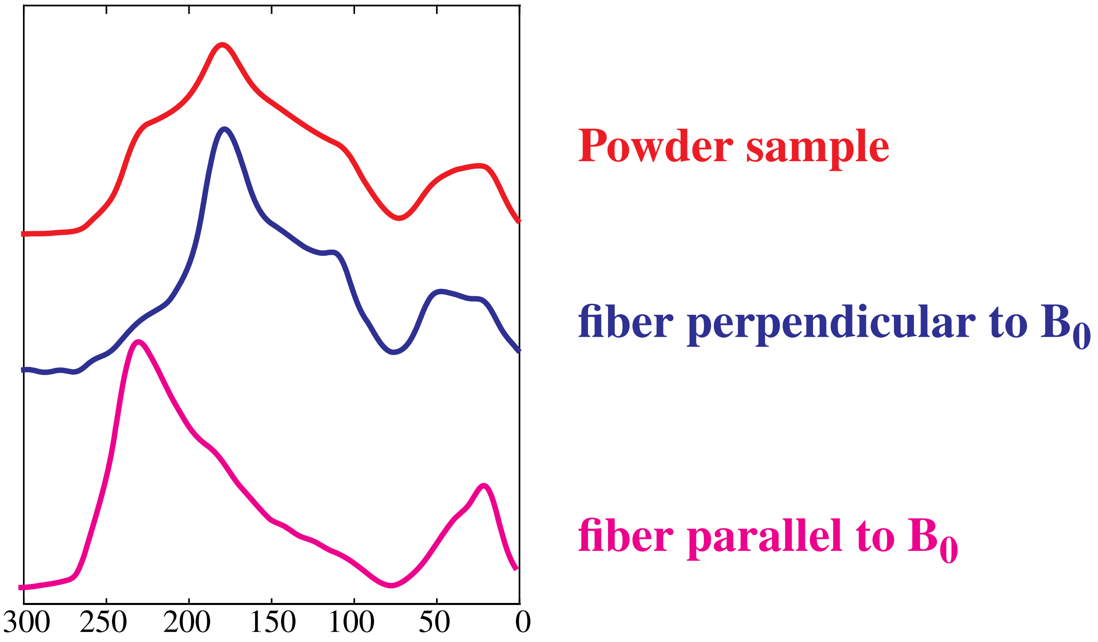

Figure 1.15: ^{13}C Spectra of powdered and uniaxially oriented samples of spider silk (Nephila edulis) (^{13}C enriched at the alanine carboxylic position)

1.5 The Indirect Spin-Spin Coupling (J-Coupling)

Here we consider the coupling between two nuclei which is mediated through the electrons. An exact description is, as in the case of the chemical shielding, a formidable task involving the quantum description of the electrons. If we restrict ourselves to the isotropic coupling, we can write the J-coupling Hamiltonian between two spins in the general form

$$\hat{\mathcal{H}}_J = 2\pi J_{12}\vec{\hat{I}}_1\vec{\hat{I}}_2 \qquad [1.39]$$

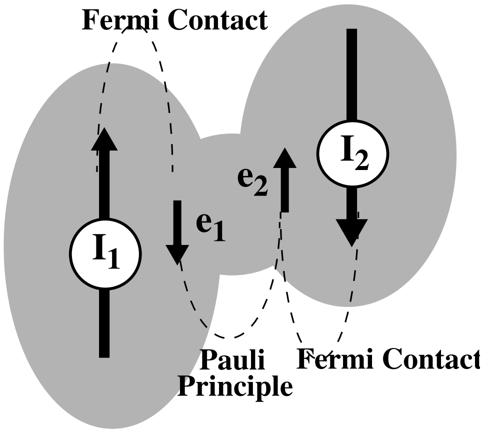

Figure 1.16: J Coupling

The coupling constant J_{12} can be obtained by quantum-chemical methods similar to the chemical shieldings. In general, the J coupling will be anisotropic, but the anisotropy is seldom of practical significance and we neglect it here.

Note that the J-coupling Hamiltonian is the same in the laboratory frame and in the rotating frame

$$\hat{\mathcal{H}}'_J = \hat{\mathcal{H}}_J \qquad [1.40]$$

because the scalar product of two vectors is independent of the coordinate system the two individual vectors are described in.

One contribution to the indirect spin-spin coupling is the Fermi contact interaction between electrons and nuclei. This interaction is proportional to the probability density of the electron at the nuclear position:

$$J = \frac{3\mu_0}{4\pi}\beta\gamma\delta(\vec{r}_e - \vec{r}_N) \ . \qquad [1.41]$$

The Fermi-contact interaction favors an antiparallel orientation of a nuclear spin. Through the correlation of the spins of two electrons in the same bonding orbital (Pauli principle), this leads to an (opposite) polarization of the other electron. As a consequence, the energy of a system with two spins that share an electron pair depends on the relative orientation of the two spins. An antiparallel arrangement is favored. Note that the Fermi-contact interaction is isotropic: it does not depend on the orientation of the molecules in the magnetic field.

For a multi-spin system, the J Hamiltonian is just the sum of the individual two-spin interactions

$$\hat{\mathcal{H}}_J = 2\pi \sum_{i<j} J_{ij} \vec{\hat{I}}_i \vec{\hat{I}}_i \ . \qquad [1.42]$$

No term with more than two spin operators appears! This is a general property of NMR Hamiltonians, only *one-particle interactions* (e.g. chemical shift) and *two-particle interactions* (e.g. J coupling) must be taken into account.

For a one-bond coupling between two like spins, *J* is usually positive (see Fig. 1.17) leading to antiparallel spins in the ground state, for a two-bond coupling, *J* is often negative because the exchange integral of overlapping orbitals favors parallel electron spins.

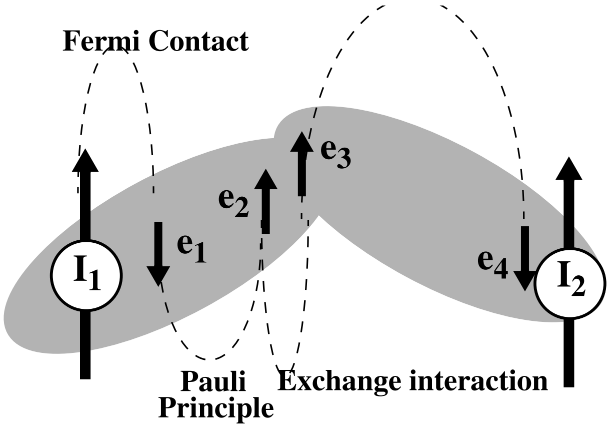

Figure 1.17: J Coupling

These rule are, however, only valid, if the Fermi contact interaction is the dominant source for the indirect coupling, e.g. for proton-proton couplings but not for fluorine-fluorine couplings. There is another source for J-coupling interactions: a dipolar interaction between the nuclear and electron spins, combined again with the Pauli principle. This mechanism provides a source for anisotropic J interactions. The anisotropy plays, however, no important role except for very heavy nuclei. Typical values for isotropic J couplings are:

spins involved	J
H-H	280 Hz
H-C-**H** ("geminal")	8-12 Hz
H-C-C-**H** ("vicinal")	0-10 Hz
H-C-**F**	40-80 Hz
F-C-**F**	150-270 Hz
H-^{13}C	100-250 Hz
H-C-**^{13}C**	0-60 Hz
^{13}C-^{13}C	30-80 Hz
^{15}N-^{13}C	2-20 Hz
^{1}H-^{15}N	70-110 Hz

Multi-bond couplings are usually dependent on the conformation of the molecule and are an important source for structural information. For vicinal protons (3-bond coupling), the *Karplus relation* holds:

$$J_{iso}^{vic} = A\cos^2\varphi + B\cos\varphi + C \qquad [1.43]$$

where, for two carbons in between the protons: A=9, B=-.5 C=-0.28.

1.6 Calculation of a Spectrum for a Two-Spin System in Liquid Phase

In isotropic liquid phase, the isotropic chemical shift and the J coupling are the only interactions necessary to describe the spin system. The Hamiltonian in the laboratory frame of reference is given by the Zeeman term (Eq. [1.2]) the chemical-shielding term (Eq. [1.21]) and the J coupling (Eq. [1.42]).

$$\begin{aligned} \hat{\mathcal{H}} &= \hat{\mathcal{H}}_Z + \hat{\mathcal{H}}_S + \hat{\mathcal{H}}_J \\ &= \omega_0(\hat{I}_{1z} + \hat{I}_{2z}) - \omega_0(\sigma_{iso}^{(1)} \cdot \hat{I}_{1z} + \sigma_{iso}^{(2)} \cdot \hat{I}_{2z}) + 2\pi J_{12}\vec{\hat{I}}_1\vec{\hat{I}}_2 \end{aligned} \qquad [1.44]$$

In the rotating frame, we have

$$\hat{\mathcal{H}}'' = \Omega_1 \cdot \hat{I}_{1z} + \Omega_2 \cdot \hat{I}_{2z} + 2\pi J_{12}\vec{\hat{I}}_1\vec{\hat{I}}_2 \qquad [1.45]$$

where Ω_1 and Ω_2 are the rotating frame frequencies of the two nuclei $\Omega_i = (1 - \sigma_{iso}^{(i)})\omega_0 - \omega_{rf}$. The Ω_i can be interpreted as the chemical shifts of the nuclei (in angular frequencies, not in ppm) measured with respect to the rf irradiation frequency.

We now calculate the spectrum after a $(\pi/2)_y$ pulse following the steps outlined in Box IV for the schematic pulse sequence shown in Fig. 1.18

I) The Hamiltonian before and after the pulse is given by $\hat{\mathcal{H}}$ of Eqs. [1.44] and [1.45] in the laboratory or rotating frame, respectively. During the pulse, the Hamiltonian is given in the rotating frame by

$$\hat{\mathcal{H}}_p'' = \Omega_1 \cdot \hat{I}_{1z} + \Omega_2 \cdot \hat{I}_{2z} + 2\pi J_{12}\vec{\hat{I}}_1\vec{\hat{I}}_2 + \omega_1(\hat{I}_{1y} + \hat{I}_{2y}) \approx \omega_1(\hat{I}_{1y} + \hat{I}_{2y}) \qquad [1.46]$$

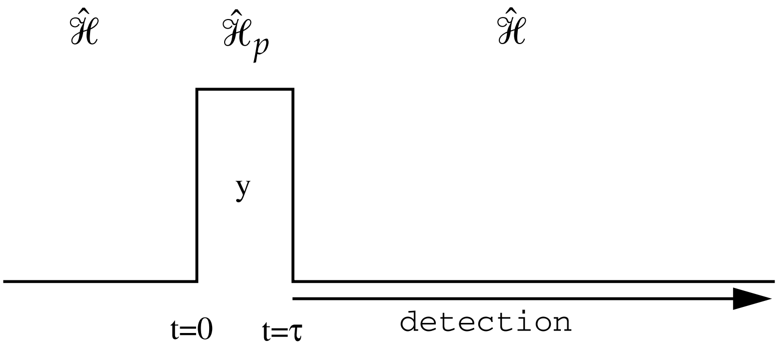

Figure 1.18: Simple 1D Pulse Sequence

if we assume that the rf-field amplitudes are much stronger than all the internal interactions.

II) The initial density operator is given by $\hat{\sigma}_0 = c \cdot \hat{\mathcal{H}}$ (see Eq. [4.64]). $\hat{\mathcal{H}}$ is the laboratory-frame Hamiltonian and in a good approximation we only need to consider the dominant Zeeman term:

$$\hat{\sigma}_0 = c \cdot (\hat{I}_{1z} + \hat{I}_{2z}) \qquad [1.47]$$

Here, c is a proportionality factor and the part of the density operator proportional to the unity operator has been omitted as discussed in Chapter 4.14.

Note that the initial density operator $\hat{\sigma}_0' = \hat{\sigma}_0$ and the rotating-frame Hamiltonian $\hat{\mathcal{H}}_p''$ only consist of one-spin terms. We can, therefore, evaluate the evolution during the pulse for each of the spins separately.

The initial density operator in matrix representation is:

$$\hat{\sigma}'_0 = c \begin{bmatrix} \frac{1}{2} & 0 \\ 0 & -\frac{1}{2} \end{bmatrix} \qquad [1.48]$$

while the Hamiltonian during the pulse is given by:

$$\mathcal{H}''_p = \omega_1 \begin{bmatrix} 0 & -\frac{i}{2} \\ \frac{i}{2} & 0 \end{bmatrix} . \qquad [1.49]$$

We can now calculate $\hat{\sigma}'(\tau)$ by application of the Liouville van Neumann equation:

$$\begin{aligned}\hat{\sigma}'(\tau) &= c \cdot \exp(-i\hat{\mathcal{H}}''_p\tau)\hat{\sigma}'_0\exp(i\hat{\mathcal{H}}''_p\tau) \\ &= c \cdot \exp\left(-i\omega_1\tau\begin{bmatrix} 0 & -\frac{i}{2} \\ \frac{i}{2} & 0 \end{bmatrix}\right)\begin{bmatrix} \frac{1}{2} & 0 \\ 0 & -\frac{1}{2} \end{bmatrix}\exp\left(i\omega_1\tau\begin{bmatrix} 0 & -\frac{i}{2} \\ \frac{i}{2} & 0 \end{bmatrix}\right).\end{aligned} \qquad [1.50]$$

We calculate e^M according to

$$e^M = R^{-1}e^{RMR^{-1}}R \qquad [1.51]$$

where $RMR^{-1} = \Lambda$ is the transformation into the eigenbase of M where Λ is a diagonal matrix. For diagonal matrices, we know that:

$$\exp\begin{bmatrix} \Lambda_{11} & 0 \\ 0 & \Lambda_{22} \end{bmatrix} = \begin{bmatrix} e^{\Lambda_{11}} & 0 \\ 0 & e^{\Lambda_{22}} \end{bmatrix}. \qquad [1.52]$$

Therefore, we need to diagonalize the matrix

$$\begin{bmatrix} 0 & -\frac{i}{2} \\ \frac{i}{2} & 0 \end{bmatrix}. \qquad [1.53]$$

The eigenvalues are obtained as solutions of

$$E^2 - \left(-\frac{i}{2}\right) \cdot \frac{i}{2} = E^2 - \frac{1}{4} = 0 \quad ; \qquad E = \pm\frac{1}{2} \qquad [1.54]$$

and the transformation is found (by determining the eigenvectors) as:

$$\frac{1}{\sqrt{2}}\begin{bmatrix} i & 1 \\ -i & 1 \end{bmatrix}\begin{bmatrix} 0 & -\frac{i}{2} \\ \frac{i}{2} & 0 \end{bmatrix}\begin{bmatrix} -i & i \\ 1 & 1 \end{bmatrix}\frac{1}{\sqrt{2}} = \begin{bmatrix} \frac{1}{2} & 0 \\ 0 & -\frac{1}{2} \end{bmatrix} \qquad [1.55]$$

Now we can determine $e^{-i\omega_1\tau\hat{I}_y}$ as:

$$\frac{1}{2}\begin{bmatrix} -i & i \\ 1 & 1 \end{bmatrix}\begin{bmatrix} e^{-\frac{i\omega_1\tau}{2}} & 0 \\ 0 & e^{\frac{i\omega_1\tau}{2}} \end{bmatrix}\begin{bmatrix} i & 1 \\ -i & 1 \end{bmatrix} = \begin{bmatrix} \cos\frac{\omega_1\tau}{2} & -\sin\frac{\omega_1\tau}{2} \\ \sin\frac{\omega_1\tau}{2} & \cos\frac{\omega_1\tau}{2} \end{bmatrix} \qquad [1.56]$$

and the density operator after the pulse is given by

$$\hat{\sigma}'(\tau) = c\begin{bmatrix} \cos\frac{\omega_1\tau}{2} & -\sin\frac{\omega_1\tau}{2} \\ \sin\frac{\omega_1\tau}{2} & \cos\frac{\omega_1\tau}{2} \end{bmatrix}\begin{bmatrix} \frac{1}{2} & 0 \\ 0 & -\frac{1}{2} \end{bmatrix}\begin{bmatrix} \cos\frac{\omega_1\tau}{2} & \sin\frac{\omega_1\tau}{2} \\ -\sin\frac{\omega_1\tau}{2} & \cos\frac{\omega_1\tau}{2} \end{bmatrix} = \frac{c}{2}\begin{bmatrix} \cos\omega_1\tau & \sin\omega_1\tau \\ \sin\omega_1\tau & -\cos\omega_1\tau \end{bmatrix} . \qquad [1.57]$$

We call $\beta = \omega_1\tau$ the flip angle of the pulse which we chose to be $\beta = \omega_1\tau = \pi/2$. Then we obtain for the density operator after the $\frac{\pi}{2}$ pulse

$$\hat{\sigma}'(\tau) = c\begin{bmatrix} 0 & \frac{1}{2} \\ \frac{1}{2} & 0 \end{bmatrix} = c\hat{I}_x \qquad [1.58]$$

To evaluate the NMR signal during detection, we need the two-spin Hamiltonian $\mathcal{H}'' = \Omega_1 \cdot \hat{I}_{1z} + \Omega_2 \cdot \hat{I}_{2z} + 2\pi J_{12}\vec{\hat{I}}_1\vec{\hat{I}}_2$. To calculate the matrix representation of this two-spin Hamiltonian, we need to know how to calculate the matrix representation of products and sums of spin operators. These rules are summarized in Box V.

The matrix representation of the density operator

$$\hat{\sigma}(\tau) = c((\hat{I}_{1x}) \otimes (E_2) + (E_1) \otimes (\hat{I}_{2x}))) \qquad [1.60]$$

in the combined two-spin Hilbert space of both spins (of dimension $2x2 = 4$) is given by

$$\sigma'(\tau) = c\begin{bmatrix} 0 & 1/2 & 1/2 & 0 \\ 1/2 & 0 & 0 & 1/2 \\ 1/2 & 0 & 0 & 1/2 \\ 0 & 1/2 & 1/2 & 0 \end{bmatrix} . \qquad [1.61]$$

Box V: Direct Product and Direct Sum of Spin Operators

- Let $\hat{A}$ and $\hat{B}$ be operators that act on the same spin.
- The matrix product is defined as $(A \cdot B) = (A) \cdot (B)$, normal matrix product.
- The matrix sum $(A + B) = (A) + (B)$, normal element-wise matrix sum. Note, both matrices have to be expressed in the same basis system.
- Let $\hat{A}$ and $\hat{B}$ be operators that act on different spins. The spin space where $\hat{A}$ is defined (e.g. spin 1) has dimension N, the one of $\hat{B}$ dimension M.
- The matrix product is defined as $(A \cdot B) = (A) \otimes (B)$, the direct matrix product:

$$(A \cdot C) = \begin{bmatrix} a_{11}(C) & .... & a_{1N}(C) \\ .... & .... & .... \\ a_{N1}(C) & .... & a_{NN}(C) \end{bmatrix} = \begin{bmatrix} \begin{bmatrix} a_{11}c_{11} & .... & a_{11}c_{1M} \\ .... & .... & .... \\ a_{11}c_{M1} & .... & a_{11}c_{MM} \end{bmatrix} & .... & \begin{bmatrix} a_{1N}c_{11} & .... & a_{1N}c_{1M} \\ .... & .... & .... \\ a_{1N}c_{M1} & .... & a_{1N}c_{MM} \end{bmatrix} \\ .... & .... & .... \\ \begin{bmatrix} a_{N1}c_{11} & .... & a_{N1}c_{1M} \\ .... & .... & .... \\ a_{N1}c_{M1} & .... & a_{N1}c_{MM} \end{bmatrix} & .... & \begin{bmatrix} a_{NN}c_{11} & .... & a_{NN}c_{1M} \\ .... & .... & .... \\ a_{NN}c_{M1} & .... & a_{NN}c_{MM} \end{bmatrix} \end{bmatrix} \qquad [1.59]$$

- The matrix sum is defined as $(A + B) = (A) \otimes (E_2) + (E_1) \otimes (B)$ where (E_1) and (E_2) are identity matrices of dimension N and M respectively.

The basis functions of the combined Hilbert space of two spin 1/2 are $|\alpha_1\alpha_2\rangle$, $|\alpha_1\beta_2\rangle$, $|\beta_1\alpha_2\rangle$ and $|\beta_1\beta_2\rangle$.

The Hamiltonian is given by:

$$\begin{aligned} \mathcal{H}" = {} & \Omega_1((\hat{I}_{1z}) \otimes (E_2)) + \Omega_2((E_1) \otimes (\hat{I}_{2z})) \\ & + 2\pi J((\hat{I}_{1x}) \otimes (\hat{I}_{2x}) + (\hat{I}_{1y}) \otimes (\hat{I}_{2y}) + (\hat{I}_{1z}) \otimes (\hat{I}_{2z})) \end{aligned} \qquad [1.62]$$

or, in matrix representation:

$$\mathcal{H}'' = \Omega_1 \begin{bmatrix} \frac{1}{2} & 0 & 0 & 0 \\ 0 & \frac{1}{2} & 0 & 0 \\ 0 & 0 & -\frac{1}{2} & 0 \\ 0 & 0 & 0 & -\frac{1}{2} \end{bmatrix} + \Omega_2 \begin{bmatrix} \frac{1}{2} & 0 & 0 & 0 \\ 0 & -\frac{1}{2} & 0 & 0 \\ 0 & 0 & \frac{1}{2} & 0 \\ 0 & 0 & 0 & -\frac{1}{2} \end{bmatrix} + 2\pi J \begin{bmatrix} \frac{1}{4} & 0 & 0 & 0 \\ 0 & -\frac{1}{4} & \frac{1}{2} & 0 \\ 0 & \frac{1}{2} & -\frac{1}{4} & 0 \\ 0 & 0 & 0 & \frac{1}{4} \end{bmatrix}$$

$$= \begin{bmatrix} \frac{\Omega_1 + \Omega_2}{2} + \frac{\pi J}{2} & 0 & 0 & 0 \\ 0 & \frac{\Omega_1 - \Omega_2}{2} - \frac{\pi J}{2} & \pi J & 0 \\ 0 & \pi J & \frac{\Omega_2 - \Omega_1}{2} - \frac{\pi J}{2} & 0 \\ 0 & 0 & 0 & \frac{-(\Omega_1 + \Omega_2)}{2} + \frac{\pi J}{2} \end{bmatrix} \quad [1.63]$$

The detection operator is given by $\hat{M}_x = \gamma(\hat{I}_{1x} + \hat{I}_{2x}) = \gamma\hat{F}_x$ (see Eq. [4.56]) which has a matrix representation of

$$(\hat{F}_x) = \begin{bmatrix} 0 & \frac{1}{2} & \frac{1}{2} & 0 \\ \frac{1}{2} & 0 & 0 & \frac{1}{2} \\ \frac{1}{2} & 0 & 0 & \frac{1}{2} \\ 0 & \frac{1}{2} & \frac{1}{2} & 0 \end{bmatrix} . \quad [1.64]$$

If all matrices were in the eigenbase of the Hamiltonian, the NMR signal could easily be evaluated by:

$$\langle \hat{M}_x \rangle(t) = \gamma \sum_k \sum_l \sigma'_{kl}(\tau)(F_x)_{lk} \exp(-i\omega_{kl}t) \quad [1.65]$$

with the four transition frequencies $\omega_{kl} = (\mathcal{H}'')_{kk} - (\mathcal{H}'')_{ll}$ and the intensities $\gamma\sigma'_{kl}(\tau)(F_x)_{lk}$ which, in our specific experiment, evaluate to $c\gamma(F_x)^2_{lk}$ because $\hat{\sigma}(\tau) = \hat{F}_x$. To diagonalize the Hamiltonian

$$\begin{bmatrix} \frac{\Omega_1+\Omega_2}{2}+\frac{\pi J}{2} & 0 & 0 & 0 \\ 0 & \frac{\Omega_1-\Omega_2}{2}-\frac{\pi J}{2} & \pi J & 0 \\ 0 & \pi J & \frac{\Omega_2-\Omega_1}{2}-\frac{\pi J}{2} & 0 \\ 0 & 0 & 0 & \frac{-(\Omega_1+\Omega_2)}{2}+\frac{\pi J}{2} \end{bmatrix} \qquad [1.66]$$

we only need to diagonalize the center 2x2 block.Using the general relation for 2x2 matrices:

$$\begin{bmatrix} \cos\alpha & \sin\alpha \\ -\sin\alpha & \cos\alpha \end{bmatrix} \begin{bmatrix} a & b \\ b & c \end{bmatrix} \begin{bmatrix} \cos\alpha & -\sin\alpha \\ \sin\alpha & \cos\alpha \end{bmatrix} = \begin{bmatrix} E_2 & 0 \\ 0 & E_3 \end{bmatrix} \qquad 2\alpha = \operatorname{atan}\left(\frac{2b}{a-c}\right) \qquad [1.67]$$

we obtain

$$\mathcal{H}'' = \begin{bmatrix} \frac{\Omega_1+\Omega_2}{2}+\frac{\pi J}{2} & 0 & 0 & 0 \\ 0 & -\frac{\pi J}{2}+S & 0 & 0 \\ 0 & 0 & -\frac{\pi J}{2}-S & 0 \\ 0 & 0 & 0 & \frac{-(\Omega_1+\Omega_2)}{2}+\frac{\pi J}{2} \end{bmatrix} \qquad [1.68]$$

with

$$S = \sqrt{\left(\frac{\Omega_1+\Omega_2}{2}\right)^2+(\pi J)^2}\ . \qquad [1.69]$$

Transforming the detection operator into the eigenbase of the Hamiltonian leads to

$$(\hat{F}_x) = \begin{bmatrix} 0 & \frac{\cos\alpha + \sin\alpha}{2} & \frac{\cos\alpha - \sin\alpha}{2} & 0 \\ \frac{\cos\alpha + \sin\alpha}{2} & 0 & 0 & \frac{\cos\alpha + \sin\alpha}{2} \\ \frac{\cos\alpha - \sin\alpha}{2} & 0 & 0 & \frac{\cos\alpha - \sin\alpha}{2} \\ 0 & \frac{\cos\alpha + \sin\alpha}{2} & \frac{\cos\alpha - \sin\alpha}{2} & 0 \end{bmatrix} \qquad [1.70]$$

where α is given by $2\alpha = \operatorname{atan}\left(\frac{2\pi J}{\Omega_1 - \Omega_2}\right)$ and we obtain 4 "allowed" transitions:

frequency	intensity
$\omega_{12} = \frac{\Omega_1 + \Omega_2}{2} + \pi J - \sqrt{\left(\frac{\Omega_2 - \Omega_1}{2}\right)^2 + (\pi J)^2}$	$I_{12} = \left(\frac{\cos\alpha + \sin\alpha}{2}\right)^2 = \frac{1 + \sin 2\alpha}{4}$
$\omega_{13} = \frac{\Omega_1 + \Omega_2}{2} + \pi J + \sqrt{\left(\frac{\Omega_2 - \Omega_1}{2}\right)^2 + (\pi J)^2}$	$I_{13} = \left(\frac{\cos\alpha + \sin\alpha}{2}\right)^2 = \frac{1 - \sin 2\alpha}{4}$
$\omega_{24} = \frac{\Omega_1 + \Omega_2}{2} - \pi J + \sqrt{\left(\frac{\Omega_2 - \Omega_1}{2}\right)^2 + (\pi J)^2}$	$I_{24} = \left(\frac{\cos\alpha + \sin\alpha}{2}\right)^2 = \frac{1 + \sin 2\alpha}{4}$
$\omega_{34} = \frac{\Omega_1 + \Omega_2}{2} - \pi J - \sqrt{\left(\frac{\Omega_2 - \Omega_1}{2}\right)^2 + (\pi J)^2}$	$I_{34} = \left(\frac{\cos\alpha + \sin\alpha}{2}\right)^2 = \frac{1 - \sin 2\alpha}{4}$

for the particular solution we have assumed that α is positive. In principle one should distinguish according to the sign of J.

The basis functions that span the eigenbase of the Hamiltonian are

$$\begin{gathered} |\alpha_1\alpha_2\rangle \\ \cos\alpha|\alpha_1\beta_2\rangle + \sin\alpha|\beta_1\alpha_2\rangle \\ -\sin\alpha|\alpha_1\beta_2\rangle + \cos\alpha|\beta_1\alpha_2\rangle \\ |\beta_1\beta_2\rangle \end{gathered} \quad . \qquad [1.71]$$

The resulting spectrum is shown in Fig. 1.19. The appearance of the spectrum as a function of the ratio $k = |(\Omega_2 - \Omega_1)/(2\pi J)|$ is displayed in Fig. 1.20.

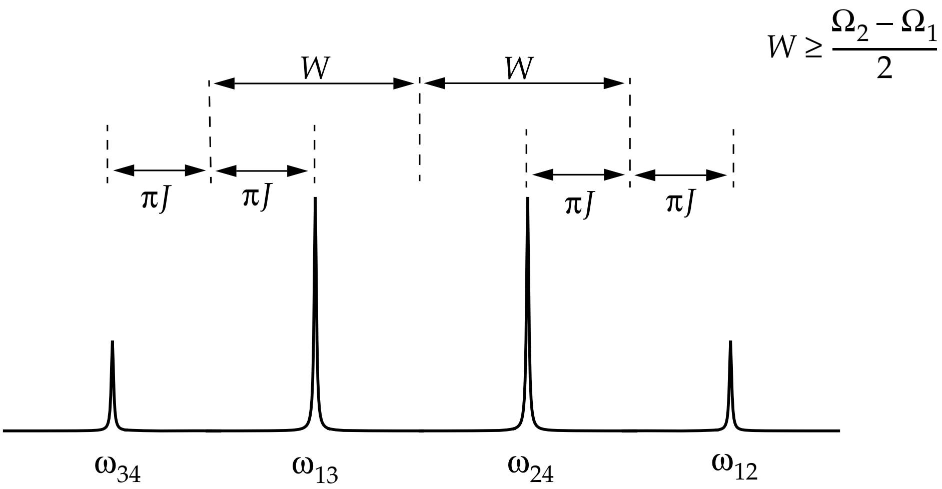

Figure 1.19: Spectrum of a J-Coupled Two-Spin System

1.7 Allowed and Forbidden Transitions

In the example presented above, we have seen that only the transitions (12), (13), (24), and (34) out of the six possible ones lead to a non-zero intensity in the spectrum. They are called allowed transitions. Such transitions can only appear where the detection operator has nonzero elements. The detection operator is always a linear combination of $\hat{F}^{+}$ and $\hat{F}^{-}$. This operator has only matrix-elements between states with a difference in the total magnetic quantum number of 1.

$$M_l = \sum_l m_{lk} \qquad [1.72]$$

Here, the m_{kl} denote the magnetic quantum numbers of the individual nuclei contained in the spin system considered (in this example, there are only two spins). This is the selection rule for magnetic resonance:

$$M_l - M_j = \pm 1 \qquad [1.73]$$

only *one-quantum transitions* are allowed. The *zero-quantum transition* (23) and the *double-quantum transition* (14) are forbidden.

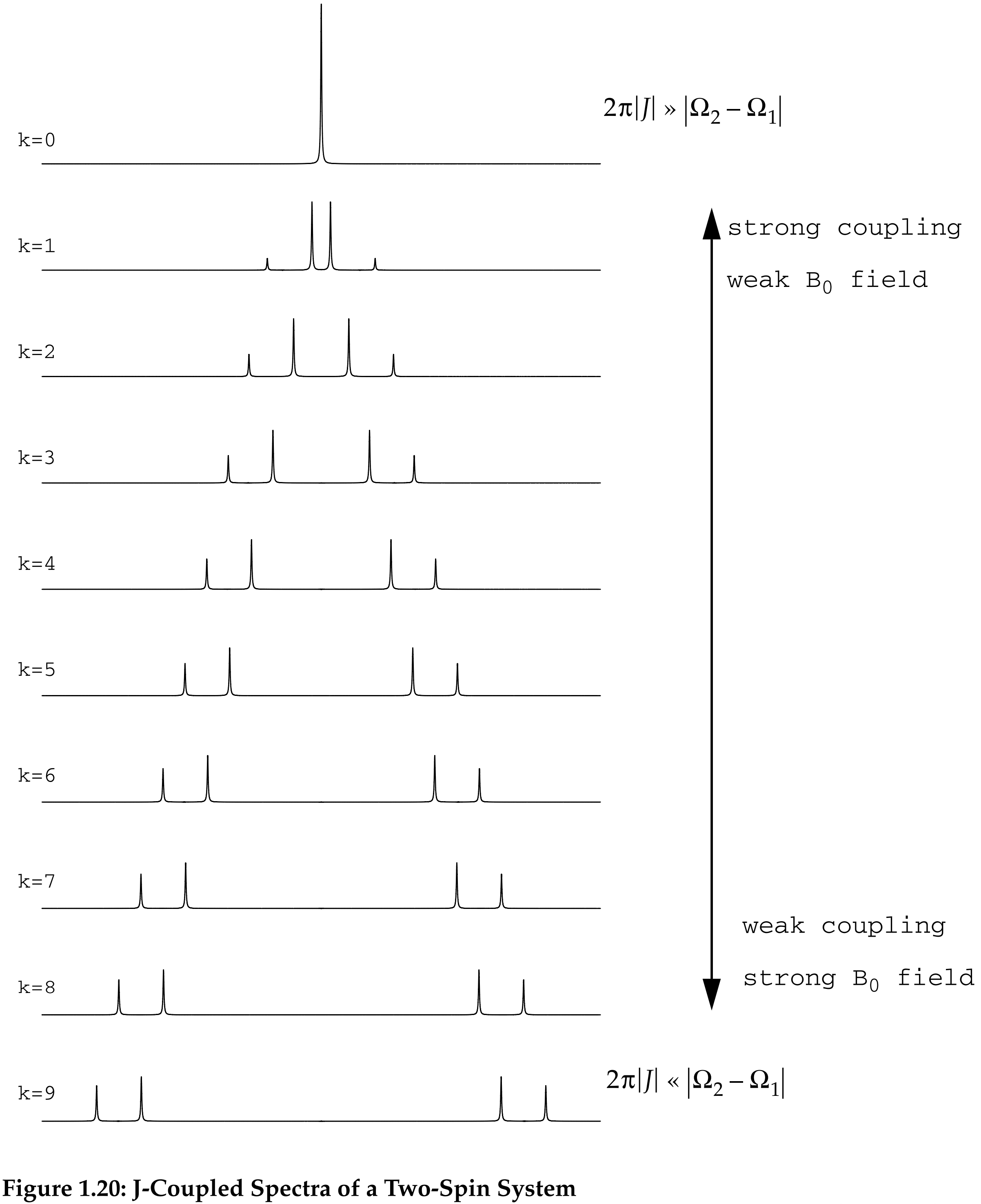

Figure 1.20: J-Coupled Spectra of a Two-Spin System
for a constant J as a function of the difference in resonance frequency $|\Omega_2 - \Omega_1|$.The parameter k is defined as $k = |(\Omega_2 - \Omega_1)/(2\pi J)|$.

1.8 The Magnetic Dipole Interaction

The magnetic dipole-dipole interaction has a classical analogy, the interaction between two magnetic (dipole) moments $\vec{\mu_1}$ and $\vec{\mu_2}$. The classical interaction energy of two magnetic moments located at positions connected by the vector $\vec{r_{12}}$ is given by:

$$E = \frac{\mu_0}{4\pi}\frac{1}{r_{12}^3}\left(\vec{\mu_1}\cdot\vec{\mu_2} - \frac{3}{r_{12}^2}(\vec{\mu_1}\cdot\vec{r_{12}})(\vec{\mu_2}\cdot\vec{r_{12}})\right) \qquad [1.74]$$

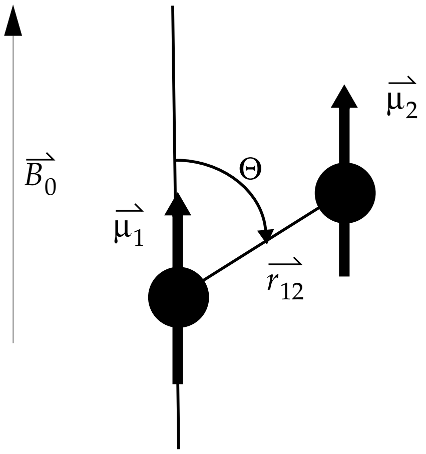

Figure 1.21: Dipole Moment

For the special case where the two magnetic moments are aligned with the z-axis ($\vec{B_0}$), the classical energy function reduces to:

$$E = \frac{\mu_0}{4\pi}\frac{1}{r_{12}^3}\mu_1\mu_2(1 - 3\cos\theta^2) \qquad [1.75]$$

The quantum-mechanical spin Hamiltonian is obtained from Eq. [1.137] as:

$$\begin{aligned}\hat{\mathcal{H}}_D &= \frac{\mu_0}{4\pi}\frac{\gamma_1\gamma_2\hbar}{r_{12}^3}\left(\vec{\hat{I}}_1\cdot\vec{\hat{I}}_2 - \frac{3}{r_{12}^2}(\vec{\hat{I}}_1\cdot\vec{r_{12}})(\vec{\hat{I}}_2\vec{r_{12}})\right) \\ &= \vec{\hat{I}}_1\underline{D}\vec{\hat{I}}_2\end{aligned} \qquad [1.76]$$

$\tilde{D}$ is a 3x3 matrix with the elements:

$$(\underset{\sim}{D})_{\alpha\beta} = \frac{\mu_0}{4\pi}\frac{\gamma_1\gamma_2\hbar}{r_{12}^3}(\delta_{\alpha\beta} - 3e_\alpha e_\beta) \qquad \alpha, \beta = x, y, z \qquad [1.77]$$

where the e_α are the components of a unit vector parallel to $\vec{r_{12}}$. For $\vec{r_{12}} = (0, 0, r_{12})$, we have

$$\underset{\sim}{D} = \frac{\mu_0}{4\pi}\frac{\gamma_1\gamma_2\hbar}{r_{12}^3}\begin{bmatrix}1 & 0 & 0\\ 0 & 1 & 0\\ 0 & 0 & -2\end{bmatrix} \qquad [1.78]$$

Using spherical coordinates for $\overrightarrow{r_{12}}$:

$$\begin{aligned} r_x &= r\sin\theta\cos\varphi \\ r_y &= r\sin\theta\sin\varphi \\ r_z &= r\cos\theta \end{aligned}$$

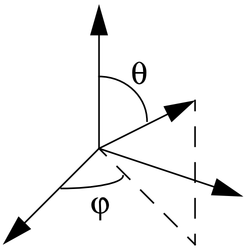

and the shift operators, the dipolar interaction can be rewritten in the so-called dipolar alphabet:

$$\hat{\mathcal{H}}_D = \frac{\mu_0}{4\pi}\frac{\gamma_1\gamma_2\hbar}{r_{12}^3}[\hat{A}+\hat{B}+\hat{C}+\hat{D}+\hat{E}+\hat{F}] \qquad [1.79]$$

with:

$$\begin{aligned} \hat{A} &= \hat{I}_{1z}\hat{I}_{2z}(1-3\cos\theta^2) \\ \hat{B} &= (\hat{I}_1^+\hat{I}_2^- + \hat{I}_1^-\hat{I}_2^+)\frac{3\cos\theta^2-1}{4} \\ \hat{C} &= (\hat{I}_1^+\hat{I}_{2z} + \hat{I}_{1z}\hat{I}_2^+)\frac{-3\sin\theta\cos\theta e^{-i\varphi}}{2} \\ \hat{D} &= (\hat{I}_1^-\hat{I}_{2z} + \hat{I}_{1z}\hat{I}_2^-)\frac{-3\sin\theta\cos\theta e^{i\varphi}}{2} \\ \hat{E} &= \hat{I}_1^+\hat{I}_2^+\frac{-3\sin\theta^2 e^{-2i\varphi}}{4} \\ \hat{F} &= \hat{I}_1^-\hat{I}_2^-\frac{-3\sin\theta^2 e^{2i\varphi}}{4} \end{aligned} \qquad [1.80]$$

In the presence of a strong Zeeman interaction, one transforms into the rotating frame. The operators $\hat{I}^+$ and $\hat{I}^-$ become time dependent and the terms $\hat{C}$ to $\hat{F}$ can be neglected as non-secular terms leading to

$$\hat{\mathcal{H}}_D' = \frac{\mu_0}{4\pi}\frac{\gamma_1\gamma_2\hbar}{r_{12}^3}(\hat{A}+\hat{B}). \qquad [1.81]$$

The term $\hat{A}$ remains obviously always invariant when going into the rotating frame since it contains only $\hat{I}_z$ operators. For the term $\hat{B}$, two situations must be distinguished:

- *Homonuclear case* (both nuclei have the same Zeeman-frequency and the same rotating frame transformation applies): Here $\hat{I}_1^+\hat{I}_2^- + \hat{I}_1^-\hat{I}_2^+$ is time-independent and must be taken into account.
- *Heteronuclear case*: Here we need two different rotating frames for the two spins rotating at their specific Larmor frequencies. In the rotating frame, the term $\hat{I}_1^+\hat{I}_2^- + \hat{I}_1^-\hat{I}_2^+$ is time-dependent with a frequency equal to the difference of the two Larmor frequencies. Therefore, it can be neglected as non secular in excellent approximation.

The simplified secular rotating-frame dipolar-coupling Hamiltonian is of the form

- for a homonuclear spin pair:

$$\hat{\mathcal{H}}'_D = \frac{\mu_0}{4\pi}\frac{\gamma_1\gamma_2\hbar}{r_{12}^3}\frac{(1-3\cos\theta^2)}{2}\left[2\hat{I}_{1z}\hat{I}_{2z} - \frac{1}{2}(\hat{I}_1^+\hat{I}_2^- + \hat{I}_1^-\hat{I}_2^+)\right] \qquad [1.82]$$

- for a heteronuclear spin pair:

$$\hat{\mathcal{H}}'_D = \frac{\mu_0}{4\pi}\frac{\gamma_1\gamma_2\hbar}{r_{12}^3}\frac{(1-3\cos\theta^2)}{2}2\hat{I}_{1z}\hat{I}_{2z} \qquad [1.83]$$

The constant

$$d = \frac{\mu_0}{4\pi}\frac{\gamma_1\gamma_2\hbar}{r_{12}^3}\frac{(1-3\cos\theta^2)}{2} \qquad [1.84]$$

is often called the dipolar coupling constant.

1.8.1 Spectrum of a Heteronuclear Dipolar-Coupled Spin Pair

Assuming that the rotating-frame Hamiltonian consists only of the dipolar interaction, it has the form:

$$\hat{\mathcal{H}}'' = \hat{\mathcal{H}}'_D = 2d\hat{I}_{1z}\hat{I}_{2z} \tag{1.85}$$

with the matrix representation

$$(\mathcal{H}'') = 2d\begin{bmatrix} \frac{1}{4} & 0 & 0 & 0 \\ 0 & -\frac{1}{4} & 0 & 0 \\ 0 & 0 & -\frac{1}{4} & 0 \\ 0 & 0 & 0 & \frac{1}{4} \end{bmatrix} \tag{1.86}$$

This leads to the transition frequencies for the allowed transitions of:

$$\begin{aligned} \omega_1 &= (\mathcal{H}'')_{11} - (\mathcal{H}'')_{22} = d \\ \omega_2 &= (\mathcal{H}'')_{33} - (\mathcal{H}'')_{44} = -d \end{aligned} \tag{1.87}$$

and a spectrum with two lines with a splitting of $2d$ as shown in Fig. 1.22.

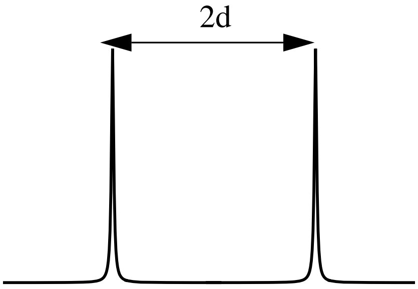

Figure 1.22: Dipolar Splitting

1.8.2 Spectrum of a Homonuclear Dipolar-Coupled Spin Pair

Here the term $\hat{B}$ must also be taken into account. In this case $\hat{\mathcal{H}}$ has permutation symmetry with respect to an exchange of the two nuclei:

$$\hat{P}(12)\hat{\mathcal{H}} = \hat{\mathcal{H}} \tag{1.88}$$

As a consequence, the eigenfunctions transform according to the irreducible representations A and B of the permutation group of two elements. From this argument we obtain immediately the Eigenfunctions:

- Symmetric representation A:

$$\begin{aligned} \phi_1 &= \alpha\alpha \\ \phi_2 &= \frac{1}{\sqrt{2}}(\alpha\beta + \beta\alpha) \\ \phi_3 &= \beta\beta \end{aligned} \tag{1.89}$$

- Anti-symmetric representation B:

$$\phi_4 = \frac{1}{\sqrt{2}}(\alpha\beta - \beta\alpha) \qquad [1.90]$$

We can now calculate the diagonal elements of $\mathcal{H}_D{}'$ in this basis and obtain

$$\begin{aligned} E_1 &= \langle\phi_1|\mathcal{H}|\phi_1\rangle = \frac{d}{2} \\ E_2 &= \langle\phi_2|\mathcal{H}|\phi_2\rangle = -d \\ E_3 &= \langle\phi_3|\mathcal{H}|\phi_3\rangle = \frac{d}{2} \\ E_4 &= \langle\phi_4|\mathcal{H}|\phi_4\rangle = 0 \end{aligned} \qquad [1.91]$$

The transition frequencies for the allowed transitions are

$$\begin{aligned} \omega_1 &= (E_1 - E_2) = \frac{3d}{2} \\ \omega_2 &= (E_2 - E_3) = \frac{-3d}{2} \end{aligned} \qquad [1.92]$$

and the spectrum has two lines with a splitting of $3d$ as shown in Fig. 1.23

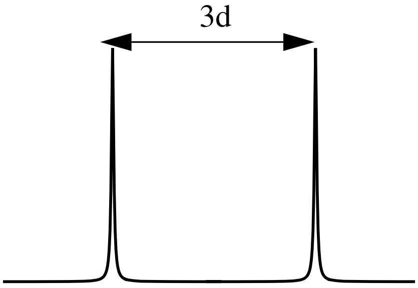

Figure 1.23: Dipolar Splitting

Exercise: Show that the allowed transitions in this case are indeed the 1-2 and 2-3 transitions.

1.8.3 Intermediate Cases

The spectrum of two dipolar-coupled nuclei can be calculated in almost complete analogy to the one of two J-coupled nuclei. The matrix representation of the Hamiltonian is given by (compare to Eq. [1.66]!):

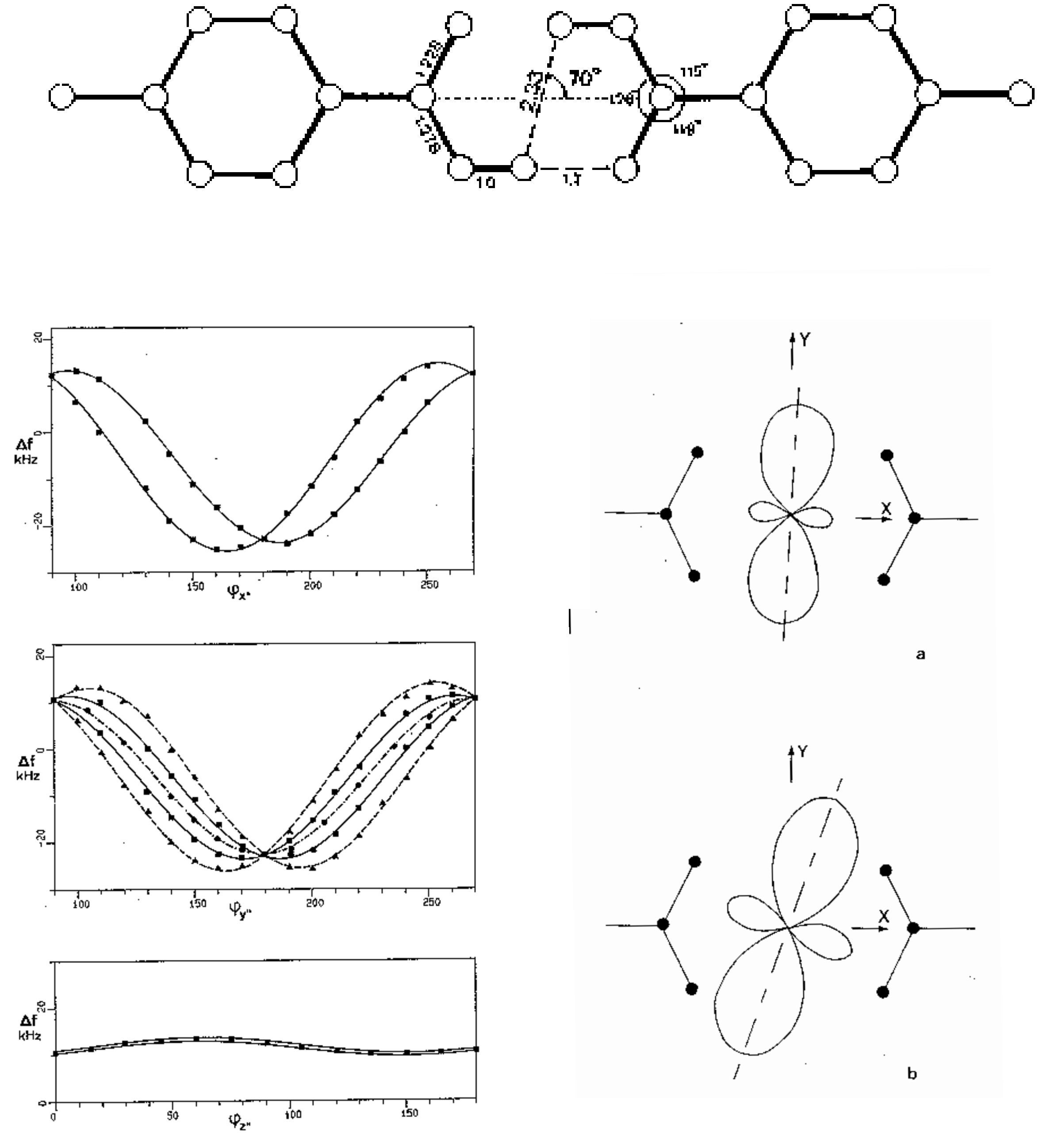

Figure 1.24: Measured Dipolar Splitting
between the two protons in p-toluoic acid at room temperature and at 10 K. The experiment manifests the proton tautometrism.

$$(\mathcal{H}_D) = \begin{bmatrix} \frac{\Omega_1+\Omega_2}{2}+\frac{d}{2} & 0 & 0 & 0 \\ 0 & \frac{\Omega_1-\Omega_2}{2}-\frac{d}{2} & -\frac{d}{2} & 0 \\ 0 & -\frac{d}{2} & \frac{\Omega_2-\Omega_1}{2}-\frac{d}{2} & 0 \\ 0 & 0 & 0 & \frac{-(\Omega_1+\Omega_2)}{2}+\frac{d}{2} \end{bmatrix} \qquad [1.93]$$

Note that the off-diagonal matrix elements have the same size as the diagonal matrix elements while, in the case of the J-coupling Hamiltonian, they were a factor two larger!

With $2\alpha = \operatorname{atan}\left(\frac{-D}{\Omega_1-\Omega_2}\right)$ we obtain again four "allowed" transitions with the following frequencies and intensities:

frequency	intensity
$\omega_{12} = \frac{\Omega_1+\Omega_2}{2}+d-\sqrt{\left(\frac{\Omega_2-\Omega_1}{2}\right)^2+\left(\frac{d}{2}\right)^2}$	$I_{12} = \left(\frac{\cos\alpha+\sin\alpha}{2}\right)^2 = \frac{1+\sin 2\alpha}{4}$
$\omega_{13} = \frac{\Omega_1+\Omega_2}{2}+d+\sqrt{\left(\frac{\Omega_2-\Omega_1}{2}\right)^2+\left(\frac{d}{2}\right)^2}$	$I_{13} = \left(\frac{\cos\alpha+\sin\alpha}{2}\right)^2 = \frac{1-\sin 2\alpha}{4}$
$\omega_{24} = \frac{\Omega_1+\Omega_2}{2}-d+\sqrt{\left(\frac{\Omega_2-\Omega_1}{2}\right)^2+\left(\frac{d}{2}\right)^2}$	$I_{24} = \left(\frac{\cos\alpha+\sin\alpha}{2}\right)^2 = \frac{1+\sin 2\alpha}{4}$
$\omega_{34} = \frac{\Omega_1+\Omega_2}{2}-d-\sqrt{\left(\frac{\Omega_2-\Omega_1}{2}\right)^2+\left(\frac{d}{2}\right)^2}$	$I_{34} = \left(\frac{\cos\alpha+\sin\alpha}{2}\right)^2 = \frac{1-\sin 2\alpha}{4}$

The resulting spectra are plotted in Fig. 1.25.

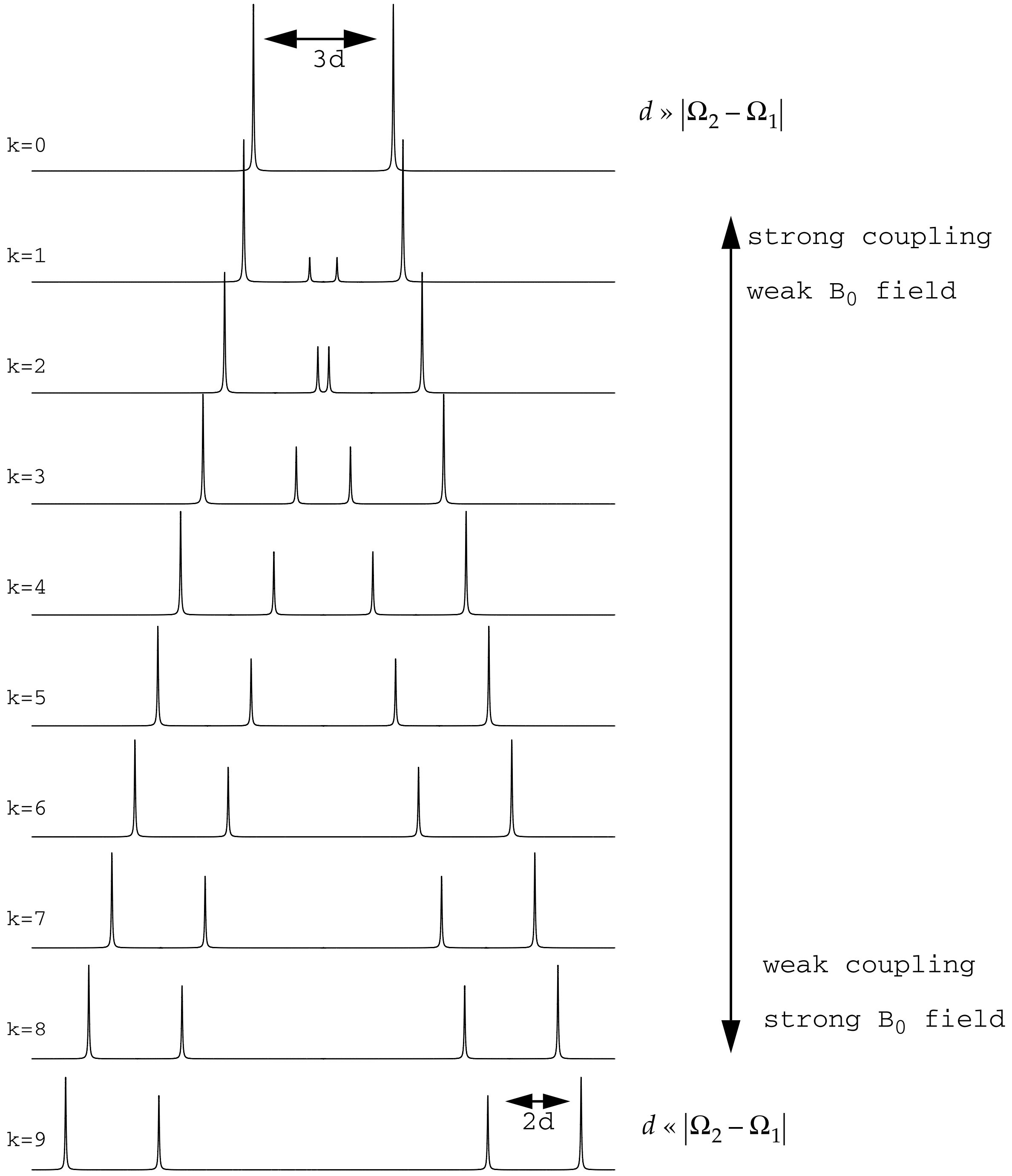

Figure 1.25: D-Coupled Spectra of a Two-Spin System
for constant D as a function of the difference in resonance frequency $|\Omega_2 - \Omega_1|$ .The parameter k is defined as $k = |(\Omega_2 - \Omega_1)/d|$.

2 The general Form of Hamiltonians, Symmetry Arguments

ccccThec

The Hamiltonians for the most important interactions in solid-state NMR are discussed in this Chapter. We introduce the interactions first in a Cartesian description where they have the general form

$$\hat{\mathcal{H}}^{(k,n)} = \vec{\hat{I}}_k \cdot A^{(k,n)} \cdot \vec{\hat{I}}_n \qquad [2.1]$$

for spin-spin interactions and

$$\hat{\mathcal{H}}^{(k,\mathrm{B})} = \vec{\hat{I}}_k \cdot A^{(k,\mathrm{B})} \cdot \vec{B} \qquad [2.2]$$

for interactions between the spin and the magnetic field. In both cases A is a 3x3 matrix that describes the strength and the angular dependence of the interaction.

In the second part, the link to a symmetry-adapted description of the spin interactions, using spatial spherical tensors and irreducible spherical-tensor operators, is provided. In such a description the laboratory-frame Hamiltonian can be written in a concise form as the scalar products between a spherical spatial tensor and a spherical spin-tensor operator. The scalar product can be expressed as a sum of products of spherical-tensor components

$$\hat{\mathcal{H}}^{(i)} = \sum_{\ell} \vec{A}_{\ell}^{(i)} \cdot \vec{\hat{\mathcal{T}}}_{\ell}^{(i)} = \sum_{\ell} \sum_{q=-\ell}^{\ell} (-1)^q A_{\ell q}^{(i)} \hat{\mathcal{T}}_{\ell,-q}^{(i)} \ . \qquad [2.3]$$

Advantages, but also limitations associated with the spherical-tensor formulation will be discussed.

2.1 The Basic Interactions

The basic spin Hamiltonians for all practically relevant interactions in magnetic resonance contain either one or two spin operators. Terms with a single spin operator appear in the context of the interaction of a spin with a classical field, e.g., the magnetic field $\vec{B}$. They are of the general form

$$\hat{\mathcal{H}}^{(k,\,\mathrm{B})} = \vec{\hat{I}}_k \cdot A^{(k,\,\mathrm{B})} \cdot \vec{B} = \begin{pmatrix} \hat{I}_{kx} & \hat{I}_{ky} & \hat{I}_{kz} \end{pmatrix} \cdot \begin{pmatrix} a_{xx} & a_{xy} & a_{xz} \\ a_{yx} & a_{yy} & a_{yz} \\ a_{zx} & a_{zy} & a_{zz} \end{pmatrix} \cdot \begin{pmatrix} B_x \\ B_y \\ B_z \end{pmatrix} \qquad [2.4]$$

where the operators $\hat{I}_{k\alpha}$ with $\alpha = x, y, z$ are the usual spin operators of spin k that can be represented by the Pauli matrices. The field $\vec{B} = (B_x, B_y, B_z)^T$ is always described as a classical quantity, the magnetic-field vector. The quantization of the field in the context of quantum electrodynamics is possible but unnecessary in magnetic resonance.

The strongest interaction in high-field NMR, the Zeeman interaction, is of this form. Details and other examples will be given below. The strength and the angular dependence of the interaction is specified by the nine components $a_{\alpha\beta}$ with $\alpha, \beta = x, y, z$ of the 3x3 matrix $A^{(k,\,\mathrm{B})}$ which is often referred to as the spatial part of the interaction, in contrast to the spin part which contains the spin operators.

Two-spin interactions between spins k and n can be formulated by a Hamiltonian of the form

$$\hat{\mathcal{H}}^{(k,\,n)} = \vec{\hat{I}}_k \cdot A^{(k,\,n)} \cdot \vec{\hat{I}}_n = \begin{pmatrix} \hat{I}_{kx} & \hat{I}_{ky} & \hat{I}_{kz} \end{pmatrix} \cdot \begin{pmatrix} a_{xx} & a_{xy} & a_{xz} \\ a_{yx} & a_{yy} & a_{yz} \\ a_{zx} & a_{zy} & a_{zz} \end{pmatrix} \cdot \begin{pmatrix} \hat{I}_{nx} \\ \hat{I}_{ny} \\ \hat{I}_{nz} \end{pmatrix} . \qquad [2.5]$$

Such a Hamiltonian describes the coupling between two spins ($k \neq n$) which can be electron or nuclear spins. Examples include the J coupling, the dipolar coupling, and the hyperfine coupling. The same form of a Hamiltonian describes the quadrupole interaction where square terms of a single spin appear and which can be written in the same form with $k = n$. The strength and the angular dependence of a spin-spin interaction are described by the matrix $A^{(k,\,n)}$.

The two basic forms for the Hamiltonian as given by Eqs. [2.4] and [2.5] can be reformulated as a scalar product of two vectors

$$\hat{\mathcal{H}}^{(k,\,\mathrm{B})} = \vec{A}^{(k,\,\mathrm{B})} \cdot \vec{\hat{I}}^{(k,\,\mathrm{B})} \qquad [2.6]$$

and

$$\hat{\mathcal{H}}^{(k,\,n)} = \vec{A}^{(k,\,n)} \cdot \vec{\hat{I}}^{(k,\,n)} , \qquad [2.7]$$

respectively, with the spatial vector

$$\vec{A}^{(k,\,n)} = (a_{xx}, a_{xy}, a_{xz}, a_{yx}, a_{yy}, a_{yz}, a_{zx}, a_{zy}, a_{zz}) \qquad [2.8]$$

and the spin vector operator

$$\vec{\hat{I}}^{(k,\,n)} = \vec{\hat{I}_k} \otimes \vec{\hat{I}_n} = (\hat{I}_{kx}\hat{I}_{nx}, \hat{I}_{kx}\hat{I}_{ny}, \hat{I}_{kx}\hat{I}_{nz}, \hat{I}_{ky}\hat{I}_{nx}, \hat{I}_{ky}\hat{I}_{ny}, \hat{I}_{ky}\hat{I}_{nz}, \hat{I}_{kz}\hat{I}_{nx}, \hat{I}_{kz}\hat{I}_{ny}, \hat{I}_{kz}\hat{I}_{nz}) \qquad [2.9]$$

or

$$\vec{\hat{I}}^{(k,\,B)} = \vec{\hat{I}_k} \otimes \vec{B} = (\hat{I}_{kx}B_x, \hat{I}_{kx}B_y, \hat{I}_{kx}B_z, \hat{I}_{ky}B_x, \hat{I}_{ky}B_y, \hat{I}_{ky}B_z, \hat{I}_{kz}B_x, \hat{I}_{kz}B_y, \hat{I}_{kz}B_z) \; . \qquad [2.10]$$

The scalar product in this vector space is defined as

$$\vec{A} \cdot \vec{\hat{I}} = \sum_i (\vec{A})_i^* (\vec{\hat{I}})_i \; . \qquad [2.11]$$

The vectors $\vec{A}^{(k,\,n)}$, $\vec{\hat{I}}^{(k,\,n)}$, and $\vec{\hat{I}}^{(k,\,B)}$ have always a dimension of nine. The vector $\vec{\hat{I}}^{(k,\,n)}$ forms a nine-dimensional subspace of the full 16-dimensional Liouville space spanned by the operators of Eq. [2.9]. The Hamiltonian describes the energy of the system and must, therefore, be a scalar quantity. This compact notation will become important in the context of the spherical-tensor notation of Hamiltonians (Chapter 2.2).

2.1.1 Some Symmetry Considerations For The Matrix *A*

It is often convenient to split the matrix A into three components

$$A = A^{(0)} + A^{(1)} + A^{(2)} \qquad [2.12]$$

with

$$A^{(0)} = \begin{pmatrix} \bar{a} & 0 & 0 \\ 0 & \bar{a} & 0 \\ 0 & 0 & \bar{a} \end{pmatrix} \qquad [2.13]$$

where the quantity $\bar{a}$ is equal to one third of the trace of the matrix A, i.e.,

$$\bar{a} = \frac{1}{3}\mathrm{Tr}\{A\} = \frac{(a_{xx} + a_{yy} + a_{zz})}{3} \,. \qquad [2.14]$$

It is well known that $\bar{a}$ is invariant under rotations of the coordinate system. The matrix $A^{(0)}$ is, therefore, often referred to as the isotropic component or the zeroth-rank component of the matrix A.

The traceless and symmetrized part of the matrix A is of the form

$$A^{(2)} = \begin{pmatrix} a_{xx} - \bar{a} & \frac{(a_{xy} + a_{yx})}{2} & \frac{(a_{xz} + a_{zx})}{2} \\ \frac{(a_{xy} + a_{yx})}{2} & a_{yy} - \bar{a} & \frac{(a_{yz} + a_{zy})}{2} \\ \frac{(a_{xz} + a_{zx})}{2} & \frac{(a_{yz} + a_{zy})}{2} & -(a_{xx} + a_{yy}) + 2\bar{a} \end{pmatrix} \qquad [2.15]$$

and is often referred to as the second-rank component.

Now we can calculate the remaining component $A^{(1)}$ as

$$A^{(1)} = \begin{pmatrix} 0 & \frac{(a_{xy} - a_{yx})}{2} & \frac{(a_{xz} - a_{zx})}{2} \\ \frac{(a_{yx} - a_{xy})}{2} & 0 & \frac{(a_{yz} - a_{zy})}{2} \\ \frac{(a_{zx} - a_{xz})}{2} & \frac{(a_{zy} - a_{yz})}{2} & 0 \end{pmatrix} . \qquad [2.16]$$

This matrix is anti symmetric and traceless and is called the first-rank component. It will turn out later, that the anti-symmetric component can normally not be observed in NMR experiments.

We will see later that the three components of the matrix A have the properties of Cartesian tensors of rank 0, rank 1, and rank 2. The properties of Cartesian tensors will be more formally introduced in Chapter 1.11. For the moment it is sufficient to keep in mind that the three matrix components and tensors are equivalent.

2.1.2 Cartesian Tensor Quantities

The field of tensor analysis in general is quite complex and forms, as an example, the basis of Einstein's treatment of general relativity. In magnetic resonance, as in many engineering sciences, a much simpler version of the full theory is sufficient. Here, we only introduce this simple treatment.

We have already noticed in Chapter 2.1.1 that a full 3x3 matrix can be decomposed into three different components. The rank-zero component is characterized by a single number, the rank-one component by three different numbers, which can be represented by a vector in normal three-dimensional space and a rank-two component which has five independent components that can be written in a matrix. Note that also the rank-zero and rank-one components can be written as matrices if desired.

A further important distinction between tensors of different rank is their transformation behavior under rotations which will be discussed in the following.

2.1.2.1 Tensors of Rank Zero: Scalars

Some physical quantities are independent of the coordinate system they are described in. One example of such a quantity is the distance r_{xy} between two points $\vec{x} = (x_1, x_2, x_3)$ and $\vec{y} = (y_1, y_2, y_3)$. The distance is given by the

$$r_{xy} = \sqrt{\sum_{i=1}^{3} (x_i - y_i)^2} \ . \qquad [2.17]$$

If we apply a coordinate transformation, the new coordinates of the two points are given by $\vec{x}' = (x'_1, x'_2, x'_3)$ and $\vec{y}' = (y'_1, y'_2, y'_3)$, the distance is given by

$$r'_{xy} = \sqrt{\sum_{i=1}^{3} (x'_i - y'_i)^2} \ . \qquad [2.18]$$

Independent of the choice of coordinate system, we will always find

$$r'_{xy} = r_{xy} \; . \qquad [2.19]$$

In a more general notation we can write for a a tensor of rank zero or a scalar quantity $\mathfrak{A}^{(0)} = \bar{a}$ under a coordinate transformation

$$\mathfrak{A}'^{(0)} = \mathfrak{A}^{(0)} \; . \qquad [2.20]$$

Since the Hamiltonian describes the energy of a system and the energy is a scalar quantity, the Hamiltonian also has to be a scalar or a tensor of rank zero.

2.1.2.2 Tensors of Rank One: Vectors

The coordinates of a point in space are an example for a tensor of rank one that can be represented by a vector. If we apply a coordinate transformation characterized by the rotation matrix R the coordinates of a point transform like

$$\begin{pmatrix} a'_x \\ a'_y \\ a'_z \end{pmatrix} = \begin{pmatrix} R_{xx} & R_{xy} & R_{xz} \\ R_{yx} & R_{yy} & R_{yz} \\ R_{zx} & R_{zy} & R_{zz} \end{pmatrix} \begin{pmatrix} a_x \\ a_y \\ a_z \end{pmatrix} \qquad [2.21]$$

or

$$a'_i = \sum_j R_{ij} a_j \; . \qquad [2.22]$$

In a more general notation we can write for a tensor of rank one, $\mathfrak{A}^{(1)} = (a_x, a_y, a_z)$, under a coordinate transformation

$$\mathfrak{A}'^{(1)} = R\mathfrak{A}^{(1)} \qquad [2.23]$$

or for the elements a_j of the first-rank tensor

$$a'_i = \sum_j R_{ij} a_j \; . \qquad [2.24]$$

2.1.2.3 Tensors of Rank Two: Symmetric Traceless Matrices

Quantities that are represented by a symmetric traceless matrix in Cartesian space, e.g., the dipolar-coupling tensor

$$D_{ij}^{(k,\,n)} = (\underset{\sim}{D}^{(k,\,n)})_{ij} = \frac{-\mu_0}{4\pi}\,\frac{\gamma_k\gamma_n\hbar}{r_{kn}^3}(\delta_{ij} - 3e_ie_j) \qquad i,j = x,y,z \tag*{[2.25]}$$

are called second-rank tensors. Under a coordinate transformation characterized by the rotation matrix R such a tensor of rank two transforms according to

$$\begin{pmatrix} D'_{xx} & D'_{xy} & D'_{xz} \\ D'_{yx} & D'_{yy} & D'_{yz} \\ D'_{zx} & D'_{zy} & D'_{zz} \end{pmatrix} = \begin{pmatrix} R_{xx} & R_{xy} & R_{xz} \\ R_{yx} & R_{yy} & R_{yz} \\ R_{zx} & R_{zy} & R_{zz} \end{pmatrix} \cdot \begin{pmatrix} D_{xx} & D_{xy} & D_{xz} \\ D_{yx} & D_{yy} & D_{yz} \\ D_{zx} & D_{zy} & D_{zz} \end{pmatrix} \cdot \begin{pmatrix} R_{xx} & R_{yx} & R_{zx} \\ R_{xy} & R_{yy} & R_{zy} \\ R_{xz} & R_{yz} & R_{zz} \end{pmatrix} \tag*{[2.26]}$$

or for the matrix elements

$$D'_{ij} = \sum_k \sum_\ell R_{ik} R_{j\ell} D_{k\ell} \tag*{[2.27]}$$

In a more general notation we can write for a tensor of rank two,

$$\mathfrak{A}^{(2)} = \begin{pmatrix} a_{xx} & a_{xy} & a_{xz} \\ a_{yx} & a_{yy} & a_{yz} \\ a_{zx} & a_{zy} & a_{zz} \end{pmatrix}, \tag*{[2.28]}$$

under a coordinate transformation

$$\mathfrak{A}'^{(2)} = R\mathfrak{A}^{(2)}R^{\mathrm{T}} \tag*{[2.29]}$$

or for the elements $a_{k\ell}$ of the second-rank tensor

$$a'_{ij} = \sum_k \sum_\ell R_{ik} R_{j\ell} a_{k\ell}\ . \tag*{[2.30]}$$

The traceless symmetric matrix that describes the second-rank tensor has 5 independent components: three linearly independent off-diagonal elements and two linearly independent diagonal elements.

A general matrix $\mathfrak{A}$ has nine independent components. As we have already seen in Chapter 2.1.1, a general matrix can be decomposed into three parts, namely the trace of the matrix

$$\bar{a} = \frac{1}{3}Tr\{\underset{\sim}{\mathfrak{A}}\} = \frac{1}{3}\sum_{k} a_{kk} \ , \qquad [2.31]$$

the traceless anti-symmetric part of the matrix (three independent components)

$$a_{ij}^{(as)} = \frac{1}{2}(a_{ij} - a_{ji}) \ , \qquad [2.32]$$

and the traceless symmetric part of the matrix (five independent components)

$$a_{ij}^{(s)} = \frac{1}{2}(a_{ij} + a_{ji}) - \delta_{ij}\bar{a} \ . \qquad [2.33]$$

Under a rotation, the components of $\underset{\sim}{\mathfrak{A}}^{(s)}$, $\underset{\sim}{\mathfrak{A}}^{(as)}$, and $\overline{\mathfrak{A}}$ transform amongst themselves, i.e., the three parts do not mix. We say that the tensor components $\underset{\sim}{\mathfrak{A}}^{(s)}, \underset{\sim}{\mathfrak{A}}^{(as)}$, and $\overline{\mathfrak{A}}$ are the irreducible components of the matrix $\mathfrak{A}$. They belong to the representations $\mathfrak{D}_2$, $\mathfrak{D}_1$ and $\mathfrak{D}_0$ of the rotation group. This implies that the trace of a general matrix is invariant under rotations, i.e., it behaves like a scalar, while the anti-symmetric part of the tensor behaves under a rotation like a vector (tensor of rank one), and the symmetric traceless component behaves like a second-rank tensor.

2.1.3 Rotation of Cartesian Tensors

As already pointed out in Chapter 2.1.2.3, we can represent a generalized second-rank tensor as a matrix. The rotation of such a matrix can be written as

$$\mathfrak{A}^{(\mathrm{new})} = R(\alpha, \beta, \gamma)\mathfrak{A}^{(\mathrm{old})}R^{-1}(\alpha, \beta, \gamma) \ . \qquad [2.34]$$

Such a rotation can also be formulated as a vector operation in the space introduced in Chapter 2.1 where we wrote the matrix $\mathfrak{A}$ as a nine-dimensional vector

$$\vec{A} = (a_{xx}, a_{xy}, a_{xz}, a_{yx}, a_{yy}, a_{yz}, a_{zx}, a_{zy}, a_{zz}) \ . \qquad [2.35]$$

The rotation is then given by

$$\vec{A}^{(\mathrm{new})} = \tilde{R}(\alpha, \beta, \gamma)\vec{A}^{(\mathrm{old})} \qquad [2.36]$$

with the 9x9 rotation matrix $\tilde{R}$ defined as

$$\tilde{R}(\alpha, \beta, \gamma) = R(\alpha, \beta, \gamma) \otimes R(\alpha, \beta, \gamma) \ . \qquad [2.37]$$

In the general case, $\tilde{R}(\alpha, \beta, \gamma)$ will be a full 9x9 matrix (see Fig. 2.1a). As discussed in Chapter 2.1.1, we can use the fact that the components belonging to different ranks do not intermix under rotations to block diagonalize the rotation matrix. The nine elements of $\vec{A}$ can be linearly combined to obtain a rank-separated basis according to Eqs. [2.14] - [2.16] to yield

$$\vec{A}' = \left(\bar{a}, \frac{a_{xy} - a_{yx}}{2}, \frac{a_{xz} - a_{zx}}{2}, \frac{a_{yz} - a_{zy}}{2}, a_{xx} - \bar{a}, a_{yy} - \bar{a}, \frac{a_{xy} + a_{yx}}{2}, \frac{a_{xz} + a_{zx}}{2}, \frac{a_{yz} + a_{zy}}{2}\right). \qquad [2.38]$$

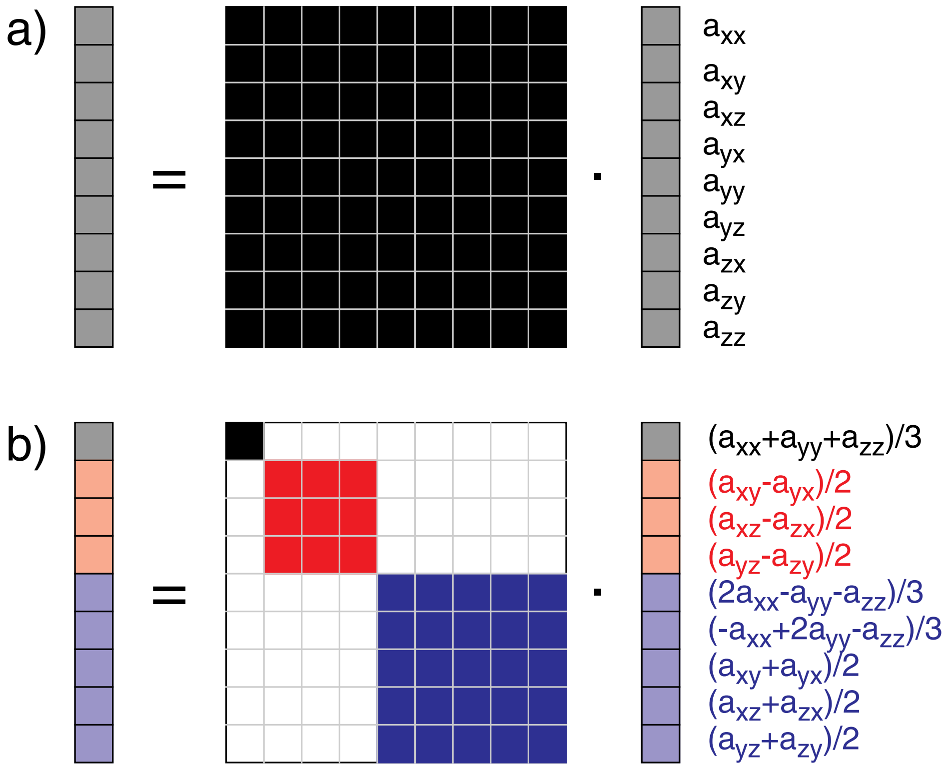

Figure 2.1: Tensor Rotations
Rotation of a Cartesian tensor in a) the standard basis and b) one possible rank-sorted basis. In the standard basis the rotation matrix is a full 9x9 block while in the rank-sorted basis the rotation matrix is block diagonal. The black 1x1 block rotates the zeroth-rank tensor, the red 3x3 block the first-rank tensor, and the blue 5x5 block the second-rank tensor.

The rotation matrix $\tilde{R}'(\alpha, \beta, \gamma)$ in this rank-separated basis is now block diagonal and consists of a 1x1 bock that rotates the isotropic component, a 3x3 block that rotates the first-rank tensor, and a 5x5 block that rotates the second-rank tensor (see Fig. 2.1b).

2.1.4 Irreducible Spherical Tensors

The irreducible spherical tensors are a special representation of the rank-separated basis discussed in the previous section. Because we use rotations, the relevant symmetry group is the one of rotations in three-dimensional space, SO3. We can describe a general Cartesian tensor of rank k in terms of a symmetry-adapted basis that belongs to the representations $\mathfrak{D}_0, \mathfrak{D}_1, \mathfrak{D}_2, \ldots, \mathfrak{D}_k$ of the rotation group. A spherical tensor of rank ℓ, $\mathfrak{S}_\ell$, is a quantity with $2\ell + 1$ components $\mathfrak{S}_{\ell m}$ which transform according to the irreducible representation $\mathfrak{D}_\ell$ of the (full) rotation group. We can write a spherical tensor of rank ℓ as a vector with $2\ell + 1$ components

$$\mathfrak{S}_\ell = (\mathfrak{S}_{\ell,-\ell}, \mathfrak{S}_{\ell,-\ell+1}, \ldots, \mathfrak{S}_{\ell,0}, \ldots, \mathfrak{S}_{\ell,\ell-1}, \mathfrak{S}_{\ell,\ell}) \qquad [2.39]$$

that can be distinguished by their "magnetic quantum number" m.

For a spherical tensor $\mathfrak{S}_\ell$ the rotation matrix (Fig. 2.2) is given by the Wigner rotation matrix of rank ℓ and the rotation of the spherical tensor can be written as

$$\mathfrak{S}_\ell^{(\text{new})} = \mathfrak{D}^\ell(\alpha, \beta, \gamma)\mathfrak{S}_\ell^{(\text{old})} \quad . \qquad [2.40]$$

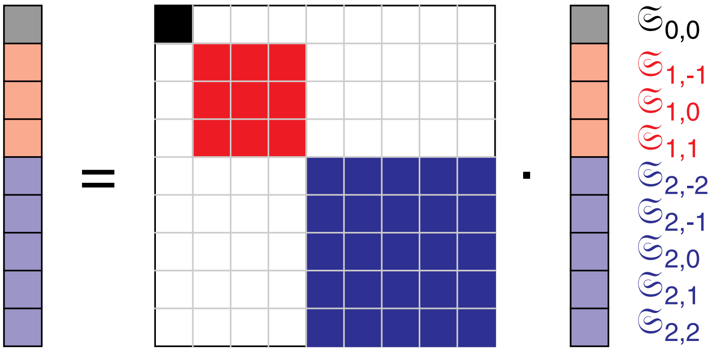

Figure 2.2: Irreducible Spherical-Tensor Rotations
Irreducible spherical tensor are a special implementation of the rank-sorted basis of Eq. [2.38]. The rotation matrix is block diagonal and the elements are the Wigner rotation-matrix elements.

The Wigner rotation matrix $\mathfrak{D}^{\ell}(\alpha, \beta, \gamma)$ can be obtained from the Cartesian rotation matrix $\tilde{R}(\alpha, \beta, \gamma)$ by the appropriate basis transformation. We can also formulate the rotation of the spherical tensor for the $2\ell + 1$ components as

$$\mathfrak{S}_{\ell m}^{(\mathrm{new})} = \sum_{m' = -\ell}^{+\ell} \mathfrak{D}_{m'm}^{\ell}(\alpha, \beta, \gamma) \mathfrak{S}_{\ell m'}^{(\mathrm{old})} . \qquad [2.41]$$

Here, the elements of the Wigner rotation matrix $\mathfrak{D}^{\ell}$ are needed which are given by

$$\mathfrak{D}_{m'm}^{\ell}(\alpha, \beta, \gamma) = e^{-i\alpha m'} d_{m'm}^{\ell}(\beta) e^{-i\gamma m} . \qquad [2.42]$$

The reduced Wigner matrix elements are given by $d_{m'm}^{\ell}(\beta)$. The Wigner rotation matrix elements can be calculated or can be found in tables for each rank ℓ. Note that both, the $\mathfrak{D}_{m'm}^{\ell}(\alpha, \beta, \gamma)$ and $d_{m'm}^{\ell}(\beta)$ depend on the Euler angles of the rotation but are just complex and real numbers, respectively, while the Wigner rotation operator $\mathfrak{D}^{\ell}$ is a matrix. Analytical expressions for the Wigner rotation matrix elements for $\ell = 0$, $\ell = 1$, and $\ell = 2$ can be found in the Appendix 12.2.

2.1.5 The Tensor Product

In order to build up higher-rank tensors, we need to know the irreducible components of the product of two tensors. This is most easily achieved using spherical tensors. The tensor product of two spherical tensors A_k and $B_{k'}$ of rank k and k', respectively, can be expressed by irreducible tensors $\mathfrak{J}_K$ of the rotation group $\mathfrak{D}_k \otimes \mathfrak{D}_{k'}$ by

$$\mathfrak{J}_{KQ}(k, k') = \sum_{q = -k}^{k} \sum_{q' = -k'}^{k'} \langle kk'qq'|KQ\rangle A_{kq} B_{k'q'} \qquad \begin{cases} (k + k') \geq K \geq |k - k'| \\ Q = q + q' \end{cases} \qquad [2.43]$$

where the $\langle kk'qq'|KQ\rangle$ are the so called Racah or Clebsch-Gordan coefficients. The Racah coefficient is related to the Wigner 3j symbols by

$$\langle kk'qq'|KQ\rangle = (-1)^{k - k' + Q} \sqrt{(2K + 1)} \begin{pmatrix} k & k' & K \\ q & q' & -Q \end{pmatrix} . \qquad [2.44]$$

This leads to the following expression for the tensor product of two spherical tensors

$$\begin{aligned}\mathfrak{I}_{KQ}(k,k') &= (-1)^{k-k'+Q}\sqrt{(2K+1)}\\ &\times \sum_{q=-k}^{k}\sum_{q'=-k'}^{k'}\begin{pmatrix} k & k' & K\\ q & q' & -Q\end{pmatrix} A_{kq}B_{k'q'} \qquad \begin{cases}(k+k')\geq K\geq |k-k'|\\ Q = q+q'\end{cases} \quad .\end{aligned} \qquad [2.45]$$

Explicit expressions for the Wigner 3j symbols can be calculated using analytical expressions in a program like Mathematica or Matlab. They can also be found tabulated in books about "angular momentum".

One can calculate the product of two first-rank tensors as

$$A_1 \otimes B_1 = \sum_{\ell=0}^{2}\sum_{m=-\ell}^{\ell}\mathfrak{I}_{\ell m} \qquad [2.46]$$

with the elements $\mathfrak{I}_{\ell m}$ according to Eq. [2.45] given by

$$\begin{aligned}\mathfrak{I}_{00} &= \frac{1}{\sqrt{3}}(A_{1,-1}B_{11} + A_{11}B_{1,-1} - A_{10}B_{10})\\ \mathfrak{I}_{10} &= \frac{1}{\sqrt{2}}(A_{11}B_{1,-1} - A_{1,-1}B_{11})\\ \mathfrak{I}_{1,\pm1} &= \mp\frac{1}{\sqrt{2}}(A_{10}B_{1,\pm1} - A_{1,\pm1}B_{10})\\ \mathfrak{I}_{20} &= \frac{1}{\sqrt{6}}(2A_{10}B_{10} + A_{11}B_{1,-1} + A_{1,-1}B_{11})\\ \mathfrak{I}_{2,\pm1} &= \frac{1}{\sqrt{2}}(A_{1,\pm1}B_{10} + A_{10}B_{1,\pm1})\\ \mathfrak{I}_{2,\pm2} &= A_{1,\pm1}B_{1,\pm1} \quad .\end{aligned} \qquad [2.47]$$

2.1.6 Spatial Tensor

The Cartesian spatial tensor of rank one is a vector $\mathfrak{A}^{(1)} = (a_x, a_y, a_z)$ in a three-dimensional Euclidean space spanned by the basis $\{\vec{e_x}, \vec{e_y}, \vec{e_z}\}$. The Cartesian second-rank spatial tensor $\mathfrak{A}^{(2)}$ is characterized by a 3x3 matrix

$$\mathfrak{A}^{(2)} = \begin{pmatrix} a_{xx} & a_{xy} & a_{xz} \\ a_{yx} & a_{yy} & a_{yz} \\ a_{zx} & a_{zy} & a_{zz} \end{pmatrix} = \begin{pmatrix} a_x^{(A)} \\ a_y^{(A)} \\ a_z^{(A)} \end{pmatrix} \otimes (a_x^{(B)}, a_y^{(B)}, a_z^{(B)}) \ . \qquad [2.48]$$

The components of the first-rank spatial spherical tensor operator are given by

$$\begin{aligned} A_{10} &= a_z \\ A_{11} &= \frac{-1}{\sqrt{2}}(a_x + ia_y) \\ A_{1,-1} &= \frac{1}{\sqrt{2}}(a_x - ia_y) \end{aligned} \ . \qquad [2.49]$$

Combining Eqs. [2.47] and [2.49] allows us to express the second-rank spherical spatial tensor in terms of the elements of the Cartesian tensor of Eq. [2.48] as

$$\begin{aligned} A_{00} &= \frac{-1}{\sqrt{3}}(a_{xx} + a_{yy} + a_{zz}) \\ A_{10} &= -\frac{i}{\sqrt{2}}(a_{xy} - a_{yx}) \\ A_{1,\pm1} &= -\frac{1}{2}(a_{zx} - a_{xz} \pm i(a_{zy} - a_{yz})) \\ A_{20} &= \frac{1}{\sqrt{6}}(3a_{zz} - (a_{xx} + a_{yy} + a_{zz})) \\ A_{2,\pm1} &= \mp\frac{1}{2}(a_{xz} + a_{zx} \pm i(a_{yz} + a_{zy})) \\ A_{2,\pm2} &= \frac{1}{2}(a_{xx} - a_{yy} \pm i(a_{xy} + a_{yx})) \end{aligned} \ . \qquad [2.50]$$

It is important to remember that all the elements of the spatial tensors are complex numbers.

2.1.7 Spin-Tensor Operators

We can also express the spin operators not only as Cartesian spin operators but also as spherical spin-tensor operators. The Cartesian one-spin tensor operator of rank zero is the identity operator $\hat{T}^{(0)} = \hat{E}$. The Cartesian one-spin tensor operators of rank one constitute a vector $\hat{T}^{(1)} = (\langle\hat{I}_x\rangle, \langle\hat{I}_y\rangle, \langle\hat{I}_z\rangle)$ in a three-dimensional space spanned by the basis $\{\vec{e}_x, \vec{e}_y, \vec{e}_z\}$. For a spin with a spin-angular momentum of $I = 1/2$, the rank 1 tensor is the highest rank that exists while for a spin with $I > 1/2$ higher-rank spin-tensor operators exist. This can also be seen from the fact that the spin operators for a spin with $I = 1/2$ can be described by the 2x2 Pauli matrixes of Eq. [1.9]. A full basis is spanned by four basis operators which are given by the zeroth-rank and the first-rank Cartesian spin-tensor operators. For a spin-1 particle, the Pauli matrices are of dimensions 3x3 and one needs nine basis operators to span the full space. Therefore, for a spin-1 nucleus zeroth-rank, first-rank, and second-rank spin-tensor operators exist.

The spherical spin-tensor operators are important since they allow the description of spin rotations in a simple way. The one-spin zeroth-rank and first-rank spherical spin-tensor operators are given by

$$\begin{aligned} \hat{T}_{00}^{(k)} &= \hat{E}_k \\ \hat{T}_{10}^{(k)} &= \hat{I}_{kz} \\ \hat{T}_{11}^{(k)} &= \frac{-1}{\sqrt{2}}\hat{I}_k^{+} \\ \hat{T}_{1,-1}^{(k)} &= \frac{1}{\sqrt{2}}\hat{I}_k^{-} \quad . \end{aligned} \qquad [2.51]$$

For a spin-1/2 this is again a full basis that spans the Hilbert space while for spins with $I > 1/2$ we need to include higher-rank spherical spin-tensor operators.

To generate the spherical spin-tensor operators in the spin space of two coupled spins, we have to calculate the tensor product of the two one-spin spherical tensor operators. For two spin-1/2 nuclei, the highest rank of the two-spin spherical tensor operators is two. Using a slightly modified version of Eq. [2.45]

$$\hat{T}_{\ell m}^{(k,n)} = (-1)^{\ell_2 - \ell_1 + m}\sqrt{2\ell+1}\sum_{m_1=-\ell_1}^{\ell_1}\begin{bmatrix} \ell_1 & \ell_2 & \ell \\ m_1 & m-m_1 & -m \end{bmatrix}\hat{T}_{\ell_1 m_1}^{(k)} \otimes \hat{T}_{\ell_2, m-m_1}^{(n)} , \qquad [2.52]$$

we can calculate the nine components of the two-spin spin-tensor operators as

$$\hat{T}_{00}^{(k,n)} = \frac{-1}{\sqrt{3}}\left[\hat{I}_{kz}\hat{I}_{nz} + \frac{1}{2}\hat{I}_k^+\hat{I}_n^- + \frac{1}{2}\hat{I}_k^-\hat{I}_n^+\right] = \frac{-1}{\sqrt{3}}(\vec{\hat{I}}_k \cdot \vec{\hat{I}}_n) \qquad [2.53]$$

$$\begin{aligned}\hat{T}_{10}^{(k,n)} &= \frac{-1}{2\sqrt{2}}[\hat{I}_k^+\hat{I}_n^- - \hat{I}_k^-\hat{I}_n^+]\\ \hat{T}_{1,\pm1}^{(k,n)} &= \frac{-1}{2}[\hat{I}_k^\pm\,\hat{I}_{nz} - \hat{I}_{kz}\hat{I}_n^\pm\,]\end{aligned} \qquad [2.54]$$

$$\begin{aligned}\hat{T}_{20}^{(k,n)} &= \frac{1}{\sqrt{6}}[3\hat{I}_{kz}\hat{I}_{nz} - (\vec{\hat{I}}_k \cdot \vec{\hat{I}}_n)]\\ \hat{T}_{2,\pm1}^{(k,n)} &= \mp\frac{1}{2}[\hat{I}_k^\pm\,\hat{I}_{nz} + \hat{I}_{kz}\hat{I}_n^\pm\,]\\ \hat{T}_{2,\pm2}^{(k,n)} &= \frac{1}{2}\cdot[\hat{I}_k^\pm\,\hat{I}_n^\pm\,]\end{aligned} \quad . \qquad [2.55]$$

We can also write down the explicit matrix representation of these spherical spin-tensor operators in the normal product basis of the Hilbert space

$$T_{00}^{(k,n)} = \frac{-1}{4\sqrt{3}}\begin{pmatrix} 1 & 0 & 0 & 0\\ 0 & -1 & 2 & 0\\ 0 & 2 & -1 & 0\\ 0 & 0 & 0 & 1\end{pmatrix}, \qquad [2.56]$$

$$T_{10}^{(k,n)} = \frac{-1}{2\sqrt{2}}\begin{pmatrix} 0 & 0 & 0 & 0\\ 0 & 0 & 1 & 0\\ 0 & -1 & 0 & 0\\ 0 & 0 & 0 & 0\end{pmatrix} \quad T_{11}^{(k,n)} = \frac{1}{4}\begin{pmatrix} 0 & 1 & -1 & 0\\ 0 & 0 & 0 & 1\\ 0 & 0 & 0 & -1\\ 0 & 0 & 0 & 0\end{pmatrix} \quad T_{1,-1}^{(k,n)} = \frac{1}{4}\begin{pmatrix} 0 & 0 & 0 & 0\\ 1 & 0 & 0 & 0\\ -1 & 0 & 0 & 0\\ 0 & 1 & -1 & 0\end{pmatrix} \qquad [2.57]$$

and

$$T_{20}^{(k,n)} = \frac{1}{2\sqrt{6}}\begin{pmatrix} 1 & 0 & 0 & 0\\ 0 & -1 & -1 & 0\\ 0 & -1 & -1 & 0\\ 0 & 0 & 0 & 1\end{pmatrix} \quad T_{21}^{(k,n)} = \frac{1}{4}\begin{pmatrix} 0 & -1 & -1 & 0\\ 0 & 0 & 0 & 1\\ 0 & 0 & 0 & 1\\ 0 & 0 & 0 & 0\end{pmatrix} \quad T_{2,-1}^{(k,n)} = \frac{1}{4}\begin{pmatrix} 0 & 0 & 0 & 0\\ 1 & 0 & 0 & 0\\ 1 & 0 & 0 & 0\\ 0 & -1 & -1 & 0\end{pmatrix}$$

$$T_{22}^{(k,n)} = \frac{1}{2}\begin{pmatrix} 0 & 0 & 0 & 1\\ 0 & 0 & 0 & 0\\ 0 & 0 & 0 & 0\\ 0 & 0 & 0 & 0\end{pmatrix} \quad T_{2,-2}^{(k,n)} = \frac{1}{2}\begin{pmatrix} 0 & 0 & 0 & 0\\ 0 & 0 & 0 & 0\\ 0 & 0 & 0 & 0\\ 1 & 0 & 0 & 0\end{pmatrix} \qquad [2.58]$$

Naturally, the two-spin tensor operators have to be expressed in the combined space of the two spins which has a dimension of 4x4 and is created by the direct product of the Pauli matrices.

2.2 Spherical-Tensor Notation Of Hamiltonians

We have already seen the Cartesian-tensor formulation for the Hamiltonians of the important interactions in NMR in Chapter 2.1. In solid-state NMR and NMR relaxation theory, the spherical notation of Hamiltonians is more often used since rotations in spin space, rotations in real space, and rotations of the static magnetic field can be expressed in a uniform formalism. If we use the spherical-tensor notation, we have to express the Hamiltonian as the scalar product of the spatial spherical tensor and the spin spherical-tensor operator as introduced in Eqs. [2.6]-[2.11]. We will denote the spherical space tensors by $A_\ell^{(i)}$ and the spin-tensor operators by $\hat{\mathcal{T}}_\ell^{(i)}$. The spin-tensor operators are defined for spin-spin interactions by

$$\hat{\vec{I}}_k \otimes \hat{\vec{I}}_n = \sum_{\ell=0}^{2} \hat{\mathcal{T}}_\ell^{(k,n)} \qquad [2.59]$$

and for interactions of the spin with the magnetic field by

$$\hat{\vec{I}}_k \otimes \vec{B} = \sum_{\ell=0}^{2} \hat{\mathcal{T}}_\ell^{(k,\mathrm{B})} \qquad [2.60]$$

The scalar product of spherical space and spin tensors leading to the scalar Hamiltonian is given by

$$\hat{\mathcal{H}} = \sum_i \sum_{\ell=0}^{2} \vec{A}_\ell^{(i)} \cdot \hat{\vec{\mathcal{T}}}_\ell^{(i)} = \sum_i \sum_{\ell=0}^{2} \sum_{q=-\ell}^{\ell} (-1)^q A_{\ell q}^{(i)} \hat{\mathcal{T}}_{\ell,-q}^{(i)} . \qquad [2.61]$$

The superscript i runs over all the interactions present in the system. The rank k is limited to two in the basic Hamiltonian which we usually consider, i.e., all interactions are of rank zero, rank one, or rank two. Higher-rank tensors can appear in the basic spin Hamiltonian of nuclei with $I \geq 3/2$ but there are only a few experimental observations of such quantities. The generalized scalar product between two tensors as defined above is equivalent to the tensor product of the two tensors where we only take the $\ell = 0, q = 0$ component of the resulting tensor

$$\hat{\mathcal{H}} = \left\{ \sum_i \sum_{\ell_1 = 0}^{2} \sum_{\ell_2 = 0}^{2} A_{\ell_1}^{(i)} \otimes \hat{\mathcal{T}}_{\ell_2}^{(i)} \right\}_{00} = \sum_i \sum_{\ell = 0}^{2} \vec{A}_{\ell}^{(i)} \cdot \hat{\vec{\mathcal{T}}}_{\ell}^{(i)} . \qquad [2.62]$$

In the rotating-frame representation, however, higher-rank tensors components will appear in the Hamiltonian if the high-field approximation is not fulfilled and second-order terms are considered. This is especially the case in quadrupolar nuclei with large quadrupolar-coupling constants. Note that only if the two spherical spin-tensor operators transform the same way under rotations, i.e., for a homonuclear spin pair under non-selective pulses, for magnetically equivalent spins, or if the two spherical spin-tensor operators refer to the same spin, the tensor products $\hat{\mathcal{T}}_{\ell}^{(i)}$ are spin-tensor operators of rank ℓ and we can write for the tensor components

$$\hat{\mathcal{T}}_{\ell m}^{(i)} = \hat{T}_{\ell m}^{(i)} . \qquad [2.63]$$

In all other cases, the $\hat{\mathcal{T}}_{\ell}^{(i)}$ are just a convenient short-hand notation for the tensor-product of two first-rank tensor components as defined by Eq. [2.47]. In this case they transform like the product of two independent first-rank tensors under rotations and the $\hat{\mathcal{T}}_{\ell m}^{(i)}$ are given by

$$\begin{aligned}
\hat{\mathcal{T}}_{00}^{(k,n)} &= \frac{1}{\sqrt{3}}\left(\hat{T}_{1,-1}^{(k)}\hat{T}_{11}^{(n)} + \hat{T}_{11}^{(k)}\hat{T}_{1,-1}^{(n)} - \hat{T}_{10}^{(k)}\hat{T}_{10}^{(n)}\right)\\
\hat{\mathcal{T}}_{10}^{(k,n)} &= \frac{1}{\sqrt{2}}\left(\hat{T}_{11}^{(k)}\hat{T}_{1,-1}^{(n)} - \hat{T}_{1,-1}^{(k)}\hat{T}_{11}^{(n)}\right)\\
\hat{\mathcal{T}}_{1,\pm1}^{(k,n)} &= \mp\frac{1}{\sqrt{2}}\left(\hat{T}_{10}^{(k)}\hat{T}_{1,\pm1}^{(n)} - \hat{T}_{1,\pm1}^{(k)}\hat{T}_{10}^{(n)}\right)\\
\hat{\mathcal{T}}_{20}^{(k,n)} &= \frac{1}{\sqrt{6}}\left(2\hat{T}_{10}^{(k)}\hat{T}_{10}^{(n)} + \hat{T}_{11}^{(k)}\hat{T}_{1,-1}^{(n)} + \hat{T}_{1,-1}^{(k)}\hat{T}_{11}^{(n)}\right)\\
\hat{\mathcal{T}}_{2,\pm1}^{(k,n)} &= \frac{1}{\sqrt{2}}\left(\hat{T}_{1,\pm1}^{(k)}\hat{T}_{10}^{(n)} + \hat{T}_{10}^{(k)}\hat{T}_{1,\pm1}^{(n)}\right)\\
\hat{\mathcal{T}}_{2,\pm2}^{(k,n)} &= \hat{T}_{1,\pm1}^{(k)}\hat{T}_{1,\pm1}^{(n)}
\end{aligned} \quad . \qquad [2.64]$$

In the case of the interaction of a spin with a magnetic field, the index of the second tensor is B instead of n.

The Hamiltonian of Eq. [2.61] is always written in the laboratory frame of reference. It is, however, often convenient to express the spatial tensors in their principal-axes system, i.e., in a basis where the symmetric part of the matrix representation of the tensor is diagonal and fully described by the three values a_{xx}, a_{yy}, and a_{zz}. The anti-symmetric part of the tensor, i.e., the rank-one contribution, is not diagonal in this basis and described by the values a_{xy}, a_{xz}, and a_{yz}. Instead of using the Cartesian components, one often uses the isotropic average of the tensor

$$\bar{a} = \frac{1}{3}\mathrm{Tr}\{A\} = \frac{a_{xx} + a_{yy} + a_{zz}}{3} , \qquad [2.65]$$

the anisotropy of the tensor

$$\delta = a_{zz} - \bar{a} , \qquad [2.66]$$

and the asymmetry of the tensor

$$\eta = \frac{a_{yy} - a_{xx}}{\delta} . \qquad [2.67]$$

In this notation, the ordering of the principal components is very important. We use the convention

$$|a_{zz} - \bar{a}| \geq |a_{xx} - \bar{a}| \geq |a_{yy} - \bar{a}| . \qquad [2.68]$$

With this definition, the asymmetry η is always positive and smaller than 1 and the anisotropy δ can be positive or negative.

The identification of the parameters $\bar{a}$ for the zeroth-rank tensor components, δ and η for the second-rank tensor component, and a_{xy}, a_{xz}, and a_{yz} for the first-rank tensor components for the various interactions discussed in Chapter 2.1 are summarized in Table 2.1.

Using these conventions, the spatial spherical-tensor components in the principal-axes system are defined as

$$\begin{aligned}
\rho_{00} &= -\sqrt{3}\bar{a} \\
\rho_{10} &= \frac{-i}{\sqrt{2}}(a_{xy}-a_{yx}) = -i\sqrt{2}a_{xy} \\
\rho_{1,\pm1} &= \frac{-1}{2}((a_{zx}-a_{xz}) \pm i(a_{zy}-a_{yz})) = a_{xz} \pm ia_{yz} \\
\rho_{20} &= \sqrt{\frac{3}{2}}\delta \\
\rho_{2,\pm1} &= 0 \\
\rho_{2\pm2} &= \frac{-1}{2}\delta\eta
\end{aligned} \quad . \qquad [2.69]$$

Note that in the PAS of the symmetric part of the tensor, only the anti-symmetric part is off diagonal and, therefore, $a_{\alpha\beta} = -a_{\beta\alpha}$ for $\alpha \neq \beta$.

We can calculate the rotated spatial spherical-tensor components in the laboratory frame by rotating the spherical space tensors ρ_ℓ from the principal-axis system to the laboratory frame system by the transformation

Table 2.1: Parameters For The Spherical-Tensor Notation Of Hamiltonians

Interaction	rank 0	rank 2		rank 1		
	$\bar{a}$	δ	η	a_{xy}	a_{xz}	a_{yz}
Zeeman Hamiltonian	$-\gamma$	0	0	0	0	0
RF-field Hamiltonian	$-\gamma$	0	0	0	0	0
chemical-shift Hamiltonian	$-\gamma_k\bar{\sigma}$	$-\gamma\sigma_{zz}$	$\frac{\sigma_{yy}-\sigma_{xx}}{\sigma_{zz}-\bar{\sigma}}$	$-\gamma\sigma_{xy}$	$-\gamma\sigma_{xz}$	$-\gamma\sigma_{yz}$
J-coupling Hamiltonian	$2\pi J$	a_{zz}	0	0	0	0
dipolar coupling Hamiltonian	0	$-2\frac{\mu_0\gamma_k\gamma_n\hbar}{4\pi r_{kn}^3}$	0	0	0	0
quadrupolar-coupling Hamiltonian	0	$\frac{e^2qQ}{2I(2I-1)\hbar}$	$\frac{V_{yy}-V_{xx}}{V_{zz}}$	0	0	0

$$A_{\ell m} = \sum_{m' = -\ell}^{\ell} \rho_{\ell m'} \mathcal{D}^{\ell}_{m'm}(\alpha, \beta, \gamma) \ . \qquad [2.70]$$

The tensor components $A_{\ell m}$ can then be used to write down the Hamiltonian of Eq. [2.61] and are given by

$$\begin{aligned}
A_{00} &= -\sqrt{3}\bar{a} \\
A_{10} &= -i\sqrt{2}[a_{xy}\cos\beta - (a_{xz}\sin\alpha - a_{yz}\cos\alpha)\sin\beta] \\
A_{1,\pm1} &= e^{\mp i\gamma}[(a_{xz} \pm ia_{yz}\cos\beta)\cos\alpha + (a_{yz} \mp ia_{xz}\cos\beta)\sin\alpha \mp ia_{xy}\sin\beta] \\
A_{20} &= \sqrt{\frac{3}{8}}\delta[(3\cos^2\beta - 1) - \eta\sin^2\beta\cos(2\alpha)] \\
A_{2,\pm1} &= \pm\frac{\delta}{2}\sin\beta e^{\mp i\gamma}[(3 + \eta\cos(2\alpha))\cos\beta \mp i\eta\sin(2\alpha)] \\
A_{2,\pm2} &= \frac{\delta}{2}e^{\mp i2\gamma}\left[\frac{3}{2}\sin^2\beta - \frac{\eta}{2}(1 + \cos^2\beta)\cos(2\alpha) \pm i\eta\cos\beta\sin(2\alpha)\right]
\end{aligned} \qquad [2.71]$$

There is a further simplification which we often make in NMR. Usually we assume that the Zeeman interaction is much larger than all the other interactions and transform the spin-part of the Hamiltonian into a frame rotating with the Zeeman frequency. This leads to a time dependence of all terms except the $\hat{T}_{\ell 0}$ terms which are invariant under a rotation about $\hat{F}_z$. The time-independent terms are often called "secular" under the rotating-frame transformation. The secular rotating-frame Hamiltonian is then given by

$$\hat{\mathcal{H}} = \sum_{i} \sum_{\ell = 0}^{2} A^{(i)}_{\ell 0} \hat{\mathcal{T}}^{(i)}_{\ell 0} \ . \qquad [2.72]$$

In the case of a homonuclear spin system, i.e., if $\hat{\mathcal{T}}^{(i)}_{\ell m} = \hat{T}^{(i)}_{\ell m}$, we find

$$\hat{\mathcal{T}}^{(i)}_{\ell 0} = \hat{T}^{(i)}_{\ell 0} \qquad [2.73]$$

while in all other cases only the terms of the tensor product containing only $\hat{T}^{(\kappa)}_{10}$ terms survive leading to

$$\begin{aligned} \hat{\mathcal{T}}_{00}^{(i)} &= \frac{-1}{\sqrt{3}} \hat{T}_{10}^{(k)} \hat{T}_{10}^{(n)} \\ \hat{\mathcal{T}}_{10}^{(i)} &= 0 \qquad . \\ \hat{\mathcal{T}}_{20}^{(i)} &= \frac{2}{\sqrt{6}} \hat{T}_{10}^{(k)} \hat{T}_{10}^{(n)} \end{aligned} \qquad [2.74]$$

From Table 2.1 it becomes clear that only the interactions of a spin with a field and the J coupling have an isotropic component. These are the only interactions that can be observed in liquid-state NMR. Second-rank tensor contributions are found for the chemical-shift, the J-coupling (almost always neglected as discussed in Chapter 1.10.3.2), the dipolar-coupling, and the quadrupolar-coupling Hamiltonian. Only the chemical-shift Hamiltonian has a first-rank contribution that is not directly manifest in the NMR spectrum. The symmetry properties of the Hamiltonians under a rotation in real space, a rotation in spin space, and a rotation of the magnetic field are summarized in Table 2.2.

Table 2.2: Tensor-Rotation Properties of Hamiltonians

Interaction	rank under spin rotation	rank under space rotation	rank under B-field rotation
Zeeman Hamiltonian	1	0	1
RF-field Hamiltonian	1	0	1
chemical-shift Hamiltonian	1	0, 1, 2	1
J-coupling Hamiltonian	0, 2 (homonuclear) 0,1+1 (heteronuclear)	0, 2	0
dipolar coupling Hamiltonian	2 (homonuclear) 1+1 (heteronuclear)	2	0
first-order quadrupolar-coupling Hamiltonian	2	2	0
second-order quadrupolar-coupling Hamiltonian	1, 3	0, 2, 4	0

The high-field approximation is sometimes not a good approximation and higher-order corrections have to be included in the rotating-frame Hamiltonian. The second-order Hamiltonian for a second-rank interaction is given by

$$\hat{\mathcal{H}}^{(2)} = \frac{1}{\omega_{0k}}\left(A_{21}^{(k)}A_{2,-1}^{(k)}[\hat{T}_{21}^{(k)}, \hat{T}_{2,-1}^{(k)}] + \frac{1}{2}A_{22}^{(k)}A_{2,-2}^{(k)}[\hat{T}_{22}^{(k)}, \hat{T}_{2,-2}^{(k)}]\right) \qquad [2.75]$$

where ω_{0k} is the Larmor frequency of spin k. Since the second-order Hamiltonian scales with the inverse of the Larmor frequency, its size will be reduced with increasing static magnetic fields. The second-order corrections to the rotating-frame Hamiltonian are especially important for quadrupolar nuclei with a large quadrupole-coupling constant and for spins with a large chemical-shift tensor. For this reason, it is often beneficial to measure quadrupolar nuclei at the highest fields available. This will be discussed in more detail in Chapter 11.

2.3 Information Content of NMR Hamiltonians

The NMR interactions discussed in this Chapter provide different types of information about the structure and the dynamic properties of the molecule. They can either be manifest directly in a one-dimensional spectrum through the magnitude of an interaction or indirectly through spectral features in two-dimensional correlation experiments.

2.3.1 Structural Information

The chemical shift depends on the local electronic environment of the spin. There is no unambiguous direct link from the chemical shift to structural parameters but chemical shifts can be calculated with quantum-mechanical methods and used in this way to obtain structural information. There is also empirical statistical information about the dependence of the chemical shifts on the dihedral angles in certain types of structural motifs, e.g., for the C_α or the CO atom in peptides and proteins.

The J coupling depends also on the local electronic structure of the spin. It provides information about chemical bonds and, therefore, the chemical structure of the molecule. A more quantitative information is the correlation of the dihedral angles with the magnitude of three-bond J couplings (Karplus equation) in various structural motifs. They are best known for the correlation of ^{3}J couplings to the dihedral angles in peptides and proteins. The J couplings can also be calculated by quantum-chemical methods and can in this way provide information about the local structure.

The dipolar coupling provides a direct link to atomic distances in a molecule. As can be seen from Eq. [1.144], the dipolar-coupling Hamiltonian is proportional to $1/r_{ij}^3$. The observed splitting in the spectra of oriented or powder samples is, therefore, a good measure for interatomic distances and can be used to determine distances in molecules with a high precision.

The quadrupolar coupling depends also on the local electronic structure. It can provide information about the local symmetry of the electronic environment. Quadrupolar coupling can also be calculated quantum chemically and can in this way provide information about the local structure of a molecule.

Tensor correlation experiments can be used to determine the relative orientation of two anisotropic interactions. Since the orientation of the dipolar-coupling tensor in the molecular frame is well defined, they are of particular interest in such experiments. One can also use the correlation between two chemical-shift tensors or the correlation of a dipolar-coupling tensor with a chemical-shift tensor if the orientation of the chemical-shift tensors in the molecular-fixed frame is known. The result of such tensor correlation experiments are dihedral angles that determine the local structure of a molecule.

2.3.2 Dynamic Information

Dynamic processes can lead to an averaging of anisotropic interactions. The time scale of the averaging process is often not directly accessible unless it is in an relaxation-active range. The amplitude of the averaging process is reflected in the scaling factor of the anisotropic interactions and can be directly obtained from the line shapes in solid-state NMR spectra.

2.3.3 Symmetry Properties

Given a certain symmetry, either static (e.g. crystal-site symmetry in a crystal) or through a time-average of a "fast" motional process (e.g. isotropic motion of small molecules in liquid solution), only certain spherical tensors may exist. As an example let us consider the A_{20} component of the chemical-shift tensor. In octahedral symmetry we have for the Cartesian components $a_{xx} = a_{yy} = a_{zz}$. Therefore, $\delta = 0$ which requires that the component A_{20} must vanish. Systematically, we find the "allowed" components by group-theoretical arguments. Note that we only expect contributions to the spectrum from the components that transform according to the total symmetric group A_1. Therefore, some types of interactions are completely impossiblein an environment of a certain symmetry as one can see from Table 2.3.

Table 2.3: Tensor Averaging Under Different Symmetries

Symmetry		Possible Tensor Ranks										
Tetragonal 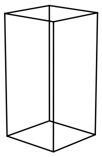	D4	0		2		4	5	6	7	8	9	10
Tetrahedral 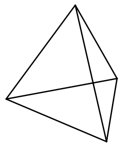	T	0			3	4		6	7	8	9	10
Octahedral 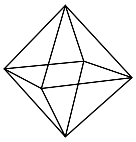	O	0				4		6		8	9	10
Icosahedral 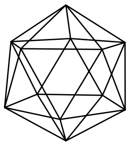	I	0						6				10
Spherical 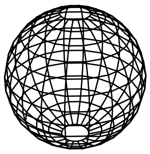	SO(3)	0										

3 Magic-Angle Spinning

Powder spectra in solid-state NMR contain a large amount of information. The size and the orientation of the chemical-shielding tensors and the dipolar-coupling tensors are contained in them, and they can give us information about the structure or dynamics of a molecule. The main problem is, however, how to get this information out of the spectrum. Due to the very broad lines we have severe overlap and cannot easily extract this information.

The standard way of removing the powder broadening in solid-state NMR is magic-angle sample spinning (Figure 3.1). We put the sample into a rotor and spin it fast about an axis which is inclined by an angle of 54.74° to the static magnetic field. The rotation about this axis removes the broadening generated by the second-rank tensors and leads to a considerable sharpening of the lines. Here we assume that the rotation is fast compared to the width of the line.

MAS rotors come in different sizes. The diameter of the rotor dictates the maximum spinning frequency and the sample volume. Typical standard sizes are 4 mm rotors, which allow spinning frequencies up to about 15-18 kHz; 2.5 mm rotors, which allow spinning frequencies up to 30-35 kHz; and 6-7 mm rotors, which allow spinning frequencies of about 6-10 kHz. There are also experimental 1.8 mm and

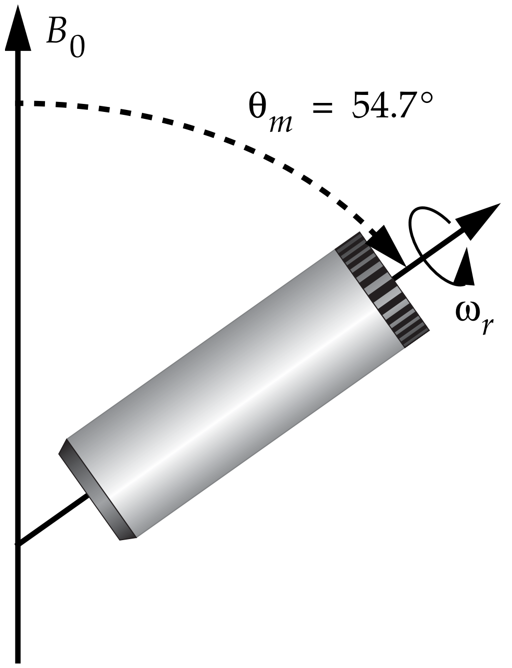

Figure 3.1: Magic-Angle Spinning
Schematic drawing of an MAS rotor which is inclined by an angle of 54.7° degrees with the static magnetic field. This angle is often called the "magic angle" because a rotation about this angle leads to an averaging of all second-rank space tensor contributions.

1.3 mm MAS rotors, which allow spinning frequencies up to 50 kHz and 70 kHz, respectively. Some companies also offer much larger rotors for very insensitive samples that do not need high spinning frequencies.

Smaller rotors and, therefore, higher spinning frequencies are of particular interest if we measure at high magnetic fields since the chemical-shift tensors scale linearly with the B_0. At a static magnetic field of 18.8 T (800 MHz proton resonance frequency) a typical carbonyl tensor is in the order of 30 kHz. To obtain a spectrum without any strong sidebands one has to spin faster than the width of the tensor, which is only possible with a 2.5 mm size rotor. Secondly, the increase in B_0 field also leads to a larger spread of the isotropic chemical shifts. If the spinning frequency matches the isotropic chemical-shift difference of two dipolar coupled spins, we see a broadening of the resonances due to an effect called rotational resonance. In a later Chapter we will hear more about this method, which can be used to measure distances between homonuclear dipolar coupled spins. To avoid this rotational-resonance recoupling condition for uniformly labelled samples, it is best to spin faster than the width of the spectrum. For a 18.8 T magnet this corresponds to a spinning frequency of 35 kHz for a ^{13}C spectrum. Lastly, it has been observed experimentally that the line width in uniformly ^{13}C labelled compounds decreases with increasing spinning frequency.

3.1 Average Hamiltonian Treatment

In Chapter 4.1.2 we have seen that the rotating-frame Hamiltonian under rotation about a single axis can be described according to Eq. [4.17] by

$$\hat{\mathcal{H}}(t) = \sum_{m=-\ell}^{\ell} e^{im\omega_r t} d^{\ell}_{m0}(\theta_r) A^{(\mathrm{rot})}_{\ell m} \hat{\mathcal{T}}_{\ell 0} \ . \qquad [3.1]$$

For a second-rank spatial tensor we find, therefore

$$\begin{aligned}\hat{\mathcal{H}}(t) = \Big[&e^{-2i\omega_r t}\sqrt{\frac{3}{8}}\sin^2\theta_r A_{2,-2}^{(rot)} + e^{-i\omega_r t}\sqrt{\frac{3}{8}}\sin(2\theta_r)A_{2,-1}^{(rot)} + \frac{3\cos^2\theta_r - 1}{2}A_{20}^{(rot)}\\ &- e^{i\omega_r t}\sqrt{\frac{3}{8}}\sin(2\theta_r)A_{21}^{(rot)} + e^{2i\omega_r t}\sqrt{\frac{3}{8}}\sin^2\theta_r A_{22}^{(rot)}\Big]\hat{\mathcal{T}}_{20}\end{aligned} \quad . \qquad [3.2]$$

If we now apply average Hamiltonian theory to the time-dependent Hamiltonian of Eq. [3.2], we obtain in zeroth-order AHT

$$\begin{aligned}\bar{\hat{\mathcal{H}}}^{(0)} &= \frac{1}{\tau_r}\int_0^{\tau_r}\hat{\mathcal{H}}(t)dt\\ &= \frac{3\cos^2\theta_r - 1}{2}A_{20}^{(rot)}\hat{\mathcal{T}}_{20}\end{aligned} \qquad [3.3]$$

where the cycle time is given by $\tau_r = 2\pi/\omega_r$. If we adjust the angle θ_r of the rotation axis such that

$$\theta_r = \mathrm{acos}\left(\frac{1}{\sqrt{3}}\right) \approx 54.7356° \qquad [3.4]$$

$\bar{\mathcal{H}}^{(0)}$ vanishes and all spatial second-rank interactions are averaged out to zeroth order. The angle where the reduced Wigner rotation matrix element $d_{00}^{2}(\beta)$ becomes zero is often called the "magic angle" indicated by the symbol θ_m. Isotropic interactions (zeroth-rank tensors) are unaffected by magic-angle spinning because

$$d_{00}^{0}(\theta_m) = 1 \qquad [3.5]$$

while first-rank tensors are scaled according to

$$d_{00}^{1}(\theta_m) = \frac{1}{\sqrt{3}} \ . \qquad [3.6]$$

As an example let us consider the chemical-shift Hamiltonian which consists of an isotropic part and a spatial second-rank tensor part. The first three orders of the average Hamiltonian are given by

$$\begin{aligned}
\hat{\bar{\mathcal{H}}}_{CS}^{(0)} &= -\sum_k \frac{\omega_{0k}}{\tau_r}\int_0^{\tau_r} \bar{\sigma}^{(k)}\hat{I}_{kz}dt + \\
&\quad -\sum_k \frac{\omega_{0k}}{3\tau_r}\int_0^{\tau_r}[e^{-2i\omega_r t}A_{2,-2}^{(rot)} + \sqrt{2}(e^{-i\omega_r t}A_{2,-1}^{(rot)} - e^{i\omega_r t}A_{21}^{(rot)}) + e^{2i\omega_r t}A_{22}^{(rot)}]\hat{I}_{kz}dt \\
&= -\sum_k \omega_{0k}\bar{\sigma}^{(k)}I_{kz} \\
\hat{\bar{\mathcal{H}}}_{CS}^{(1)} &= \frac{-i}{2\tau_r}\int_0^{\tau_r}dt_2\int_0^{t_2}[\hat{\mathcal{H}}_{CS}(t_2), \hat{\mathcal{H}}_{CS}(t_1)]dt_1 = 0 \\
\hat{\bar{\mathcal{H}}}_{CS}^{(2)} &= 0
\end{aligned} \qquad . \quad [3.7]$$

Here, the zeroth-order average Hamiltonian is actually the full average Hamiltonian and describes the time evolution of the system exactly if we restrict ourselves to stroboscopic sampling. Such an interaction where $\hat{\bar{\mathcal{H}}} = \hat{\bar{\mathcal{H}}}^{(0)}$ is called an heterogeneous interaction with respect to sample rotation. The stroboscopic sampling, however, limits the spectral width to the spinning frequency. All spinning side bands which can occur at multiples of the spinning frequency are folded back onto the center band because the spectral width is equal to the spinning frequency.

As a second example let us consider a system of homonuclear dipolar-coupled spins. For a single spin pair the time-dependent rotating-frame Hamiltonian is given by Eq. [3.2]. For an arbitrary number of dipolar coupled spins we obtain a vanishing zeroth-order average Hamiltonian if the sample is spun at the magic angle

$$\hat{\bar{\mathcal{H}}}_D^{(0)} = \sum_{k \neq \ell} \frac{3\cos^2\theta_m - 1}{2} A_{20}^{(rot)} \hat{\mathcal{T}}_{20}^{(k,\ell)} = 0 \ . \qquad [3.8]$$

For the first-order average Hamiltonian we find a non-vanishing contribution if we have multiple dipolar couplings

$$\begin{aligned}\hat{\bar{\mathcal{H}}}_{\mathrm{D}}^{(1)} &= \frac{-i}{2\tau_r}\int_0^{\tau_r} dt_2 \int_0^{t_2} [\hat{\mathcal{H}}_{\mathrm{D}}(t_2), \hat{\mathcal{H}}_{\mathrm{D}}(t_1)]dt_1 \\ &= \sum_{k \neq \ell \neq m} \frac{A_{2,2}^{(k,\ell)}A_{2,-2}^{(k,m)} - A_{2,-2}^{(k,\ell)}A_{2,2}^{(k,m)} + 4(A_{2,-1}^{(k,\ell)}A_{2,2}^{(k,m)} - A_{2,1}^{(k,\ell)}A_{2-1}^{(k,m)})}{24\omega_{\mathrm{r}}} \\ &\qquad \times [\hat{T}_{2,0}^{(k,\ell)}, \hat{T}_{2,0}^{(k,m)}]\end{aligned} \qquad [3.9]$$

since the $\hat{T}_{20}^{(k,\ell)}$ terms of two spin pairs where one of the spins is the same do not commute with each other. Therefore, we obtain contributions to the higher-order average Hamiltonian and we call the interaction a homogeneous interaction with respect to sample rotation. Since the higher-order terms are non zero, they will contribute to the spectrum and lead, typically, to a broadening of the lines in the side-band spectrum.

Figure 3.2a shows a numerical simulation for a dipolar-coupled two-spin system under stroboscopic observation, i.e., all the side bands are folded back onto the center band which is observed. The Hamiltonian for this system is heterogeneous because it commutes with itself at all times and leads to a sharp spectrum. The spectrum in Figure 3.2b shows a homonuclear dipolar-coupled three-spin system which is homogeneous with respect to sample rotation. One can clearly see that the lines are broadened due to higher-order average-Hamiltonian terms.

As a third example let us consider spinning a second-rank space tensor off the magic angle. The zeroth-order average Hamiltonian in such a case is given by Eq. [3.3] as

$$\begin{aligned}\hat{\bar{\mathcal{H}}}^{(0)} &= \frac{3\cos^2\theta_r - 1}{2} A_{20}^{(rot)} \hat{\mathcal{T}}_{20} \\ &= \frac{3\cos^2\theta_r - 1}{2} \hat{\mathcal{H}}^{(\mathrm{static})}\end{aligned} \qquad [3.10]$$

and we obtain a scaled static Hamiltonian. The function

$$P_2(\cos\theta_r) = d_{00}^2(\theta_r) = \frac{3\cos^2\theta_r - 1}{2} \qquad [3.11]$$

is called the second-order Legendre Polynomial. For $\theta_r = 0°$ we find a scaling factor of 1 and for $\theta_r = 90°$ we find a scaling factor of -1/2. The dependence of $P_m(\cos\theta_r)$ on the angle is shown in Figure 3.3 for m = 0 to 4. From such a graph we can see that the "magic angles" for tensors of different rank have different values and that the scaling behavior has a different angle dependence. We find, for example, that for a rank-1 tensor a rotation about an axis inclined by 90° with the static magnetic field leads to a full averaging of the tensor.

An example of an axially symmetric CSA tensor spinning at different rotation angles θ_r is shown in Figure 3.4 under stroboscopic observation, i.e., all the side bands are folded back onto the center band which is the only part of the spectrum that

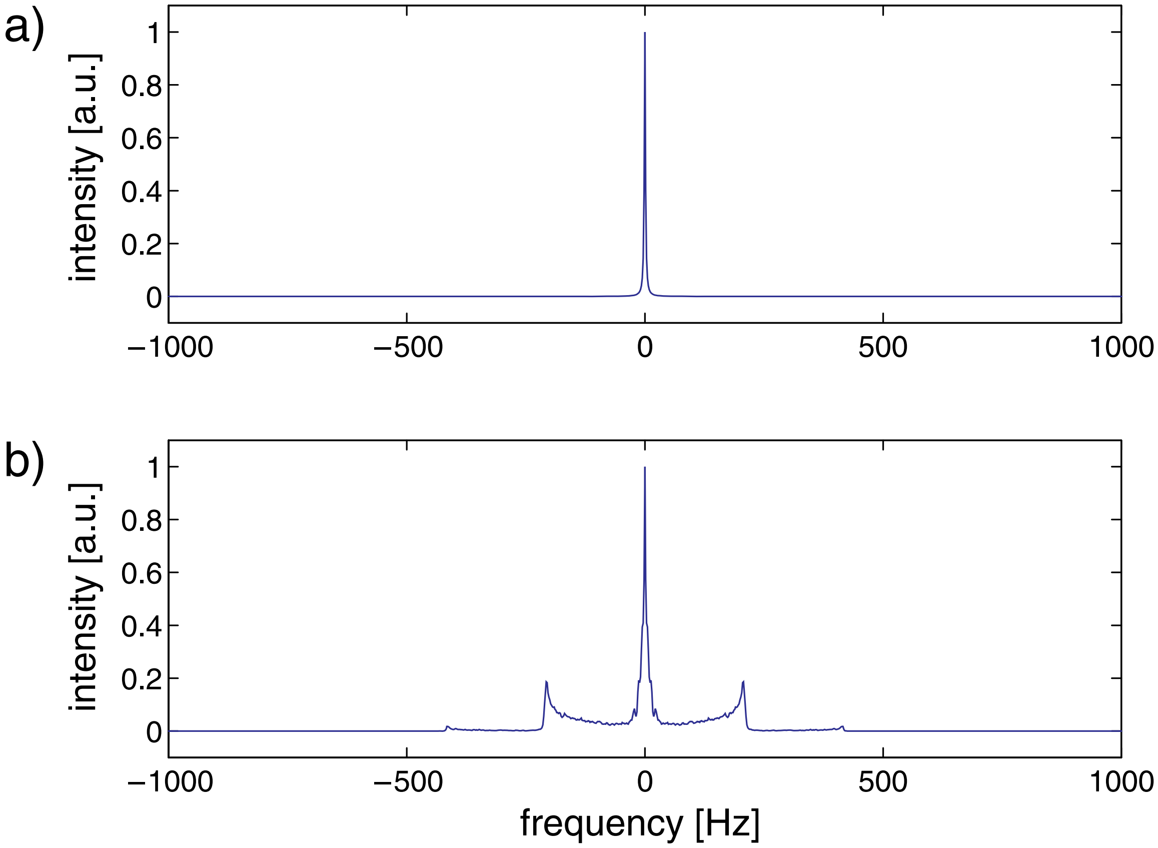

Figure 3.2: Heterogeneous vs. Homogeneous Hamiltonians
a) Dipolar-coupled homonuclear two-spin system under MAS and stroboscopic observation leading to a sharp line. The observable line width is due to exponential line broadening applied during processing. b) Dipolar-coupled homonuclear three-spin system under MAS and stroboscopic observation leading to a broadened spectrum. The dipolar couplings were set to $\delta_D/(2\pi) = 20\,\text{kHz}$, the spinning frequency was $\omega_r/(2\pi) = 30\,\text{kHz}$ and the angle between the dipolar coupling tensors was $\beta = 120°$. Only part of the spectra is shown.

is observed. One can clearly see that the shape of the tensor remains the same and only the width is scaled by the second-order Legendre Polynomial $P_2(\cos\theta_r)$. The direction of the tensor is reversed when going through the magic angle reflecting the sign change in the scaling factor.

3.2 Explicit Calculation of the Time Evolution Under MAS

To describe the time evolution between the sampling points given by the stroboscopic sampling in order to get a correct description of the spectrum for non-synchronized sampling, we have to take the explicit time dependence into account. For the chemical-shift Hamiltonian, this is relatively simple because only a single spin operator appears in the Hamiltonian and the Hamiltonian commutes with itself at all times. We can, therefore, write

$$\hat{\mathcal{H}}_{CS}(t) = \sum_k \omega_k(\alpha^{(k)}, \beta^{(k)}, \gamma^{(k)}, t)\hat{I}_{kz} \qquad [3.12]$$

where $\omega_k(\alpha^{(k)}, \beta^{(k)}, \gamma^{(k)}, t_0)$ is the instantaneous resonance frequency at time t_0. For simplicity of notation, we restrict the discussion to a single spin. If we would stop the rotor at any given time t_0, the resonance frequency of a crystallite with orientation

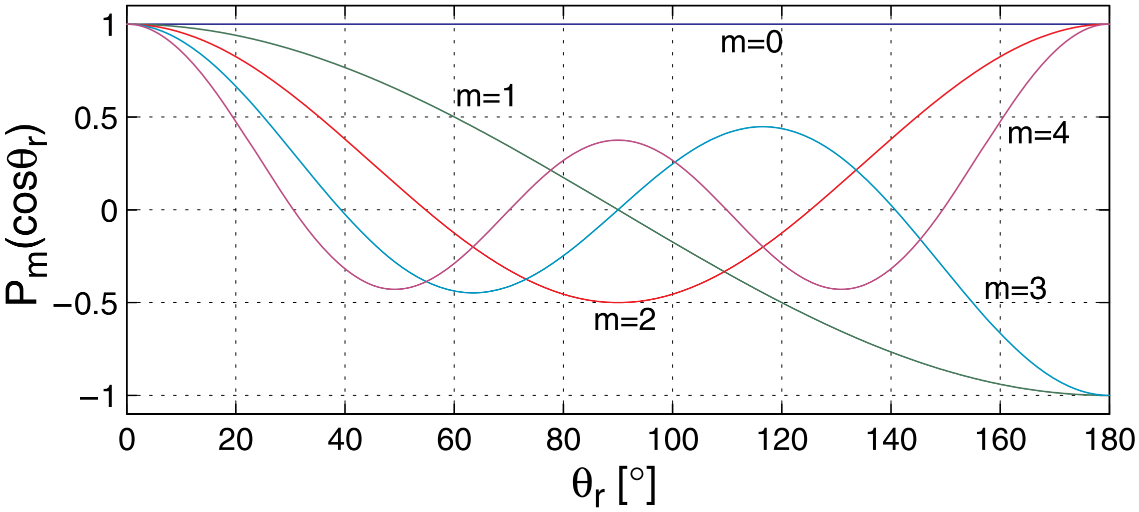

Figure 3.3: Legendre Polynomials
The value of the Legendre Polynomials $P_m(\cos\theta_r) = d^m_{00}(\theta_r)$ as a function of the rotation angle θ_r is shown for m =0 to 4. The values for P_m are always between -1 and 1. The zero crossing correspond to the "magic angle" of a rank-m tensor.

(α, β, γ) would be $\omega(\alpha, \beta, \gamma, t_0)$ and the spectrum would be a single line at frequency $\omega(\alpha, \beta, \gamma, t_0)$.

We can decompose the transition frequency into a time-independent and a time-dependent part according to

$$\omega(\alpha, \beta, \gamma, t) = \omega^{\text{iso}} + \omega^{\text{csa}}(\alpha, \beta, \gamma, t) \qquad [3.13]$$

and identify the time-independent part with the isotropic chemical shift

$$\omega^{\text{iso}} = -\omega_{0k}\bar{\sigma}^{(k)} \qquad [3.14]$$

and the time-dependent part with the second-rank tensor contribution

$$\omega^{\text{csa}}(\alpha, \beta, \gamma, t) = \frac{-\omega_0}{3}[e^{-2i\omega_r t}A^{(rot)}_{2,-2} + \sqrt{2}(e^{-i\omega_r t}A^{(rot)}_{2,-1} - e^{i\omega_r t}A^{(rot)}_{21}) + e^{2i\omega_r t}A^{(rot)}_{22}] \ . \qquad [3.15]$$

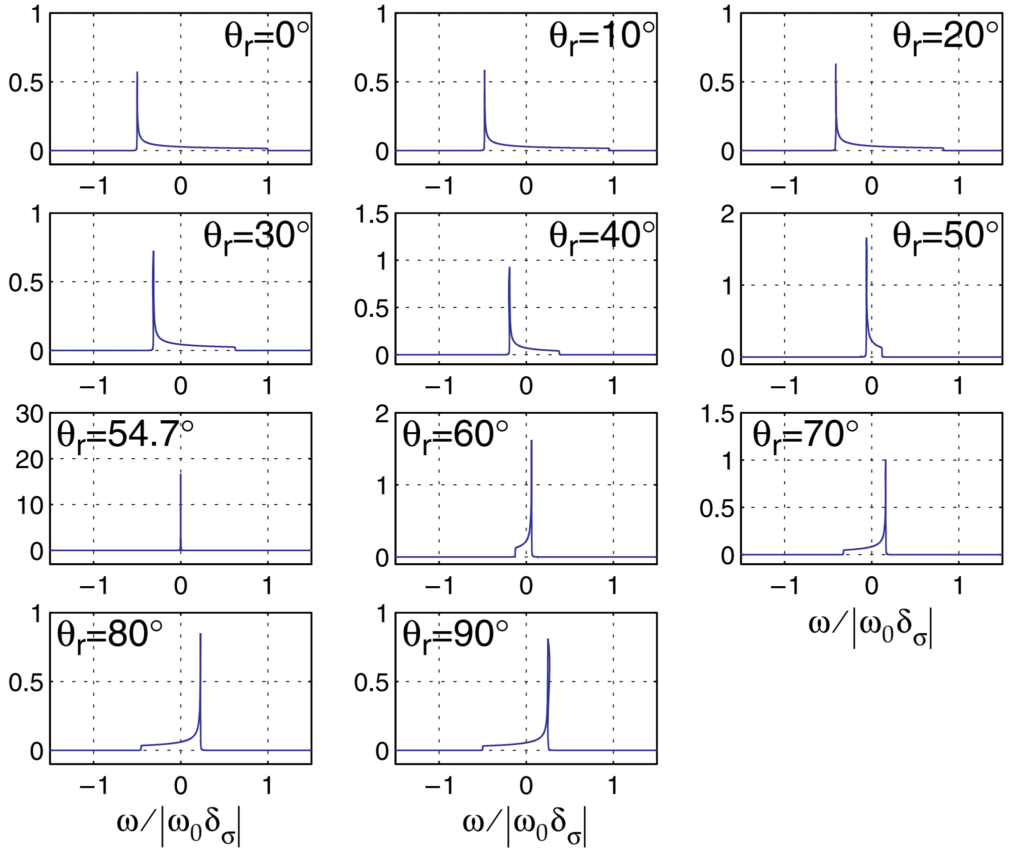

Figure 3.4: CSA Tensor Under Rotation About a Single Axes
Axially symmetric chemical-shift tensor under single-axis rotation with the rotation axis inclined by different angles with the static magnetic field. The tensor is scaled by the second-order Legendre Polynomial $P_2(\cos\theta_r)$. Note the different scales of the plots since the integral over the line must be constant.

Inserting Eq. xx into [3.15] leads to the following expression for the time-dependent transition frequency

$$
\begin{aligned}
\omega^{\mathrm{csa}}(\alpha, \beta, \gamma, t) &= \frac{-\omega_0 \delta_\sigma^{(k)}}{6} \\
&\times \Bigg[\left(\frac{3}{2}\sin^2\beta^{(k)} - \frac{\eta_\sigma^{(k)}}{2}(1 + \cos^2\beta^{(k)})\cos 2\alpha^{(k)} - i\eta_\sigma^{(k)}\cos\beta^{(k)}\sin 2\alpha^{(k)} \right) e^{-2i(\omega_r t - \gamma^{(k)})} \\
&- \sqrt{2}\sin\beta^{(k)}[(3 + \eta_\sigma^{(k)}\cos(2\alpha^{(k)}))\cos\beta^{(k)} + i\eta_\sigma^{(k)}\sin(2\alpha^{(k)})]e^{-i(\omega_r t - \gamma^{(k)})} \\
&- \sqrt{2}\sin\beta^{(k)}[(3 + \eta_\sigma^{(k)}\cos(2\alpha^{(k)}))\cos\beta^{(k)} - i\eta_\sigma^{(k)}\sin(2\alpha^{(k)})]e^{i(\omega_r t - \gamma^{(k)})} \\
&+ \left(\frac{3}{2}\sin^2\beta^{(k)} - \frac{\eta_\sigma^{(k)}}{2}(1 + \cos^2\beta^{(k)})\cos 2\alpha^{(k)} + i\eta_\sigma^{(k)}\cos\beta^{(k)}\sin 2\alpha^{(k)} \right) e^{2i(\omega_r t - \gamma^{(k)})} \Bigg]
\end{aligned}
\tag{3.16}
$$

which can be expressed as a sum of four trigonometric functions

$$
\begin{aligned}
\omega^{\mathrm{csa}}(\alpha, \beta, \gamma, t) &= C_1\cos(\omega t - \gamma^{(k)}) + S_1\sin(\omega t - \gamma^{(k)}) \\
&\quad + C_2\cos(2\omega t - 2\gamma^{(k)}) + S_2\sin(2\omega t - 2\gamma^{(k)})
\end{aligned}
\tag{3.17}
$$

with

$$
\begin{aligned}
C_1 &= \frac{\sqrt{2}}{3}\omega_0\delta_\sigma^{(k)}\sin\beta^{(k)}\cos\beta^{(k)}[3 + \eta_\sigma^{(k)}\cos(2\alpha^{(k)})] \\
S_1 &= \frac{\sqrt{2}}{3}\omega_0\delta_\sigma^{(k)}\sin\beta^{(k)}\eta_\sigma^{(k)}\sin(2\alpha^{(k)}) \\
C_2 &= \frac{-\omega_0\delta_\sigma^{(k)}}{3}\left(\frac{3}{2}\sin^2\beta^{(k)} - \frac{\eta_\sigma^{(k)}}{2}(1 + \cos^2\beta^{(k)})\cos(2\alpha^{(k)}) \right) \\
S_2 &= \frac{\omega_0\delta_\sigma^{(k)}}{3}\eta_\sigma^{(k)}\cos\beta^{(k)}\sin(2\alpha^{(k)}) \qquad .
\end{aligned}
\tag{3.18}
$$

The formal solution for the signal of a single crystallite under the Hamiltonian of Eq. [3.12] is given by

$$
\begin{aligned}
\mathcal{S}(\alpha, \beta, \gamma, t) &= \frac{1}{4}\exp\left(-i\int_0^t \omega_k(\alpha^{(k)}, \beta^{(k)}, \gamma^{(k)}, t')dt' \right) \\
&= \frac{1}{4}\exp(-i[\Phi(\alpha, \beta, \gamma, t) - \Phi(\alpha, \beta, \gamma, 0)])
\end{aligned}
\tag{3.19}
$$

and the powder average is given by

$$\begin{aligned}\mathcal{S}(t) &= \frac{1}{8\pi^2}\int_0^{2\pi}\delta\alpha\int_0^{\pi}\delta\beta\sin\beta\int_0^{2\pi}\delta\gamma\mathcal{S}(\alpha,\beta,\gamma,t)\\ &= \frac{1}{32\pi^2}\int_0^{2\pi}\delta\alpha\int_0^{\pi}\delta\beta\sin\beta\int_0^{2\pi}\delta\gamma\exp(-i[\Phi(\alpha,\beta,\gamma,t)-\Phi(\alpha,\beta,\gamma,0)])\end{aligned}\quad . \qquad [3.20]$$

The phase of the exponential function can be separated into two parts in the same way as the transition frequency

$$\Phi(\alpha,\beta,\gamma,t) = \Phi^{\mathrm{iso}}(t)+\Phi^{\mathrm{csa}}(\alpha,\beta,\gamma,t) \qquad [3.21]$$

where

$$\Phi^{\mathrm{iso}}(t) = \omega^{\mathrm{iso}}t \qquad [3.22]$$

and

$$\begin{aligned}\Phi^{\mathrm{csa}}(\alpha,\beta,\gamma,t) &= \frac{C_1}{\omega_r}\sin(\omega_r t-\gamma)-\frac{S_1}{\omega_r}\cos(\omega_r t-\gamma)\\ &\quad+\frac{C_2}{2\omega_r}\sin(2\omega_r t-2\gamma)-\frac{S_2}{2\omega_r}\cos(2\omega_r t-2\gamma)\end{aligned}\quad . \qquad [3.23]$$

Note that the accumulated phase $\Phi^{\mathrm{csa}}(\alpha,\beta,\gamma,t)$ is cyclic with a period of the sample rotation $\tau_r = 2\pi/\omega_r$, i.e., $\Phi^{\mathrm{csa}}(\alpha,\beta,\gamma,t) = \Phi^{\mathrm{csa}}(\alpha,\beta,\gamma,t+n\tau_r)$. In addition, after each full rotor period the time-dependent phase $\Phi^{\mathrm{csa}}(\alpha,\beta,\gamma,n\tau_r)$ - $\Phi^{\mathrm{csa}}(\alpha,\beta,\gamma,0) = 0$ and, therefore, the FID is refocused for $t = n\tau_r$. We call this phenomenon a rotational echo which is illustrated in Figure 3.5. At these time points, the time evolution of the echo is only determined by the isotropic chemical shift according to

$$\mathcal{S}(\alpha,\beta,\gamma,n\tau_r) = \frac{1}{4}\exp(-i\Phi^{\mathrm{iso}}(n\tau_r)) = \frac{1}{4}\exp(-i\omega^{\mathrm{iso}}n\tau_r) \ . \qquad [3.24]$$

This agrees with Eq. [3.7] where we have seen that the time evolution is only determined by the isotropic chemical shift if the observation is stroboscopic with a cycle time τ_r.

In order to calculate the time evolution between the stroboscopic sampling points we have to evaluate the expression

$$\mathcal{S}^{\mathrm{csa}}(\alpha, \beta, \gamma, t) = \exp(-i[\Phi^{\mathrm{csa}}(\alpha, \beta, \gamma, t) - \Phi^{\mathrm{csa}}(\alpha, \beta, \gamma, 0)]) \ . \qquad [3.25]$$

The frequency-domain signal is given by the Fourier transformation of the time-domain signal

$$\mathcal{S}^{\mathrm{csa}}(\alpha, \beta, \gamma, \omega) = \frac{1}{\tau_r}\int_0^{\tau_r} \mathcal{S}^{\mathrm{csa}}(\alpha, \beta, \gamma, t) e^{-i\omega t} dt \ . \qquad [3.26]$$

a) FID

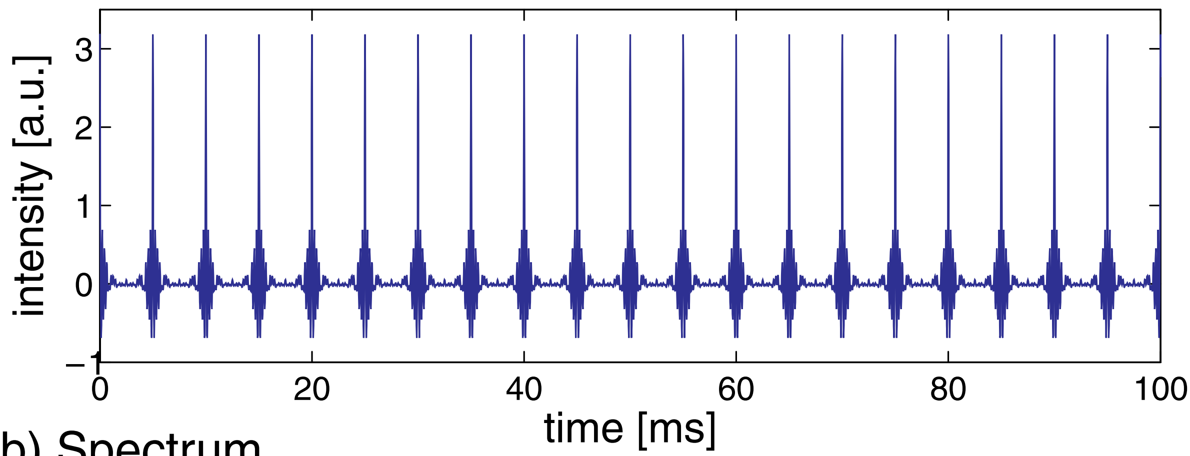

b) Spectrum

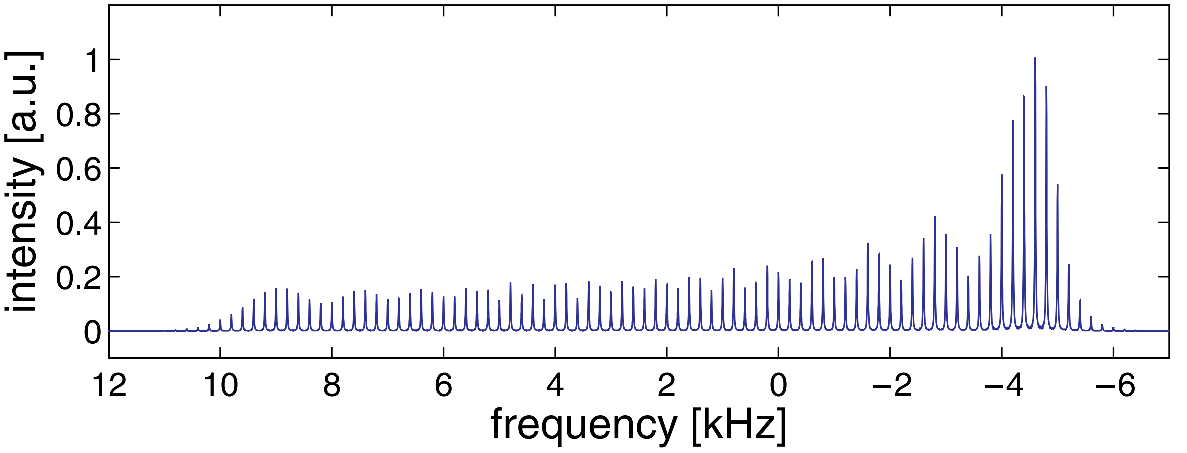

Figure 3.5: Simulation of the FID for a Powder Sample
a) FID and b) Fourier-transformed spectrum of a CSA tensor ($\omega_{0k}\delta_{\sigma}^{(k)} = 10$ kHz, $\eta_{\sigma}^{(k)} = 0$) at an MAS frequency of 200 Hz. One can clearly see the rotor echoes in the FID spaced by 5 ms which corresponds to the inverse of the rotor frequency. In the spectrum we see side bands spaced by the rotor frequency.

Since the signal is cyclic with τ_r, we only have to consider the times between 0 and τ_r which will result in intensity only at multiples of ω_r. Therefore, we can rewrite the Fourier transformation as

$$\begin{aligned}\mathcal{S}^{\mathrm{csa}}(\alpha, \beta, \gamma, N\omega_r) &= \frac{1}{\tau_r}\int_0^{\tau_r} \mathcal{S}^{\mathrm{csa}}(\alpha, \beta, \gamma, t)e^{-iN\omega_r t}dt \\ &= \exp(i\Phi^{\mathrm{csa}}(\alpha, \beta, \gamma, 0))\frac{1}{\tau_r}\int_0^{\tau_r} \exp(-i\Phi^{\mathrm{csa}}(\alpha, \beta, \gamma, t))e^{-iN\omega_r t}dt\end{aligned} \quad . \quad [3.27]$$

Because the phase γ and $\omega_r t$ appear always together, we can perform a variable transformation in the Fourier transformation defined by $\gamma' = \gamma - \omega_r t$ and $dt = -d\gamma'/\omega_r$ leading to

$$\begin{aligned}\mathcal{S}^{\mathrm{csa}}(\alpha, \beta, \gamma, N\omega_r) &= \exp(i\Phi^{\mathrm{csa}}(\alpha, \beta, \gamma, 0))\frac{1}{2\pi}\int_0^{\tau_r} \exp(-i\Phi^{\mathrm{csa}}(\alpha, \beta, \gamma', 0))e^{-iN(\gamma - \gamma')}d\gamma' \\ &= \exp(i\Phi^{\mathrm{csa}}(\alpha, \beta, \gamma, 0))e^{-iN\gamma}\left(\frac{-1}{2\pi}\int_0^{\tau_r} \exp(-i\Phi^{\mathrm{csa}}(\alpha, \beta, \gamma', 0))e^{iN\gamma'}d\gamma'\right) \\ &= \exp(i\Phi^{\mathrm{csa}}(\alpha, \beta, \gamma, 0))e^{-iN\gamma}F(\alpha, \beta, N\omega_r)\end{aligned} \quad [3.28]$$

For a single crystallite the intensities of the side bands are in general complex numbers leading to an arbitrary phase. Integrating over the powder angle γ leads to

$$\begin{aligned}\mathcal{S}^{\mathrm{csa}}(\alpha, \beta, N\omega_r) &= \frac{1}{2\pi}\int_0^{2\pi} \mathcal{S}^{\mathrm{csa}}(\alpha, \beta, \gamma, N\omega_r)d\gamma \\ &= F(\alpha, \beta, N\omega_r)\frac{1}{2\pi}\int_0^{2\pi} \exp(i\Phi^{\mathrm{csa}}(\alpha, \beta, \gamma, 0))e^{-iN\gamma}d\gamma \\ &= F(\alpha, \beta, N\omega_r)F^*(\alpha, \beta, N\omega_r) \\ &= |F(\alpha, \beta, N\omega_r)|^2\end{aligned} \quad . \quad [3.29]$$

This shows that all the sidebands in a powder are in phase (see Figure 3.6) because the intensities are real and have the same sign as the center band. The full signal is the convolution of the frequency-domain signal from the isotropic part of the

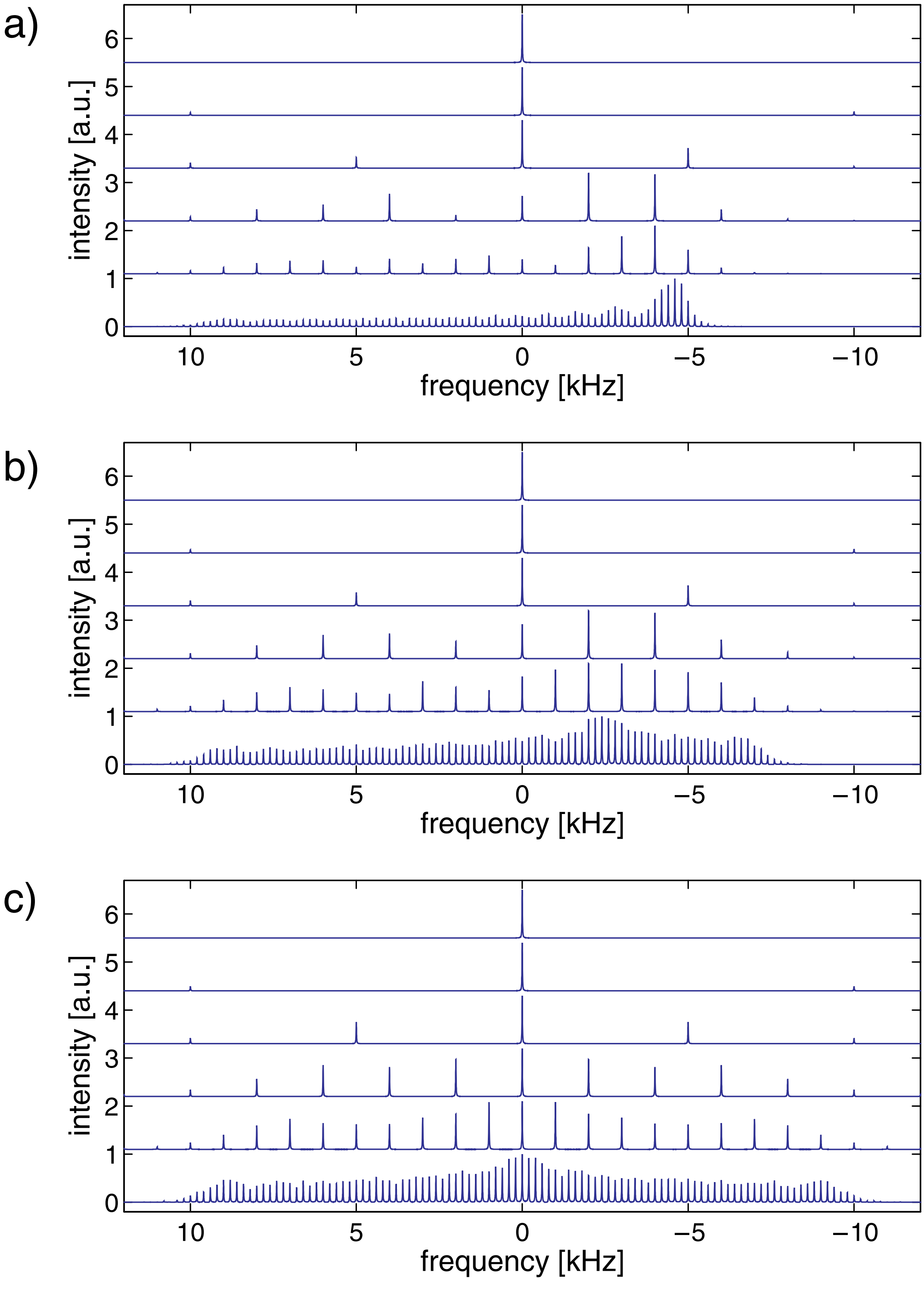

Figure 3.6: MAS Side-Band Spectra for CSA Tensors.
Side-band spectra for CSA tensors ($\omega_{0k}\delta_\sigma^{(k)}$ = 10 kHz, a) $\eta_\sigma^{(k)}$ = 0, b) $\eta_\sigma^{(k)}$ = 0.5, and c) $\eta_\sigma^{(k)}$ = 1) under MAS for six different spinning frequencies: 200, 1000, 2000, 5000, 10000, and 20000 Hz. The intensities are scaled such that the highest peak in each spectrum has the intensity 1.

Hamiltonian with the signal from the anisotropic part. We, therefore, obtain a set of side bands which is centered at the isotropic chemical shift, ω^{iso}. The side-band intensities can be expressed analytically as an infinite sum over Bessel functions

$$F(\alpha, \beta, N\omega_r) = \sum_{j=-\infty}^{\infty} \sum_{k=-\infty}^{\infty} \sum_{m=-\infty}^{\infty} J_j\left(\frac{C_2}{\omega_\mathrm{r}}\right) J_k\left(\frac{S_2}{\omega_\mathrm{r}}\right) J_{N-2j-2k-m}\left(\frac{C_1}{\omega_\mathrm{r}}\right) J_m\left(\frac{S_1}{\omega_\mathrm{r}}\right) e^{i(k+m)\pi/2} \qquad [3.30]$$

and evaluated numerically.

The side-band intensities in an MAS spectrum of a powder sample given by

$$\mathcal{S}^{\mathrm{csa}}(N\omega_r) = \frac{1}{4\pi} \int_0^{2\pi} \delta\alpha \int_0^{\pi} \delta\beta \sin\beta \left|F(\alpha, \beta, N\omega_r)\right|^2 \qquad [3.31]$$

depends exclusively on the spinning speed ω_r and on the anisotropy, δ, and asymmetry, η, of the tensor through the parameters C_1, C_2, S_1, and S_2. One can, therefore, determine these tensor values from measured side-band intensities in an MAS spectrum of a powder. Herzfeld and Berger (J. Chem. Phys, **73** (1980) 6021) have calculated contour plots (Figure 3.7) of $\mathcal{S}^{\mathrm{csa}}(N\omega_r)/\mathcal{S}^{\mathrm{csa}}(0)$ for $N = -5, \ldots, 5$ as a function of the two parameters δ and η. From these plots, δ and η can be determined graphically. There are also computer programs available to fit these two parameters to the side-band intensity.

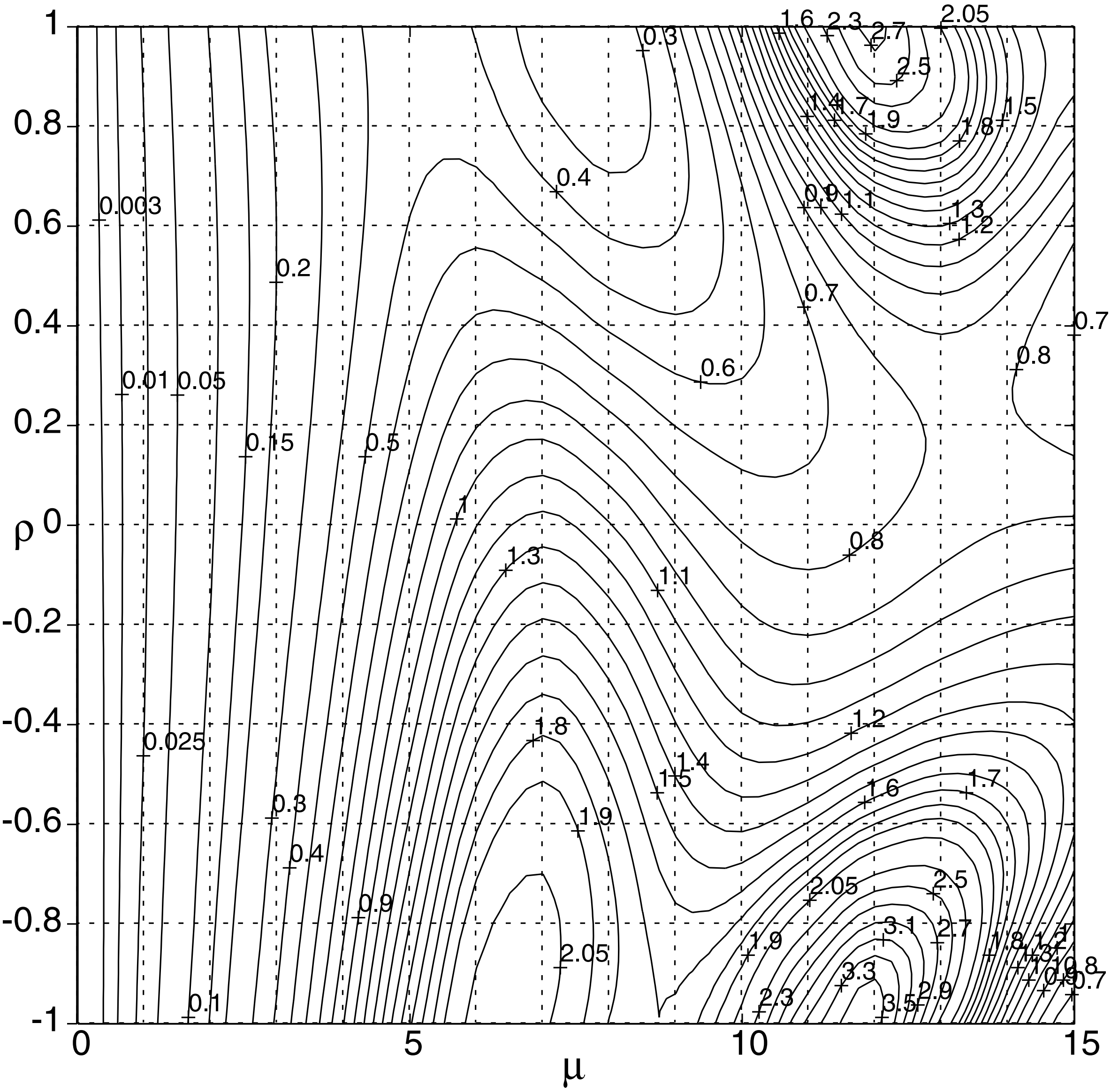

Figure 3.7: Herzfeld-Berger Contour Plot for Side-Band Intensities
This is the N = -1 contour plot for the relative side-band intensity used in a Herzfeld-Berger analysis. The tensor is parametrized using the two variables $\mu = (\omega_0 \cdot (\sigma_{zz} - \sigma_{xx}))/\omega_r$ and $\rho = (\sigma_{xx} + \sigma_{zz} - 2\sigma_{yy})/(\sigma_{zz} - \sigma_{xx})$.

4 Recoupling Techniques Under MAS

Recoupling techniques utilize the constructive interference between rotations in real space (magic-angle spinning) and rotations in spin space (rf irradiation) to make certain parts of the system Hamiltonian time independent. In this way it is possible to avoid the averaging of anisotropic interactions by MAS and design Hamiltonians with the properties required by the experiment.

There are several classes of recoupling experiments: (i) experiments without rf irradiation, (ii) experiments using discrete pulses, (iii) experiments using cw irradiation, and (iv) experiments using phase-modulated rf irradiation. There is a large number of experiments in each of these classes and we will discuss the properties of some sequences in detail here.

4.1 Introduction

We have seen in Chapter 6 that in zeroth-order average Hamiltonian theory all anisotropic interactions are averaged by magic-angle spinning. If we want to use any of the anisotropic interaction during an MAS experiment we need to reintroduce the anisotropic interactions under MAS by interfering with the averaging of the spatial part through manipulations of the spin part. The most important application of such recoupling techniques is the reintroduction of dipolar couplings under MAS for homonuclear or heteronuclear polarization transfer. We have already seen one example for such a recoupling of the heteronuclear dipolar coupling in Chapter 7.2 (Cross Polarization Under MAS) where the heteronuclear dipolar coupling was recovered under MAS by adjusting the amplitude difference of the cw rf irradiation of the I and S spins such that it matched $\pm\omega_r$ or $\pm 2\omega_r$. A large number of such recoupling sequences has been developed in solid-state NMR with different properties and applications using various principles to prevent the total averaging of the dipolar coupling under MAS. A second less important application is the reintroduction of the chemical-shift tensor under MAS in order to measure the size and the orientation of the CSA tensor.

Recoupling sequences can be classified according to different properties: homonuclear and heteronuclear recoupling sequences, broadband and selective recoupling sequences, or based on the principles they use to prevent the full averaging of the dipolar coupling. We can distinguish basically four different principles that are used for recoupling sequences: (i) Recoupling sequences without rf irradiation of the recoupled spin. Examples for such sequences are proton-driven or rf-driven spin diffusion and rotational resonance. (ii) Recoupling sequences that use discrete pulses (delta-pulse limit) in order to reintroduce the dipolar coupling Hamiltonian. Examples for such sequences are REDOR, RFDR, and DRAMA. (iii) Recoupling sequences based on cw irradiation of the spin system. Examples for such sequences are CP, HORROR, and R^3. (iv) Recoupling sequences with continuous but phase modulated rf irradiation. Examples of such sequences are C7, SPC5, and the generalized C-type and R-type sequences. In this chapter we will discuss some important representatives of these sequences and the principles they are based on.

4.2 Recoupling Sequences Without RF Irradiation

We have seen in Chapter 6 that in zeroth-order approximation MAS will average out all anisotropic interactions. The CSA tensor and the heteronuclear interaction are heterogeneous interactions and all higher orders of the average Hamiltonian are also zero. The homonuclear interaction, however is a homogeneous interaction and higher-order terms in the average Hamiltonian expansion are non zero leading to a residual first-order homonuclear dipolar coupling under MAS. In recoupling sequences without any rf irradiation we either have to rely on this residual coupling or we have to utilize an interference effect between the spinning of the sample and the internal spin-system Hamiltonian.

4.2.1 Proton-Driven Spin Diffusion

4.2.1.1 Introduction

Proton-driven spin diffusion was one of the first experiments used for dipolar-mediated polarization transfer under MAS. The experiment relies on the fact that MAS does not fully average the homonuclear dipolar coupling Hamiltonian (see Chapter 6.1) and we obtain a first-order average Hamiltonian which mediates polarization transfer. The compensation for resonance offsets is provided by the residual line broadening due to the incomplete averaging of the heteronuclear dipolar couplings by MAS. The basic pulse sequence for proton-driven spin diffusion is shown in Figure 4.1. At low spinning frequencies no rf irradiation is needed during the mixing time τ_m while at higher spinning frequencies, irradiation of the protons at the rotary-resonance ($\omega_1 = \omega_r$) or HORROR ($\omega_1 = \omega_r/2$) condition (see Chapter 4.4) can speed up the polarization-transfer process significantly. Typical mixing times in protonated organic solids are in the order of 10 ms for transfer via direct bonds up to several 100 ms for long-range transfer.

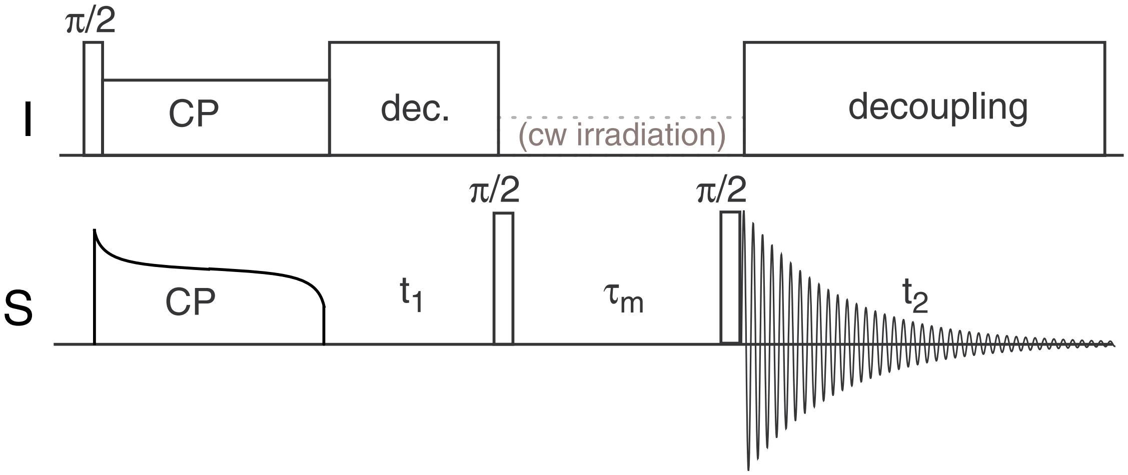

Figure 4.1: Pulse Sequence for Proton-Driven Spin Diffusion
After initial cross polarization and the evolution time t_1, the magnetization is stored along the z direction during the mixing time τ_m. No proton decoupling is applied during the mixing time in order to speed up the polarization transfer process. After the mixing time the magnetization is put back into the x-y plane and detected during t_2 under proton decoupling. During the mixing time, cw irradiation at the rotary-resonance or HORROR condition (see Chapter 4.4) can be employed to increase the polarization transfer speed.

4.2.1.2 Theoretical Description

If we consider a purely homonuclear dipolar Hamiltonian we obtain according to Eq. [6.10] a first-order average Hamiltonian of the form

$$
\begin{aligned}
\hat{\bar{\mathcal{H}}}_{\mathrm{D}}^{(1)} &= \sum_{k \neq \ell \neq m} \frac{A_{22}^{(k,\ell)} A_{2,-2}^{(k,m)} - A_{2,-2}^{(k,\ell)} A_{22}^{(k,m)} + 4(A_{2,-1}^{(k,\ell)} A_{21}^{(k,m)} - A_{21}^{(k,\ell)} A_{2-1}^{(k,m)})}{-288\omega_{\mathrm{r}}} \\
&\qquad \times [\hat{S}_{kz}(\hat{S}_\ell^+ \hat{S}_m^- - \hat{S}_m^+ \hat{S}_\ell^-) + 2\hat{S}_{\ell z}(\hat{S}_k^+ \hat{S}_m^- - \hat{S}_m^+ \hat{S}_k^-) - 2\hat{S}_{mz}(\hat{S}_k^+ \hat{S}_\ell^- - \hat{S}_\ell^+ \hat{S}_k^-)] \\
&= \sum_{k \neq \ell < m} \frac{2\hat{S}_{kz}(\hat{S}_\ell^+ \hat{S}_m^- - \hat{S}_m^+ \hat{S}_\ell^-)}{18\omega_{\mathrm{r}}} \sum_{q=1}^{2} \left[\frac{(-1)^q}{q^2}(A_{2,-q}^{(k,\ell)} A_{2,q}^{(k,m)} - A_{2,q}^{(k,\ell)} A_{2,-q}^{(k,m)}) \right. \\
&\qquad - 2\frac{(-1)^q}{q^2}(A_{2,-q}^{(k,m)} A_{2,q}^{(\ell,m)} - A_{2,q}^{(k,m)} A_{2,-q}^{(\ell,m)}) \\
&\qquad \left. + 2\frac{(-1)^q}{q^2}(A_{2,-q}^{(k,\ell)} A_{2,q}^{(\ell,m)} - A_{2,q}^{(k,\ell)} A_{2,-q}^{(\ell,m)}) \right] \quad . [4.1]
\end{aligned}
$$

Note that the differences $A_{2,-q}^{(k,\ell)} A_{2,q}^{(k,m)} - A_{2,q}^{(k,\ell)} A_{2,-q}^{(k,m)} = 2Im(A_{2,-q}^{(k,\ell)} A_{2,q}^{(k,m)})$ since in general $A_{\ell,m} = (A_{\ell,-m})^*$ which leads to a final first-order homonuclear dipolar average Hamiltonian under MAS of

$$
\begin{aligned}
\hat{\bar{\mathcal{H}}}_{\mathrm{D}}^{(1)} &= \sum_{k \neq \ell < m} \frac{2\hat{S}_{kz}(\hat{S}_\ell^+ \hat{S}_m^- - \hat{S}_m^+ \hat{S}_\ell^-)}{9\omega_{\mathrm{r}}} \\
&\quad \times \sum_{q=1}^{2} \frac{(-1)^q}{q^2}[Im(A_{2,-q}^{(k,\ell)} A_{2,q}^{(k,m)}) - 2Im(A_{2,-q}^{(k,m)} A_{2,q}^{(\ell,m)}) + 2Im(A_{2,-q}^{(k,\ell)} A_{2,q}^{(\ell,m)})] \quad [4.2]
\end{aligned}
$$

Such a three-spin Hamiltonian also promotes polarization transfer between the spins ℓ and m in a similar way as the normal zero-quantum dipolar-coupling Hamiltonian. Figure 4.2 shows the time evolution under such a first-order average Hamiltonian in a homonuclear dipolar-coupled three-spin system. One can clearly see that we obtain a oscillatory polarization transfer in much the same way as it is obtained under a regular dipolar coupling. The main difference to the case with a static dipolar coupling is the much smaller size of the first-order average Hamiltonian especially at higher MAS frequencies due to the scaling by $1/\omega_{\mathrm{r}}$. For a directly bonded C-C-C three-spin system we find a transfer of the magnetization within roughly 10 ms at a spinning frequency of 10 kHz (Figure 4.3) while at 30 kHz MAS frequency the polarization transfer is much slower and the maximum transfer is only reached after approximately 30 ms. For short times the first-order average Hamiltonian dominates the time evolution which scales under this condition with $1/\omega_r$. For longer times, higher orders of the average Hamiltonian become also important and the scaling of the time evolution will be more complicated.

The main problem associated with polarization transfer through the dipolar coupling is the quenching of the polarization-transfer process by the differences in the chemical shifts. Figure 4.4 shows the same simulations as in Fig. 4.3 but the chemical shift of spin 2 was changed from on resonance to an off-resonance value of 1 kHz. Even for such a small chemical shift, the polarization transfer is almost fully quenched and we see only transfer of magnetization between spins 1 and 3. The simplest way to eliminate the resonance offsets is by irradiating the spins with a strong cw rf field,

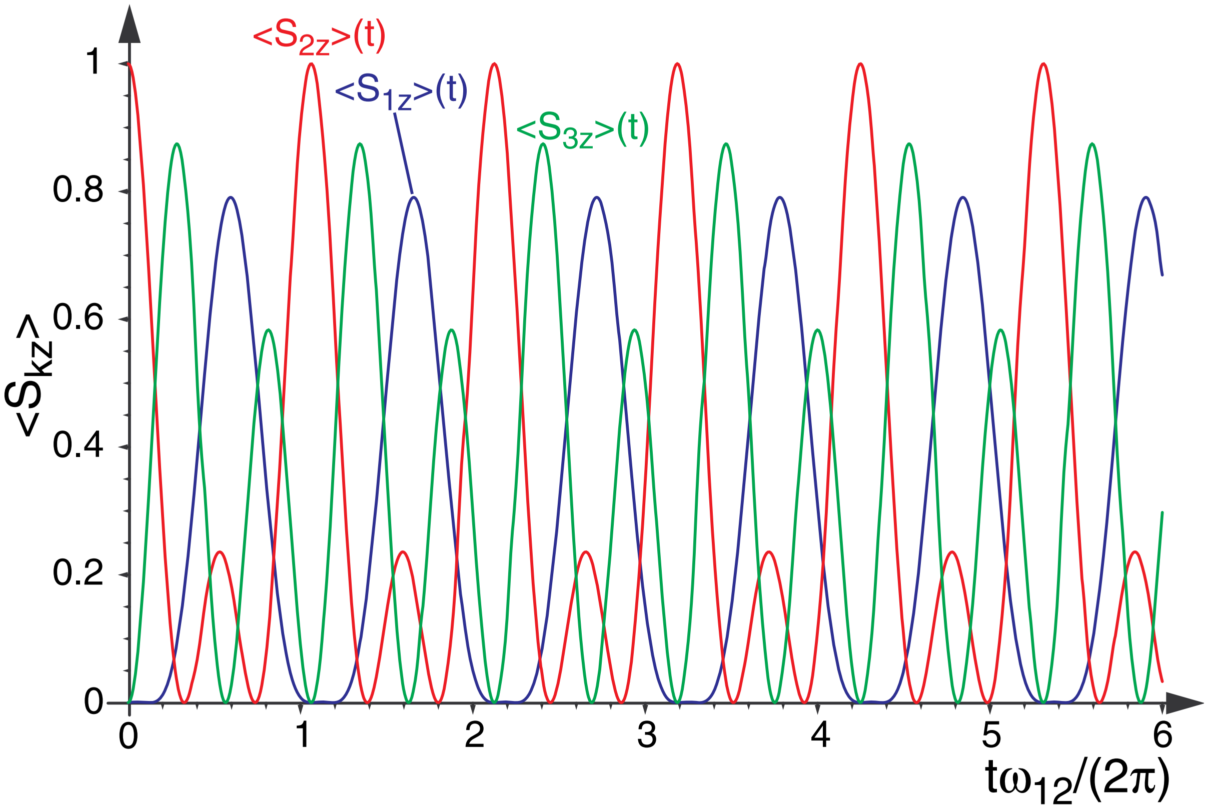

Figure 4.2: Polarization-Transfer Dynamics in a Three-Spin System Under MAS
Polarization-transfer dynamics in a homonuclear dipolar-coupled three-spin system under MAS with $\hat{\rho}_0 = \hat{S}_{2z}$, $\omega_{13} = 3\omega_{12}$, and $\omega_{23} = 5\omega_{12}$. The expectation values of the three spins are plotted as $\langle S_{1z}\rangle(t)$ (blue), $\langle S_{2z}\rangle(t)$ (red), and $\langle S_{3z}\rangle(t)$ (green).

effectively implementing the experiment in the rotating frame. This will also change the structure of the effective Hamiltonian and lead, in the limit of the rf nutation frequency much larger than the MAS frequency, to a scaling of the Hamiltonian by a factor of 1/4. Instead of cw irradiation, more complicated pulse sequences like WALTZ or DIPSI can be used that compensate resonance offsets better at lower rf-field amplitudes. This experiment is known as rf-driven spin diffusion. Due to the high rf-field amplitudes and the slower polarization-transfer dynamics this experiment is not used very often.

In proton-driven spin diffusion the offset compensation is provided by the residual line broadening of the carbons under MAS due to the dipolar couplings to the protons and among the protons. As we will see in more detail in Chapter 8.1 when we discuss heteronuclear spin decoupling, MAS alone will not fully average out the heteronuclear dipolar coupling in the presence of a strong homonuclear dipolar-coupled network of proton spins. At slower MAS frequencies the residual line

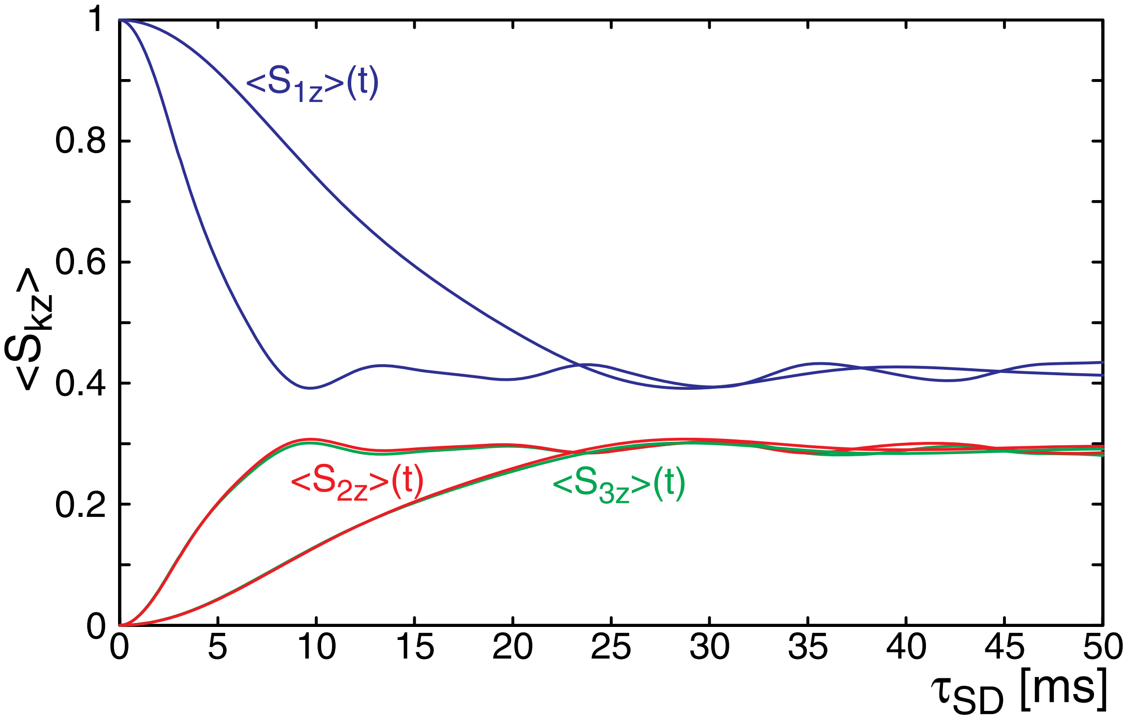

Figure 4.3: Polarization-Transfer Dynamics in a Three-Spin System Under MAS
Polarization-transfer dynamics in a three-spin system calculated for a bond-angle of 109.5°, a bond length of 1.5 Å using an initial state of $\hat{\rho}_0 = \hat{S}_{1z}$. The MAS frequency was 10 kHz and 30 kHz, respectively, and powder averaging was performed. All three spins were on resonance.

broadening of the ^{13}C is large enough that we have a significant overlap of the different resonance lines in the single-quantum spectrum. At higher MAS frequencies, the overlap of the single-quantum resonances becomes small and the spin-diffusion process, therefore, slow. In this case a broadening of the ^{13}C single-quantum lines can be achieved by irradiating the proton spins at the rotary-resonance ($\omega_1 = \omega_r$ or $\omega_1 = 2\omega_r$) or the HORROR ($\omega_1 = \omega_r/2$) condition. In the first case the heteronuclear dipolar coupling is reintroduced while in the latter case the homonuclear dipolar coupling of the protons is reintroduced. These two processes will be discussed in a different context in more detail in Chapter 4.4.

The size of the overlap of the single-quantum lines in the ^{13}C spectrum will influence the rate of the polarization-transfer process in addition to the dipolar couplings involved in the process. In addition, the rate of the polarization transfer between two spins m and ℓ is not only influenced by the dipolar coupling $\delta_D^{(m,\ell)}$ but also by all the dipolar couplings between spins m and ℓ to all the other spins in the

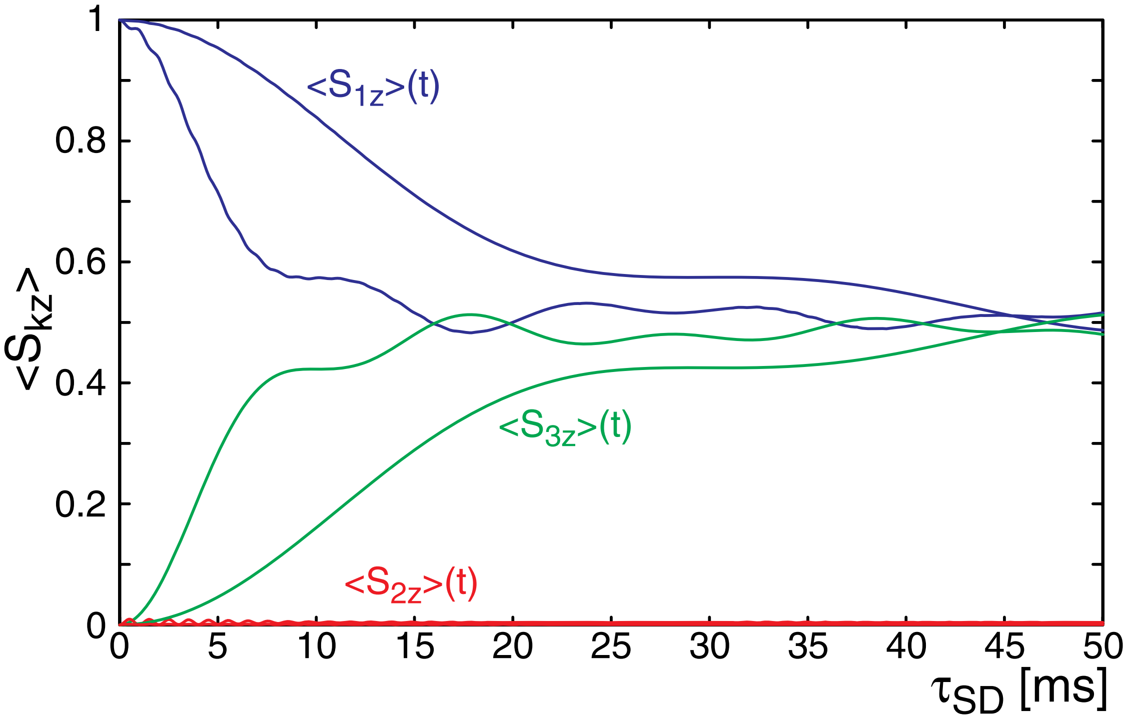

Figure 4.4: Polarization-Transfer Dynamics in a Three-Spin System Under MAS
Polarization-transfer dynamics in a three-spin system calculated for a bond-angle of 109.5°, a bond length of 1.5 Å using an initial state of $\hat{\rho}_0 = \hat{S}_{1z}$. The MAS frequency was 10 kHz and 30 kHz, respectively, and powder averaging was performed. Spins 1 and 3 were on resonance while spin 2 had a resonance offset of 1 kHz

neighborhood (see Eq. [4.2]). Therefore, no simple correlation between the rate of the polarization transfer and the dipolar coupling or the distance between two spins can be given.

The polarization-transfer process in the proton-driven spin-diffusion experiment can often be described approximately by a diffusion process although it is strictly speaking a coherent polarization-transfer process. The same reasoning as to why this makes sense apply as in the case of cross polarization (see Chapter 7.1.2).

4.2.1.3 Examples

Proton-driven spin diffusion is a simple, robust, and easy to implement experiment. Therefore, it has found wide application in different fields of solid-state NMR. On the negative side is the slow rate of polarization transfer as well as the low efficiency of the polarization-transfer process. It is used in two-dimensional correlation spectra as the polarization-transfer mechanism especially at lower MAS frequencies. The mixing-time dependence is illustrated in Figure 4.5 for the example of a triply-labelled 1,3,4-^{13}C Gly-Gly sample (H_2N-$^{*}CH_2$-$^{*}CO$-NH-CH_2-$^{*}COOH$). There is a fast cross-peak build up for the C_3-C_4 cross peak ($\delta_D^{(3,4)} = 4300$ Hz) with the associated fast decrease in intensity of the corresponding diagonal peaks. The other two cross peaks show a much slower build up due to the larger distance between the spins ($\delta_D^{(1,3)} = 280$ Hz and $\delta_D^{(1,4)} = 130$ Hz). The overall decay of the magnetization for longer mixing times is due to relaxation effects.

Figure 4.6 shows a 2D ^{13}C chemical-shift correlation spectrum of the protein ubiquitin using proton-driven spin diffusion with a mixing time of 200 ms. The spinning frequency was 40 kHz and rotary-resonance recoupling was used on the protons to accelerate the polarization-transfer process. The protein was uniformly ^{13}C labelled. Such a spectrum can be used to assign the resonances in the backbone and in the side chains of the protein.

4.2.2 Rotational Resonance (R^2)

4.2.2.1 Introduction

In rotational resonance or "rotor-driven" spin diffusion the spinning frequency of the MAS rotor is adjusted such that the isotropic chemical-shift difference between two spins is an integer multiple of the rotor frequency, i.e.,

$$n\omega_r = \omega_{\text{iso}}^{(k)} - \omega_{\text{iso}}^{(j)} . \qquad [4.3]$$

Under this condition one observes a broadening of the lines in the 1D spectrum as can be seen in Figure 4.7. This broadening is due to a partial reintroduction of the

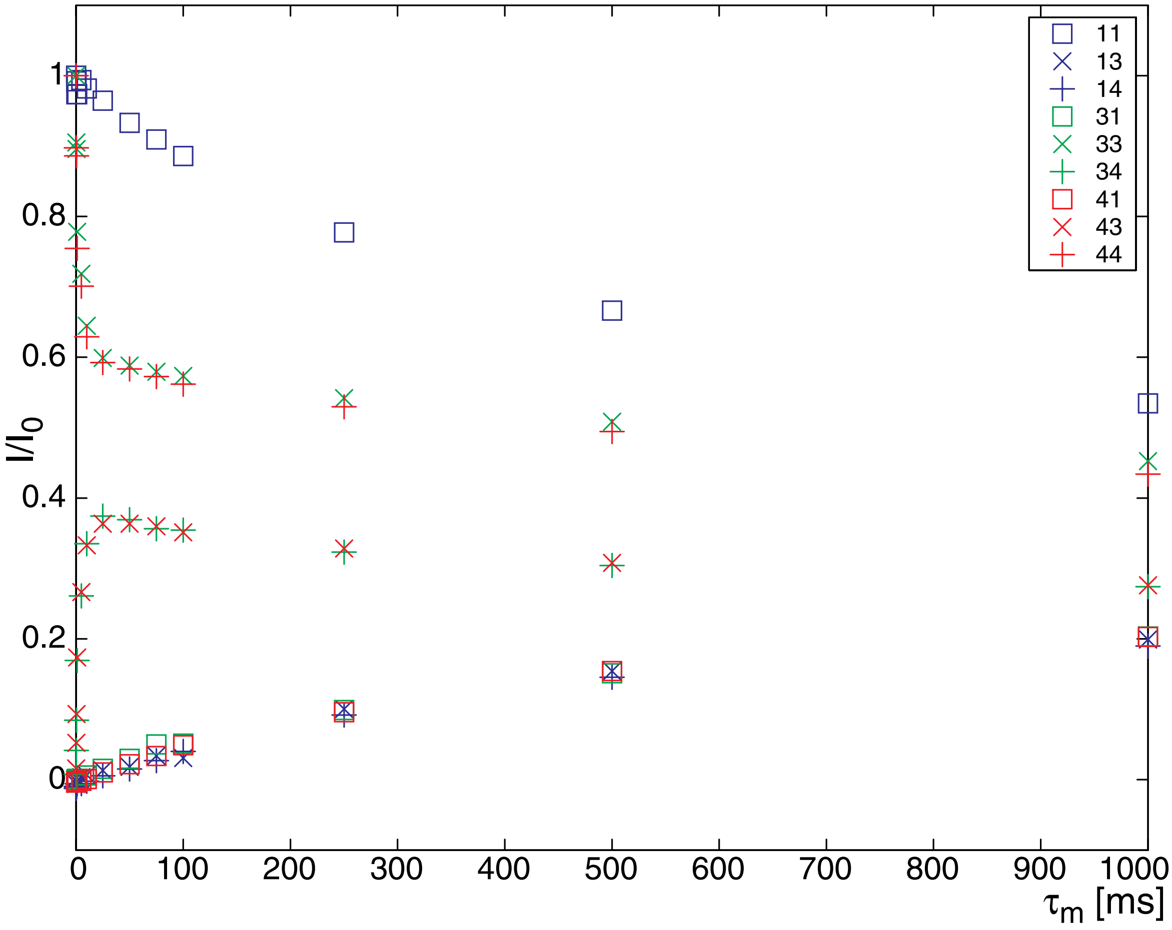

Figure 4.5: Integrated Intensities in a Spin Diffusion Experiment
Time dependence of the diagonal and cross-peak intensity in triply-labelled 1,3,4-^{13}C Gly-Gly sample (H_2N-$^*CH_2$-$^*CO$-NH-CH_2-$^*COOH$) as a function of the mixing time τ_m in a proton-driven spin-diffusion experiment at 7 kHz MAS frequency.

homonuclear dipolar coupling if the rotational-resonance condition of Eq. [4.3] is fulfilled. Such line broadening is usually unwanted since they reduce the resolution of the spectrum. One can, however, use rotational-resonance recoupling as a selective polarization-transfer method since only spins which fulfill the rotational-resonance condition will experience a homonuclear dipolar coupling. In the presence of chemical-shielding tensors one can also observe rotational-resonance recoupling for matching conditions with $n > 2$. They are usually weaker than the $n = 1, 2$ rotational-resonance conditions.

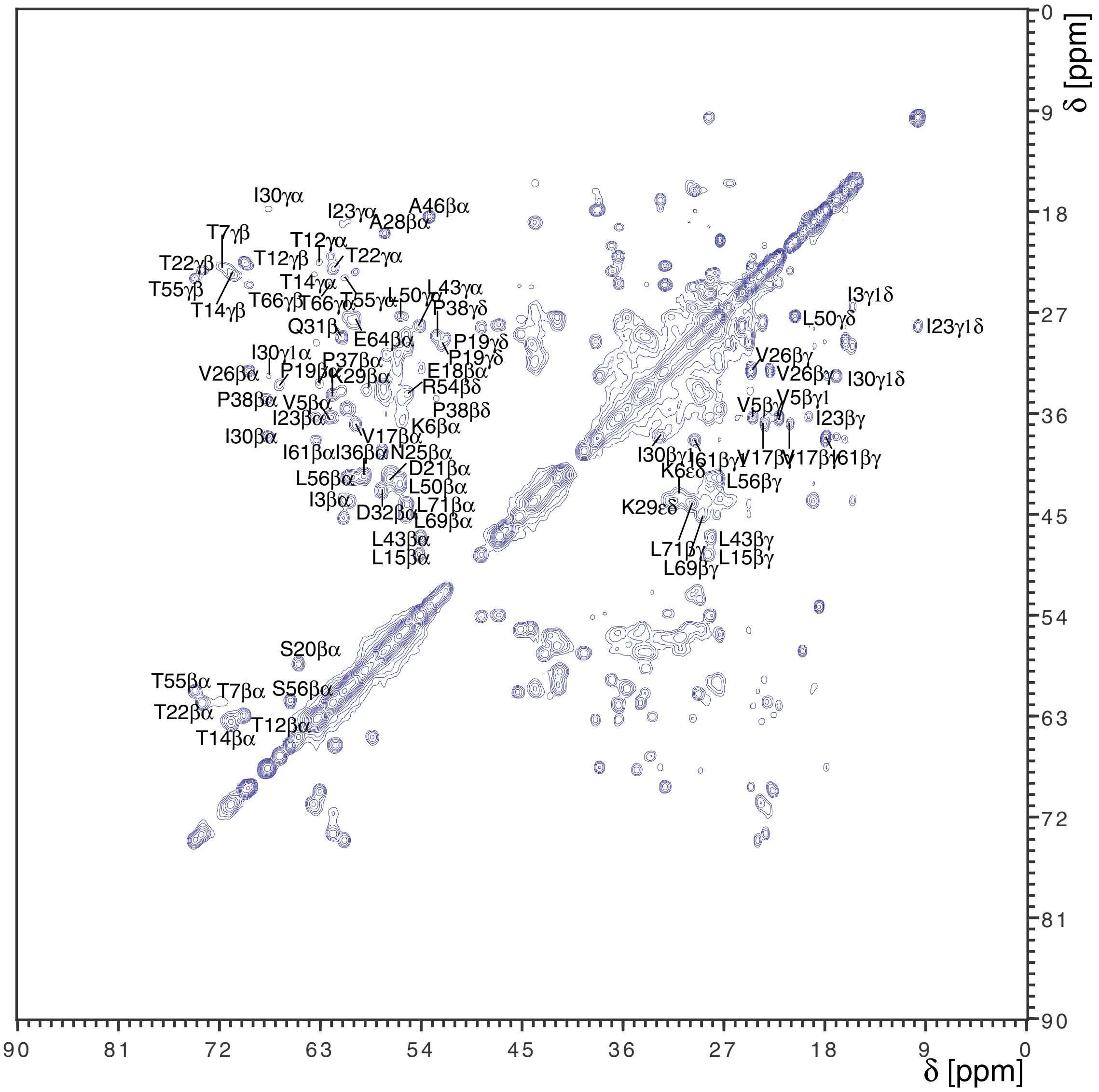

Figure 4.6: Proton-Driven Spin Diffusion Spectrum of Ubiquitin
Two-dimensional ^{13}C chemical-shift correlation spectrum using proton-driven spin diffusion with a mixing time of τ_m = 200 ms on the uniformly labelled protein ubiquitin. The MAS frequency was 40 kHz and rotary-resonance recoupling was used during the mixing time.

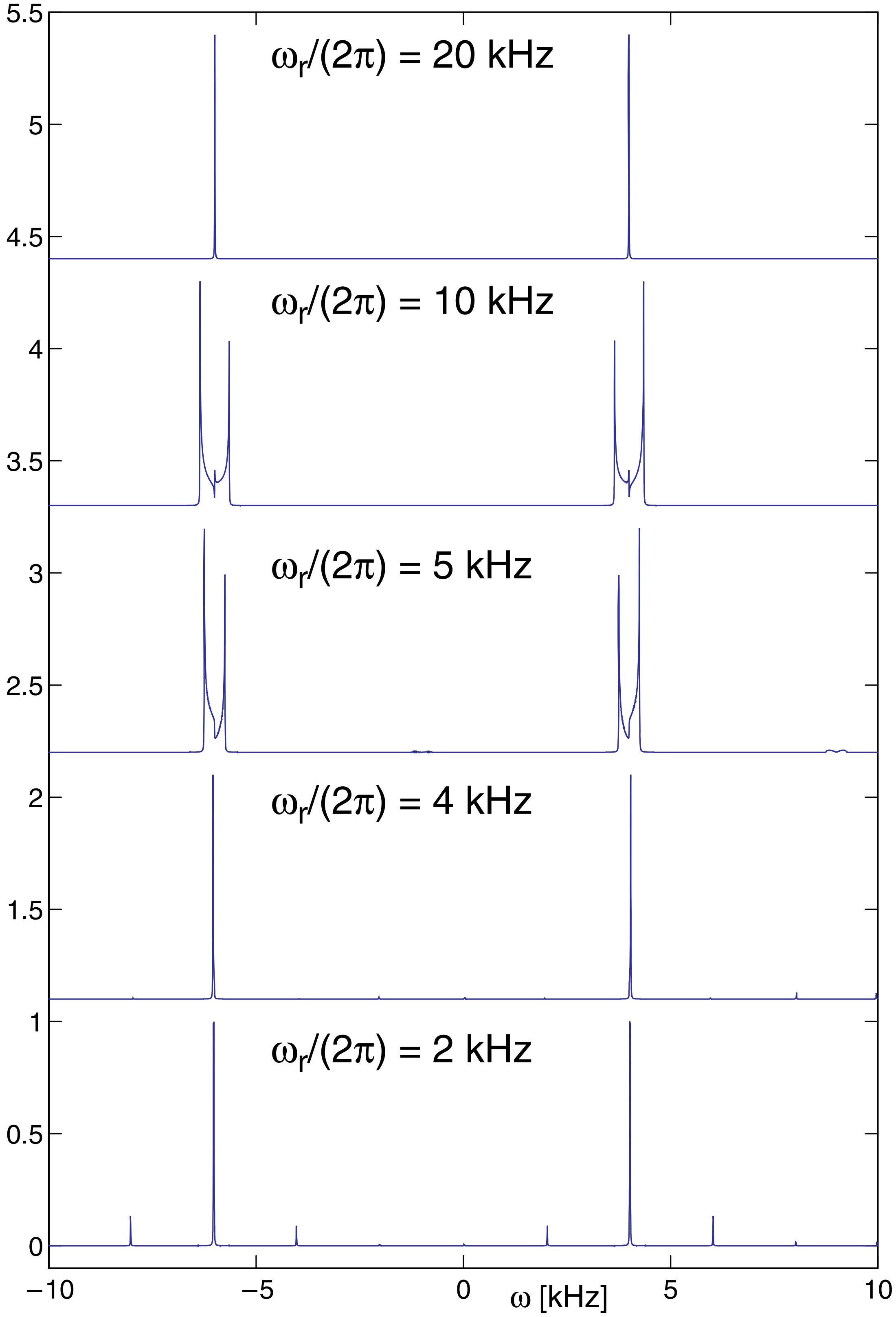

Figure 4.7: Rotational-Resonance Line Broadening
If the isotropic chemical-shift difference matches an integer multiple of the spinning frequency, line broadening is observed in homonuclear dipolar-coupled spin systems due to a reintroduction of the dipolar coupling through rotational resonance.

As a polarization-transfer method to determine the size of dipolar couplings, the rotational-resonance experiment is usually applied in a one-dimensional experiment to doubly labelled compounds as shown in Figure 4.8. After an initial cross-polarization period, one of the two resonances is inverted by a selective pulse or a DANTE pulse train. The initial density operator $\hat{\rho}_0 = \hat{S}_{1z} - \hat{S}_{2z}$ evolves then under the recoupled homonuclear dipolar coupling for a time τ_m under proton decoupling. Since there is no radio-frequency irradiation on the S spins during this time, the assumption of an isolated homonuclear S-spin pair is a good approximation and we can ignore the proton spins. We detect a series of normal 1D spectra under decoupling as a function of the mixing time τ_m. The initial density operator $\hat{\rho}_0$ will evolve under the homonuclear dipolar coupling and leads to a time evolution of the difference magnetization which is equivalent to a polarization-transfer process. One can also carry out the rotational-resonance experiment in a two-dimensional correlation experiment where the cross-peak intensity is a measure for the amount of transferred polarization. This is only necessary if rotational resonance is applied in fully labelled samples in order to achieve the required spectral resolution.

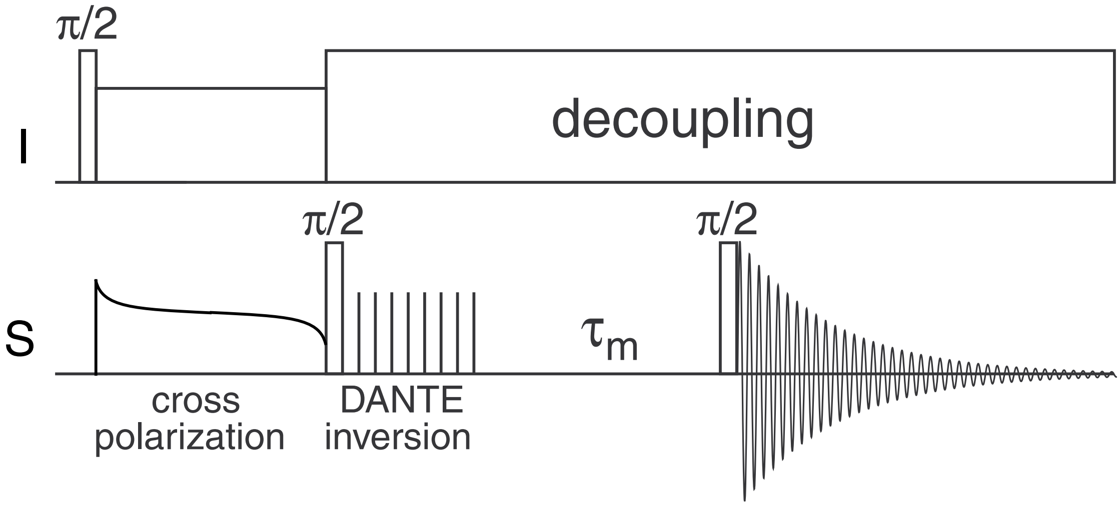

Figure 4.8: Pulse Sequence for Rotational-Resonance Polarization Transfer
After initial cross polarization, one of the two spins is inverted by a DANTE pulse sequence. The magnetization evolves then under the rotational-resonance recoupled dipolar Hamiltonian during τ_m which is varied in a set of experiments. The difference magnetization is then plotted as a function of time.

4.2.2.2 Average-Hamiltonian Description in the Interaction Frame

If we assume that we have a doubly ^{13}C-labelled compound and good proton decoupling, the Hamiltonian for the homonuclear dipolar-coupled two-spin system is given by

$$\hat{\mathcal{H}}(t) = \omega_{\text{iso}}^{(1)}\hat{S}_{1z} + \omega_{\text{iso}}^{(2)}\hat{S}_{2z} + \omega_{SS}^{(1,2)}(t)\left(3\hat{S}_{1z}\hat{S}_{2z} - \vec{\hat{S}}_1 \cdot \vec{\hat{S}}_2\right) \qquad [4.4]$$

and the initial density operator in the rotational-resonance experiment is defined as

$$\hat{\rho}_0 = S_{1z} - S_{2z} \ . \qquad [4.5]$$

We can write this Hamiltonian and the density operator as a sum of two commuting subspaces, the double-quantum and the zero-quantum subspace

$$\hat{\mathcal{H}}(t) = \hat{\mathcal{H}}^{\Sigma}(t) + \hat{\mathcal{H}}^{\Delta}(t) \qquad [4.6]$$

with

$$\begin{aligned}
\hat{\mathcal{H}}^{\Sigma}(t) &= (\omega_{\text{iso}}^{(1)} + \omega_{\text{iso}}^{(2)})\hat{S}_z^{\Sigma} + \frac{1}{2}\omega_{SS}^{(1,2)}(t)\hat{1}^{\Sigma} \\
\hat{\mathcal{H}}^{\Delta}(t) &= (\omega_{\text{iso}}^{(1)} - \omega_{\text{iso}}^{(2)})\hat{S}_z^{\Delta} + \frac{1}{2}\omega_{SS}^{(1,2)}(t)\hat{1}^{\Delta} - \omega_{SS}^{(1,2)}(t)\hat{S}_x^{\Delta}
\end{aligned} \qquad [4.7]$$

and

$$\begin{aligned}
\hat{\rho}_0^{\Sigma} &= 0 \\
\hat{\rho}_0^{\Delta} &= \hat{S}_z^{\Delta}
\end{aligned} \ . \qquad [4.8]$$

The problem is now very similar to the problem of cross-polarization (Chapter 7.1.1.1). There will be no evolution in the double-quantum subspace and we only have to calculate the time evolution of the density operator in the zero-quantum subspace. For rare spins the dominant terms in the Hamiltonian is the chemical-shift term since the couplings are typically small due to the low gyromagnetic ratio. We transform the Hamiltonian of Eq. [4.7] into an interaction frame with the difference of the isotropic chemical shifts

$$\hat{\mathcal{H}}_1 = (\omega_{\mathrm{iso}}^{(1)} - \omega_{\mathrm{iso}}^{(2)})\hat{S}_z^{\Delta} = \Delta\omega_{\mathrm{iso}}^{(1,2)}\hat{S}_z^{\Delta} \qquad [4.9]$$

leading to an interaction-frame zero-quantum Hamiltonian of

$$\hat{\mathcal{H}}'^{\Delta}(t) = -\omega_{SS}^{(1,2)}(t)[\hat{S}_x^{\Delta}\cos(\Delta\omega_{\mathrm{iso}}^{(1,2)}t) + \hat{S}_y^{\Delta}\sin(\Delta\omega_{\mathrm{iso}}^{(1,2)}t)] \qquad [4.10]$$

where we have neglected the term proportional to the identity operator. Expanding the time-dependent dipolar coupling as

$$\omega_{SS}^{(1,2)}(t) = \frac{1}{\sqrt{6}}\sum_{m'=-2}^{2} e^{im'\omega_r t} d_{m'0}^{2}(\theta_m) A_{\ell m'}^{(1,2)}(\beta,\gamma) \qquad [4.11]$$

leads to an interaction-frame Hamiltonian of

$$\hat{\mathcal{H}}'^{\Delta}(t) = \frac{-1}{2\sqrt{6}}\sum_{m=-2}^{2} e^{im\omega_r t} d_{m0}^{2}(\theta_m) A_{2m}^{(1,2)}(\beta,\gamma)[\hat{S}_{\Delta}^{+} e^{i\Delta\omega_{\mathrm{iso}}t} + \hat{S}_{\Delta}^{-} e^{-i\Delta\omega_{\mathrm{iso}}t}] \qquad [4.12]$$

which has non vanishing terms in zeroth-order average Hamiltonian theory if the condition

$$|m|\omega_r = \left|\Delta\omega_{\mathrm{iso}}^{(1,2)}\right| \qquad [4.13]$$

with $m = \pm 1, \pm 2$ is fulfilled. In this case we obtain a zeroth-order average Hamiltonian of

$$\begin{aligned}\bar{\hat{\mathcal{H}}}^{(0)} &= \frac{-1}{2\sqrt{6}}[d_{-m0}^{2}(\theta_m) A_{2,-m}^{(1,2)}(\beta,\gamma)\hat{S}_{\Delta}^{+} + d_{m0}^{2}(\theta_m) A_{2m}^{(1,2)}(\beta,\gamma)\hat{S}_{\Delta}^{-}] \\ &= \frac{-1}{4}\left|d_{m0}^{2}(\theta_m)\right|\left|d_{0m}^{2}(\beta^{(1,2)})\right|\delta_D^{(1,2)}[e^{im\gamma}\hat{S}_{\Delta}^{+} + e^{-im\gamma}\hat{S}_{\Delta}^{-}] \\ &= \frac{-1}{2}\left|d_{m0}^{2}(\theta_m)\right|\left|d_{0m}^{2}(\beta^{(1,2)})\right|\delta_D^{(1,2)}[\hat{S}_x^{\Delta}\cos(m\gamma) + \hat{S}_y^{\Delta}\sin(m\gamma)]\end{aligned} \qquad . \qquad [4.14]$$

This corresponds to a nutation of the initial density operator $\hat{S}_z^{\Delta}$ about an axis in the x-y plane where the nutation frequency depends on the Euler angle β and the phase of the nutation axis on the Euler angle γ. The angle γ represents a rotation of the Hamiltonian about the z axis which has no influence on the polarization transfer and can be neglected. For the $m = 1$ rotational-resonance condition this leads to the Hamiltonian

$$\hat{\bar{\mathcal{H}}}^{(0)} = \frac{-1}{4\sqrt{2}}\sin(2\beta^{(1,2)})\delta_D^{(1,2)}\hat{S}_x^{\Delta} \ . \tag{4.15}$$

The time evolution of the difference magnetization $\langle \hat{S}_{1z} - \hat{S}_{2z}\rangle(t)$ under such a Hamiltonian is shown in Figure 4.9. We see an oscillation of the difference magnetization which dephases due to the orientation-dependence of the oscillation frequency. This behavior is basically the same as the one we have seen in Hartmann-Hahn polarization transfer under MAS (see Figure 7.11 and Chapter 7.2.1) because the average Hamiltonian has the same structure.

The off resonance behavior in rotational resonance is also very similar to the one in Hartmann-Hahn cross polarization under MAS. The average Hamiltonian for the $m = 1$ rotational-resonance condition has the form

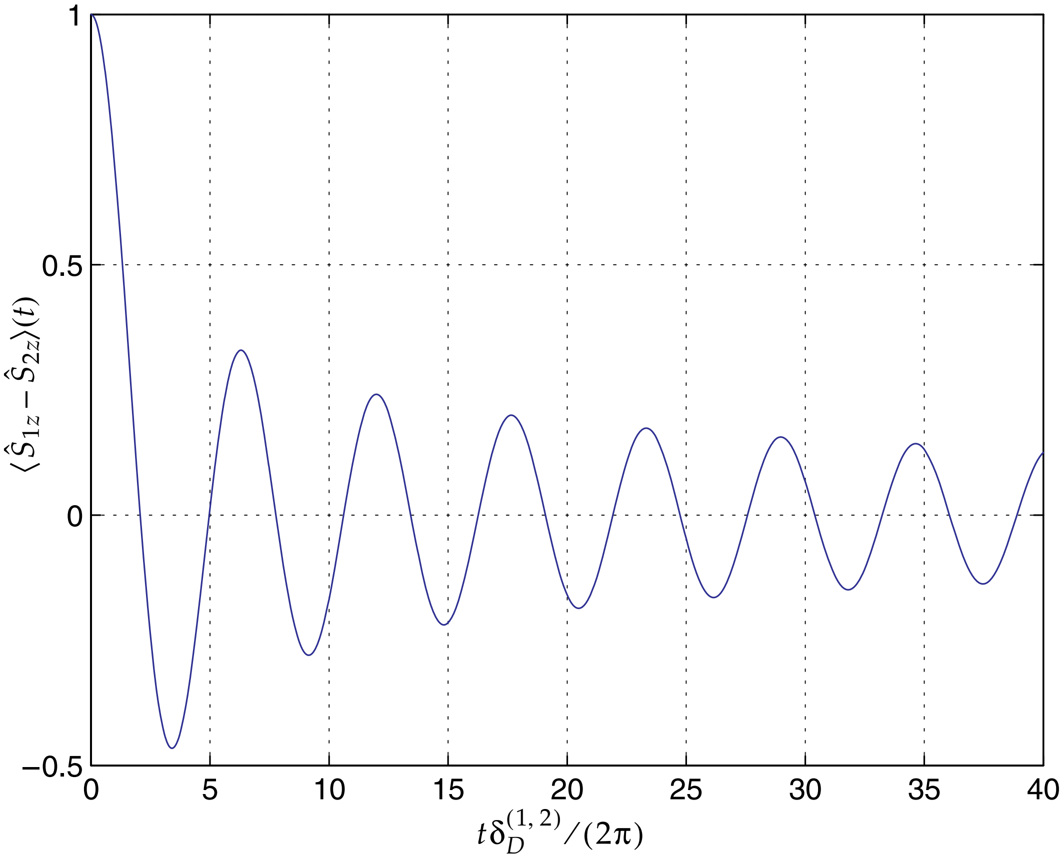

Figure 4.9: Time Evolution of Difference Magnetization at Rotational Resonance
Time evolution of the difference magnetization $\langle \hat{S}_{1z} - \hat{S}_{2z}\rangle(t)$ as a function of the mixing time τ_m scaled by the anisotropy of the dipolar coupling. The dephasing due to the orientation-dependent oscillation frequency leads to a quasi-equilibrium value of the difference magnetization of zero.

$$\hat{\tilde{\mathcal{H}}}^{(0)} = (\Delta\omega_{\mathrm{iso}}^{(1,2)} - \omega_r)\hat{S}_z^{\Delta} - \frac{1}{4\sqrt{2}}\sin(2\beta^{(1,2)})\delta_D^{(1,2)}\hat{S}_x^{\Delta} \qquad [4.16]$$

leading to an increase of the oscillation frequency and a reduced amplitude of the oscillation as we have seen in the case of Hartmann-Hahn cross polarization. The width of the matching condition is a described by a Lorentzian line with a width proportional to $\delta_D^{(1,2)}$. Figure 4.10 shows a simulation for the time evolution of the difference magnetization for a mismatch of $\Delta\omega_{\mathrm{iso}}^{(1,2)} - \omega_r = \delta_D^{(1,2)}/50$ where the offset in the quasi-equilibrium value is clearly visible. For a one-bond ^{13}C coupling with $\delta_D^{(1,2)}/(2\pi) \approx 4.5$ kHz this corresponds to a mismatch of about 90 Hz. Off-match conditions are mainly arising from a distribution of the isotropic chemical shifts in a sample since the theoretical matching condition can be measured with high accuracy

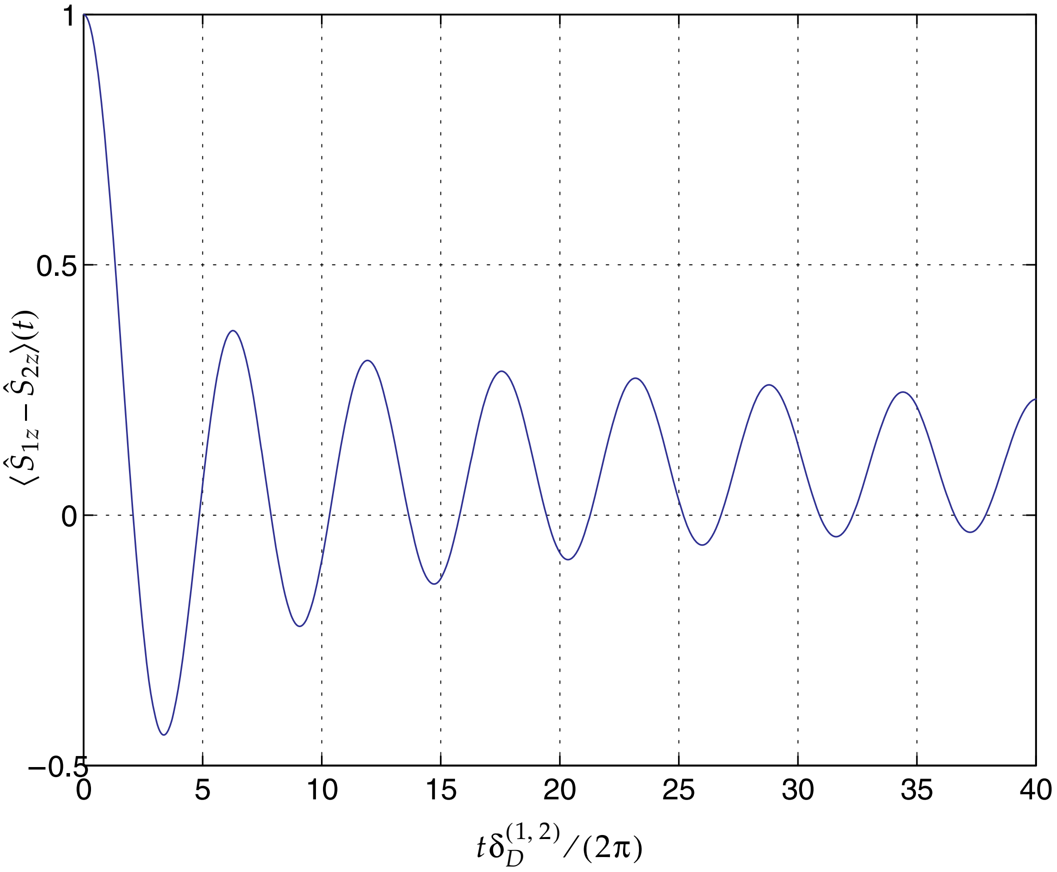

Figure 4.10: Time Evolution of Difference Magnetization at Rotational Resonance
Time evolution of the difference magnetization $\langle \hat{S}_{1z} - \hat{S}_{2z} \rangle(t)$ under mismatch conditions with $\Delta\omega_{\mathrm{iso}}^{(1,2)} - \omega_r = \delta_D^{(1,2)}/50$ as a function of the mixing time τ_m scaled by the anisotropy of the dipolar coupling. The dephasing due to the orientation-dependent oscillation frequency leads to a quasi-equilibrium value of the difference magnetization of zero.

and the spinning frequency of the sample can often be controlled to within a few Hz. Such a distribution of isotropic chemical shifts leads to a situation where only some of the spins are on the exact rotational-resonance condition while others are mismatched. This partial mismatch leads mainly to a non zero quasi-equilibrium value for the difference magnetization. Such effects have to be taken into account if one wants to extract quantitative distances from rotational-resonance polarization-transfer curves.

The description so far does not take into account relaxation effects which lead to a decay of the polarization during the mixing time. Such effects are very important and are one of the main limiting points for the application of rotational resonance in real spin systems. Since our problem can be described by a fictitious spin-1/2 system, we can describe the relaxation in terms of classical Bloch equations (in the usual rotating frame and not in the interaction frame!)

$$\frac{d}{dt}\begin{bmatrix}\langle\hat{S}_x^{\Delta}\rangle(t)\\ \langle\hat{S}_y^{\Delta}\rangle(t)\\ \langle\hat{S}_z^{\Delta}\rangle(t)\end{bmatrix} = \begin{bmatrix}\frac{-1}{T_{ZQ}} & -\Delta\omega_{\text{cs}}^{(1,2)}(t) & 0\\ \Delta\omega_{\text{cs}}^{(1,2)}(t) & \frac{-1}{T_{ZQ}} & -\omega_{SS}^{(1,2)}(t)\\ 0 & \omega_{SS}^{(1,2)}(t) & \frac{-1}{T_1}\end{bmatrix}\begin{bmatrix}\langle\hat{S}_x^{\Delta}\rangle(t)\\ \langle\hat{S}_y^{\Delta}\rangle(t)\\ \langle\hat{S}_z^{\Delta}\rangle(t)\end{bmatrix} \qquad [4.17]$$

where $1/T_{ZQ}$ is the relaxation-rate constant for the zero-quantum relaxation, while $1/T_1$ is the rate constant for the longitudinal relaxation. Typically, T_1 is much longer than T_{ZQ} and neglected in the calculations. Here we have replaced the time-independent isotropic chemical-shift difference $\Delta\omega_{\text{iso}}^{(1,2)}$ by the time-dependent difference of the full chemical shifts $\Delta\omega_{\text{cs}}^{(1,2)}(t)$. This equation is usually used to extract distances from rotational-resonance magnetization exchange curves $\langle\hat{S}_z^{\Delta}\rangle(t)$ by fitting the distance between the two spins, the zero-quantum relaxation rate constant, and possibly, a distribution of isotropic chemical shifts to the experimental data.

One can also implement the rotational-resonance experiment in an adiabatic fashion. The slowly changing Hamiltonian is in this case given by

$$\hat{\tilde{\mathcal{H}}}^{(0)}(T) = (\Delta\omega_{\text{iso}}^{(1,2)} - \omega_r(T))\hat{S}_z^{\Delta} - \frac{1}{4\sqrt{2}}\sin(2\beta^{(1,2)})\delta_D^{(1,2)}\hat{S}_x^{\Delta} \qquad [4.18]$$

which has the same basic structure as the Hamiltonian in Eq. [7.29] which described the adiabatic Hartmann-Hahn cross-polarization process. If we again start with an initial density operator proportional to the initial Hamiltonian $\sigma_0 = \hat{S}_{1z}$ we can obtain full polarization transfer with $\sigma(\tau_m) = \hat{S}_{2z}$. The problem of this method is an experimental one. It is experimentally not easy to implement such sweeps of the rotor speed because one has to speed up or slow down the rotor with a high acceleration to minimize loss of magnetization due to relaxation effects. In addition one cannot control the profile of the rotor frequency sweep and in practise only almost linear ramps have been implemented.

One can also carry out the rotational-resonance experiment in a tilted frame where we have an additional (small) radio-frequency field present (rotational-resonance tickling). The Hamiltonian in such a case is given by

$$\hat{\mathcal{H}}(t) = \omega_{\text{iso}}^{(1)}\hat{S}_{1z} + \omega_{\text{iso}}^{(2)}\hat{S}_{2z} + \omega_1(\hat{S}_{1x} + \hat{S}_{2x}) + \omega_{SS}^{(1,2)}(t)\left(3\hat{S}_{1z}\hat{S}_{2z} - \vec{\hat{S}}_1 \cdot \vec{\hat{S}}_2\right). \qquad [4.19]$$

We can transform the Hamiltonian into a frame of reference where the effective fields are along the z-axis by a rotation of each spin about $\hat{S}_{ky}$ with an angle $\theta_k = \arctan(\omega_1/\omega_{\text{iso}}^{(k)})$. The effective fields are then given by $\omega_{\text{eff}}^{(k)} = \sqrt{(\omega_{\text{iso}}^{(k)})^2 + \omega_1^2}$. We now have to match the difference or the sum of the effective chemical shifts by an integer multiple of the MAS frequency depending on the carrier frequency. If the carrier frequency is outside the chemical-shift range ($\omega_{\text{iso}}^{(1)}$ and $\omega_{\text{iso}}^{(2)}$ have the same sign) we have to match the difference of the effective fields. If the carrier frequency is in the center between the two chemical shifts ($\omega_{\text{iso}}^{(1)}$ and $\omega_{\text{iso}}^{(2)}$ have opposite signs), we have to match the sum of the effective fields. This behavior is illustrated in Figure 4.11 which shows the effective fields for the two cases. The Hamiltonian in this tilted frame is given by

$$
\begin{aligned}
\hat{\mathscr{H}}(t) \;=\; & \omega_{\mathrm{eff}}^{(1)}\hat{S}_{1z}+\omega_{\mathrm{eff}}^{(2)}\hat{S}_{2z} \\
& +\omega_{SS}^{(1,2)}(t)2(\hat{S}_{1z}\cos\theta_1+\hat{S}_{1x}\sin\theta_1)(\hat{S}_{2z}\cos\theta_2+\hat{S}_{2x}\sin\theta_2) \\
& +\omega_{SS}^{(1,2)}(t)(\hat{S}_{1x}\cos\theta_1-\hat{S}_{1z}\sin\theta_1)(\hat{S}_{2x}\cos\theta_2-\hat{S}_{2z}\sin\theta_2) \\
& +\omega_{SS}^{(1,2)}(t)\hat{S}_{1y}\hat{S}_{2y}]
\end{aligned}
\quad . \qquad [4.20]
$$

One can now transform this Hamiltonian in the tilted frame into an interaction frame by the difference or sum of the effective chemical shifts depending on the relative sign of the isotropic chemical shifts. The situation is now more complicated because we cannot separate the zero-quantum and the double-quantum subspace anymore. One finds, however, that there is also a recoupling of the time-dependent dipolar Hamiltonian if the condition

$$
m\omega_r \;=\; \omega_{\mathrm{eff}}^{(1)}\pm\omega_{\mathrm{eff}}^{(2)} \qquad [4.21]
$$

is fulfilled. There are three advantages of the rotational-resonance tickling experiment over the normal rotational-resonance experiment: (i) One can turn on and off the

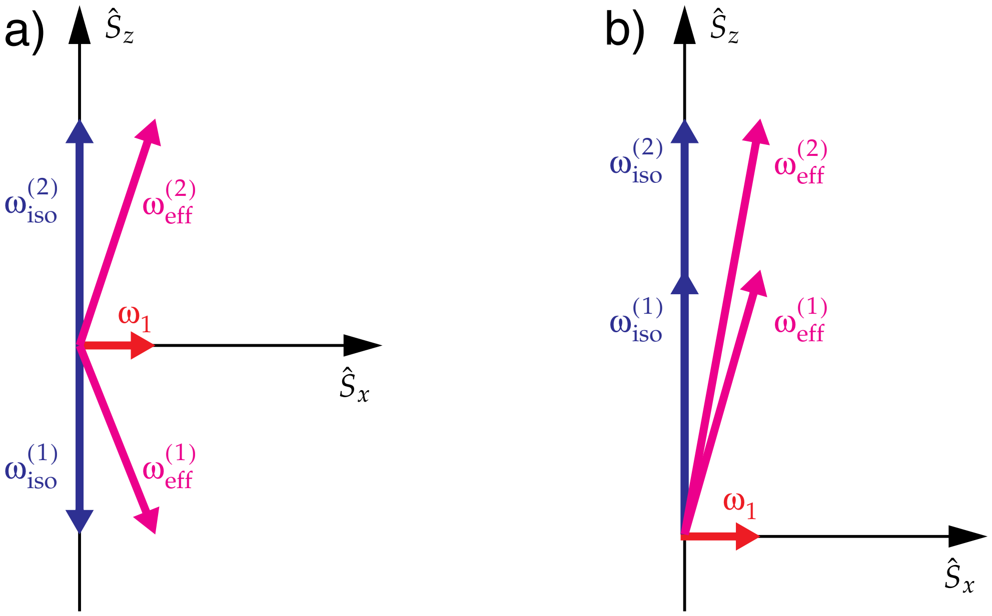

Figure 4.11: Rotational Resonance in the Tilted Frame
Effective-field directions in the tilted frame of reference for the rotational-resonance tickling experiment. In the case a) the chemical shifts have opposite signs while in case b) the signs of the chemical shifts are the same.

rotational-resonance matching during an experiment by simply changing the radio-frequency field. This allows us to have high-resolution spectra during the acquisition time while polarization transfer happens during the mixing time. (ii) One can implement an adiabatic rotational-resonance polarization-transfer experiment without having to change the rotor spinning frequency. One simply changes the rf amplitude in a suitable way in order to obtain an adiabatic sweep through the rotational-resonance condition in the tilted frame of reference. (iii) The chemical-shift range in which polarization transfer can occur is larger than in the standard rotational-resonance experiment but the range can be controlled by the amplitude of the rf field. This allows the implementation of band-selective polarization transfer.

4.2.2.3 Example

Figure 4.12 shows some experimental spectra for rotational-resonance spectra recorded at different mixing times. After the initial cross-polarization period, the C′ carbon was selectively inverted and the difference magnetization evolved under the m=1 rotational-resonance condition. One can see quite well the line broadening induced by the recoupled dipolar coupling on the C′ and C^{β} carbon. The magnetization can be measured by integrating the two lines and calculating the difference magnetization. A plot of the experimental difference magnetization as a function of the mixing time is shown in Figure 4.13 (circles) for the C′-C^{α} and the C′-C^{γ} spin pairs. The C′-C^{α} spin pair is directly bond (r_{CC} = 1.54 Å based on neutron diffraction data) and we see strong oscillations of the difference magnetization as one would expect for such a case. The C′-C^{γ} spin pair has only a long-range coupling (r_{CC} = 3.09 Å based on neutron diffraction data) and we see only strongly damped slow oscillations. One can fit the experimental data with simulations obtained from Eq. [4.17] and determine the dipolar coupling and the distance between the two spins. The best fit to the experimental data of a modified version of Eq. [4.17] is shown in Figure 4.13 as a solid line. The parameters obtained were r_{CC} = 1.56 Å for the C′-C^{α} spin pair and r_{CC} = 2.93 Å for the C′-C^{γ} spin pair. The precision of the obtained distance depends on the quality of the data (signal-to-noise ratio) and on the distance itself. For larger distances the oscillations are heavily damped and the distance and the zero-quantum relaxation-rate constant become highly correlated. Since there is no simple way of measuring T_{ZQ} experimentally, it has to be estimated from transverse one-quantum relaxation times or fitted as a free parameter. Typically, one can obtain distances for ^{13}C spins up to 4 Å with a precision of about 10%. A detailed analysis of the error surface of the fit and the correlation between the fitted parameters is very important.

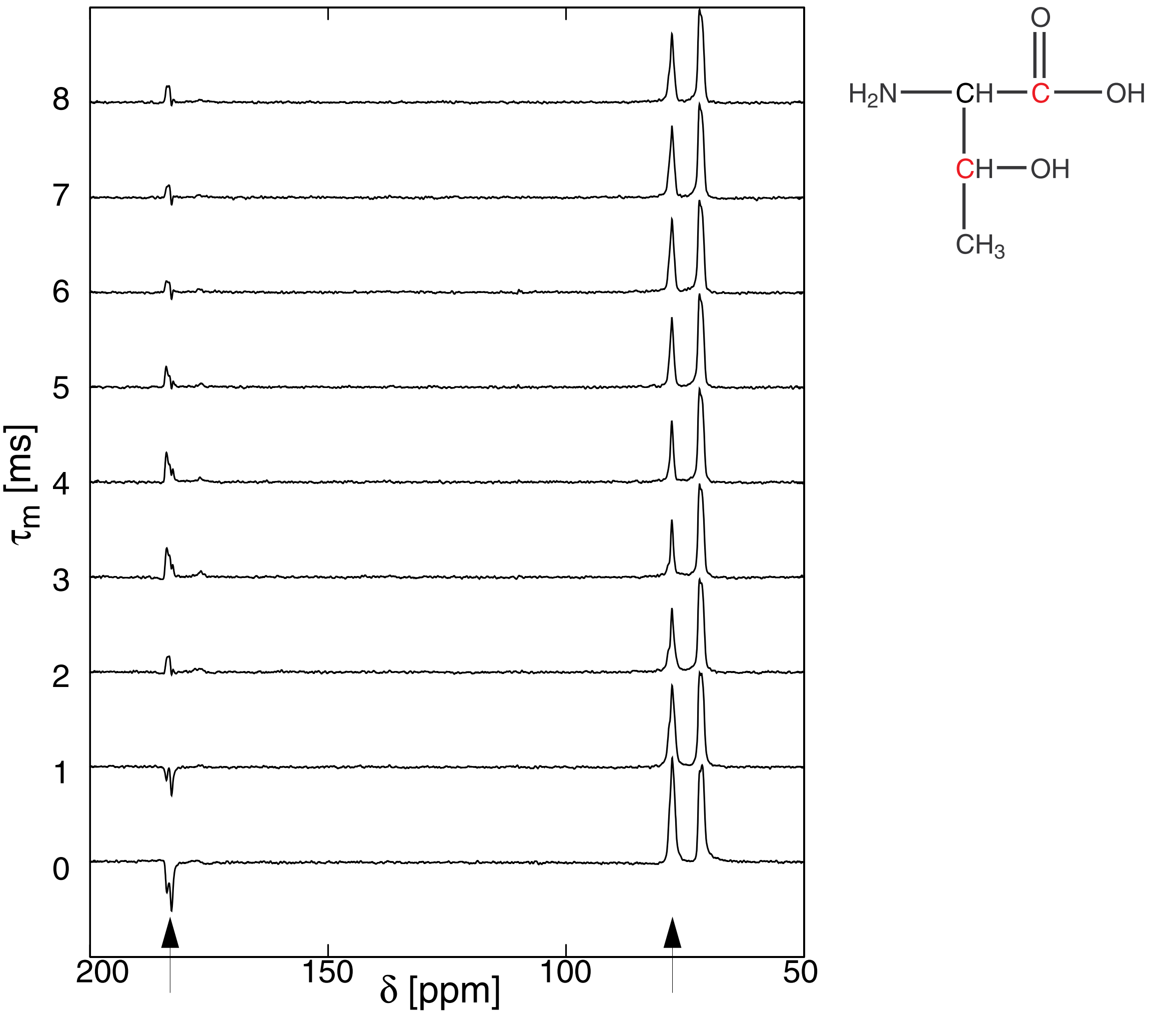

Figure 4.12: Experimental Rotational-Resonance Spectra
Experimental rotational-resonance spectra of threonine where the spinning frequency was adjusted to the isotropic chemical-shift difference between the C′ and the C^{β} carbon.

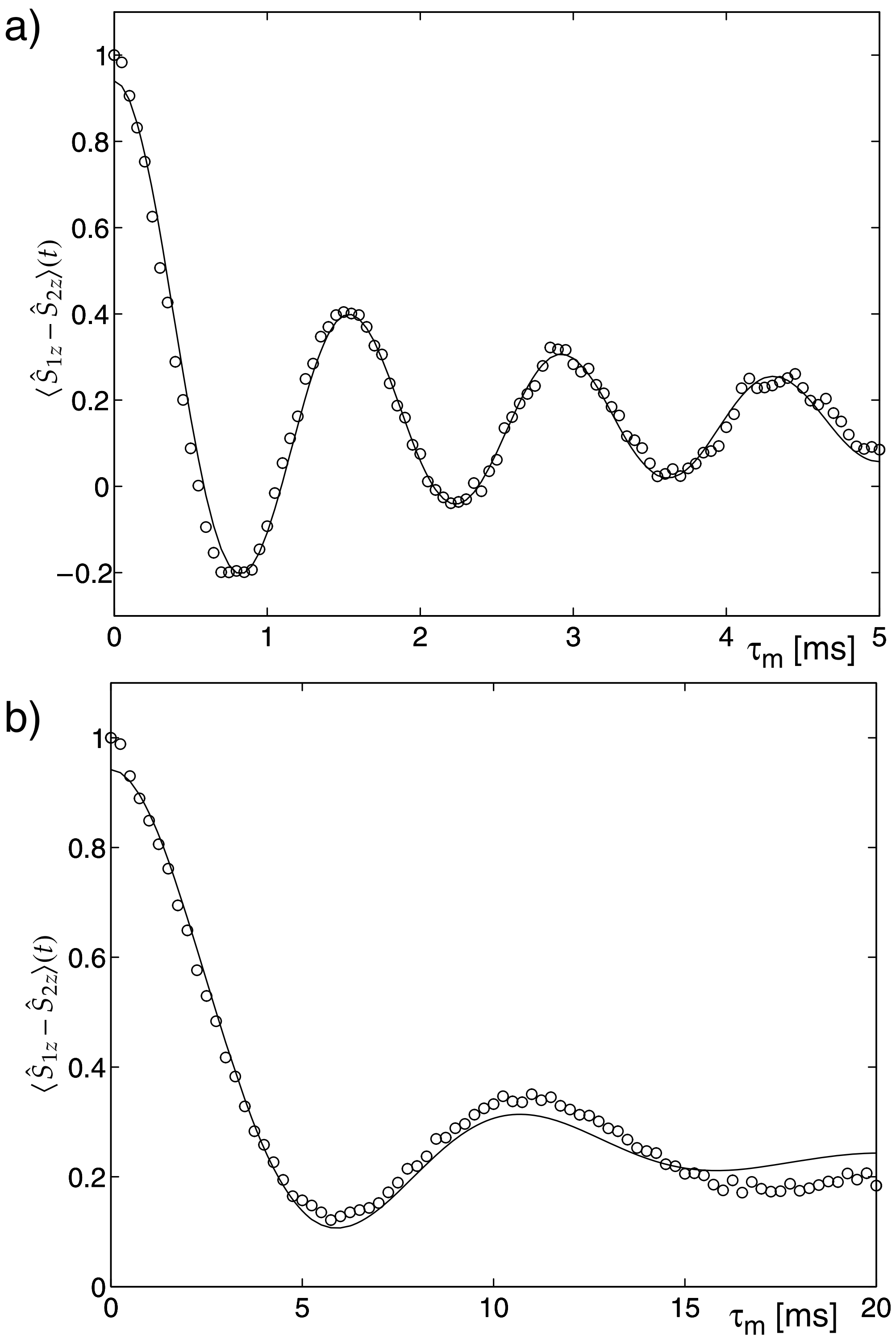

Figure 4.13: Experimental Rotational-Resonance Magnetization-Exchange Curves
Experimental (circles) rotational-resonance magnetization-exchange curves and best fit (solid lines) in threonine: a) for C′-C$^{\alpha}$ and b) for C′-C$^{\gamma}$.

4.3 Recoupling Sequences With Discrete Pulses

In the last Chapter we have discussed sequences which do not require rf irradiation on the spins that are recoupled. The next level in complication are sequences which use discrete pulses in order to prevent the full averaging of the dipolar coupling under MAS. Such sequences can best be described by a toggling frame approach where we assume that the pulses are infinitely short (delta-pulse approximation) and the coordinate system is reoriented instantaneously. There are quite a few recoupling sequences in this category and many date back to the early days of dipolar recoupling under MAS.

4.3.1 Radio-Frequency Driven Recoupling (RFDR)

4.3.1.1 Introduction

Radio-frequency driven recoupling (RFDR) is a homonuclear dipolar-recoupling technique where a π pulse is applied in the center of a rotor period to prevent the full averaging of the dipolar coupling through MAS. The basic pulse sequence for a two-dimensional correlation spectrum is shown in Figure 4.14. RFDR is a broadband recoupling method but the efficiency depends strongly on the isotropic chemical-shift difference which is equivalent to the distance of the cross peak from the diagonal of the spectrum. One can view the RFDR experiment as a rotational-resonance experiment where the strong dependence of the recoupling efficiency on the isotropic chemical-shift difference has been broadened by partially refocusing the chemical shifts.

4.3.1.2 Theoretical Description

The time-dependent Hamiltonian in RFDR is the same as in rotational-resonance recoupling and we can again write the Hamiltonian as the sum of two commuting subspaces, the zero-quantum and the double-quantum subspace (see Eqs.

[4.4]-[4.8]. Only the zero-quantum subspace is important for the RFDR experiment and the Hamiltonian is given by Eq. [4.7] as

$$\hat{\mathcal{H}}^{\Delta}(t) = (\omega_{\mathrm{iso}}^{(1)} - \omega_{\mathrm{iso}}^{(2)})\hat{S}_z^{\Delta} - \omega_{SS}^{(1,2)}(t)\hat{S}_x^{\Delta} = \Delta\omega_{\mathrm{iso}}^{(1,2)}\hat{S}_z^{\Delta} - \omega_{SS}^{(1,2)}(t)\hat{S}_x^{\Delta} \quad . \qquad [4.22]$$

The 180° pulse per rotor period can be described by an interaction-frame transformation where the frame of reference is rotated by 180° around the x axis. The chemical-shift Hamiltonian is inverted by this interaction-frame transformation while the dipolar-coupling Hamiltonian is left unchanged. This Hamiltonian is only cyclic after two rotor periods. In this interaction frame our Hamiltonian is defined piece wise and we find

$$\hat{\mathcal{H}}'(t) = \begin{cases} +\Delta\omega_{\mathrm{iso}}\hat{S}_z^{\Delta} - \omega_{SS}(t)\hat{S}_x^{\Delta} & 0 < t < \tau_r/2,\ 3\tau_r/2 < t < 2\tau_r \\ -\Delta\omega_{\mathrm{iso}}\hat{S}_z^{\Delta} - \omega_{SS}(t)\hat{S}_x^{\Delta} & \tau_r/2 < t < 3\tau_r/2 \end{cases} \quad . \qquad [4.23]$$

We now transform the Hamiltonian into a second interaction frame with the MAS frequency and obtain in the second interaction frame again a piece-wise defined Hamiltonian

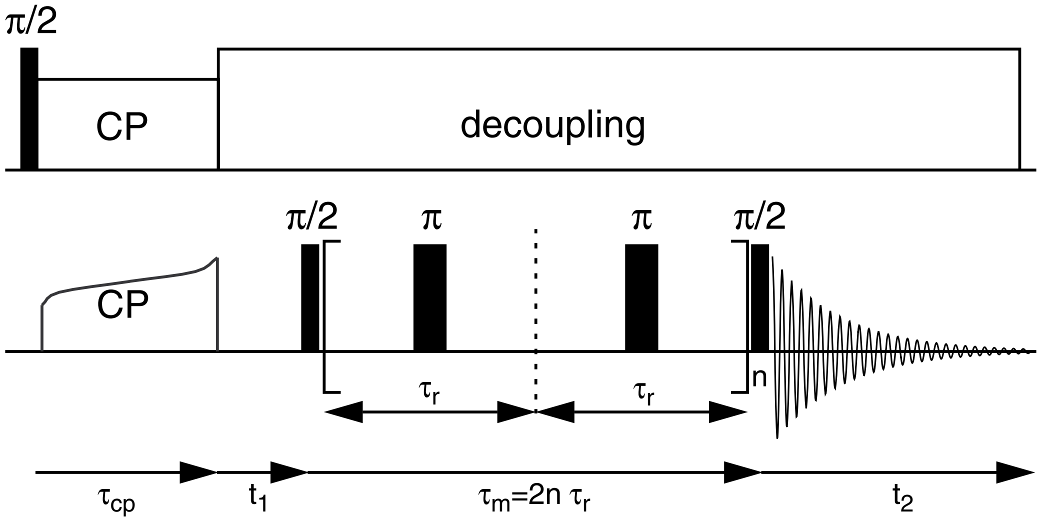

Figure 4.14: Pulse Sequence for RFDR Experiment
RFDR sequence for the broad-band recoupling of homonuclear dipolar couplings. After cross polarization, the magnetization is stored along the z axis and the averaging of the homonuclear dipolar couplings is prevented by a rotor-synchronized π pulse per rotor cycle.

$$\hat{\mathcal{H}}''(t) = \begin{cases} +(\Delta\omega_{\mathrm{iso}} - \omega_{\mathrm{r}})\hat{S}_z^{\Delta} - \omega_{SS}(t)[\cos(\omega_r t)\hat{S}_x^{\Delta} + \sin(\omega_r t)\hat{S}_y^{\Delta}] \\ -(\Delta\omega_{\mathrm{iso}} - \omega_{\mathrm{r}})\hat{S}_z^{\Delta} - \omega_{SS}(t + \frac{\tau_r}{2})\left[\cos\left(\omega_r\left(t - \frac{\tau_r}{2}\right)\right)\hat{S}_x^{\Delta} + \sin\left(\omega_r\left(t - \frac{\tau_r}{2}\right)\right)\hat{S}_y^{\Delta}\right] \\ +(\Delta\omega_{\mathrm{iso}} - \omega_{\mathrm{r}})\hat{S}_z^{\Delta} - \omega_{SS}(t + \frac{\tau_r}{2})\left[\cos\left(\omega_r\left(t - \frac{\tau_r}{2}\right)\right)\hat{S}_x^{\Delta} - \sin\left(\omega_r\left(t - \frac{\tau_r}{2}\right)\right)\hat{S}_y^{\Delta}\right] \end{cases} \qquad [4.24]$$

which we can integrate after substituting

$$\omega_{SS}(t) = \frac{-\sqrt{2}}{4}\delta_D \sin(2\beta)\cos(\omega_r t + \gamma) + \frac{1}{4}\delta_D \sin^2\beta\cos(2\omega_r t + 2\gamma) \ . \qquad [4.25]$$

Note that the time for the integration of each of the three intervals starts always at zero. A lengthy but straightforward calculation leads to the zeroth-order average Hamiltonian of

$$\begin{aligned} \overline{\mathcal{H}}^0 &= \frac{-\delta_D}{4\pi}\sin\left(\pi\frac{\Delta\omega_{\mathrm{iso}}}{\omega_r}\right)\left[\frac{\Delta\omega_{\mathrm{iso}}/\omega_r}{(\Delta\omega_{\mathrm{iso}}/\omega_r)^2 - 4}\sin^2\beta + \frac{\Delta\omega_{\mathrm{iso}}/\omega_r}{(\Delta\omega_{\mathrm{iso}}/\omega_r)^2 - 1}\sqrt{2}\sin(2\beta)\right]\hat{S}_x^{\Delta} \\ &= -\bar{\omega}_{\mathrm{eff}}(\beta, \Delta\omega_{\mathrm{iso}}/\omega_r)\hat{S}_x^{\Delta} \end{aligned} \ . \qquad [4.26]$$

The Hamiltonian in the full Hilbert space is then given by

$$\overline{\mathcal{H}}^0 = \frac{\bar{\omega}_{\mathrm{eff}}(\beta, \Delta\omega_{\mathrm{iso}}/\omega_r)}{2}[\hat{S}_1^+\hat{S}_2^- + \hat{S}_1^-\hat{S}_2^+] \qquad [4.27]$$

leading for an initial density operator of $\hat{\rho}_0 = \hat{S}_{1z}$ to a time evolution of the density operator of

$$\hat{\rho}(t) = \hat{S}_{1z}\left(\frac{1 + \cos(\bar{\omega}_{\mathrm{eff}}t)}{2}\right) + \hat{S}_{2z}\left(\frac{1 - \cos(\bar{\omega}_{\mathrm{eff}}t)}{2}\right) + (\hat{S}_{1y}\hat{S}_{2x} - \hat{S}_{1x}\hat{S}_{2y})\sin(\bar{\omega}_{\mathrm{eff}}t) \ . \qquad [4.28]$$

The transfer efficiency depends strongly on the isotropic chemical-shift difference because the effective dipolar-coupling frequency $\bar{\omega}_{\mathrm{eff}}(\beta, \Delta\omega_{\mathrm{iso}}/\omega_r)$ depends not only on the Euler angle β but also on the ratio $\Delta\omega_{\mathrm{iso}}/\omega_r$. The dependence of $\bar{\omega}_{\mathrm{eff}}$ on the two parameters is plotted in Figure 4.15. One can see that the effective dipolar-coupling frequencies are largest around the broadened $m = 1$ $(\omega_r/\Delta\omega_{\mathrm{iso}} = 1)$ and $m = 2$ $(\omega_r/\Delta\omega_{\mathrm{iso}} = 0.5)$ rotational-resonance conditions. For large isotropic chemical-shift differences $(\omega_r/\Delta\omega_{\mathrm{iso}} < 0.5$ the effective dipolar-coupling frequency becomes quite small and oscillates fast. For small isotropic chemical-shift differences $\omega_r/\Delta\omega_{\mathrm{iso}} > 2$ one finds decrease of the effective dipolar-coupling frequency towards zero.

The theoretical description of the RFDR experiment was done in the limit of δ pulses, i.e., pulses which correspond to instantaneous rotations. The effects of real pulses which is especially important at high MAS frequencies can be included in the theoretical treatment. Their effects can be minimized by using an appropriate phase cycle on the train of 180° pulses. If the rf-field to MAS frequency ratio becomes 1/2, one can describe the RFDR experiment with the usual phase cycle on the 180 °pulses as a $R4_4^1$ sequence as described in Chapter 4.5.1.

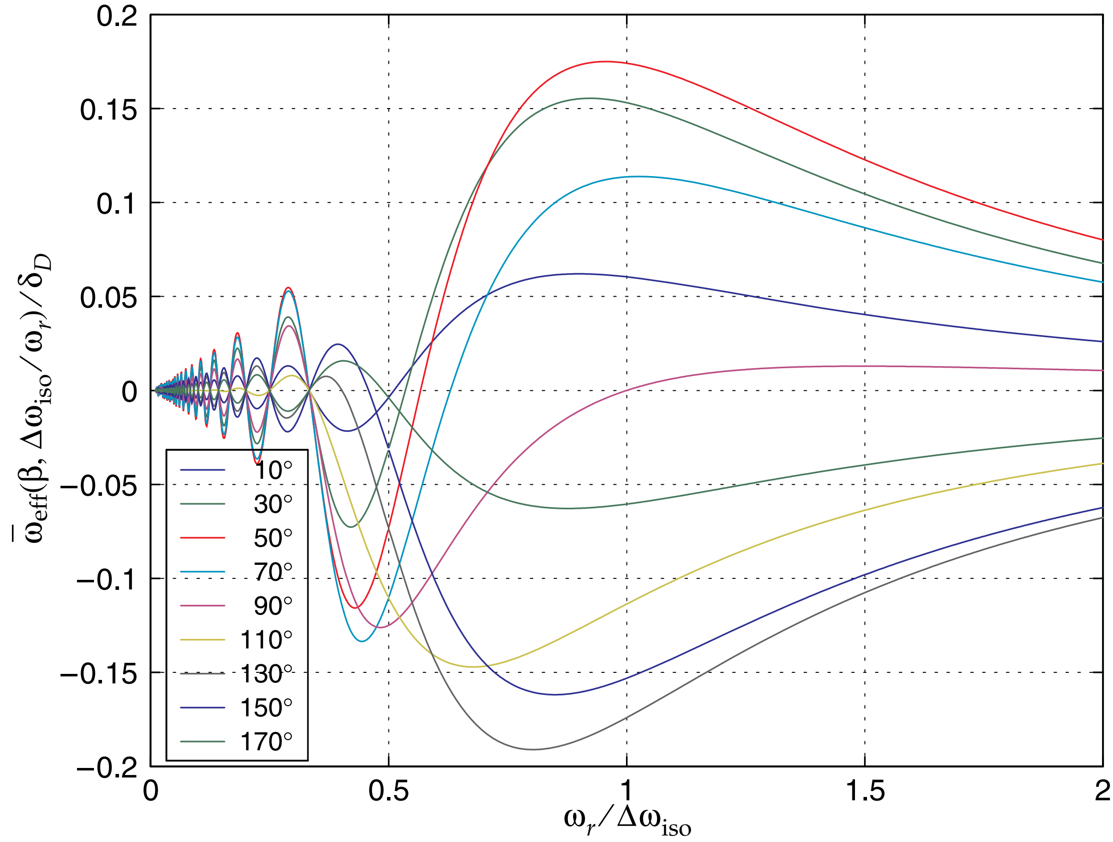

Figure 4.15: Effective Dipolar Coupling Frequency in the RFDR Experiment
Effective dipolar coupling in the RFDR experiment as a function of the isotropic chemical-shift difference $\omega_r/\Delta\omega_{\mathrm{iso}}$ for several values of the Euler angle β. One can clearly see that the effective coupling becomes quite small for large offsets.

4.3.1.3 Examples

Two-dimensional chemical-shift spectra using RFDR as a mixing sequence have mostly been used to assign resonances based on the coupling pattern. Directly bond carbons have the strongest couplings and this can be used to determine the resonance assignment of neighboring atoms. Figure 4.16 shows an example of RFDR applied to fully ^{13}C labelled bacteriochlorophyll c in order to obtain a homonuclear correlation spectrum. Some of the cross peaks which allow the assignment of directly bond carbons are indicated by their number in the spectra. The numbering of the bacteriochlorophyll c is shown in Figure 4.16 C and D. The spectra in A and B were recorded at a relatively low MAS frequency of 8 kHz which explains the strong side diagonals in the spectra. The spectrum in E was recorded with an MAS frequency of 15 kHz and at a higher static magnetic field and shows significantly weaker side bands. In this case the assignment of the resonances was used to determine the change in chemical shift relative to the chemical shift of bacteriochlorophyll c in solution. These chemical-shift differences were used to develop a stacking model of the bacteriochlorophyll c in chlorosomes.

The strong side diagonals in the spectra are experimental artifacts which appear in phase-sensitive two-dimensional MAS spectra with polarization transfer if the acquisition is not properly synchronized with the MAS rotation. They can be avoided by recording two data sets where either the mixing time or the t_1 time plus the mixing time is synchronized with the sample rotation and the correct coherence selection by phase cycling is applied.

4.3.2 REDOR

4.3.2.1 Introduction

Rotational echo double resonance (REDOR) is a heteronuclear recoupling method where the averaging of the heteronuclear dipolar coupling is prevented by 180° pulses which are spaced by half a rotor period. The basic pulse sequence is

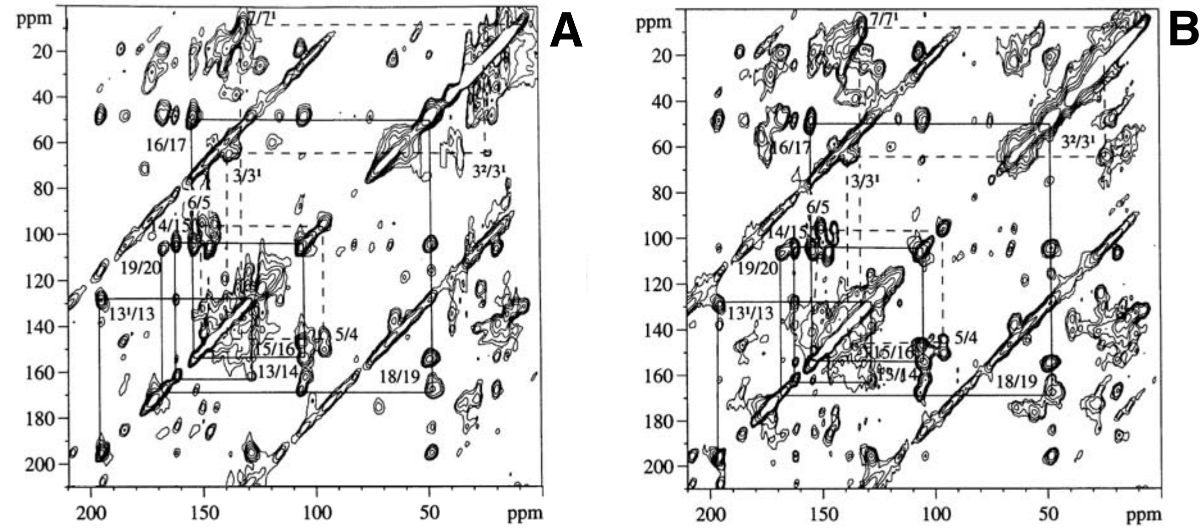

Contour plots of 2-D MAS dipolar correlation NMR spectra of uniformly 13C labeled chlorosomes (A), and 13C labeled bacteriochlorophyll c aggregates (B), recorded in a magnetic field of 9.4 T. The spinning speed was 8. kHz and a polarization transfer time of 1 ms was used. The lines indicate sequences of nearest neighbor correlations. The assignments of correlations (x:y) on the plot correspond with the numbering of the bacteriochlorophyll

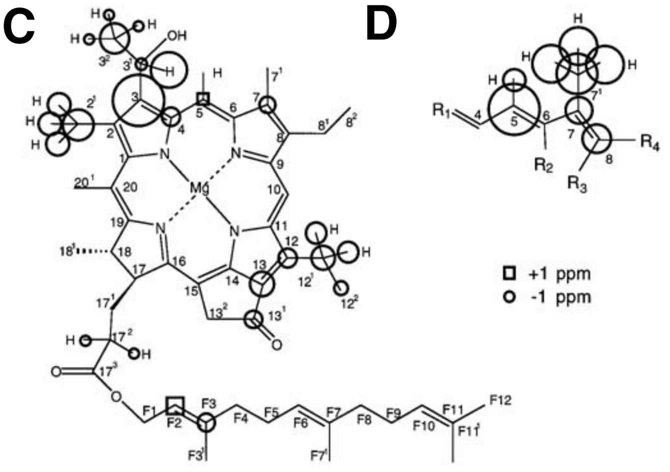

Numbering of the carbon atoms in bacteriochlorophyll c. Visual representation of the aggregation shifts $\Delta\sigma_i = \sigma_{liq} - \sigma_i$. The two components shown in part E by the solid and dashed lines are indicated separately in (C) and

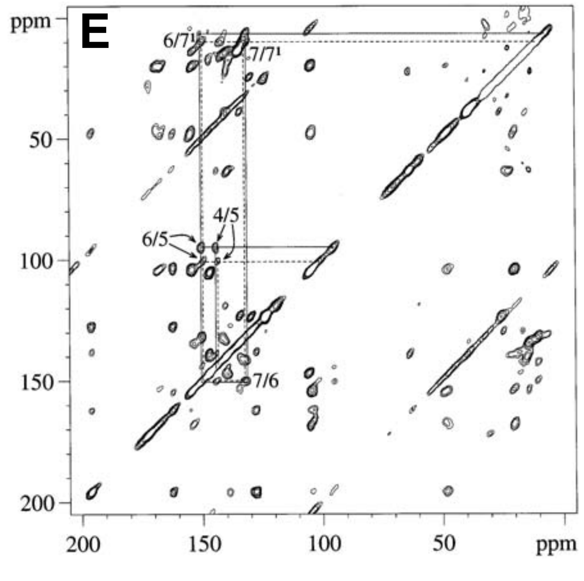

(E) Contour plot of a 2-D MAS ^{13}C ^{13}C dipolar correlation NMR spectrum of uniformly ^{13}C enriched chlorosomes collected in a magnetic field of 14.1 T. The spectrum was recorded with a spinning speed of 15 kHz and with a polarization transfer time of 1 ms. The solid and dashed lines indicate the correlation networks 4-5-6-7-7^1 for the two components.

Figure 4.16: Application of RFDR to Resonance Assignment in Chlorophyll
B.-J. van Rossum, G.J. Boender, F.M. Mulder, J. Raap, T.S. Balaban, A. Holzwarth, K. Schaffner, S. Prytulla, H. Oschkinat, H.J.M. de Groot “Multidimensional CP-MAS ^{13}C NMR of uniformly enriched chlorophyll”, Spectrochimica Acta Part A **54** (1998) 1167 1176.

shown in Figure 4.17 but there are many variations which lead, in principle, to the same result. The REDOR pulse sequence is a triple-resonance experiment. After initial cross polarization from the protons to the carbons, the magnetization evolves under the influence of the recoupled heteronuclear dipolar coupling leading to a partial dephasing of the carbon magnetization. The isotropic chemical shift of the carbons is refocused by the central 180° pulse on the carbons. The carbon signal is then measured as a function of the rotor periods. The experiment is usually carried out as a difference experiment to eliminate the influence of relaxation effects on the dipolar-coupling determination. The intensity of the carbon signal in the dephased experiment as described before is called S. The control experiment where all the pulses on the nitrogen channel are eliminated and no dephasing happens is called S_0. The REDOR curve is a plot of

$$\frac{S_0(n\tau_r) - S(n\tau_r)}{S_0(n\tau_r)} = \frac{\Delta S(n\tau_r)}{S_0(n\tau_r)} \qquad [4.29]$$

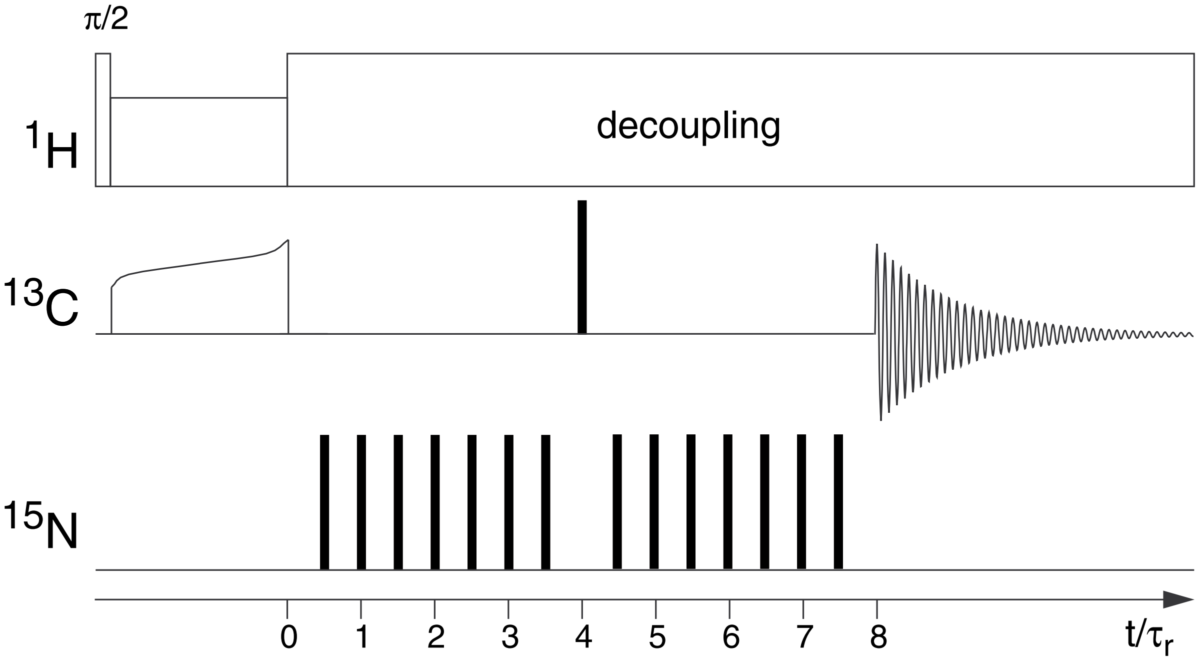

Figure 4.17: Pulse Sequence for the REDOR Experiment
REDOR pulse sequence for the determination of dipolar couplings between ^{13}C and ^{15}N. Initially ^{13}C polarization is generated by cross polarization from the protons. During the following evolution period π pulses are used to prevent the averaging of the heteronuclear dipolar coupling. In a reference experiment, all the ^{15}N pulses are left out to obtain the non-dephased spectrum.

as a function of the mixing time which can then be fitted to the theoretical REDOR curve. There is also a REDOR transform which directly converts the measured REDOR curve into a dipolar coupling or a distance.

4.3.2.2 Theoretical Description

We assume a heteronuclear two-spin system with a time-dependent Hamiltonian due to MAS of

$$\hat{\mathcal{H}}(t) = \omega_I(t)\hat{I}_z + \omega_S(t)\hat{S}_z + \omega_{IS}(t)2\hat{I}_z\hat{S}_z \ . \tag{4.30}$$

Here, the I spin is the passive (^{15}N) spin while the S spin is the active (^{13}C) detected spin. The basic building block of the REDOR pulse sequence is shown in Figure 4.18. There are two 180° pulses per rotor cycle spaced by half a rotor cycle. We can view the 180° pulses as an interaction frame transformation which is described by the Wigner rotation matrix elements $\mathfrak{D}^{\ell}_{m'm}(0, \pi, 0)$ acting on the S-spin space. The time-dependent Hamiltonian in the interaction frame is defined piece wise

$$\hat{\mathcal{H}}(t) = \begin{cases} \omega_S(t)\hat{S}_z + \omega_I(t)\hat{I}_z + \omega_{IS}(t)2\hat{I}_z\hat{S}_z & 0 \le t \le \tau_r/2 \\ \omega_S(t)\hat{S}_z - \omega_I(t)\hat{I}_z - \omega_{IS}(t)2\hat{I}_z\hat{S}_z & \tau_r/2 < t \le \tau_r \end{cases} \tag{4.31}$$

with

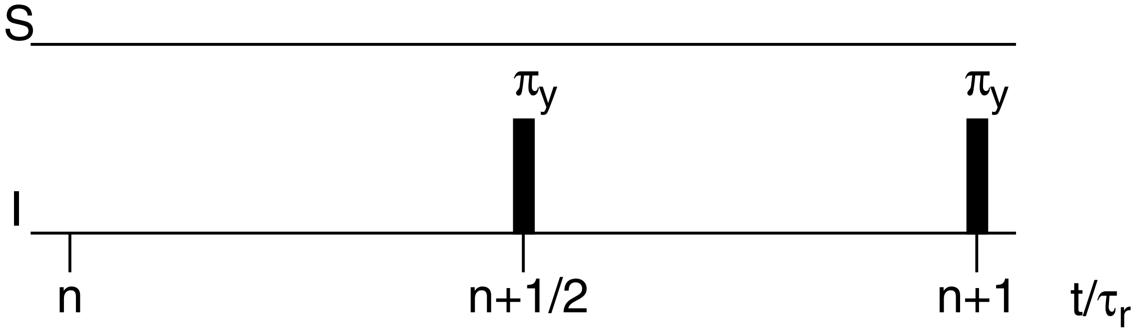

Figure 4.18: Basic Building Block in the REDOR Experiment
Basic building block for a single rotor period for the REDOR sequence. Such a pulse sequence recouples the heteronuclear dipolar coupling while the isotropic J coupling and the chemical shift on the I spin are averaged out.

$$\omega_S(t) = \omega_S^{\mathrm{iso}} + \frac{2}{\sqrt{6}} \sum_{m=-2}^{2} e^{im\omega_r t} d_{m0}^2(\theta_m) A_{2m}^S(\alpha^{(S)}, \beta^{(S)}, \gamma^{(S)}) , \qquad [4.32]$$

$$\omega_I(t) = \omega_I^{\mathrm{iso}} + \frac{2}{\sqrt{6}} \sum_{m=-2}^{2} e^{im\omega_r t} d_{m0}^2(\theta_m) A_{2m}^I(\alpha^{(I)}, \beta^{(I)}, \gamma^{(I)}) , \qquad [4.33]$$

and

$$\omega_{IS}(t) = \pi J + \frac{1}{\sqrt{6}} \sum_{m=-2}^{2} e^{im\omega_r t} d_{m0}^2(\theta_m) A_{2m}^{IS}(\alpha^{(IS)}, \beta^{(IS)}, \gamma^{(IS)}) . \qquad [4.34]$$

To calculate the zeroth-order average Hamiltonian we have to integrate the time-dependent interaction-frame Hamiltonian of Eq. [4.31] over a full rotor period

$$\begin{aligned} \hat{\bar{\mathcal{H}}}^{(0)} &= \frac{1}{\tau_r} \int_0^{\tau_r/2} (\omega_S(t)\hat{S}_z + \omega_I(t)\hat{I}_z + \omega_{IS}(t)2\hat{I}_z\hat{S}_z)dt \\ &\quad + \frac{1}{\tau_r} \int_{\tau_r/2}^{\tau_r} (\omega_S(t)\hat{S}_z - \omega_I(t)\hat{I}_z - \omega_{IS}(t)2\hat{I}_z\hat{S}_z)dt \\ &= \frac{1}{\tau_r}\int_0^{\tau_r} \omega_S(t)\hat{S}_z dt + \frac{1}{\tau_r} \int_0^{\tau_r/2} (\omega_I(t)\hat{I}_z + \omega_{IS}(t)2\hat{I}_z\hat{S}_z)dt \\ &\quad - \frac{1}{\tau_r} \int_{\tau_r/2}^{\tau_r} (\omega_I(t)\hat{I}_z + \omega_{IS}(t)2\hat{I}_z\hat{S}_z)dt \end{aligned} \quad . \qquad [4.35]$$

There are some obvious simplifications that we can make:

- The anisotropic chemical-shift tensor of the S spin is averaged out since the integration is over a full rotor cycle.
- The isotropic chemical shift of the S spin is not averaged out over one rotor period.
- The isotropic chemical shift of the I spin is refocused by the central π pulse.
- The isotropic heteronuclear J coupling is refocused by the central π pulse.
- The $m = \pm 2$ terms of the chemical-shift tensor of the I spin as well as the heteronuclear dipolar coupling are averaged over half a rotor cycle.

This leaves us with the isotropic chemical shift of the S spin and the $m = \pm 1$ terms of the chemical-shift tensor of the I spin and the heteronuclear dipolar coupling tensor in the zeroth-order average Hamiltonian

$$\begin{aligned}
\hat{\bar{\mathcal{H}}}^{(0)} &= \omega_S^{\text{iso}} \hat{S}_z + \frac{1}{\tau_r} \int_0^{\tau_r/2} \frac{2}{\sqrt{6}} \sum_{m = -1, 1} e^{im\omega_r t} d_{m0}^2(\theta_m) A_{2m}^I(\alpha^{(I)}, \beta^{(I)}, \gamma^{(I)}) \hat{I}_z dt \\
&+ \frac{1}{\tau_r} \int_0^{\tau_r/2} \frac{1}{\sqrt{6}} \sum_{m = -1, 1} e^{im\omega_r t} d_{m0}^2(\theta_m) A_{2m}^{IS}(\alpha^{(IS)}, \beta^{(IS)}, \gamma^{(IS)}) 2\hat{I}_z \hat{S}_z dt \\
&- \frac{1}{\tau_r} \int_{\tau_r/2}^{\tau_r} \frac{2}{\sqrt{6}} \sum_{m = -1, 1} e^{im\omega_r t} d_{m0}^2(\theta_m) A_{2m}^I(\alpha^{(I)}, \beta^{(I)}, \gamma^{(I)}) \hat{I}_z dt \\
&- \frac{1}{\tau_r} \int_{\tau_r/2}^{\tau_r} \frac{1}{\sqrt{6}} \sum_{m = -1, 1} e^{im\omega_r t} d_{m0}^2(\theta_m) A_{2m}^{IS}(\alpha^{(IS)}, \beta^{(IS)}, \gamma^{(IS)}) 2\hat{I}_z \hat{S}_z dt \quad . \qquad [4.36]
\end{aligned}$$

Using the relation

$$-\int_{\tau_r/2}^{\tau_r} e^{\pm i\omega_r t} dt = \int_0^{\tau_r/2} e^{\pm i\omega_r t} dt = \pm 2i \qquad [4.37]$$

we obtain after some calculations and assuming that the chemical-shift tensor is axially symmetric

$$\begin{aligned}
\hat{\bar{\mathcal{H}}}^{(0)} &= \omega_S^{\text{iso}} \hat{S}_z - \frac{4\sqrt{2}i}{6\pi}(A_{21}^I(\alpha^{(I)}, \beta^{(I)}, \gamma^{(I)}) + A_{2,-1}^I(\alpha^{(I)}, \beta^{(I)}, \gamma^{(I)}))\hat{I}_z \\
&- \frac{4\sqrt{2}i}{6\pi}(A_{21}^I(\alpha^{(I)}, \beta^{(I)}, \gamma^{(I)}) + A_{2,-1}^I(\alpha^{(I)}, \beta^{(I)}, \gamma^{(I)}))2\hat{I}_z \hat{S}_z \\
&= \omega_S^{\text{iso}} \hat{S}_z - \frac{\sqrt{2}}{\pi} \sin(2\beta^{(I))}) \sin\gamma^{(I)} \delta_\sigma^{(I)} \hat{I}_z - \frac{\sqrt{2}}{\pi} \sin(2\beta^{(IS)}) \sin\gamma^{(IS)} \delta_D^{(IS)} 2\hat{I}_z \hat{S}_z \quad . \qquad [4.38]
\end{aligned}$$

Over the full REDOR sequence, the isotropic chemical shift of the S spin is also averaged by the 180° pulse on the S spins. The chemical-shift on the I spins is not important since it commutes with the Hamiltonian at all times. We end, therefore up with an average REDOR Hamiltonian of the form

$$\hat{\bar{\mathcal{H}}}^{(0)} = -\frac{\sqrt{2}}{\pi} \sin(2\beta^{(IS)}) \sin\gamma^{(IS)} \delta_D^{(IS)} 2\hat{I}_z \hat{S}_z = \bar{\omega}_D^{(IS)}(\beta, \gamma)(2\hat{I}_z \hat{S}_z) \ . \qquad [4.39]$$

If we assume ideal pulses and have no homonuclear dipolar coupling, the zeroth-order average Hamiltonian is the exact REDOR Hamiltonian. In the presence of homonuclear dipolar couplings the situation becomes more complicated because the time-dependent interaction-frame Hamiltonian does no longer commute with itself. The time evolution of the initial density operator $\hat{\rho}_0 = \hat{S}_x$ under the REDOR Hamiltonian can be calculated easily and we obtain the REODR signal as

$$S(n\tau_r) = \cos\left(\frac{\sqrt{2}}{\pi}\sin(2\beta^{(IS)})\sin\gamma^{(IS)}\delta_D^{(IS)}n\tau_r\right) . \qquad [4.40]$$

For the reference experiment we eliminate the pulses on the I spins and obtain an average Hamiltonian of

$$\bar{\hat{\mathcal{H}}}^{(0)} = 0 , \qquad [4.41]$$

i.e., a full refocusing of all the interactions by the rotor and the central 180° pulse on the S spins. With this information we can now calculate the REDOR curve

$$\frac{\Delta S(n\tau_r)}{S_0} = 1 - \cos\left(\frac{\sqrt{2}}{\pi}\sin(2\beta^{(IS)})\sin\gamma^{(IS)}\delta_D^{(IS)}n\tau_r\right) \qquad [4.42]$$

as a generalized function of $\delta_D^{(IS)}n\tau_r$ which is shown in Figure 4.19. Such a buildup is typical for the REDOR experiment and can be used to fit the heteronuclear dipolar-coupling constant to the experimental data. In this way one can obtain relatively precise distances between heteronuclear spins in selectively labelled systems.

The effects of real pulses, i.e., finite pulse length which are not negligible compared to the rotor period can be included in the treatment. This is especially important for REDOR under fast MAS since the rotor period can become quite short under this condition. In the limiting case where the ratio of rf-field strength and pulse length approaches one, the REDOR experiment with the usual phase cycle can be described as an $R4_2^1$ experiment in the context of Chapter 4.5.1. In multi-spin systems, the influence of several couplings have to be taken into account. This problem has been solved analytically but is beyond the scope of this lecture.

The REDOR recoupling method can also be used in a polarization transfer method called TEDOR (transferred echo double resonance). The basic TEDOR pulse sequence shown in Figure 4.20 is based on the INEPT principle. The initial density operator is given by $\hat{\rho}(0) = S_x$ which evolves under the recoupled heteronuclear dipolar coupling $\overline{\omega}_D^{(IS)}(\beta, \gamma)$ leading to a density operator at time $t = n_1\tau_r$ of

$$\hat{\rho}(n_1\tau_r) = \hat{S}_x\cos(\overline{\omega}_D^{(IS)}(\beta, \gamma)n_1\tau_r) - 2\hat{S}_y\hat{I}_z\sin(\overline{\omega}_D^{(IS)}(\beta, \gamma)n_1\tau_r) \ . \qquad [4.43]$$

The two 90° pulses in the center of the sequence convert the anti-phase S-spin magnetization into anti-phase I-spin magnetization which then evolves again under recoupled heteronuclear dipolar coupling refocusing the anti-phase magnetization into in-phase I-spin magnetization leading to a density operator before the start of detection of

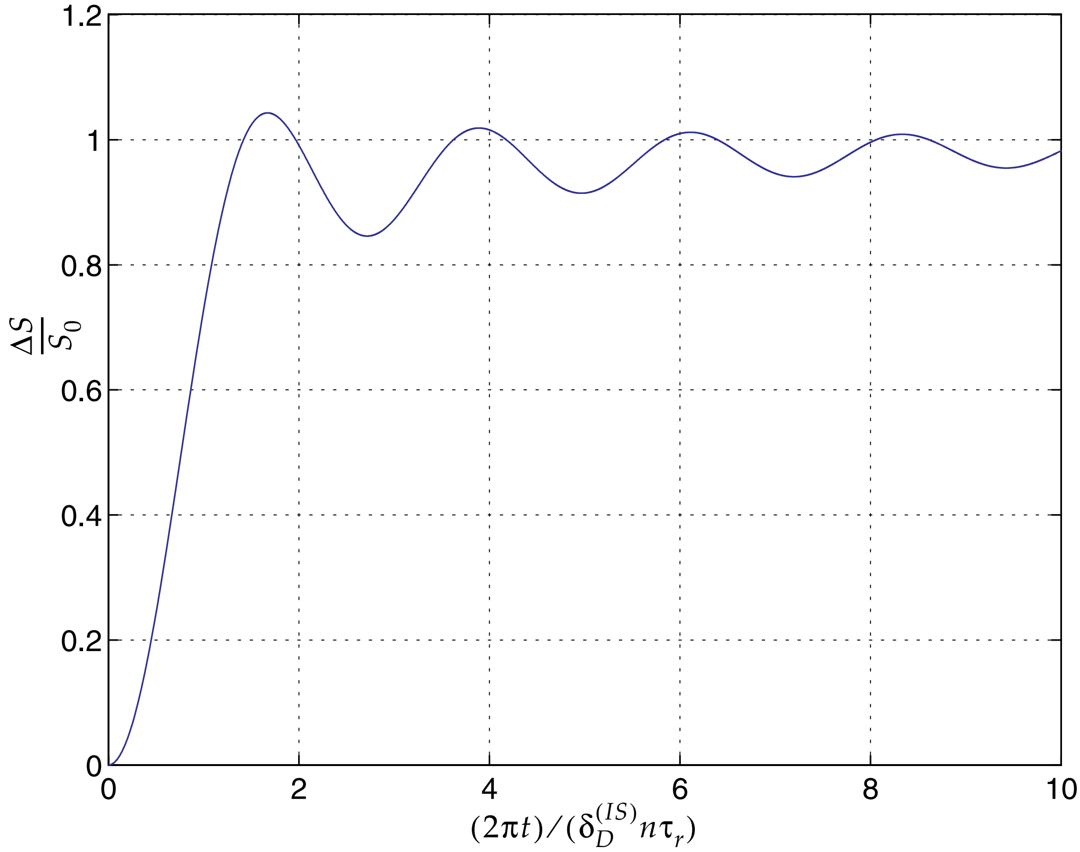

Figure 4.19: Theoretical REDOR Curve
Calculated REDOR curve $\Delta S(n\tau_r)/S_0$ as a function of the universal parameter $(2\pi t)/(\delta_D^{(IS)} n\tau_r)$.

$$
\begin{aligned}
\hat{\rho}((n_1+n_2)\tau_r) = {} & \hat{S}_x \cos(\overline{\omega}_D^{(IS)}(\beta,\gamma) n_1 \tau_r) \cos(\overline{\omega}_D^{(IS)}(\beta,\gamma) n_2 \tau_r) \\
& - \hat{S}_y \hat{I}_z \cos(\overline{\omega}_D^{(IS)}(\beta,\gamma) n_1 \tau_r) \sin(\overline{\omega}_D^{(IS)}(\beta,\gamma) n_2 \tau_r) \\
& - 2\hat{S}_z \hat{I}_y \sin(\overline{\omega}_D^{(IS)}(\beta,\gamma) n_1 \tau_r) \cos(\overline{\omega}_D^{(IS)}(\beta,\gamma) n_2 \tau_r) \\
& + \hat{I}_x \sin(\overline{\omega}_D^{(IS)}(\beta,\gamma) n_1 \tau_r) \sin(\overline{\omega}_D^{(IS)}(\beta,\gamma) n_2 \tau_r) \quad .
\end{aligned}
\tag{4.44}
$$

The final detectable signal in an ideal two-spin system is, therefore, given by

$$
\langle \hat{I}_x \rangle ((n_1+n_2)\tau_r) = \sin(\overline{\omega}_D^{(IS)}(\beta,\gamma) n_1 \tau_r) \sin(\overline{\omega}_D^{(IS)}(\beta,\gamma) n_2 \tau_r) \tag{4.45}
$$

which is plotted in Figure 4.21. The maximum polarization transfer is about 52% of the initial S-spin polarization if we assume that $n_1 = n_2$.

In multi-spin systems the polarization-transfer dynamics is more complicated and the best polarization transfer is not necessarily reached for equal length dephasing and refocusing times. In addition, homonuclear dipolar couplings as well as relaxation effects lead to a dephasing of the magnetization which reduces the polarization-transfer efficiency.

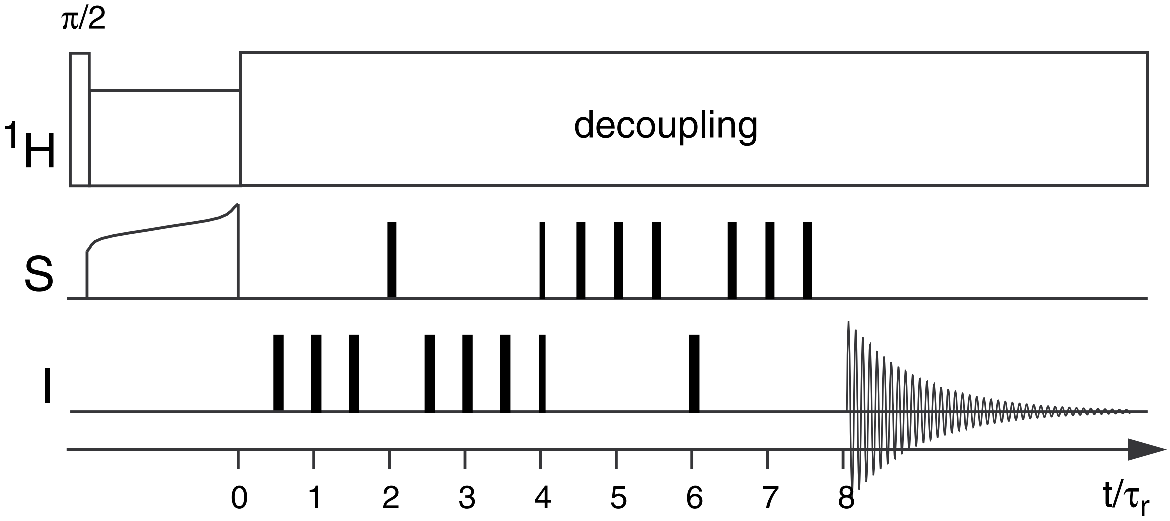

Figure 4.20: Pulse Sequence for the TEDOR Experiment
The TEDOR experiment is based on the INEPT polarization-transfer principle but uses the dipolar coupling which is reintroduced by two REDOR sequences instead of the isotropic J coupling.

4.3.2.3 Examples

An experimental example of a REDOR curve measured on a model substance is shown in Figure 4.22. The REDOR curve was measured on 5% labelled 1-^{13}C-^{15}N-glycine by two different detection methods. The data show the typical features of the theoretical REDOR curve as it has been shown in Figure 4.19. This curve could be used to fit the experimental data and obtain the distance between the two atoms. In this example the error bars are quite small due to the good signal-to-noise ratio one can achieve in measurements on such small molecules.

The following two paragraphs are copied with modifications from: John J. Balbach, Jun Yang, David P. Weliky, Peter J. Steinbach, Vitali Tugarinov, Jacob Anglister, and Robert Tycko "Probing hydrogen bonds in the antibody-bound HIV-1

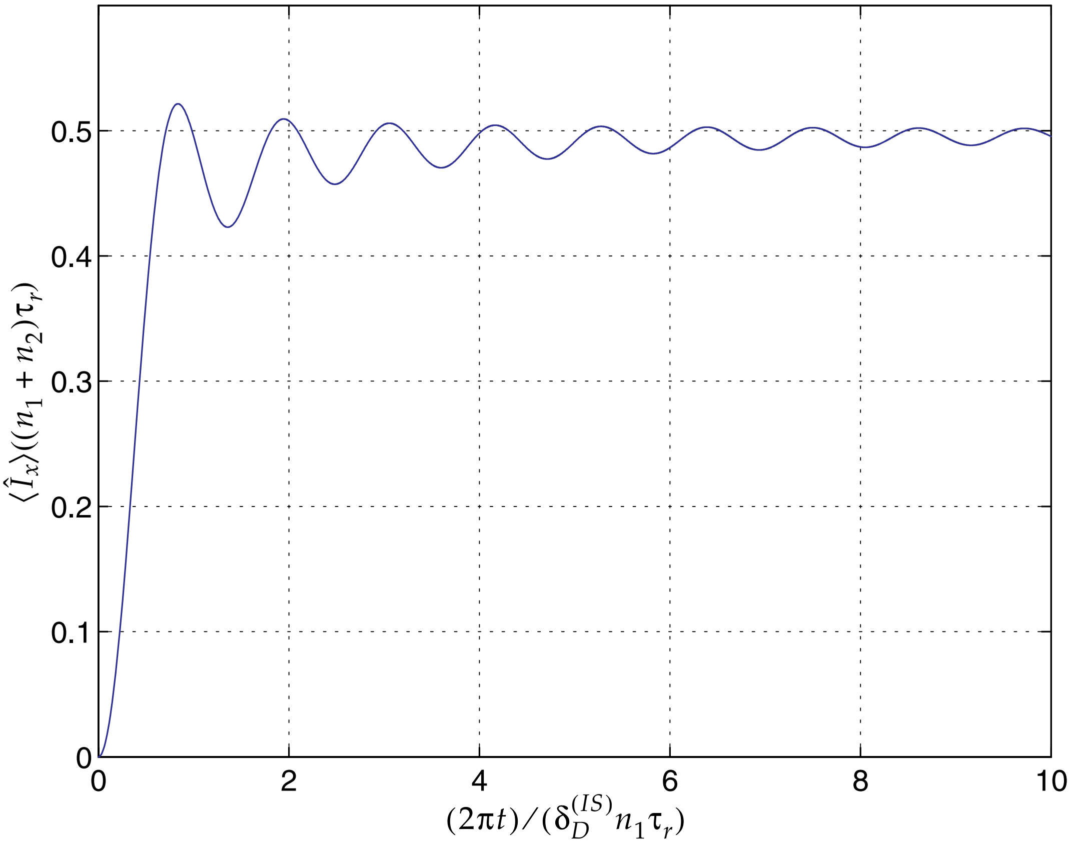

Figure 4.21: Polarization-Transfer Efficiency in the TEDOR Experiment
Plot of the transferred polarization in a TEDOR experiment with $n_1 = n_2$ as a function of the recoupling time $n_1\tau_r$. The maximum polarization transfer to the I spin is about 52% of the initial S-spin polarization.

gp120 V3 loop by solid state NMR REDOR measurements", Journal of Biomolecular NMR **16**, 313-327 (2000).

"In the second example, a 17 amino-acid residue peptide, MB(i+4)EK with the sequence Ac-AEAAAKEAAAKEAAAKANH$_2$, with Ac and NH$_2$ representing N-terminal acetylation and C-terminal amidation. This peptide is known to have a high helix content in solution and also in frozen solution of glycerol/water below the glass-transition temperature. The peptide is labelled with ^{15}N at the amide nitrogen of Ala8 and with ^{13}C at the carbonyl carbons of Ala4 and Ala10. Assuming an a-helical conformation, the Ala8-Ala4 and Ala8-Ala10 ^{15}N-^{13}C distances should be

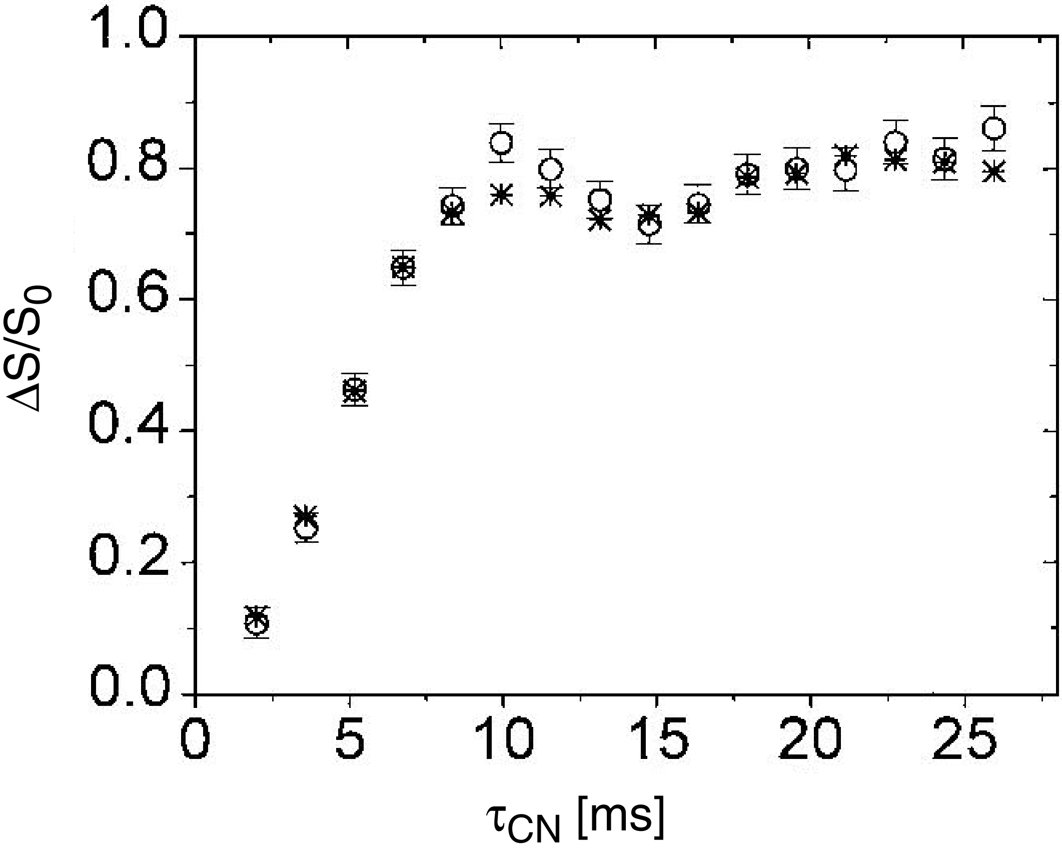

Figure 4.22: Application of REDOR to Distance Measurement in a Model Substance
^{13}C-detected ^{13}C/^{15}N REDOR data for glycine-1-^{13}C,^{15}N (5% labeled molecules). REDOR build-up curves measured with (asterisks) and without (open circles) PSL. Error bars shown for data without PSL represent uncertainty derived from the root-mean-squared noise in the experimental spectra. Corresponding uncertainty for data with PSL is about equal to the size of the symbols. Copied from: Aneta T. Petkova and Robert Tycko "Sensitivity Enhancement in Structural Measurements by Solid State NMR through Pulsed Spin Locking", Journal of Magnetic Resonance **155**, 293-299 (2002).

approximately 4.2 Å and 5.6 Å, respectively, based on examination of a-helical segments of proteins with known high-resolution structures.

Figure 4.23 a and b shows ^{13}C-detected REDOR S (a) and S_0 (b) spectra of the frozen ^{15}N,^{13}C$_2$-MB(i+4)EK solution with a 38.8 ms REDOR dephasing period. The carbonyl signal intensity in the S spectrum is clearly less than in the S_0 spectrum, demonstrating the REDOR dephasing effect. Figure 4.23 c shows the dependence of

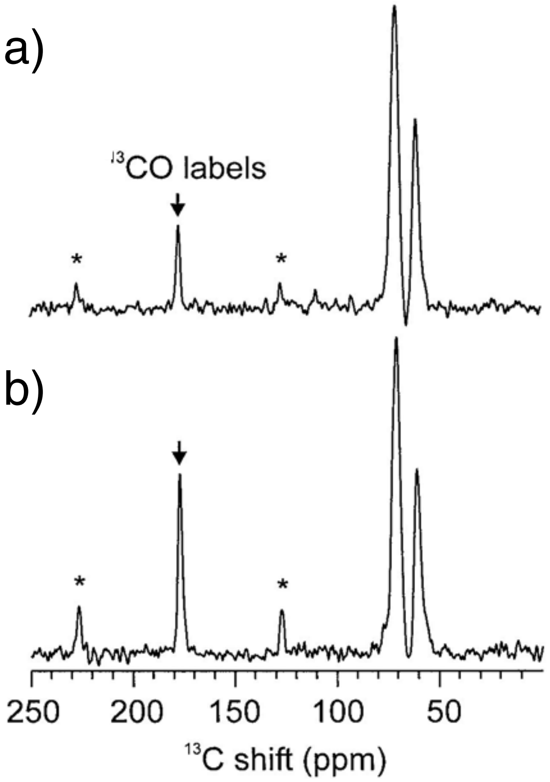

^{13}C NMR spectra of the triply labeled MB(i+4)EK sample obtained with a REDOR pulse sequence, both with (a) and without (b) the application of ^{15}N pulses. The period for REDOR dephasing is 38.8 ms. Each spectrum results from 3600 scans. The difference in intensity of the carbonyl signal at 177 ppm is due to ^{13}C-^{15}N dephasing when the ^{15}N pulses are applied. Asterisks indicate spinning sidebands.

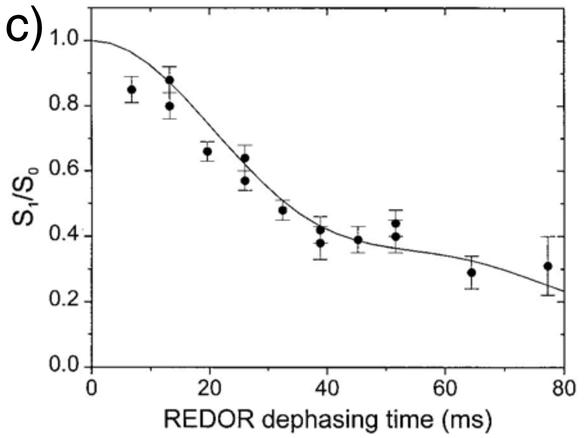

c) REDOR dephasing curve for the triply labeled MB(i+4)EK sample. The ordinate represents the ratio of carbonyl signal intensities with (S_1) and without (S_0) the application of ^{15}N pulses. Filled circles are experimental data points. The solid line is a simulated dephasing curve, assuming that 40% of the carbonyl ^{13}C nuclei are dephased by dipole-dipole coupling to ^{15}N with an internuclear distance of 4.2 Å, 40% are dephased by coupling to ^{15}N with an internuclear distance of 5.6 Å, and 20% are not coupled to ^{15}N.

Figure 4.23: Application of REDOR to Distance Measurements in Proteins
Copied from: John J. Balbach, Jun Yang, David P. Weliky, Peter J. Steinbach, Vitali Tugarinov, Jacob Anglister, and Robert Tycko "Probing hydrogen bonds in the antibody-bound HIV-1 gp120 V3 loop by solid state NMR REDOR measurements", Journal of Biomolecular NMR, **16**: 313-327, 2000.

S/S_0, measured by integrating the carbonyl ^{13}C signal intensities in spectra such as in Figure 4.23 a and b over the range from 172 ppm to 182 ppm, on the dephasing period. The simulated dephasing curve in Figure 4.23 c was calculated with the assumption that 40% of the carbonyl ^{13}C nuclei are coupled to a ^{15}N nucleus at a 4.2 Å distance, 40% are coupled to a ^{15}N nucleus at a 5.6 Å distance, and 20% are not coupled to ^{15}N nuclei. The uncoupled ^{13}C nuclei probably include natural-abundance carbonyl 13C nuclei that are more than 6 Å away from the ^{15}N label at Ala8 in helical MB(iC4)EK molecules and ^{13}C labels in MB(i+4)EK molecules that are non-helical, in roughly equal numbers. The good agreement between the simulated REDOR dephasing curve and the experimental data supports the predominance of the α-helical conformation in frozen solutions of MB(i+4)EK and establishes our ability to detect ^{15}N-^{13}C dipole-dipole couplings in the range that is relevant to the RP135/0.5β Fab measurements described above."

4.4 Recoupling Sequences With CW RF Irradiation

Using cw rf irradiation we can introduce interference effects between the rf-nutation frequency of the spins and the MAS frequency of the sample rotation. One such effect we have already seen in Chapter 7.2 in the description of cross polarization under MAS. There we have seen that we had to adjust the difference of the two nutation frequencies such that they equal one or two times the spinning frequency, i.e., $|\omega_{1S} - \omega_{1I}| = m \cdot \omega_r$, in order to obtain a time-independent part of the dipolar coupling.

Similar effects can also be observed in homonuclear cw rf irradiation. We observe recoupling effects for several conditions which are illustrated by the experimental cw decoupling line intensity in Figure 4.24: (i) For $\omega_1 = \omega_r/2$ we find a recoupling of the homonuclear dipolar coupling. This condition is called homonuclear rotary resonance (HORROR). The line intensity of the decoupled line is increased due to the enhanced "self decoupling" (see Chapter 8.1.2) (ii) For $\omega_1 = \omega_r$ we find a recoupling of the CSA tensor, the heteronuclear dipolar coupling and the homonuclear dipolar coupling. (iii) For $\omega_1 = 2\omega_r$ we find a recoupling of the CSA tensor and the heteronuclear dipolar coupling. The last two conditions are called rotary resonance (R^3). Note, that rotary resonance (R^3) and rotational resonance (R^2) are very different phenomena and should not be mixed up. They are manifest in the line intensity under cw decoupling as very low intensities due to the reintroduction of the heteronuclear dipolar coupling. (iv) There are also higher-order rotary-resonance conditions ($\omega_1 = 3\omega_r$ and $\omega_1 = 4\omega_r$) but they are much weaker and more difficult to observe. (v) There is also a fractional rotary-resonance condition at $\omega_1 = \omega_r/3$ which is also quite weak and can only be observed at fast MAS. There are currently no applications for this recoupling condition.

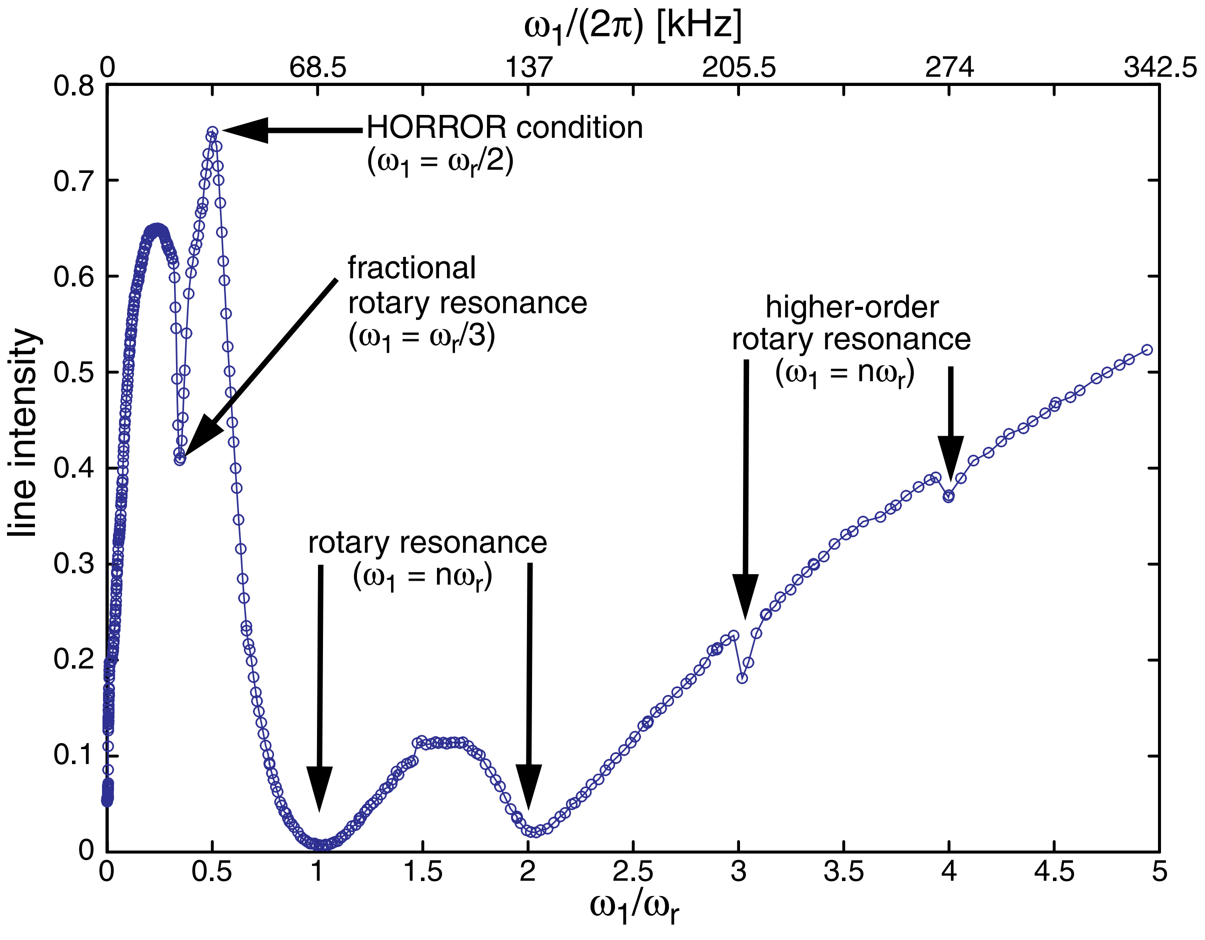

Figure 4.24: Recoupling Conditions Under CW RF Irradiation
Line intensity of the α-carbon resonance in 2-^{13}C glycine under cw rf irradiation as a function of the rf-field amplitude. The MAS frequency was 68.5 kHz. One can clearly see the strong rotary-resonance conditions as intensity minima because the heteronuclear dipolar coupling is reintroduced. The higher-order rotary-resonance conditions are much weaker. At the HORROR condition the line intensity is increased due to the "self decoupling" (see Chapter 8.1.2).

We have seen in the description of cw decoupling (Chpater 8.1.2) that such a Hamiltonian with two time dependencies can be analyzed using Floquet theory. The Fourier coefficients of the interaction-frame Hamiltonian for an I_NS spin system under cw irradiation of the I spins was given by Eq. [8.3] as

$$\begin{aligned}
\tilde{\hat{\mathcal{H}}}^{(0,0)} &= \omega_S^{(0)} S_z + \sum_{\ell < m} \omega_{I_\ell I_m}^{(0)} (\vec{I_\ell} \cdot \vec{I_m}) \\
\tilde{\hat{\mathcal{H}}}^{(n,0)} &= \omega_S^{(n)} S_z - \omega_{I_\ell I_m}^{(n)} \left[I_{\ell z} I_{mz} - \frac{1}{2}(I_{\ell x} I_{mx} + I_{\ell y} I_{my}) \right] \\
\tilde{\hat{\mathcal{H}}}^{(0,\pm 1)} &= -\sum_{\ell} \frac{\omega_{I_\ell}^{(0)}}{2} I_\ell^{\pm} - \sum_{\ell} \omega_{SI_\ell}^{(0)} S_z I_\ell^{\pm} \\
\tilde{\hat{\mathcal{H}}}^{(n,\pm 1)} &= -\sum_{\ell} \frac{\omega_{I_\ell}^{(n)}}{2} I_\ell^{\pm} - \sum_{\ell} \omega_{SI_\ell}^{(n)} S_z I_\ell^{\pm} \\
\tilde{\hat{\mathcal{H}}}^{(n,\pm 2)} &= \sum_{\ell < m} \frac{3}{4} \omega_{I_\ell I_m}^{(n)} I_\ell^{\pm} I_m^{\pm}
\end{aligned} \quad . \qquad [4.46]$$

We can use the effective Hamiltonians obtained from the Floquet description also to characterize the resonance conditions. For a resonance condition which is characterized by $n_0\omega_r + k_0\omega_1 = 0$, the effective Hamiltonian is given by

$$\hat{\bar{\mathcal{H}}} = \hat{\mathcal{H}}^{(0,0)} + \hat{\mathcal{H}}^{(n_0,k_0)} + \hat{\mathcal{H}}^{(-n_0,-k_0)} + \ldots \quad . \qquad [4.47]$$

4.4.1 HORROR and DREAM

4.4.1.1 Introduction

In the homonuclear rotary-resonance experiment (HORROR) the rf-field amplitude is adjusted such that the condition

$$\frac{1}{2}\omega_r = \omega_1 \qquad [4.48]$$

is fulfilled. Under this condition the homonuclear dipolar coupling is not averaged out and one observes polarization transfer between dipolar coupled spins. Due to the resonance condition, the rf-field amplitude in the HORROR experiment is quite low.

This leads, on one hand, to a high sensitivity of the experiment to resonance offsets but allows on the other hand very efficient decoupling of the protons. The DREAM (dipolar recoupling enhanced by amplitude modulation) experiment is an adiabatic version of the HORROR experiment where we sweep through the HORROR condition. In this implementation, the very narrow matching condition as well as the sensitivity of the HORROR experiment to resonance offsets is significantly reduced.

As a polarization-transfer method, the HORROR or DREAM experiment is usually employed as the mixing step in a two-dimensional experiment as shown in Figure 4.25. After the initial cross polarization, the magnetization is frequency labelled during t_1. The polarization transfer during τ_m happens under the HORROR condition or a DREAM sweep (dotted line) and the signal is the detected during t_2. This leads to a two-dimensional homonuclear chemical-shift correlation spectrum where we observe cross peaks if two spins are dipolar coupled. The HORROR and DREAM experiment can also be used as a double-quantum filter in solid-state NMR under MAS. Especially the DREAM experiment shows a very high efficiency due to the adiabatic nature of the experiment.

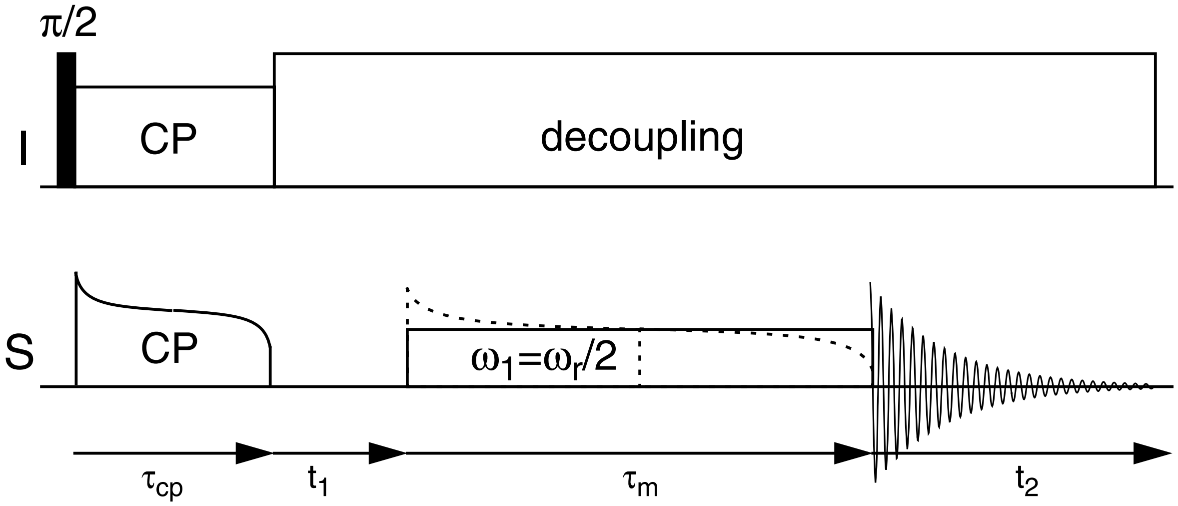

Figure 4.25: Pulse Sequence for the HORROR and DREAM Experiment
After an initial cross-polarization period, the magnetization is frequency labelled during t_1. The polarization transfer during τ_m happens under the HORROR condition or a DREAM sweep (dotted line) and the signal is then detected during t_2. This leads to a two-dimensional homonuclear chemical-shift correlation spectrum where we observe cross peaks if two spins are dipolar coupled.

4.4.1.2 Theoretical Description

The resonance condition in terms of the Floquet formalism are given by $n_0\omega_\mathrm{r} + k_0\omega_1 = 0$ where (n_0, k_0) equals $(1, -2)$ and the effective Hamiltonian is given by

$$\begin{aligned}\hat{\bar{\mathcal{H}}} &= \hat{\mathcal{H}}^{(0,0)} + \hat{\mathcal{H}}^{(1,-2)} + \hat{\mathcal{H}}^{(-1,2)} \\ &\approx \omega_S^{(0)} S_z + \sum_{\ell < m} \omega_{I_\ell I_m}^{(0)} (\vec{I_\ell} \cdot \vec{I_m}) + \frac{3}{4} \sum_{\ell < m} (\omega_{I_\ell I_m}^{(-1)} I_\ell^+ I_m^+ + \omega_{I_\ell I_m}^{(+1)} I_\ell^- I_m^-) \end{aligned} \quad . \qquad [4.49]$$

To illustrate the similarity of the DREAM experiment with the rotational-resonance experiment, we will also discuss the DREAM experiment in terms of average Hamiltonians in the double-quantum and zero-quantum subspaces. The Hamiltonian for a homonuclear dipolar coupled two-spin system under the HORROR condition in the tilted frame of reference (rf along the z axis) is given by

$$\hat{\mathcal{H}}(t) = \omega_1 (\hat{S}_{1z} + \hat{S}_{2z}) + \omega_{SS}^{(1,2)}(t)\left(3\hat{S}_{1x}\hat{S}_{2x} - \vec{\hat{S}_1} \cdot \vec{\hat{S}_2}\right) \qquad [4.50]$$

if we assume that the rf field amplitude is much larger than the chemical shifts. We can again split up the Hamiltonian into two commuting subspaces, the zero-quantum and the double-quantum Hamiltonian

$$\hat{\mathcal{H}}(t) = \hat{\mathcal{H}}^{\Sigma}(t) + \hat{\mathcal{H}}^{\Delta}(t) \qquad [4.51]$$

with

$$\begin{aligned}\hat{\mathcal{H}}^{\Sigma}(t) &= 2\omega_1 \hat{S}_z^{\Sigma} - \frac{1}{4}\omega_{SS}^{(1,2}(t)\hat{1}^{\Sigma} - \frac{3}{2}\omega_{SS}^{(1,2}(t)\hat{S}_x^{\Sigma} \\ \hat{\mathcal{H}}^{\Delta}(t) &= \frac{1}{4}\omega_{SS}^{(1,2)}(t)\hat{1}^{\Delta} + \frac{1}{4}\omega_{SS}^{(1,2)}(t)\hat{S}_x^{\Delta}\end{aligned} \quad . \qquad [4.52]$$

The initial density operator is given by $\hat{\rho}_0 = \hat{S}_{1z} + \hat{S}_{2z}$ which gives in the two sub spaces

$$\begin{aligned}\hat{\rho}_0^{\Sigma} &= 2\hat{S}_z^{\Sigma} \\ \hat{\rho}_0^{\Delta} &= 0\end{aligned} \quad . \qquad [4.53]$$

The transformation into the interaction-frame representation with

$$\hat{\mathcal{H}}_1 = \omega_1(\hat{S}_{1z} + \hat{S}_{2z}) = 2\omega_1 \hat{S}_z^{\Sigma} \qquad [4.54]$$

leads to a time-dependent double-quantum Hamiltonian in the interaction frame of the form

$$\hat{\mathcal{H}}'^{\Sigma}(t) = -\frac{3}{2}\omega_{SS}^{(1,2)}(t)[\hat{S}_x^{\Sigma}\cos(2\omega_1 t) + \hat{S}_y^{\Sigma}\sin(2\omega_1 t)] \qquad [4.55]$$

where we have again neglected the terms proportional to the identity operator. We expand again the time-dependent dipolar coupling in the Fourier series and obtain in full analogy to the treatment of rotational resonance in Chapter 4.2.2.2 a non-vanishing zeroth-order average Hamiltonian for $\omega_1 = \omega_r/2$ of

$$\hat{\bar{\mathcal{H}}}^{(0)} = \frac{-3}{8\sqrt{2}}\sin(2\beta^{(1,2)})\delta_D^{(1,2)}\hat{S}_x^{\Sigma} . \qquad [4.56]$$

Except for a different scaling of the effective Hamiltonian and the fact that we consider now the double-quantum sub space of the Hamiltonian instead of the zero-quantum subspace, we obtain the same zeroth-order average Hamiltonian as in rotational-resonance recoupling. Figure 4.26 shows a simulated polarization-transfer curve where the initial density operator is $\hat{\rho}_0 = \hat{S}_{1z}$ and the expectation value of $\hat{S}_{2z}$ is plotted as a function of the mixing time. One can clearly see that the transferred polarization has a negative sign which is due to the double-quantum nature of the HORROR recoupling condition. This can be seen if we write the density operator as the sum of the zero-quantum and double-quantum sub space

$$\hat{\rho}_0 = \hat{S}_{1z} = \hat{S}_z^{\Delta} + \hat{S}_z^{\Sigma} \qquad [4.57]$$

and

$$\begin{aligned}\hat{\rho}(\tau_m) &= \hat{S}_z^{\Delta} + \hat{S}_z^{\Sigma}\cos(\omega_{\mathrm{eff}}t) - \hat{S}_y^{\Sigma}\sin(\omega_{\mathrm{eff}}t) \\ &= \hat{S}_{1z}(1 + \cos(\omega_{\mathrm{eff}}t)) - \hat{S}_{2z}(1 - \cos(\omega_{\mathrm{eff}}t)) + \text{DQ terms}\end{aligned} \qquad [4.58]$$

where

$$\omega_{\text{eff}} = \frac{-3}{8\sqrt{2}}\sin(2\beta^{(1,2)})\delta_D^{(1,2)} \qquad [4.59]$$

is the effective angle-dependent nutation frequency of the double-quantum subspace under the HORROR condition.

If the chemical-shift offsets cannot be neglected, we have to describe the HORROR experiment in a tilted frame where the z direction is along the effective field direction. The Hamiltonian in this case is given by

$$\hat{\mathcal{H}}(t) = \omega_{\text{iso}}^{(1)}\hat{S}_{1z} + \omega_{\text{iso}}^{(2)}\hat{S}_{2z} + \omega_1(\hat{S}_{1x} + \hat{S}_{2x}) + \omega_{SS}^{(1,2)}(t)\left(3\hat{S}_{1z}\hat{S}_{2z} - \vec{\hat{S}}_1 \cdot \vec{\hat{S}}_2\right) \qquad [4.60]$$

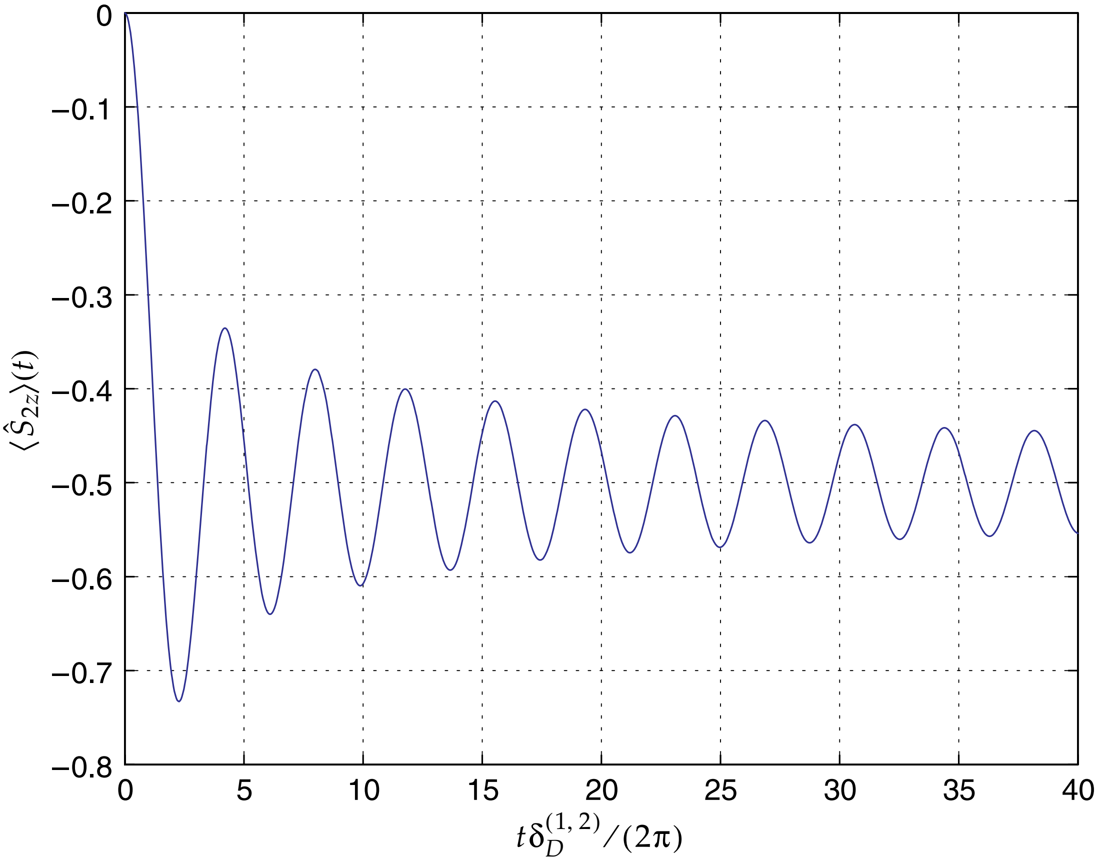

Figure 4.26: Polarization Transfer Under the HORROR Condition
Time dependence of the polarization transfer from $\hat{S}_{1z}$ to $\hat{S}_{2z}$ under the HORROR condition. Due to the double-quantum nature of the polarization transfer, the transferred polarization appears with negative intensity. The maximum polarization transfer is 73% as one expects for a γ-encoded pulse sequence.

which is the same Hamiltonian as in the case of the rotational-resonance tickling experiment. We again transform the Hamiltonian into the tilted frame by a rotation of each spin about $\hat{S}_{ky}$ with an angle $\theta_k = \arctan(\omega_1/\omega_{\text{iso}}^{(k)})$. The effective fields are then given by $\omega_{\text{eff}}^{(k)} = \sqrt{(\omega_{\text{iso}}^{(k)})^2 + \omega_1^2}$. We now have to match the sum of the effective fields by the MAS frequency and we assume that the carrier frequency is in the center between the two chemical shifts. This behavior is illustrated in Figure 4.11a which shows the effective fields. In the case of the HORROR recoupling we assume that the rf fields are larger than the chemical-shift offsets. The Hamiltonian in the tilted frame is the same as given by Eq. [4.20] and the corresponding matching conditions is defined by

$$\omega_r = \omega_{\text{eff}}^{(1)} + \omega_{\text{eff}}^{(2)} . \qquad [4.61]$$

The HORROR condition is a double-quantum recoupling condition while the rotational-resonance condition is a zero-quantum recoupling condition. In the tilted frame, however, we see a continuos transition between the two recoupling conditions. This illustrates that in the tilted frame we obtain a partial recoupling in both subspaces of the Hamiltonian.

The HORROR experiment can easily be implemented as an adiabatic experiment which has been called DREAM. The effective slowly time-dependent Hamiltonian in the interaction-frame representation is given by

$$\hat{\bar{\mathcal{H}}}^{(0)} = (2\omega_1(T) - \omega_r)\hat{S}_z^{\Sigma} - \frac{3}{8\sqrt{2}}\sin(2\beta^{(1,2)})\delta_D^{(1,2)}\hat{S}_x^{\Sigma} \qquad [4.62]$$

where the rf-field amplitude is changed such that we sweep through the HORROR condition. If one prepares an initial density operator which is proportional to $\hat{S}_z^{\Sigma}$ one obtains after an adiabatic passage through the HORROR condition a final density operator which is given by $-\hat{S}_z^{\Sigma}$. This corresponds to a full polarization transfer from $\hat{S}_{1z}$ to $-\hat{S}_{2z}$. Since the polarization transfer is not oscillatory with the effective angle-dependent dipolar coupling frequency one can, in principle, reach polarization-transfer efficiencies of 100% in a powder sample. In addition to the higher efficiency, the sensitivity to the precise setting of the matching condition is significantly reduced compared to the standard HORROR experiment.

4.4.1.3 Examples

Figure 4.27 shows a two-dimensional chemical-shift correlation spectrum of U-^{13}C-tyrosine at a spinning frequency of ω_r = 26 kHz using the pulse sequence of Figure 4.25 with an adiabatic DREAM sweep through the HORROR condition. The

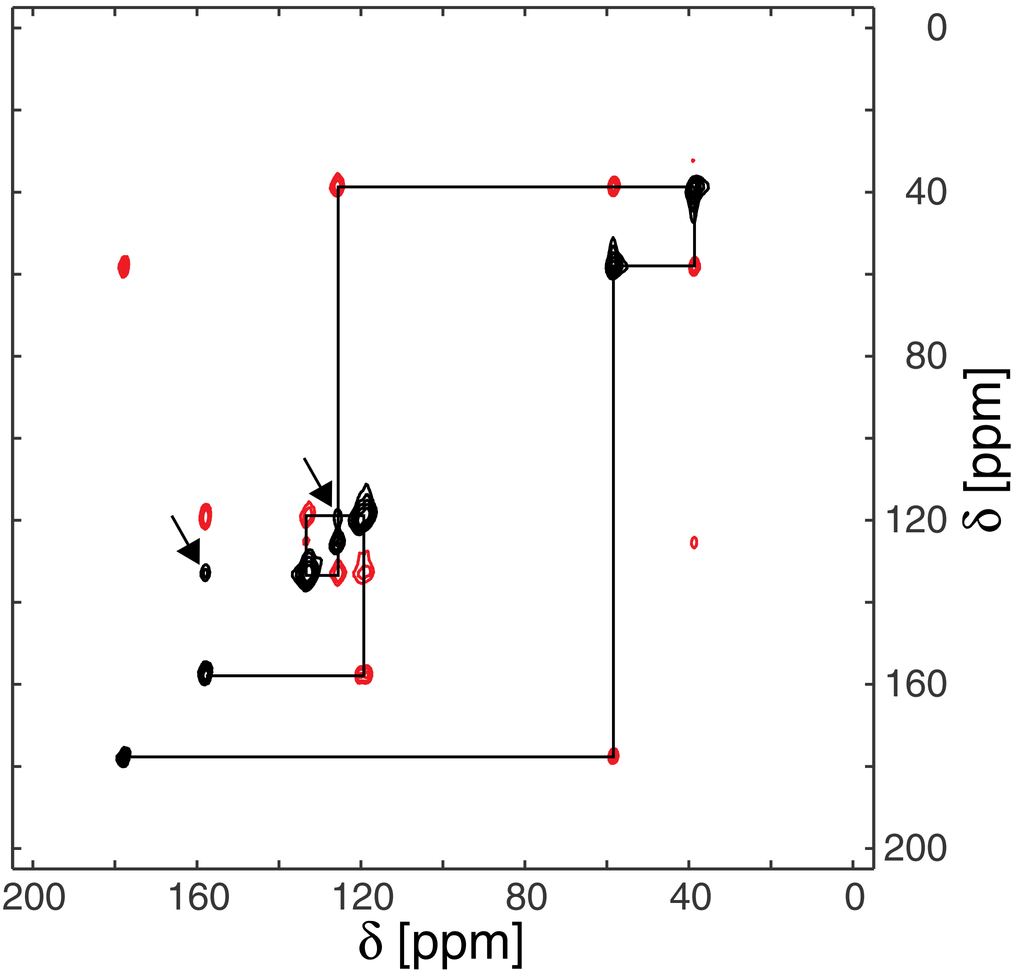

Figure 4.27: Two-Dimensional Chemical-Shift Correlation Spectrum Using DREAM
Two-dimensional chemical-shift correlation spectrum of U-^{13}C-tyrosine using the pulse sequence of Figure 4.25. The total duration of the sweep was set to 0.5 ms leading to a non adiabatic behavior. The amplitude of the sweep at the center point was chosen to be $\bar{\omega}_1 =$ 11.5 kHz. The lines indicate the directly bonded carbon atoms while the arrows indicated cross peaks in phase with the signals on the diagonal due to multi-step transfers.

spectrum shows the characteristic sign change of double-quantum polarization transfer of the cross peaks with respect to the diagonal peaks. All negative cross peaks indicate correlations between directly bond carbon atoms while positive cross peaks indicate multi-step or relay polarization transfer where the polarization is transferred via an intermediate spin. This shows that multi-step transfer through one-bond dipolar couplings can be faster than the direct transfer through a long-range dipolar coupling. Some of the big advantages of the DREAM method compared to other broadband homonuclear polarization-transfer schemes is its low rf-field requirement and the fact that the method performs better at higher MAS spinning frequencies.

One can also use the DREAM sweep as an efficient spin-pair filter under MAS as is shown in Figure 4.28. This is an important application to suppress natural-abundance background signals in a partially labelled compound and high efficiencies as well as good suppression of the isolated spins is important. The sample consisted of a mixture of 1-$^{13}C_1$-alanine, natural-abundance methionine and natural-abundance

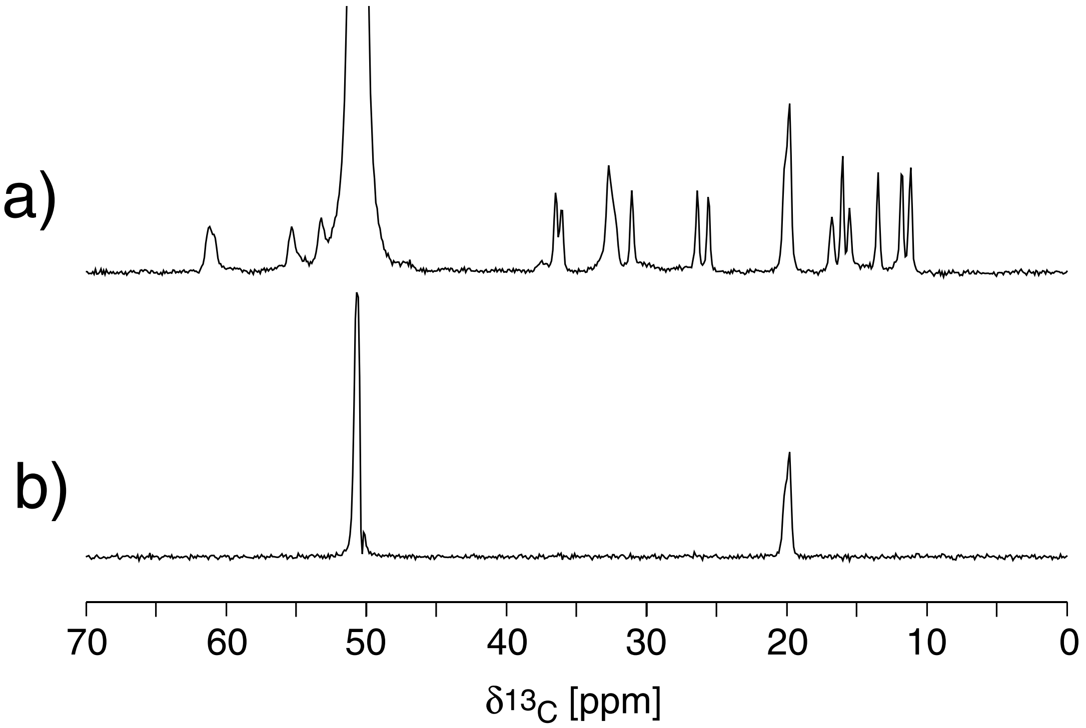

Figure 4.28: Spin-Pair Filter Under MAS Using the DREAM Sequence
(a) Cross polarization and (b) DREAM SPS spectra of a mixture of 1-$^{13}C_1$-alanine, natural-abundance methionine and natural-abundance iso-leucine. The three substances were mixed in approximately equal weight parts and the sample restricted to the central region of the rotor with a total length of about 3 mm. The efficiency of the spin-pair filter is about 61%.

iso-leucine. The three substances were mixed in approximately equal weight parts. The suppression of the isolated spins is better than 99% and the efficiency of the spin-pair filter is about 61%. Under fully optimized conditions in test substances, filter efficiencies of better than 80% have been reached. The pulse sequence used to implement the DREAM spin-pair selection is shown in Figure 4.29. It is not based on a double-quantum but on the inversion properties of coupled and uncoupled spin-pairs under the DREAM sweep as illustrated in more detail in Figure 4.30. By adding or subtracting the appropriate scans one can either select the coupled spin pairs or the uncoupled, isolated spins.

4.4.2 Rotary-Resonance Recoupling (R^3)

4.4.2.1 Introduction

As we have seen in Figure 4.24 there are also recoupling conditions where the rf-field amplitude is matched to an integer multiple of the spinning frequency. The condition

$$n\omega_r = \omega_1 \qquad [4.63]$$

for n = 1,2 is called the rotary-resonance condition. At the n = 1 rotary resonance condition, the chemical-shift tensor, the heteronuclear dipolar coupling, and the homonuclear dipolar coupling are all partially recoupled. At the n = 2 rotary resonance condition, only the chemical-shift tensor and the heteronuclear dipolar coupling are partially recoupled. Higher-order rotary-resonance conditions are possible if several interactions are present at the same time but they are significantly weaker than the n = 1,2 rotary-resonance condition as can be seen in Figure 4.24 which shows only a weak decrease in the line intensity for the n = 3,4 rotary-resonance condition. The rotary-resonance recoupling experiment is mainly used to measure tensor values under MAS (Figure 4.31) and not so often for polarization transfer experiments.

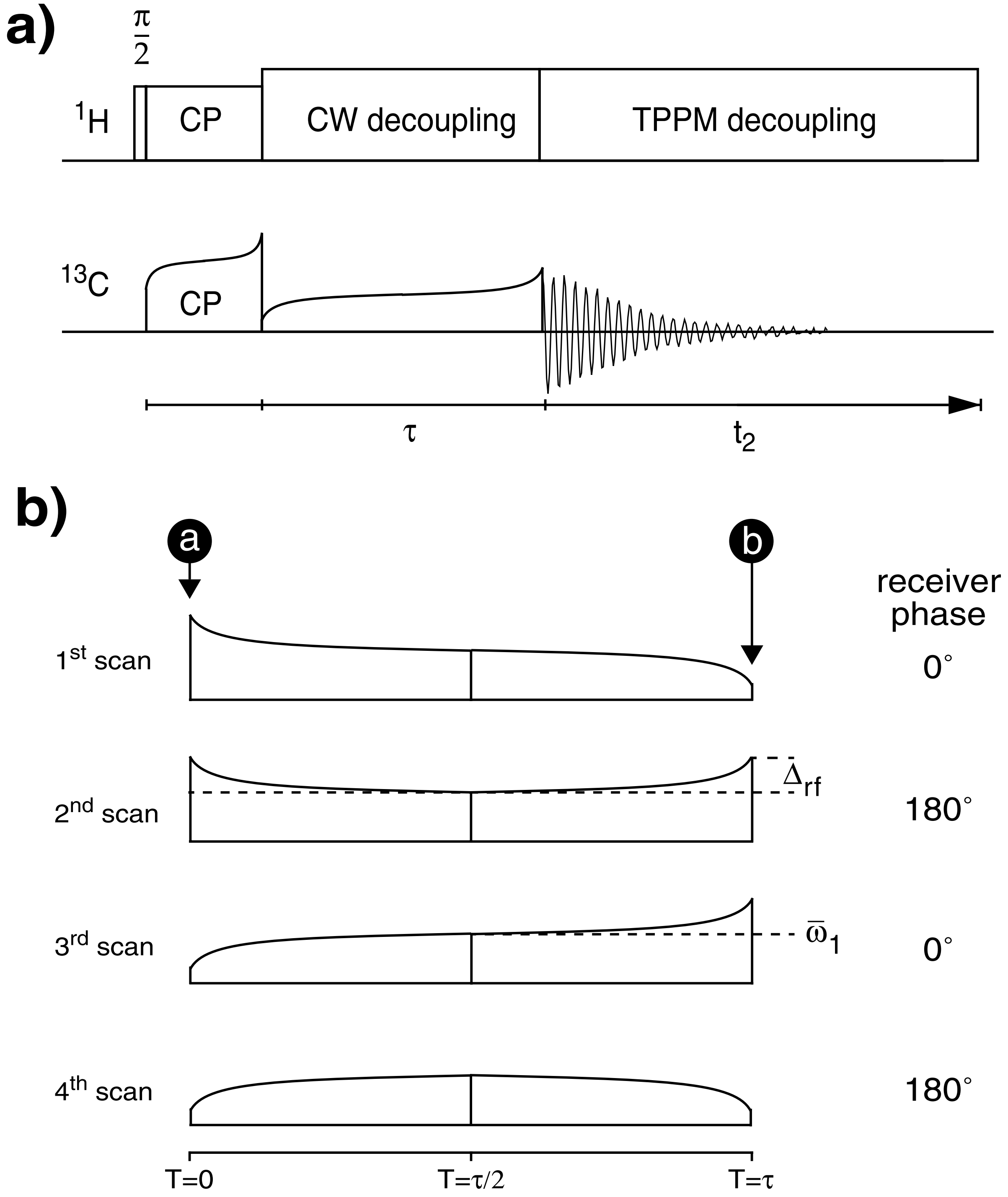

Figure 4.29: Pulse-Sequence for the DREAM Spin-Pair Filter
(a) Pulse sequence for the DREAM spin-pair selective experiments. (b) Four different amplitude shapes which can be used in the spin-pair filter experiment and appropriate modification of the receiver phase. The up-down and the down-up scan lead to an inversion of the dipolar coupled spins while isolated spins stay unchanged. The up-up and down-down scans leave all spins unchanged. Subtraction of the two type of experiments leads to a suppression of the isolated spins. This principle is illustrated in more detail in Figure 4.30

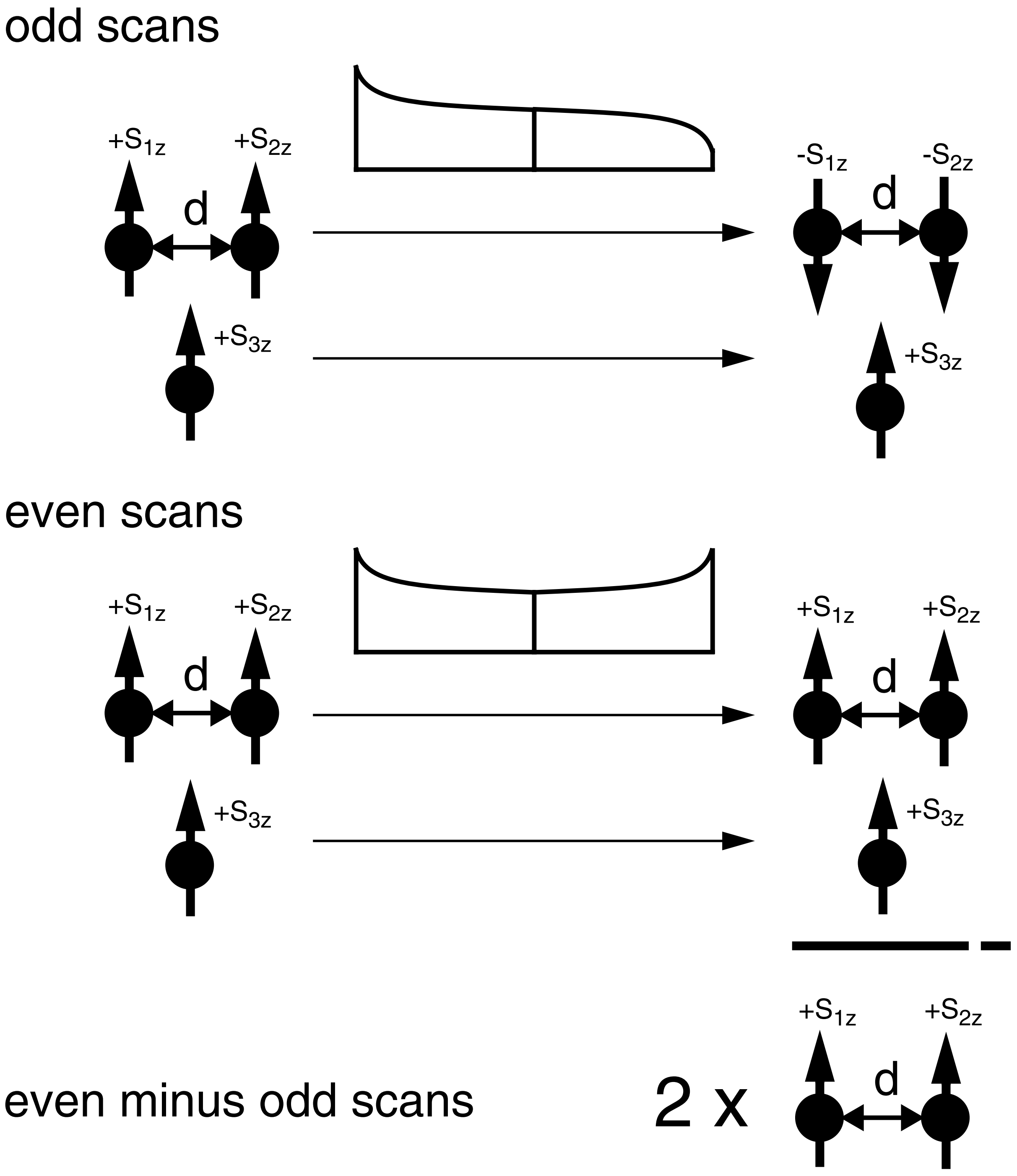

Figure 4.30: Principle of DREAM Spin-Pair Selection
Schematic representation of a DREAM spin-pair filter. The odd scans lead to an inversion of the magnetization of coupled spin pairs while they do not change the magnetization of uncoupled spins. The even scans leave coupled and uncoupled spins invariant. The difference of the two experiments yields a spectrum that contains only signals from the coupled spins. One could also add the two scans to select the signals from the uncoupled spins only.

4.4.2.2 Theoretical Description

The resonance condition in terms of the Floquet formalism are given by $n_0\omega_r + k_0\omega_1 = 0$ where (n_0, k_0) equals $(1, -1)$ and $(2, -2)$ for the n = 1 and $(2, -1)$ for the n = 2 rotary-resonance condition. Using Eqs. [4.46] and [4.47], we can directly write down the effective Hamiltonian in the interaction frame. For the n = 1 rotary-resonance condition we obtain

$$\begin{aligned}\bar{\hat{\mathcal{H}}} &= \hat{\mathcal{H}}^{(0,\,0)} + \hat{\mathcal{H}}^{(1,\,-1)} + \hat{\mathcal{H}}^{(-1,\,1)} + \hat{\mathcal{H}}^{(2,\,-2)} + \hat{\mathcal{H}}^{(-2,\,2)} \\ &\approx \omega_S^{(0)} S_z + \sum_{\ell < m} \omega_{I_\ell I_m}^{(0)} (\vec{I_\ell} \cdot \vec{I_m}) \\ &\quad - \frac{1}{2}\sum_{\ell} (\omega_{I_\ell}^{(-1)} I_\ell^+ + \omega_{I_\ell}^{(+1)} I_\ell^-) - \sum_{\ell} (\omega_{SI_\ell}^{(-1)} S_z I_\ell^+ + \omega_{SI_\ell}^{(+1)} S_z I_\ell^-) \\ &\quad + \frac{3}{4}\sum_{\ell < m} (\omega_{I_\ell I_m}^{(-2)} I_\ell^+ I_m^+ + \omega_{I_\ell I_m}^{(+2)} I_\ell^- I_m^-)\end{aligned} \qquad [4.64]$$

while for the n = 2 condition we obtain

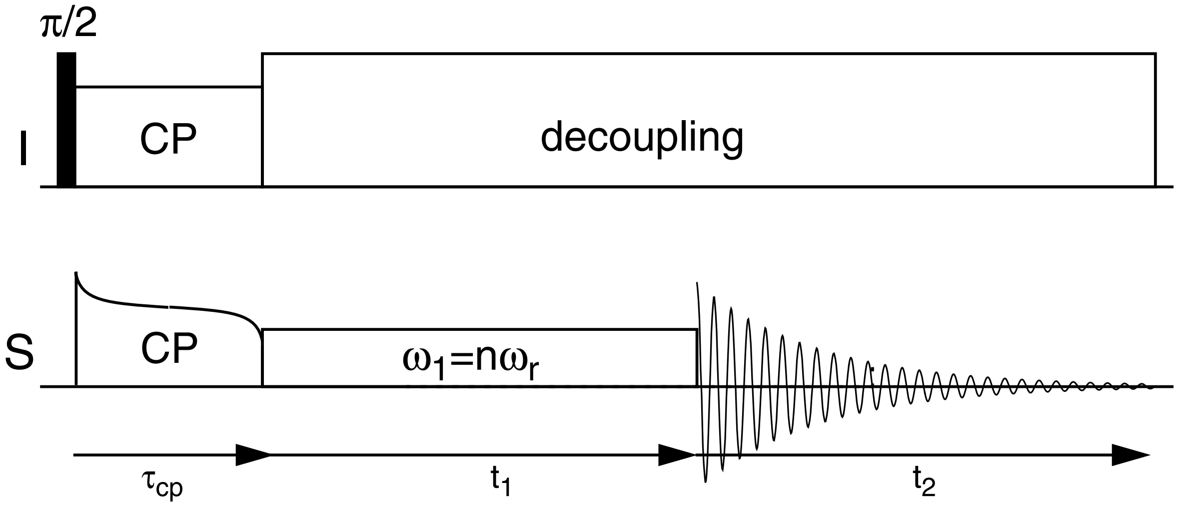

Figure 4.31: Pulse Sequence for the R^3 experiment to measure CSA tensors
After an initial cross-polarization period, the magnetization evolves during t_1 under the R^3 condition leading to a recoupling of the CSA tensor. The heteronuclear dipolar coupling is not recoupled if the decoupling power level is adjusted correctly. The signal is then detected during t_2. This leads to a two-dimensional correlation spectrum of the CSA tensor and the isotropic chemical shift.

$$
\begin{aligned}
\bar{\hat{\mathcal{H}}} &= \hat{\mathcal{H}}^{(0,0)} + \hat{\mathcal{H}}^{(1,-1)} + \hat{\mathcal{H}}^{(-1,1)} + \hat{\mathcal{H}}^{(2,-2)} + \hat{\mathcal{H}}^{(-2,2)} \\
&\approx \omega_S^{(0)} S_z + \sum_{\ell < m} \omega_{I_\ell I_m}^{(0)} (\vec{I_\ell} \cdot \vec{I_m}) \\
&\quad - \frac{1}{2} \sum_{\ell} (\omega_{I_\ell}^{(-2)} I_\ell^{+} + \omega_{I_\ell}^{(+2)} I_\ell^{-}) - \sum_{\ell} (\omega_{SI_\ell}^{(-2)} S_z I_\ell^{+} + \omega_{SI_\ell}^{(+2)} S_z I_\ell^{-}) \quad .
\end{aligned}
\qquad [4.65]
$$

The n = 1 and 2 rotary-resonance conditions recouple the chemical-shift tensor and the heteronuclear dipolar coupling. At the n = 1 condition we obtain in adiition also a recoupling of the homonuclear dipolar coupling. Higher order rotary-resonance conditions can also be calculated using the Floquet formalism.

4.4.2.3 Examples

Rotary-resonance recoupling has been used in MAS solid-state NMR to measure the CSA tensors of isolated spins by reintroducing the CSA tensor during t_1 in a two-dimensional correlation experiment. Figure 4.31 shows the basic 2D pulse sequence which can be used to measure the CSA tensor. A more advanced application is the measurement of dynamics by recording two-dimensional CSA-CSA tensor-correlation spectra under MAS (Figure 4.32). Such an experiment requires, however,

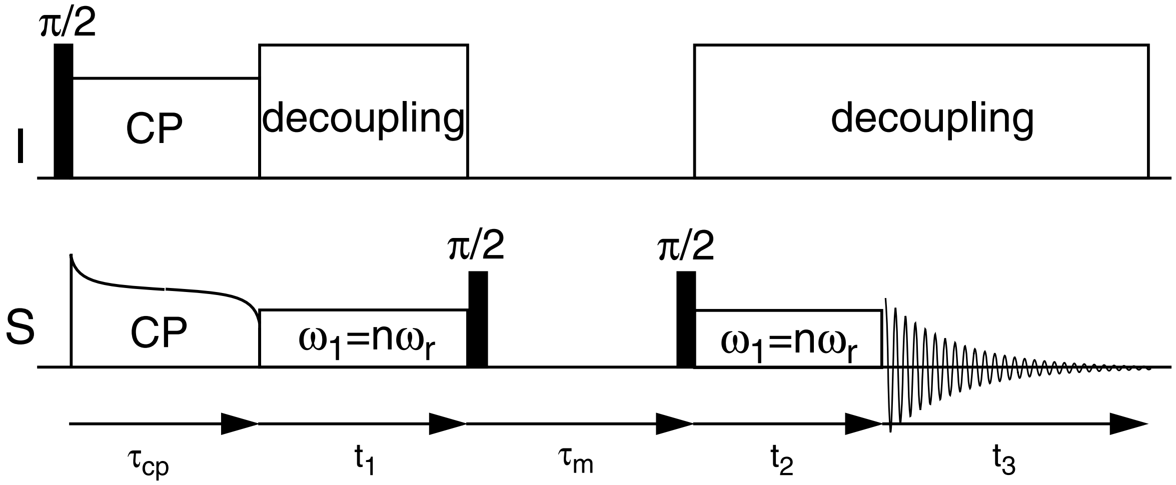

Figure 4.32: Pulse Sequence for 3D R^3 CSA tensor correlation
After an initial cross-polarization period, the magnetization evolves during t_1 under the R^3 condition leading to a recoupling of the CSA tensor. The magnetization is stored along the z direction and evolves again during t_2 under R^3 recoupling. The signal is then detected during t_3. This leads to a three-dimensional correlation spectrum of the CSA tensor with itself and the isotropic chemical shift.

the acquisition of a three-dimensional data set since the rotary-resonance recoupling for the CSA tensor correlation has to be in an indirect dimension while the direct dimension provides the resolution for the chemical-shift separation. Such a spectrum is very similar to a static 2D chemical-exchange powder correlation spectrum but in addition it provides chemical-shift resolution in the direct dimension where all the anisotropic interactions are averaged to zero.

Figure 4.33 shows an application to the chemical-exchange problem of solid tropolone. Using two-dimensional MAS exchange spectroscopy one can show that there is a pair-wise exchange between the carbon atoms 1-2, 4-6, and 3-7. The carbon atom C_5 remains unchanged for symmetry reasons (Fig. 4.33a). X-ray diffraction measurements showed sharp reflections indicating that the exchange process does not perturb the crystal symmetry. This can be explained by π flips of the molecule along with simultaneous hydrogen transfer which basically regenerates the original molecular conformation where the carbon atoms 1-2, 4-6, and 3-7 are exchanged. More detailed studies by an analysis of the side-band pattern in MAS spectra showed that there is also molecular self diffusion in the crystal between several magnetically equivalent and non-equivalent sides (Fig 4.33b). This self diffusion is accompanied by π-ring flips and hydrogen transfer in some of the cases. The CSA-tensor correlation spectra (Fig. 4.33c) for each of the sites are a superposition of all the four possible processes weighed by their probability. A fit of the tensor patterns allows the extraction of the CSA tensor from a normal two-dimensional R^3 spectrum. The 2D CSA patterns can now be fitted with the parameters of the dynamic process, i.e., the probabilities and the geometry of the four different processes. This allows a full characterization of the dynamics in tropolone which is more complicated using other techniques since they either lack the resolution (static methods) or do not provide easy access to tensor-correlation patterns (MAS methods).

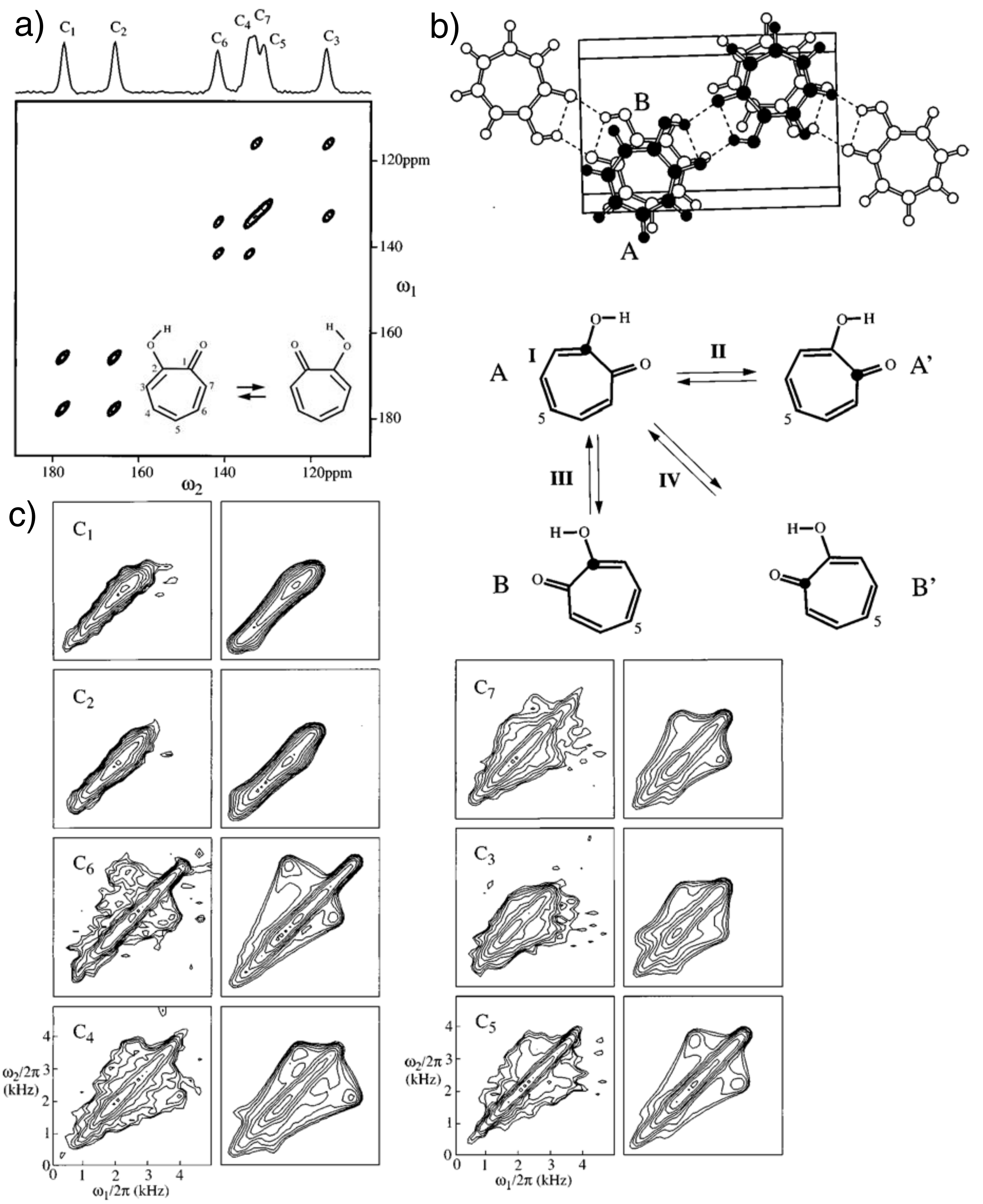

Figure 4.33: 3D R^3 Exchange Spectrum of Tropolone
a) Standard 2D MAS exchange spectrum of tropolone (τ_m = 3 s, ν_r = 8 kHz). The exchange looks like a two-site exchange between carbon atoms 1-2, 4-6, and 3-7. The exchange process, however, is more complicated as can be seen from X-ray diffraction and spinning side-band intensity analysis. The model which agrees with experimental observations is schematically shown in b). There is translational lattice diffusion between equivalent and non-equivalent sites some of which are combined with a simultaneous hydrogen transfer. c) The CSA tensor patterns allow the fit of the CSA parameters and the dynamic processes (angles and populations).

4.5 Recoupling Sequences With Continuous but Phase-Modulated Irradiation

4.5.1 C-Type and R-Type Sequences

4.5.1.1 Introduction

A few years ago, a new type of rotor-synchronized recoupling sequences was introduced. They are based on continuous rf irradiation with phase shifted pulses where an integer number of pulse elements spans an integer number of rotor cycles. The first example of such a sequence was the C7 double-quantum recoupling sequence which is shown in Figure 4.34. The sequence contains seven identical blocks each of which is phase shifted by $2\pi/7$ relative to the previous one. The basic blocks consists of two 2π pulses which are phase shifted by 180°. The seven blocks are synchronized with two rotor cycles. This leads to an rf-field requirement of

$$\omega_1 = 7\omega_r \ . \qquad [4.66]$$

The synchronization of the pulses and the MAS rotation is shown graphically in Figure 4.34. As in the case of the HORROR recoupling, this sequence generates a pure double-quantum Hamiltonian and is γ encoded since only one of the components of the dipolar Hamiltonian is retained. There were modifications of the C7 sequence suggested, like the POST-C7 sequence where the basic building block was replaced by a $(\pi/2)_\phi(2\pi)_{\phi+\pi}(3\pi/2)_\phi$ element which had better offset compensation than the original $(2\pi)_\phi(2\pi)_{\phi+\pi}$ element of the C7 sequence. The CMR-7 sequence uses a super cycle with two different basic elements and the SPC-5 sequence uses the POST element but has only five elements per two rotor cycles reducing the rf-field requirement to $\omega_1 = 5\omega_r$.

Since the introduction of these first sequences, the classification of such sequences has been systematized and there are two classes of sequences:

- CN_n^ν sequences consist of a basic rf-building block called "C" which rotates the spins through an integer multiple of a 2π rotation. This basic building block is repeated N times fit into n rotor periods with a phase shift between two C elements of $2\pi\nu/N$. One can interpret this such that the space part of the Hamiltonian is rotated n times while the spin part is rotated ν times. The rf-field requirement of such a sequence depends on the length of the basic C element. If the basic C element contains z 2π rotation, the condition $\omega_1 = zN\omega_r/n$ defines the rf-field requirement.

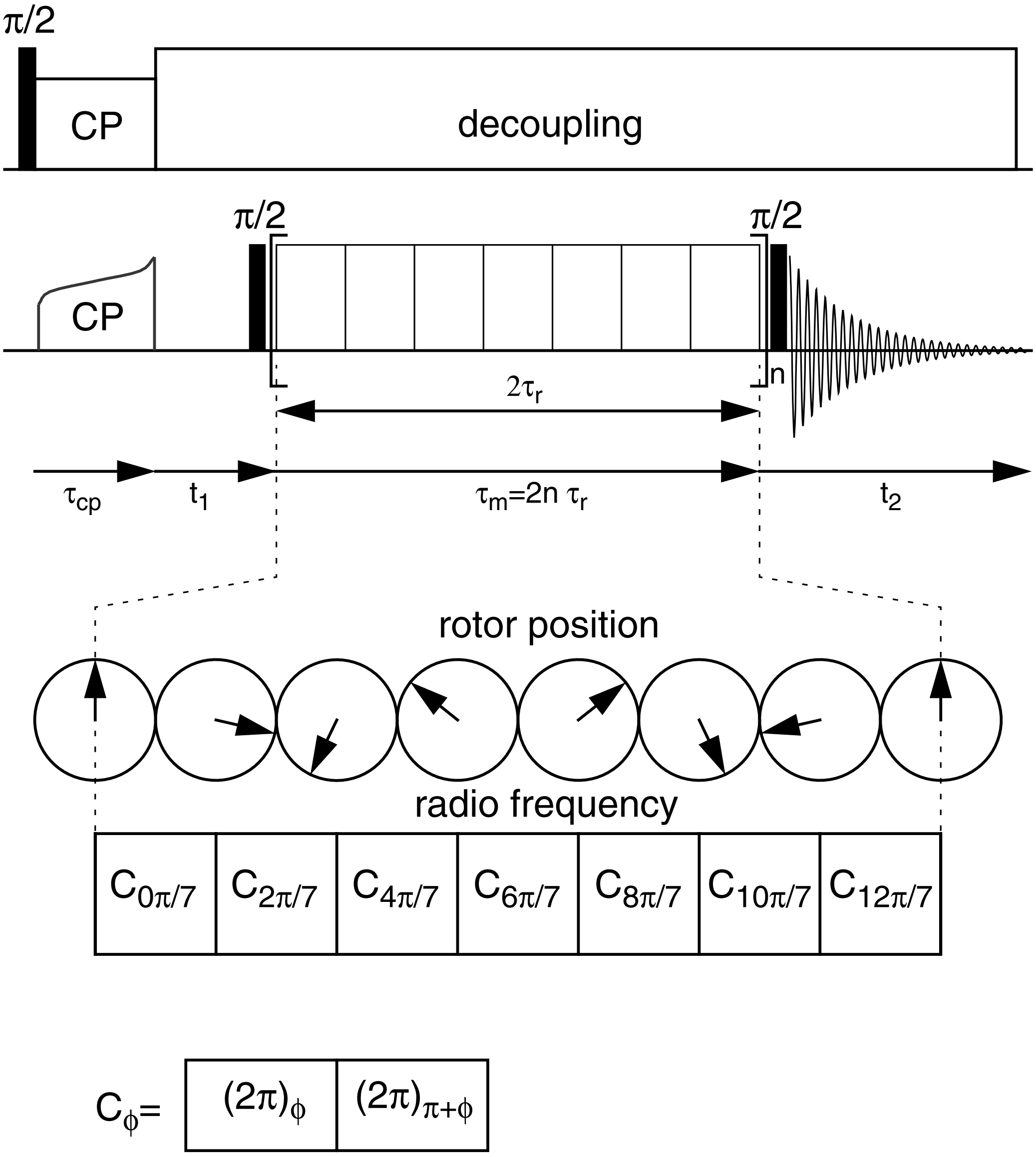

Figure 4.34: Pulse Sequence for a C7 Sequence
C7 pulse sequence for broad-band homonuclear double-quantum recoupling. The sequence consists of seven pulse elements which are phase shifted by $2\pi/7$. The whole sequence is synchronized with two rotor periods. Each pulse element consists of two 2π pulses which are phase shifted by π.

- RN_n^ν sequences consist of a basic rf-building block called "R" which rotates the spins through 180° about the x axis. The full sequence which spans n rotor cycles is built up of N/2 elements $R_\phi R_{-\phi}$ where the phase $\phi = \pi\nu/N$ describes the rotation axis of the 180° pulse R.

Such sequences can be described by rotations of the spherical tensors in spin and real space. Symmetry-based selection rules can be defined for both types of sequences which allow in a simple way to predict which spin interactions are allowed or forbidden in a C-type or R-type sequence.

4.5.1.2 Theoretical Description

We can write the time-dependent Hamiltonian under MAS as

$$\hat{\mathcal{H}}(t) = \sum_{\ell, \lambda, m, i} \hat{\mathcal{H}}^{(i)}_{\ell m, \lambda 0}(t) = \sum_{\ell, \lambda, m, i} A^{(i)}_{\ell m} d^{\ell}_{mo}(\theta_m) e^{im(\omega_r t - \gamma)} \hat{\mathcal{T}}^{(i)}_{\lambda 0} \qquad [4.67]$$

where (i) describes one of the spin interactions with a tensor rank ℓ in real space and tensor rank λ in spin space as defined in Table 2.2. The $A^{(i)}_{\ell m}$ are the spatial tensor operators of interaction (i) in the rotor-fixed coordinate system as defined by Eq. [4.15]. The general scheme and the notation used for the timing are shown in Figure 4.35 for the C-type and the R-type sequences. If we describe the spin rotations by Euler angles we find time-symmetry relations for the Euler angles β and γ of the rf propagator at time point t_q. For the C-type sequences the Euler angles during the interval q are related to the Euler angles during the interval 0 by

$$\beta_q = \beta_0 \qquad \gamma_q = \gamma_0 - q\frac{2\pi\nu}{N} \; . \qquad [4.68]$$

This can be understood by the fact that a full cycle of the C-type sequence has a propagator which is unity and only the phase of the sequence is shifted. For the R-type sequences the Euler angles during the interval q are related to the Euler angles during the interval 0 by

$$\beta_q = \beta_0 + q\pi \qquad \gamma_q = \gamma_0 - q\frac{2\pi\nu}{N} \; . \qquad [4.69]$$

This can be understood by the fact that a $\pi_\phi\pi_{-\phi}$ sequence leads to a rotation of the density operator by 4ϕ around the z axis. The symmetry relations for the space part of the Hamiltonian are defined by the rotation of the sample and are given by

$$\gamma_q = \gamma_0 - q\frac{2\pi n}{N} \ . \qquad [4.70]$$

The laboratory-frame Hamiltonian during element q can, therefore, be expressed through the symmetry relation by the Hamiltonian during the first cycle as

$$\hat{\mathcal{H}}^{(i)}_{\ell m,\lambda 0}(t_q) = \hat{\mathcal{H}}^{(i)}_{\ell m,\lambda 0}(t_0)\exp\left\{i\frac{2\pi m n}{N}q\right\} . \qquad [4.71]$$

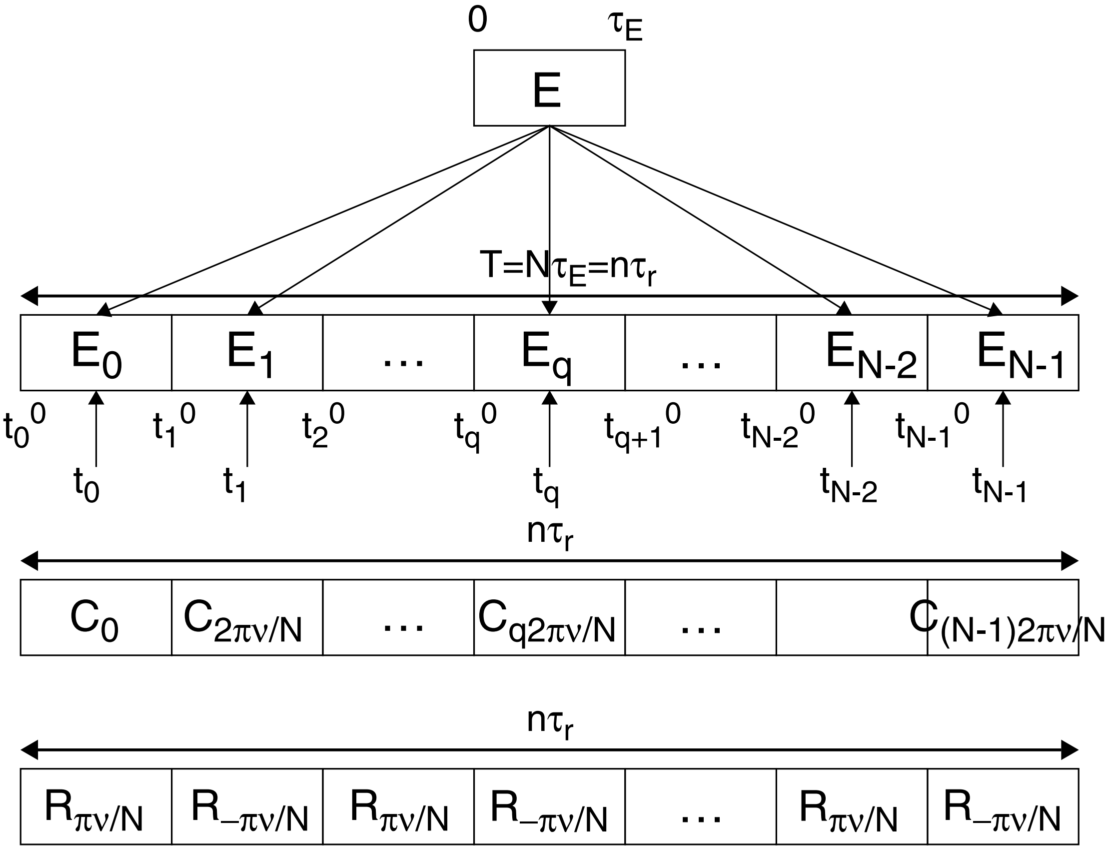

Figure 4.35: Definition of Rotor-Synchronized C-Type and R-Type Sequences.
The basic cycle E is used in a phase-shifted manner to build up the total pulse sequence which consists of N elements and spans n rotor cycles.

One can now transform the Hamiltonian into an interaction frame with the radio-frequency irradiation. Based on the symmetry relation of the rf irradiation of Eqs. [4.68] and [4.69], one can again express the Hamiltonian during the element q by the Hamiltonian during the first cycle and obtains

$$\hat{\mathcal{H}}'^{(i)}_{\ell m,\lambda\mu}(t_q) = \hat{\mathcal{H}}'^{(i)}_{\ell m,\lambda\mu}(t_0)\exp\left\{i\frac{2\pi}{N}q(mn-\mu\nu)\right\} \qquad [4.72]$$

for the C-type sequences and

$$\hat{\mathcal{H}}'^{(i)}_{\ell m,\lambda\mu}(t_q) = \hat{\mathcal{H}}'^{(i)}_{\ell m,\lambda\mu}(t_0)\exp\left\{i\frac{2\pi}{N}q(mn-\mu\nu)-\frac{\lambda N}{2}\right\} \qquad [4.73]$$

for the R-type sequences. The main difference is the additional term $\lambda N/2$ which comes from the additional $q\pi$ term in Eq. [4.69]. This has major consequences for the selection rules.

One can now calculate the average Hamiltonian over a full cycle of the pulse sequence by integrating the various components of the interaction-frame Hamiltonian. This can be a quite time-consuming procedure but there are some rules which allow based on symmetry rules to decide which terms are averaged to zero and which are not. For the C-type sequences one finds the following selection rule for the zeroth-order average Hamiltonian

$$\bar{\hat{\mathcal{H}}}^{(i)}_{\ell m,\lambda\mu} = 0 \qquad \text{if} \quad mn-\mu\nu \neq NZ \qquad [4.74]$$

where Z is any integer. For the R-type sequences one finds a similar selection rule for the zeroth-order average Hamiltonian

$$\bar{\hat{\mathcal{H}}}^{(i)}_{\ell m,\lambda\mu} = 0 \qquad \text{if} \quad mn-\mu\nu \neq \frac{N}{2}Z_\lambda \qquad [4.75]$$

where Z_λ is an integer which has the same parity (even or odd) as the spin-tensor rank λ of the considered interaction. There are similar selection rules for higher-order average Hamiltonians.

Equations [4.74] and [4.75] allow us to decide very easily whether a certain spin interaction is averaged out by a certain C-type or R-type pulse sequence. If the interaction is not averaged based on the symmetry properties of the pulse sequence, one has to calculate the scaling factor in order to know how large the averaged interaction is. This amounts basically to an explicit calculation of the zeroth-order average Hamiltonian which can also be done analytically for a general pulse sequence of this type. The scaling factor is strongly influenced by the choice of the basic cycle for the C-type or R-type sequence. There are no general rules which type of pulse sequence performs best for what sequence and only numerical simulations and experiments can tell.

One can use a space-spin selection diagram in order to graphically represent the selection rules imposed by the pulse sequence. This is illustrated in Figure 4.36 for the $C7_2^1$ pulse sequence. The graphical representation plots the combination of all possible values of mn with all possible values of $\mu\nu$. Only multiples of $N = 7$ are allowed and not averaged by the pulse sequence. Form Figure 4.36 we can see that the $m = 1$, $\mu = 2$ component and the $m = -1$, $\mu = -2$ component (not shown) of the dipolar-coupling tensor is not symmetry forbidden. All elements of the chemical-shift tensor are averaged due to the symmetry condition but the $m = 0$, $\mu = 0$ components of the isotropic chemical shift and the J coupling are symmetry allowed. The heteronuclear dipolar coupling behaves exactly like the chemical-shift tensor and is also averaged out. This shows that the $C7_2^1$ sequence is a homonuclear double-quantum recoupling sequence ($\mu = \pm 2$)which selects only the $m = \pm 1$ spatial component and is therefore γ encoded, i.e., independent of the Euler angle γ.

A second example for such space-spin selection diagrams is shown in Figure 4.37 for the $R18_1^7$ sequence. In this case only even or odd multiples of 18/2 are allowed depending on the parity of the spin rank λ of the interaction. From Figure 4.37 we can see that all elements of the dipolar-coupling tensor will be averaged out by the $R18_1^7$ sequence as well as all components of the isotropic chemical shift as well as the isotropic J coupling (not shown). Only the $m = 2$, $\mu = -1$ component of the chemical-shift tensor is symmetry allowed. The heteronuclear dipolar-coupling tensor

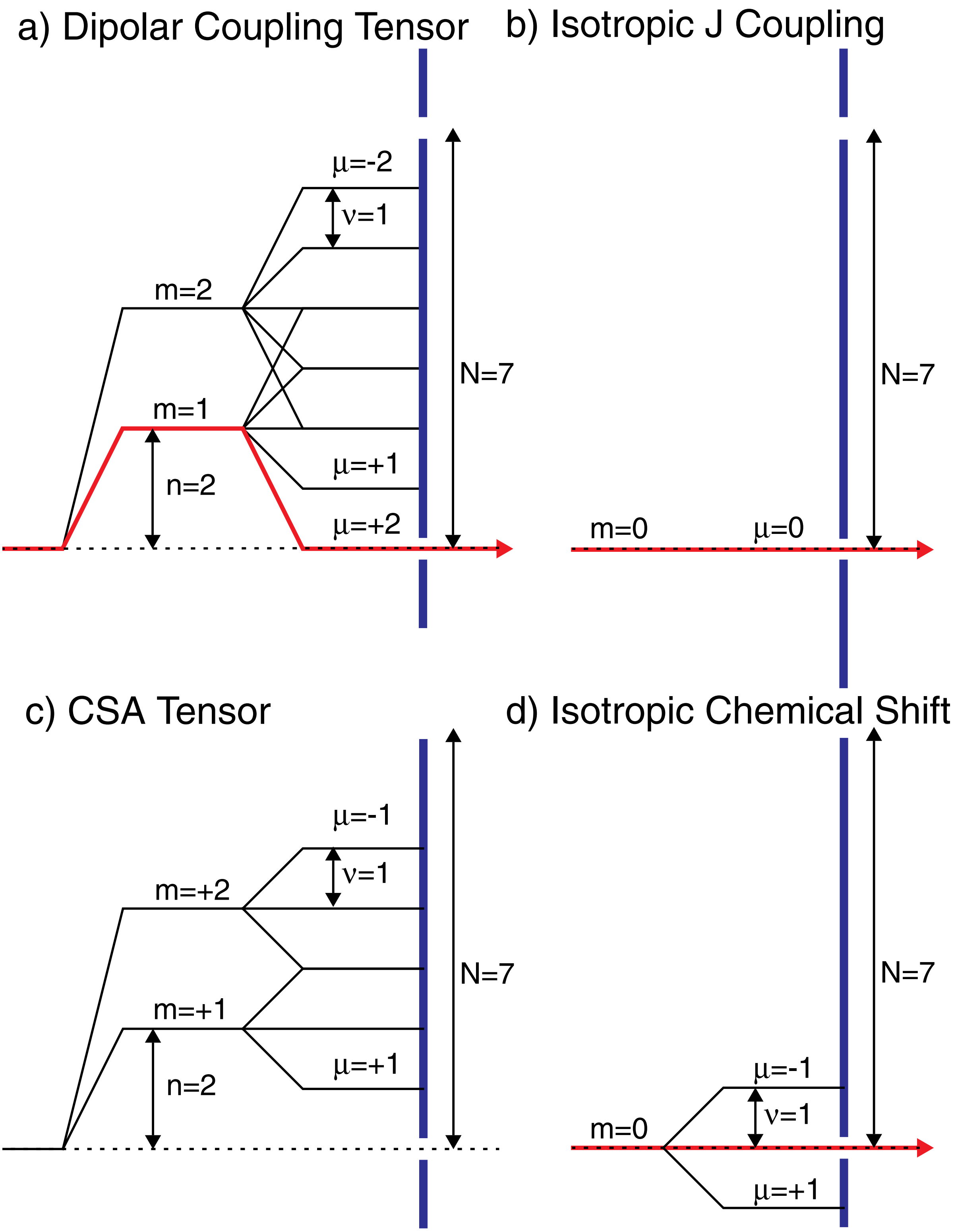

a) Dipolar Coupling Tensor

b) Isotropic J Coupling

c) CSA Tensor

d) Isotropic Chemical Shift

Figure 4.36: Space-Spin Selection Diagrams
Space-spin selection diagrams for the $C7_2^1$ pulse sequence showing only the $m \geq 0$ part. For this sequence the parameters are $n = 2$, $\nu = 1$, and $N = 7$. The diagrams show that the CSA tensor is averaged out while the $m = 1$, $\mu = -2$ part of the dipolar coupling is allowed. The isotropic contributions ($m = 0$, $\mu = 0$) of the J coupling and the chemical shift are also retained.

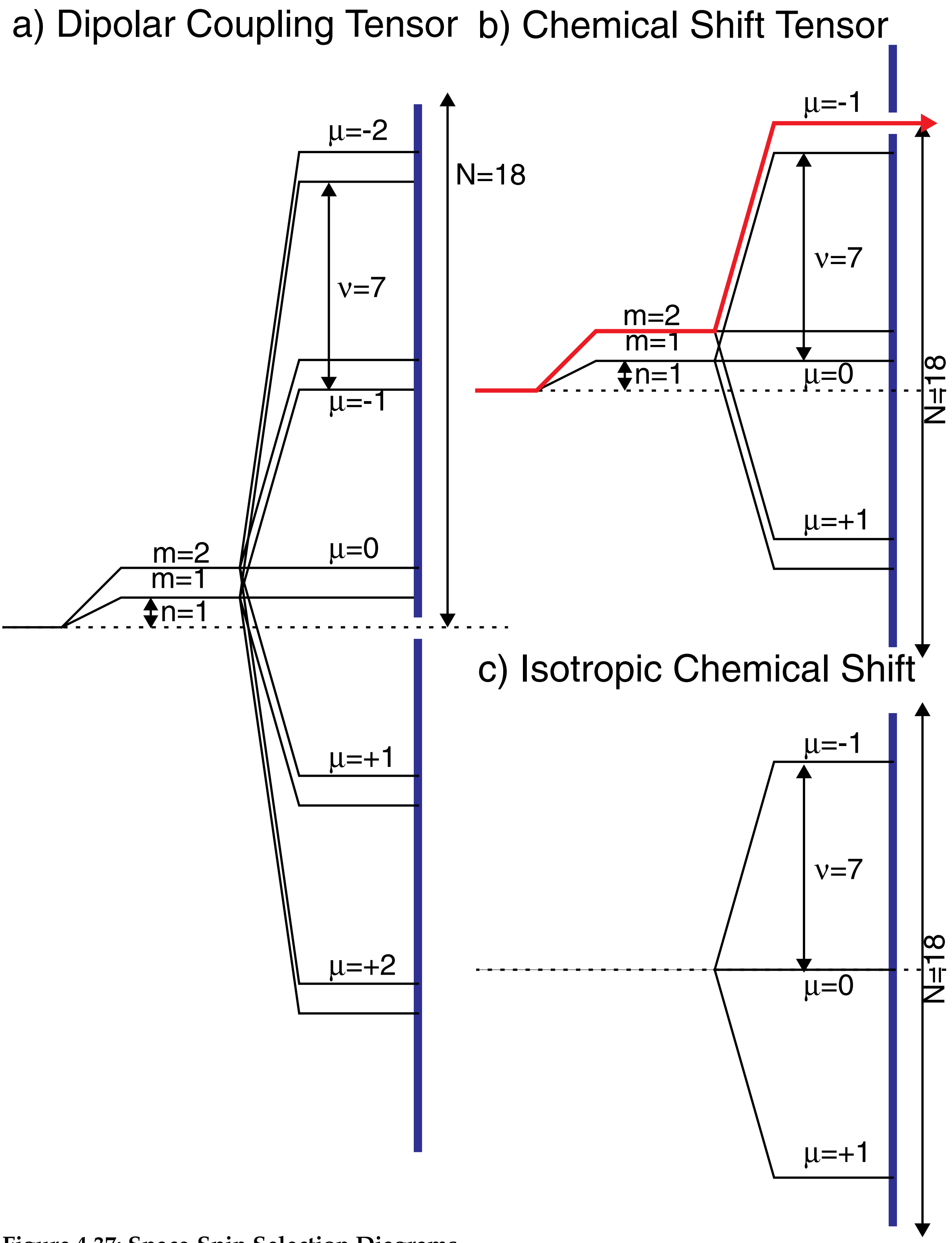

Figure 4.37: Space-Spin Selection Diagrams
Space-spin selection diagrams for the $R18_1^7$ pulse sequence showing only the $m \geq 0$ part. For this sequence the parameters are $n = 1$, $\nu = 7$, and $N = 18$. The diagrams show that the dipolar-coupling tensor is averaged out while the $m = 2$, $\mu = -1$ part of the chemical-shift tensor is symmetry allowed. The isotropic contributions ($m = 0$, $\mu = 0$) of the J coupling (not shown) and the chemical shift are also averaged out.

behaves in the same way as the chemical-shift tensor. Therefore, the $m = 2$, $\mu = -1$ component of the chemical-shift tensor is also symmetry allowed.

One can also implement supercycles on top of the C-type or R-type sequences to improve the suppression of unwanted pathways by eliminating higher-order average Hamiltonian terms. The principle of these rotor-synchronized pulse sequences has also been applied to heteronuclear experiments where two such sequences are applied to the two nuclei. The two sequences can be of the same type (C-type or R-type sequence) or different. Such heteronuclear sequences are beyond the scope of this lecture.

4.5.1.3 Examples

There is an infinite number of possible sequences which can be implemented using the C-type or R-type sequences. Their basic properties can be predicted by the symmetry rules discussed in the last chapter. Their detailed properties, however, can only be determined experimentally. here are many factors which play a role when selecting one of the many sequences. A key factor is certainly the MAS spinning frequency and the maximum rf-field requirements of the sequence. High MAS frequencies mandate the use of sequences which have a lower rf-field requirement. Another important factor is the required range of chemical-shift offsets which depends on the intended application. As an example, the experimentally measured offset dependence of various double-quantum recoupling sequences are shown in Figure 4.38. There are clearly large differences which cannot be explained by the zeroth-order average Hamiltonian approximation of the symmetry rules. This clearly indicates that higher-order average Hamiltonian terms play a significant role especially when offset effects are concerned.

Figure 4.39 shows an experimental example of a two-dimensional double-quantum single-quantum correlation spectrum of fully labelled tyrosine using the SC14 sequence.The SC14 sequence is a super-cycled sequence which has better offset compensation (see Figure 4.38) than the underlying basic $C14_4^5$ sequence. The spectrum was recorded at a static magnetic field of 9.4 T and the sequence covers the full range of chemical shifts of about 20 kHz. Judging from Figure 4.38 it would have not been possible to record such a spectrum with the basic $C14_4^5$ sequence. The spectrum was recorded with a short excitation time of 400 µs and a reconversion time of 100 µs. Only double-quantum peaks between directly bond atoms can be seen in the spectrum.

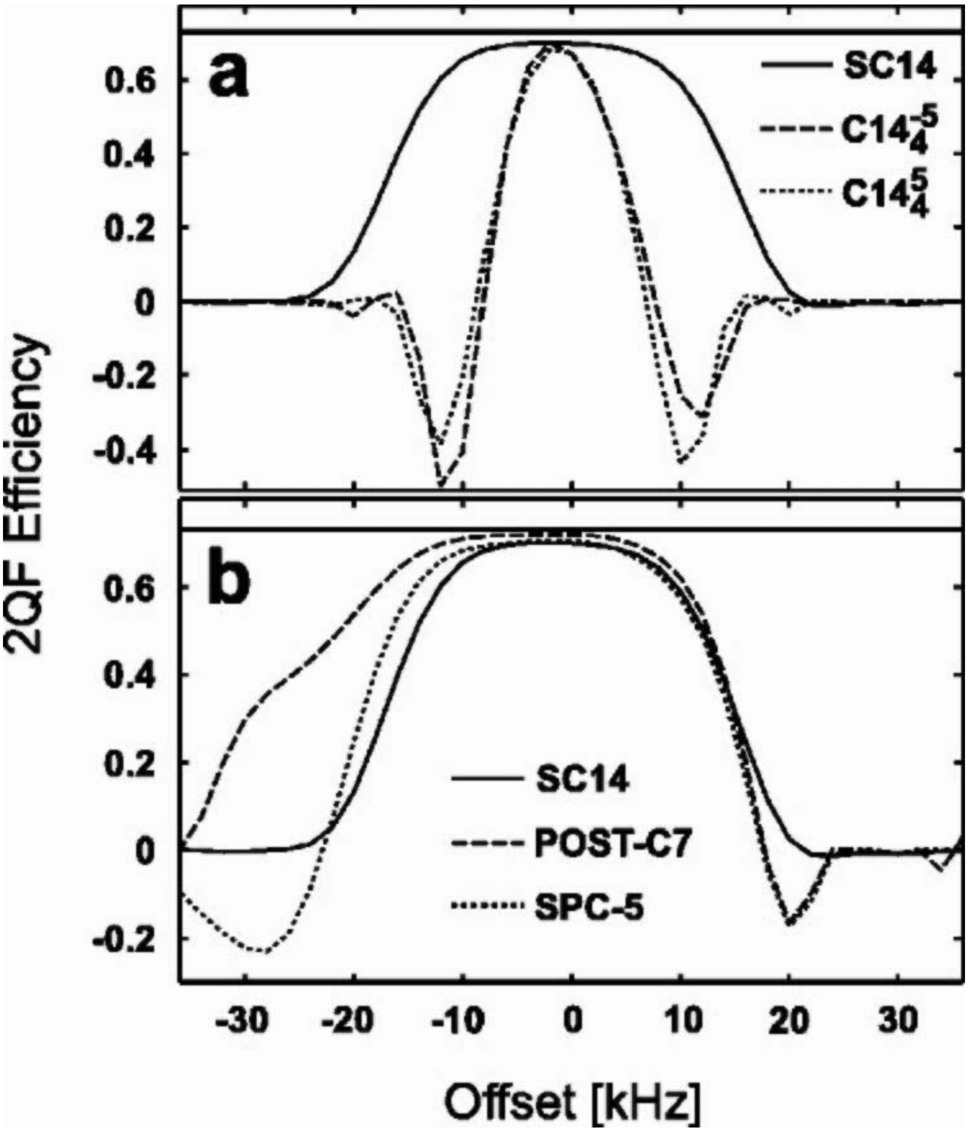

Figure 4.38: Offset Dependence of Various Double-Quantum Recoupling Sequences
Comparison of the offset dependence of the sequences $C14_4^5$, $C14_4^{-5}$, and the super-cycled SC14 sequence. In addition, a comparison with POST-C7 and SPC-5 is shown. (Copied from: Andreas Brinkmann, Mattias Edén, and Malcolm H. Levitt "Synchronous helical pulse sequences in magic-angle spinning nuclear magnetic resonance: Double quantum recoupling of multiple-spin systems." Journal of Chemical Physics **112**, 8539-8554 (2000).)

Figure 4.40 shows an experimental zero-quantum chemical-shift correlation spectrum of tyrosine for a long mixing time of 9.9 ms using a super-cycled $R6_6^2$ sequence. Cross peaks between all the carbon atoms can be observed for the long mixing time which indicates that the mixing sequence has distributed the magnetization almost evenly over all the carbon atoms and that the offset range of

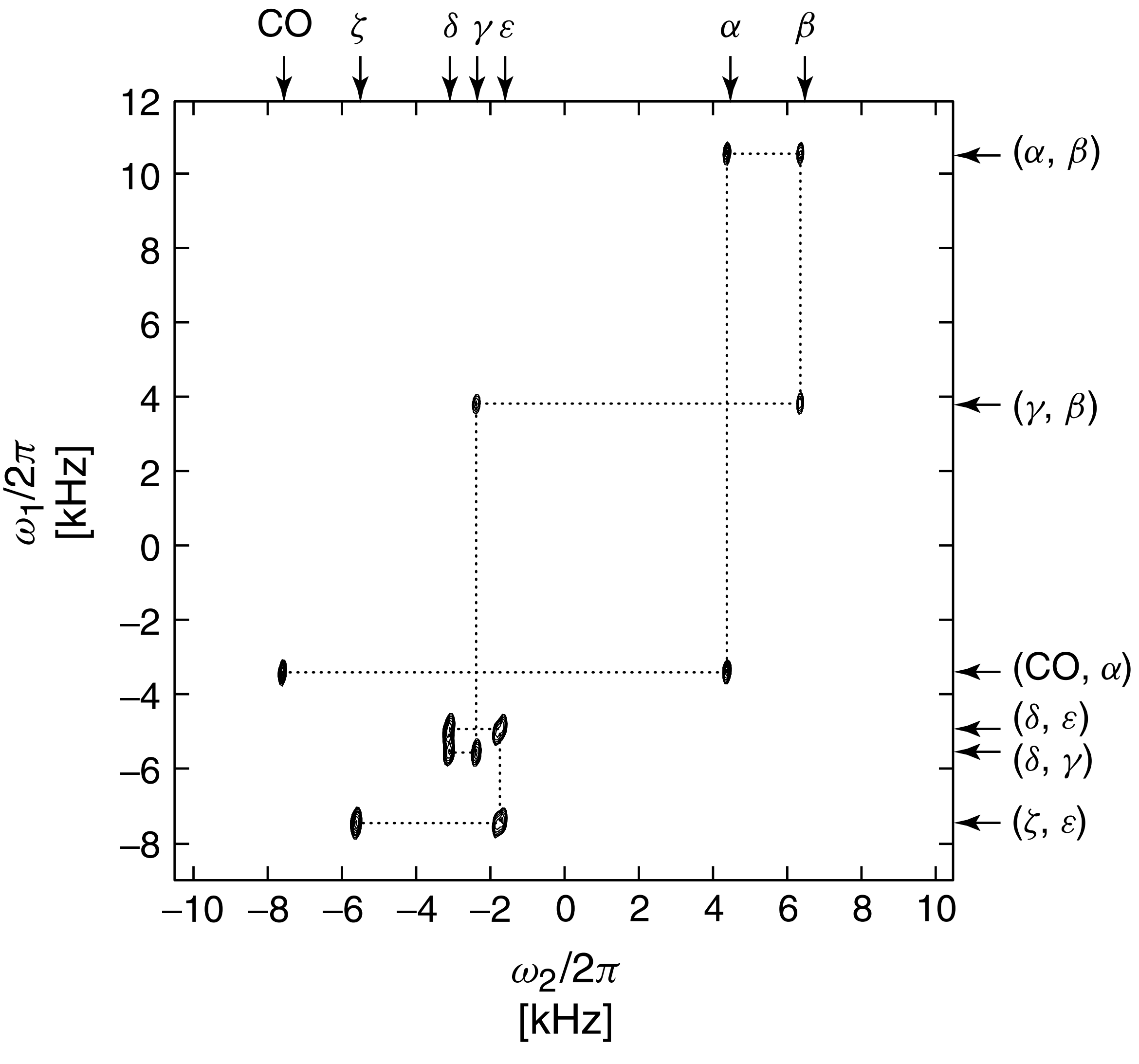

Figure 4.39: Double-Quantum Spectrum of Tyrosine Using the SC14 Sequence
Two-dimensional double-quantum spectrum of [U ^{13}C]- L-tyrosine, obtained at a field of 9.4 T and a spinning frequency of 20 kHz, using the SC14 pulse sequence which is derived from the $C14_4^5$ sequence. The dashed lines are guides for the eye. (Copied from M. H. Levitt, "Symmetry-Based Pulse Sequences in Magic-Angle Spinning Solid-State NMR" in "Encyclopedia of Nuclear Magnetic Resonance: Supplementary Volume" edited by D. M. Grant and R. K. Harris (Wiley, Chichester, England, 2002), pp. 165-196.)

this sequence is large enough to cover the full carbon chemical-shift range at a static magnetic field of 9.4 T.

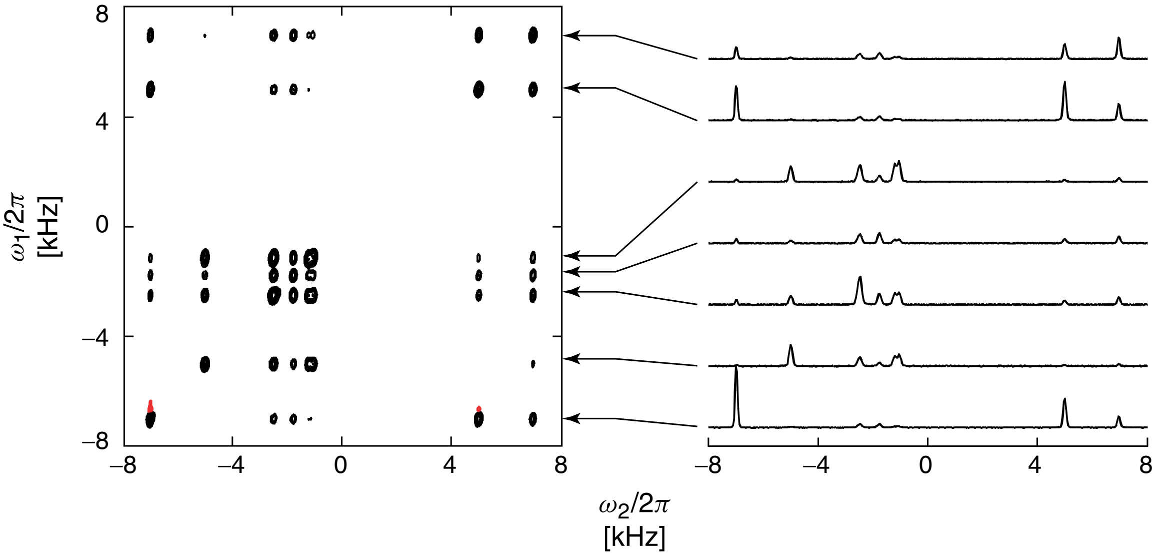

Figure 4.40: Zero-Quantum Spectrum of Tyrosine Using the $R6_6^2$ Sequence
Two-dimensional correlation spectrum of [U 13C]-L-tyrosine, obtained at a field of 9.4 T and a spinning frequency of 23 kHz, using a super-cycled $R6_6^2$ pulse sequence, with a mixing interval of 9.9 ms. (Copied from M. H. Levitt, "Symmetry-Based Pulse Sequences in Magic-Angle Spinning Solid-State NMR" in "Encyclopedia of Nuclear Magnetic Resonance: Supplementary Volume" edited by D. M. Grant and R. K. Harris (Wiley, Chichester, England, 2002), pp. 165-196.)